Université de Montréal

Étude de la cinématique HI (21cm) et Hα de la galaxie du Triangle (M33)

par

Sié Zacharie KAM

Département de Physique
Faculté des arts et des sciences
Université de Montréal

Thèse présentée à la Faculté des études supérieures et postdoctoral de l'Université de
Montréal en vue de l'obtention du grade de Philosophiæ Doctor (Ph.D.)
en Physique

Mai, 2015

Université de Montréal
Faculté des études supérieures et postdoctoral

Cette thèse intitulée :

Étude de la cinématique H I (21cm) et Hα de la galaxie du Triangle (M33)

présentée à l'Université de Montréal par :

Sié Zacharie KAM

est soumise à l' évaluation du jury composé des personnes suivantes :

Nicole St-Louis ,	**Présidente-rapporteuse et Représentante du Doyen de la FES**
Claude Carignan,	**Directeur de recherche**
Gilles Fontaine,	**Membre du jury**
Rodrigo A. Ibata,	**Examinateur externe**

Thèse acceptée le : 18 Juin 2015

Résumé

Cette thèse, intitulée *Étude de la cinématique* HI *(21cm) et H*α *de la galaxie du Triangle (M33)*, porte sur l'analyse de la cinématique et de la distribution de la matière noire dans la galaxie M33. M33 est une galaxie spirale appartenant au Groupe Local de galaxies. Elle est située à ~ 840 kpc et a une luminosité de 3.7×10^9 $L_\odot$ dans la bande V.

L'étude cinématique présentée dans ce document est basée sur des données Hα (optiques) obtenues à l'OMM et des données radio HI à 21 cm obtenues avec l'interféromètre du DRAO et l'antenne radio d' Arecibo. La cartographie Hα a permis d'obtenir une meilleure couverture des régions HII de M33 et a produit une bonne détermination de la courbe de rotation dans les régions internes en améliorant ainsi l'étude cinématique de M33.

Cette étude montre également une rotation croissante du gaz dans les régions externes pouvant atteindre des vitesses de l'ordre de ~135 km.s^{-1}(deux côtés) et une forte variation de l'angle de position dans les données HI, confirmant le disque gauchi de M33. Les données Hα ont permis de donner une plus grande précision dans la partie montante de la courbe de rotation. Nous présentons également dans ce document une étude à grande échelle de la dispersion des vitesses dans cette galaxie en utilisant les données Hα. Avec les données HI nous avons obtenu une courbe de rotation plus étendue et la vitesse au dernier point (~ 22 kpc) permet de trouver une masse $\sim 2 \times 10^{11} M_\odot$ jusqu'à ce rayon.

Les modèles de masse utilisant un halo de matière sombre (ISO, NFW, EIN) montrent une forte présence de matière sombre avec un rapport masse baryonnique à masse manquante $\lll 1$ au delà du disque optique . Les modèles de masse dérivés du formalisme MOND décrivent bien les régions intérieures mais convergent difficilement avec les données de haute résolution Hα et HI combinées.

Mots clés : techniques : interférométrie, champ intégral, Fabry-Perot – galaxie : individuelle : M 33 – galaxies : cinématique et dynamique – galaxies : ISM (Hα, HI, régions HII)– cosmologie : Matière sombre

Summary

This thesis, entitled *Étude de la cinématique* H*I (21cm) et* Hα *de la galaxie du Triangle (M33)*, focuses on the analysis of the kinematics and distribution of dark matter in the galaxy M33. M33 is a spiral galaxy of the Local Group of galaxies. It is located at ~ 840 kpc with a luminosity of 3.7×10^9 L$_\odot$ in the V band.

The kinematics study presented in this document is based on Hα data (optical) obtained at the OMM and HI data at 21 cm obtained with the DRAO interferometer and the Arecibo single dish radio telescope. Mapping Hα yielded a better coverage of the HII regions of M33, produced a good determination of the rotation curve in the inner regions and improved the kinematical study of M33.

The new study of the kinematics of the optical disk of M33 presented in this document, shows an increasing rotation of the gas in the outer regions reaching velocities of ~135 km.s^{-1}(both sides) and strong variations of the position angle. This confirms again the M33 warped HI disc. The Hα data allowed to get with great accuracy the rising portion of the rotation curve. We also present in this paper a large-scale study of the velocity dispersions in this galaxy using the Hα data. With the HI data, we were able to derive the rotation curve much further out (~ 22 kpc), which allowed us to derive a mass $\sim 2 \times 10^{11}$ M$_\odot$ at that point..

The mass models using a dark matter halo (ISO, NFW, EIN) show a strong presence of dark matter with a mass ratio baryonnic - missing mass $\lll 1$ beyond the optical disk. The mass models derived using the MOND formalism describe adequately the inner regions but hardly converge using the combined Hα and HI rotation curve.

Subjects headings : techniques : interferometric, integral field, Fabry-Perot – galaxies : individual : M 33 – galaxies : kinematics and dynamics – galaxies : ISM(Hα, HI, HII regions) – cosmology : dark matter

Crédits

Dans le cadre de ces travaux de thèse, j'ai utilisé les outils suivants :

- Le compilateur LaTeX pour la rédaction.
- L'Observatoire du Mont Mégantic, télescope de 1.6 m géré par le Centre de Recherche en Astrophysique du Québec (CRAQ).
- IDL (routines pour les données FP) , Montage, Karma, CIAO pour construire les routines de réduction et pour produire les courbes et les images.
- NASA/IPAC Extragalactic Database (NED).
- Les données des télescopes Spitzer et WISE pour des images de référence.
- Les images du National Radio Astronomy Observatory (NRAO).

Table des matières

Liste des tableaux

Table des figures

Abréviations

Å	Unité de longueur du Angström, soit 10^{-10} mètre
al	Année-lumière
BVRIJHL ,UGRIZ	Bandes de longueurs d'ondes
cm	Centimètre
e^{-}	Électron
g	Kilogramme
h	Constante de Planck
Hz	Hertz
K	Kelvin
K_B	Température d'antenne en Kelvin
Kg	Kilogramme
km s^{-1}	Kilomètre par seconde
$\mathrm{L}_{\odot}$	Luminosité solaire
$\mathrm{M}_{\odot}$	Masse solaire
pc	3.26 al
ϵ_o	Permittivité du vide
′	Minute d'arc
″	Seconde d'arc
^{o}C	Degrés Celcius
^{o}	Degrés

Abréviations suite

a_0	Constante dans le formalisme de MOND
B_o	Paramètre du continuum
C_{obs}	Nombre de comptes observé
CO	Monoxyde de Carbone
E_c	Énergie cinétique
E_p	Énergie potentielle
FAC	Facteur de conversion du nombre de comptes en unité de flux
F_g	Force gravitationnelle
G	Constante gravitationnelle
g	Accélération gravitationnelle
HI	Raie à 21 cm de l'hydrogène neutre
$H\alpha$	Raie de recombinaison de l'hydrogène à 6562.78Å
H_2	Hydrogène moléculaire
HII	Hydrogène ionisé
i, INCL	Inclinaison
I_o	Intensité
$L_{H\alpha}$	Luminosité $H\alpha$
M_{dark}/M_{lum}	Rapport de la matière sombre sur la matière lumineuse
M/L	Rapport de la masse sur la luminosité
M_{obs}	Magnitude apparente
OB	Étoiles de type spectral OB
PA	Angle de position
R_o	Rayon à $\rho = \rho_o$
R_{25}	Rayon optique
T	Température
V_{obs}	Vitesse observée le long de la ligne de visée
V_{sys}	Vitesse systémique de la galaxie
V_{rot}	Vitesse de rotation
v_o	Vitesse centrale
X	Masse d'air
w_λ	Largeur d'une fonction gaussienne
λ_c	Longueur d'onde centrale
σ	Dispersion

Abréviations suite

${\chi^2}_r$	Chi-carré réduit
$\Delta\lambda$	Différence en longueur d'onde
$\sigma_{H\alpha}$	Brillance de surface en Hα
λ	Longueur d'onde
ρ	Densité de masse
ρ_o	Densité de masse du coeur du halo de matière sombre

Liste des sigles

DM	Dark Matter
DN	Data Number
DRAO	Dominion Radio Astrophysical Observatory
EIN	Profil de Einasto
EMCCD	Electron Multiplying Charge Coupled Device
FP	Fabry-Perot
FSR	Free Spectral Range
FWHM	Full-Width Half Maximum (pleine largeur à mi-hauteur)
GIPSY	Groningen Image Processing System
IDL	Interactive Data Language
ISL	Intervalle Spectral Libre
ISM ou MIS	Milieu Interstellaire
ISO	Sphère Isotherme
ΛCDM	Simulation cosmologique : Lambda Cold Dark Matter
M33	Messier 33
MOND	Modified Newton Dynamics
MW	Milky Way (Notre Galaxie)
Ne	Néon
NED	NASA/IPAC Extragalactique Database
NFW	Profil de densité Navarro-Frenk-White
NGC	New General Catalogue
S/B, SN, S/N	Rapport signal sur bruit
SFR	Taux de Formation Stellaire
Spitzer	Télescope spatial IR

À mes très Chers Parents

Ladia & Pascal KAM

≪... Les choses révélées sont à nous et à nos enfants, à perpétuité...≫

Det 29 :29

Remerciements

Montréal a été une étape importante de ma vie d'étudiant. Dans l'aspect scientifique comme social j'ai appris et je me suis formé. Si aujourd'hui quelque chose existe dans les lignes de ce document, c'est à travers une multitude de circonstances, d'aides, de contributions et d'acceptation de qui je suis.

Mes remerciements vont à Claude CARIGNAN mon professeur qui m'a donné cette chance de goutter et d'explorer le monde de l'astronomie et de l'astrophysique. Un monde que j'ignorais totalement. Merci Professeur pour ta présence, pour ta compréhension et ta générosité. Ça été plus que faire le coach ; c'était un total soutien à une formation dans la vie. Malgré votre programme vous avez su me donner de votre temps. Je ne saurai réellement trouver les mots justes pour décrire cette trace que vous avez laissée en moi. Si le travail du Pr Carignan a été, c'est grâce à Monique Mujawamariya sa femme, que nous appelons affectueusement Tanti Monique. Merci Tanti d'avoir amené le Professeur à s'investir dans la formation d'une élite africaine (en particulier au Burkina Faso) en astrophysique. Merci pour cette générosité dont vous avez fait preuve pendant ces années d'étude.

J'exprime ma profonde gratitude à M. Jean Koulidiati, Professeur titulaire à l'Université de Ouagadougou, pour ce leadership dont il fait montre dans la mise en place du Projet d'astrophysique (et le physique en général) au Burkina Faso. Merci pour la confiance, l'attention et les conseils et ce grand travail au sein du LPCE. Je remercie le Ministère des enseignements secondaires supérieurs et de la recherche scientifique du Burkina, qui m'a soutenu financièrement à travers les bourses du CIOSP-B.

Marseille et Cape Town ont également été des étapes décisives dans mes études. Je garde de chacune de ces villes, de grand souvenirs. Je tiens à remercier grandement le Pr. Philippe Amram, Laurent Chemin et Benoît Épinat qui ont su me donner le coup d'accélérateur qu'il fallait dans mes travaux d'analyse. Merci pour ce temps que vous m'avez consacré pendant ma période de stage au LAM. Merci au tout le personel de l'OMM pour le soutien. Merci au directeur exécutif Robert Lamontagne pour les temps d'observation, merci aux techniciens Ghislain Turcotte et Bernard Malenfant pour ces soutiens dans le dôme, merci à Pierre Luc Lévesque et Phillippe Vallée pour leur grand soutien sur la mise en route des caméras, du *réducteur PANO I et les bancs de test. Merci à Bernard Breault et à Mme Christine Blais pour le soutien multiforme pendant les missions à l'OMM. Merci à Luc Turbide pour cet énorme soutien informatique, merci pour ton écoute et ton humour qui m'ont permis de passer de bons moments.*

Je tiens surtout à remercier ceux qui ont partagé avec moi le cursus universitaire ou les personnes avec lesquelles j'ai partagé le même bureau au Burkina, au Canada ou en Afrique du Sud. Merci pour les bons temps de discussions et d'échanges et les divergence de points de vue qui m'ont donné une nouvelle dynamique. Merci aux ainés qui m'ont écouté et soutenu. Je tiens à remercier Olivier Hernandez, Olivier Daigle, Etienne Artigau, Marie-Maude De Denus Baillargeon qui m'ont sans hésitation apporté leur aimable soutien. Merci à Philippe Balard et Jean Luc Gach qui m'ont apporté leur soutien et conseils pour la mise en route des caméras de l'OMM.
Je dis merci au personnel administratif du département de physique de l'université de Montréal qui m'a énormément aidé dans mes procédures administratives. Merci à Mme Anne Gosselin, Mme Lynda Syvrais, M. Louis Lemay et aux directeurs. Merci au corps enseignant du département de physique pour le plaisir d'avoir partagé vos acquis.
Une occasion pour remercier les amis de Montréal pour ces merveilleux moments qu'ils ont partagés avec moi. Merci à Yentéma Onadja, Amina Watalusu, Ousseynou Diop, Juste Somé, Yacouba Djabo. Un grand merci à la famille Philippe Coulidiati, à Tonton Didier Belem et les frères de l'Eglise Baptiste des Nations. À Amidou Sorgho et Blaise Tabsoba de Cape Town, Marie Korsaga, Issa Ouattara du LAM, Issouf Kafando de Laval, tous mes remerciements pour votre soutien et encouragement. Merci à Gaston Kané, Cyril Somé, Marcel Kebré et amis de promo UO pour la complicité. Un grand Merci à Esther Hien qui m'a énormément supporté. Merci pour ton courage et ton grand soutien, ta présence et ta compréhension pendant ces moments d'étude.
Je tiens à remercier l'ensemble de mon jury de thèse pour avoir accepté de remplir ce grand et noble rôle. Merci pour vos remarques, vos suggestions, conseils et orientations qui ont permis de rendre un produit de qualité.

Je finis par dire merci à mes parents Pascal Kam et Ouobi Kam, à mes frères, soeurs, tontons, tantis et Cous qui ont su me comprendre et me soutenir. Merci pour ce sacrifice que vous aviez fait pendant ses multiples années. Papa, Maman, Merci pour vos prières, vos conseils, merci pour la grande sagesse et ce grand respect dont vous avez fait preuve face à mes choix académiques.

Introduction

Chapitre 1

Introduction

Sommaire

Résumé

Nous présentons dans cette partie les généralités sur les galaxies, leur formation et leur cinématique. Une attention particulière est portée sur le Groupe Local de galaxies et sur M33 en particulier. Pour une introduction des deux traceurs utilisés dans cette thèse, nous avons fait une description de l'atome d'hydrogène, ensuite nous avons donné une description de quelques constituants de l'univers et enfin donné les méthodes d'étude de la cinématique.

1.1 Généralités

L'univers observable, comme il se révèle à nous, est principalement constitué de gaz et de poussière dans des états, des compositions et des densités différentes. Ensemble, ces éléments peuvent former des structures beaucoup plus complexes comme les systèmes planétaires, les nébuleuses, les étoiles, les amas d'étoiles, les galaxies, les amas de galaxies, les super amas de galaxies ! Chacun des constituants de l'univers a une particularité et une histoire. L'atome d'hydrogène joue non seulement un rôle important dans cette histoire mais occupe également une place de choix dans la constitution de l'univers observable.

1.1.1 L'hydrogène dans le milieu interstellaire

1.1.1.1 L'atome d'hydrogène

L'atome d'hydrogène, premier élément de la table de Mendeleïev, est l'élément atomique le plus simple (1 proton + 1 électron) et le plus abondant dans l'univers. L'étude de cet atome est aussi bien importante en mécanique quantique qu'en physique ou chimie atomique et moléculaire. Sa compréhension passe par l'analyse de ses états, de ses niveaux d'énergie ainsi que de son spectre.

- *Modèles* :
  Plusieurs modèles sont proposés pour décrire l'atome d'hydrogène. Le premier modèle est celui dit de *"l'atome de Bohr*[a]". Dans ce modèle, l'atome d'hydrogène est décrit comme un ensemble proton-électron. L'électron gravite autour du proton sur une orbite circulaire de rayon r. La quantité de mouvement p est liée à l'onde λ par la constante de Planck h ($p = \frac{h}{\lambda}$). Les ondes stationnaires de l'atome sont celles qui décrivent un nombre entier d'orbites : $2\pi r = n\lambda$ ou $r = np\frac{\hbar}{2\pi}$. Sachant que le moment cinétique L est décrit par $\vec{L} = \vec{r} \wedge \vec{p}$; et en considérant m la masse de l'électron et $-e$ sa charge, on arrive à prouver que le rayon est sous une forme quantifiée avec $r = n^2\frac{4\pi\epsilon_0\hbar^2}{me^2}$.
  De même on a une quantification de l'énergie avec $E_n = -\frac{E_0}{n^2}$, où $E_0 = \frac{me^4}{2\hbar^2}$ = -13.6 eV et n ne prend que des valeurs entières : 1, 2, 3... À l'état fondamental (n=1) le rayon de l'orbite de l'électron est de l'ordre de 10^{-11} m soit 10000 fois plus que le rayon du noyau. L'énergie

---

[a] Niels Bohr [1885 -1962] est un physicien danois, prix Nobel de physique de 1922. Il proposa en 1913 un modèle pour l'atome d'hydrogène et à la fin de 1930 il proposa "le modèle de la goutte" pour décrire tous les noyaux atomiques.

peut donc varier en fonction de la position que l'électron occupe. Le modèle de Bohr fait penser aux travaux de Balmer généralisés par Rydberg et Ritz sur les séries de raies de l'atome d'hydrogène.

D'autres modèles comme *le modèle quantique, le modèle de la structure fine et le modèle de la structure hyperfine* sont des modèles proposés pour décrire l'atome d'hydrogène

- Les états d'énergie, les orbitales et le spectre

L'hydrogène est l'élément le plus abondant dans l'univers, principal combustible dans les étoiles durant la plus grande fraction de leur vie. Il se retrouve dans le milieu interstellaire et intergalactique sous différentes formes. La variation de son état, selon son environnement, permet de détecter sa présence à cause de son rayonnement. La Figure 1.1 donne des transitions et niveaux d'énergie de l'atome d'hydrogène ; elle montre également les raies possibles.

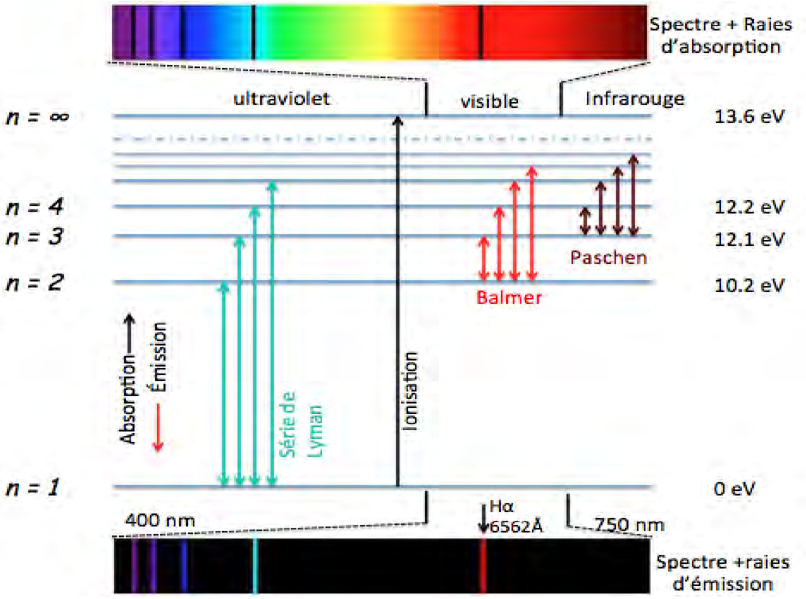

FIGURE 1.1: Séries de transitions de l'atome d'Hydrogène et le spectre visible.

L'électron sur sa couche externe se trouve dans un potentiel V donné par l'équation (1.1) pour un orbite de rayon r.

$$V = -\frac{e^2}{4\pi\epsilon_o r} \tag{1.1}$$

L'énergie de cet atome est bien décrite par les équations (1.2) et (1.3) qui sont les équations de Schrödinger.

$$\hat{H}_0\psi - E\psi = 0 \quad avec \quad \hat{H}_0 = \frac{\hat{p}^2}{2\mu} - \frac{e^2}{4\pi\epsilon_0 r} \tag{1.2}$$

soit

$$\frac{\hbar^2\Delta\psi(\vec{r})}{2\mu} + (E + \frac{e^2}{4\pi\epsilon_0 r})\psi(\vec{r}) = 0 \tag{1.3}$$

où μ est la masse relative de l'ensemble proton+electron en mouvement. Dans les équations (1.2) et (1.3) (données pour états stationnaires), ψ est la fonction d'onde spatiale, une composante de la fonction d'état $\psi(\vec{r}, \sigma)$. La fonction d'état se décompose en une fonction d'onde spatiale $\psi(\vec{r})$ et une fonction d'onde de spin $\tau(\vec{\sigma})$.

À chaque instant, on peut associer à toute distance r du noyau, une probabilité $dP(r,t)$. Elle donne la probabilité de trouver l'électron dans un volume dV autour d'un point situé à r du centre de masse. P(r) est la densité de probabilité décrite par l'équation (1.4)

$$dP(r,t) = ||\psi(r,t)||^2 dV \tag{1.4}$$

$||\psi(r,t)||^2$ définissant ainsi la densité de probabilité.

L'état quantique d'un atome H est décrit par les nombres quantiques n (principal), l (azimutal) et m (tertiaire) (son énergie est dite quantifiée). On peut ajouter le spin s décrivant l'orientation de l'électron pour la description des structures hyperfines. Le nombre quantique principal est un entier positif, $0 < l < n - 1$, $-l < m < l - 1$ et le spin prend les valeurs $\pm 1/2$. À chaque orbitale correspond une valeur possible de l'énergie, solution de l'équation de Schrödinger. Une bonne compréhension de l'atome d'hydrogène, de ses états d'énergie et de ses interactions avec d'autres éléments permet de décrire les étoiles et le milieu interstellaire.

L'hydrogène neutre HI et l'émission Hα sont deux grandes formes de l'hydrogène (puissants traceurs) qui sont utilisées dans l'étude de la cinématique des galaxies et des ensembles de galaxies.

1.1.1.2 L'hydrogène neutre HI

Les ondes radio sont à des longueurs d'onde centimétriques (du centimètre à une dizaine de mètres) soit des fréquences autour de la dizaine à des milliers de MHz. La raie de 21 cm a été prédite et découverte par Van der Hulst en 1944. Cette raie dérive d'une perturbation hyperfine de l'atome d'hydrogène. En effet, comme l'indique la figure (1.2), le passage du noyau et de l'électron de cet atome à des spins opposés engendre une émission à la longueur d'onde de 21 cm.

À l'émission HI on peut associer la fréquence $\nu_{H\textsc{i}} \sim 1420.4$ MHz et une température de spin $T_s \sim 150$ K. Son moment dipolaire magnétique est $\mu^*_{10} = 9.27 \times 10^{-21}\mathrm{erg.Gauss}^{-1}$, sa détection dans les galaxies (HI à 21 cm) s'étend à grand échelle. Elle permet de décrire les interactions entre galaxies dans un même amas de galaxie.

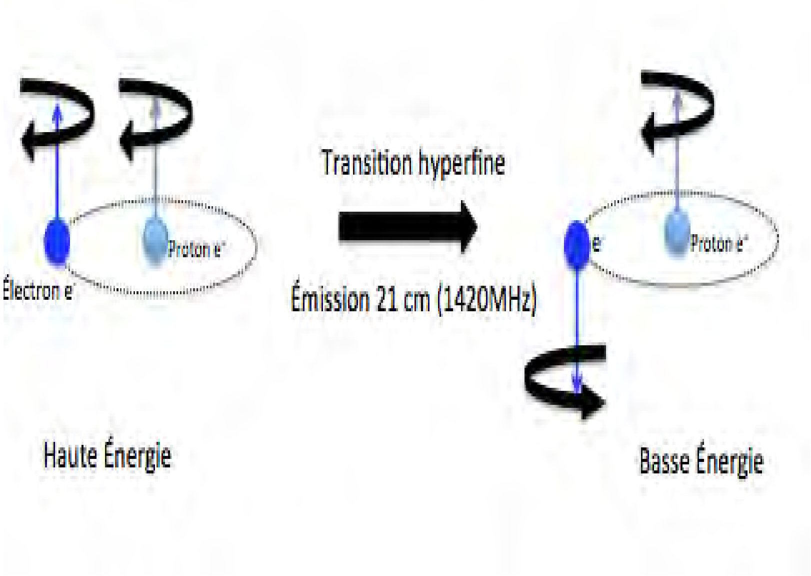

FIGURE 1.2: Transition Hyperfine de l'atome d'hydrogène : émission HI

1.1.1.3 Le gaz ionisé Hα

La raie Hα est observable à la longueur d'onde de 656.3 nanomètre, dans la partie rouge du spectre visible. L'étude de cette raie est le moyen le plus simple pour les astronomes de tracer le contenu en *hydrogène ionisé* des nuages de gaz.

Cette raie est intense car l'énergie nécessaire pour ioniser l'hydrogène est quasiment la même que celle nécessaire pour faire passer un électron du niveau n = 1 au niveau n = 3. La probabilité qu'un électron ne soit pas éjecté de l'atome mais passe vers ce niveau n = 3 reste très faible. Après ionisation, l'électron et le proton vont se recombiner pour former un nouvel atome d'hydrogène. Dans ce nouvel atome, l'électron peut se trouver sur n'importe quel niveau d'énergie, et ensuite, va cascader vers le niveau fondamental (n = 1), en émettant un photon lors de chaque transition. Environ une fois sur deux, cette cascade comprend la transition n = 3 vers n = 2 et l'atome va alors émettre la raie Hα. Cette raie décrit donc un atome à l'état ionisé.

1.1.2 Les grandes structures

1.1.2.1 Les galaxies

Plusieurs milliards d'étoiles de différents types (les plus jeunes brulant dans leurs coeurs l'hydrogène qui produit l'énergie nécessaire pour ioniser leur environnement) peuvent se trouver en équilibre gravitationnel avec du gaz et de la poussière, dans un ensemble appelé galaxie. Le nombre d'étoiles dans une galaxie peut aller d'une dizaine de milliards pour les galaxies naines, à des milliers de milliards pour les plus massives. Les galaxies ont des masses stellaires de l'ordre $\sim 10^{11}$ $M_\odot$ et présentent souvent des trous noirs massifs au centre. Les travaux de Hubble (1926) ont permis de mettre en place différents types morphologiques (figure 1.3).

1. *Types, morphologie*

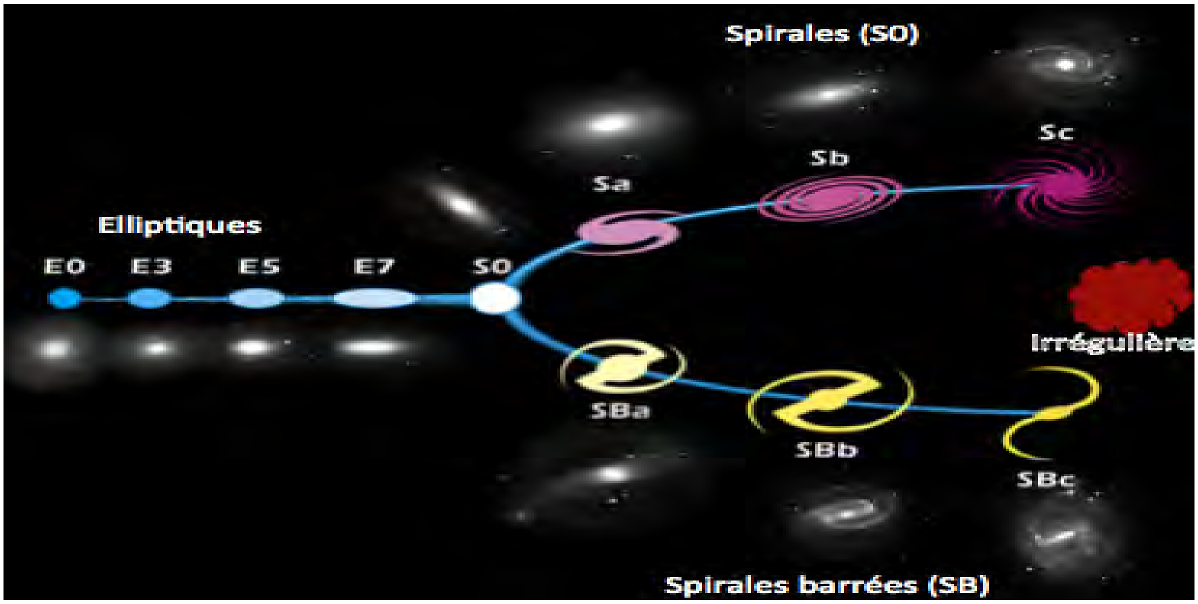

FIGURE 1.3: Classification des galaxies selon Hubble : l'image, originale crédit PD-Hubble, montre une classification qui met un accent sur le déploiement des bras et cette classification est également reprise dans Kormendy & Bender (2012)

La figure 1.3 donne une classification des galaxies selon Hubble (1926). On note, des
galaxies elliptiques (E0 à E7)
galaxies lenticulaires (SO, SBO) 0, 0a
galaxies spirales (barrées ou non-barrées).

Dans le schéma de classification de Hubble (Hubble, 1926), les spirales sont constituées d'un disque en rotation composé d'étoiles et de gaz interstellaire. Elles possèdent un bulbe central constitué d'étoiles généralement plus anciennes (Carroll & Ostlie, 1996). De ce bulbe partent des bras spiraux.

Dans la classification de Hubble, on distingue des galaxies spirales régulières (S ou SA) et les galaxies spirales barrées (SB). Les deux classes de spirales présentent des sous classes a, b et c suivant l'enroulement des bras, l'importance du noyau et la luminosité. Les sous classes d et m ont été introduites par de Vaucouleurs (1959). Pour plus de précision sur la morphologie d'une galaxie, il existe des classes intermédiaires comme des Sab, Sbc et autres. On peut également ajouter des notations r, s ou rs (ringed, spindle ou intermédiaire), AB (intermédiaire entre normale et barrée) et les SBm, Sm, SABm (galaxies spirales dites de type magellanique) pour mieux donner une idée sur la morphologie de la galaxie que l'on décrit.

En plus des elliptiques et des spirales peut s'ajouter le groupe des galaxies naines. Elles ont une taille pouvant atteindre 1% de celle de la Voie lactée, et contiennent seulement quelques milliards, voir quelques centaines de millions d'étoiles.

galaxies irrégulières (Ir ou Im) :

Les galaxies irrégulières manquent de bulbe central et sont non-axisymétriques et moins résolues. Il est difficile d'identifier leurs structures spirales, mais certaines présentent souvent des amas d'étoiles jeunes permettant de supposer des bras potentiels.

2. *Formation et évolution :*

   Le modèle standard de la cosmologie, à l'instar de plusieurs modèles cosmologiques proposés, donne une bonne description de l'ensemble des observations de l'univers. Le modèle standard décrit la formation et l'existence des différents éléments de la nature depuis le big bang. La formation des galaxies déstabilisa l'Univers, jadis homogène comme décrit par l'observation du fond diffus cosmologique (CMB). Les premières galaxies sont nées des *fluctuations primordiales de densité*. Avec la baisse des températures dans l'univers, se formaient et s'accumulaient les premiers halos de matière noire. Des zones plus denses attirèrent vers les halos de matière noire le gaz (principalement l'hydrogène et l'hélium) pour former des protogalaxies d'où naitront les premières étoiles.

   L'amoncellement hiérarchique (Abraham & van den Bergh, 2001; Ellis et al., 2000) est le modèle qui décrit le mieux la formation des galaxies par rapport au modèle classique. En effet dans le modèle de l'amoncellement hiérarchique, les fluctuations de l'univers homogène donnent lieu à la formation de halos de matière sombre. La fusion de ces halos de matière sombre entrainera l'apparition de milieux propices à la formation stellaire. Il se forme ainsi par effondrement un disque à l'intérieur d'un vaste halo de matière sombre.

Les étoiles et les amas globulaires se forment. Le disque devient plus mince par contraction et l'augmentation de la formation stellaire donne naissance aux bras spiraux. Avec les agitations de l'univers, les galaxies spirales fusionnent pour donner d'autres types. Selon Dressler (1980), l'environnement joue un grand rôle dans l'évolution des galaxies. Il propose deux mécanismes décrivant la formation des galaxies plus évoluées :

La fusion de deux spirales pour donner une elliptique.

L'effet de l'environnement, la pression, l'influence du milieu intergalactique, l'attraction des galaxies plus massives dans un amas : l'effet "ram pressure", peut transformer une galaxie spirale en une galaxie lenticulaire en la vidant de sa composante gazeuse. Cela expliquerait la forte concentration des elliptiques et des lenticulaires au centre des amas et une densité plus forte de spirales dans la périphérie.

D'autres mécanismes comme les collisions, les interactions gravitationnelles ou le "cannibalisme" des galaxies contribueraient à l'évolution des galaxies.

1.1.2.2 Les amas et superamas de galaxies.

Les amas de galaxies sont des ensembles dans lesquels les galaxies se retrouvent reliées gravitationnellement. Un amas est formé d'au moins une centaine de galaxies. L'espace intergalactique dans les amas est constitué de gaz de faible densité et parfois à haute température $10 - 100 \times 10^6$ K. Le Groupe Local (figure 1.4) est le groupe de galaxies dans lequel se trouve la Voie Lactée. Notre galaxie forme avec une trentaine d'autres galaxies cet amas Local, largement dominé par des galaxies naines (Ellis, 1997; Mateo, 1998).

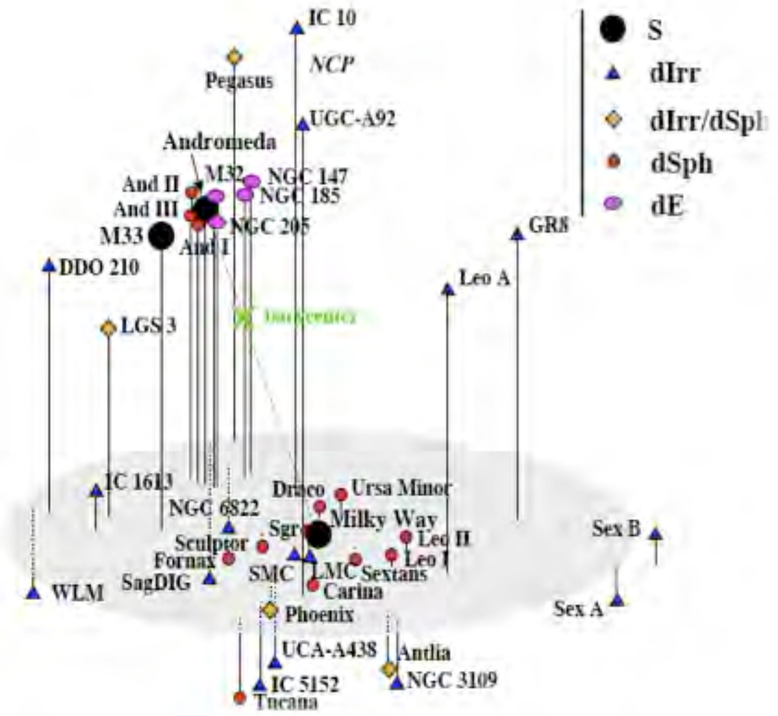

FIGURE 1.4: Représentation du Groupe Local. La figure montre des galaxies naines qui se regroupent autour de la Voie Lactée centrée dans un plan en bas et autour de M31 (Andromède) en haut. On voit bien M33 voisine de M31. La légende en haut à droite donne les types morphologiques (source : http ://www.astro.uu.se/ns/).

Les amas de galaxies comme celui de la Vierge comprendraient plus de 2000 galaxies. Les amas se regroupent en superamas avec potentiellement plus de 100 000 galaxies. L'existence des superamas est vérifiée. Ils sont prévus par les simulations numériques du genre "simulation du millenium" (Springel et al., 2005). Les effets des structures comme le "Great Attractor" sont observables (Lynden-Bell et al., 1988). En effet, les grands amas observables semblent se diriger vers cette zone de l'univers. Les simulations cosmologiques qui mettent en évidence ces grandes structures révèlent également l'existence des filaments intergalactiques. La question de structures comme les filaments galactiques plus grands que les superamas reste discutable.
Au delà des observables, l'univers renferme des mystères aussi bien sur ses débuts, sur sa masse, ses constituants que son futur.

1.1.2.3 La matière noire et l'énergie sombre

La formation et l'existence des différentes structures de l'univers sont vérifiées dans le modèle standard par le scénario de l'amoncellement hiérarchique (Frenk et al., 1985; Baugh et al., 1996;

Cole & Lacey, 1996; White & Rees, 1978). En effet, dans le modèle ΛCDM, toutes les structures dérivent de l'effondrement de halos de matière sombre et la stabilité des grands ensembles comme les galaxies, les amas de galaxies et les supers amas de galaxies nécessite plus que la matière visible ou mesurable. Une forte quantité de la matière est manquante dans les bilans d'observations : $\sim$ 33% dans le voisinage solaire à 99% dans les amas de galaxies. Cette situation a été soulevée par Zwicky dès 1933 (Zwicky, 1937) avec l'exemple de Coma puis Smith (Smith, 1936) avec l'amas de la Vierge et Freeman à l'échelle des galaxies suite a l'étude de NGC 300 (Freeman, 1970; Ostriker & Peebles, 1973).

Sa nature reste encore méconnue ; elle serait de nature baryonique : matière ordinaire dont on connait l'existence mais qui reste invisible (étoiles à neutrons, trous noirs, hydrogène moléculaire, etc...). Cette classe a fait l'objet de programmes comme les programmes MACHO[b], EROS[c] ou AGAPE[d] en direction d'Andromède et du Grand Nuage de Magellan. Sa seconde nature serait non baryonique (e.g. neutrinos, WIMP[e], dérivés supersymétriques du modèle standard) et serait la principale composante.

D'un autre côté, l'énergie sombre constitue $\sim$73% de la densité d'énergie totale de l'univers tandis que la matière noire elle représente 23% et la matière baryonique 5%. Cette énergie permet de justifier l'expansion de l'univers et peut être liée à la constante cosmologique Λ (de l'équation d'Einstein).

Les galaxies Messier[f] 31 (M31) et Messier 33 (figure 1.5), sont voisines de notre galaxie. Ces deux galaxies sont aussi reliées par un passé commun (Lockman et al., 2012). Les travaux de Wolfe et al. (2013); Cockcroft et al. (2013); McConnachie et al. (2010, 2009) prouvent que ces deux galaxies ont subies entre elles des interactions pendant leur évolution.
Ces galaxies appartiennent au Groupe Local de galaxies (figure 1.4), qui est un ensemble de galaxies voisines de la nôtre : la Voie Lactée ("la Galaxie" ou Milky Way (MW) en anglais).

Contrairement à certains amas qui sont majoritairement constitués de galaxies massives, l'amas Local comporte seulement quatre galaxies spirales (La Voie Lactée, M31, M33 et en considérant le grand nuage de Magellan) et plusieurs galaxies naines.

L'absence au sein du Groupe Local d'elliptiques géantes, est simplement due à sa petite taille ($\sim$3.1 Mpc). Mais c'est un groupe assez représentatif des groupes de galaxies à cause de sa

---

[b] MAssive Compact Halo Objects

[c] Expérience pour la Recherche d'Objets Sombres

[d] Andromeda Galaxy Amplified Pixel Experiment

[e] Weakly Interactive Massive Particules

[f] On écrit M pour désigner le Catalogue de Messier. Charles Messier [1730-1817] est un passionné de comètes mais est beaucoup connu pour ses travaux sur les objets du ciel profond.

population : une quarantaine de galaxies constituées de plusieurs types morphologiques dont des naines sphéroïdales, des naines elliptiques, des irrégulières et des spirales.

M33 a probablement été identifiée en premier par Hodierna avant 1654. Elle est un des premiers objets reconnus comme galaxie (Hubble, 1929). De grandes régions HII appartenant à ses bras spiraux, les objets comme NGC[g] 604 et de NGC 595, font de cette galaxie un objet très souvent observé.

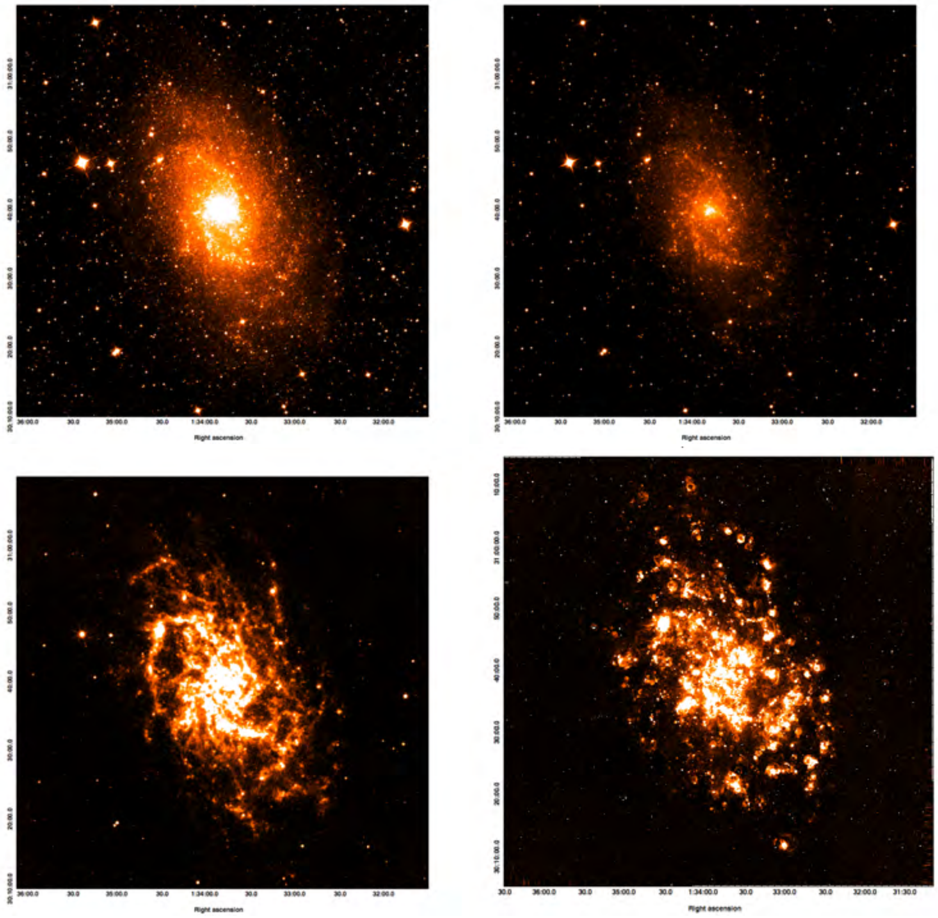

FIGURE 1.5: M33 dans différentes bandes d'observation (WISE w1, w2, w3 & $H\alpha$)

M31 et M33 constituent, avec la Voie Lactée, les trois galaxies les plus massives du Groupe Local. La Voie Lactée et M31 sont les centres de deux sous-groupes. Le premier sous-groupe est constitué de la Galaxie et de ses compagnons les nuages de Magellan, le Grand Chien, le Sagittaire, la Petite Ourse, le Dragon, la Carène, Sextans, Sculpteur, le Fourneau, le Lion et le Toucan. Le second est formé de Messier 32 (NGC 221), NGC 205, NGC 147, NGC 185, And[h] I,

---

[g] NGC : New General Catalogue, Catalogue d'objets astrophysiques.

[h] Andromède (And) : désignant des galaxies naines voisines de M31

And II, And III, And IV et la galaxie du Triangle (M33) (Collins et al., 2010), qui est la troisième galaxie la plus massive du Groupe Local regroupées autour de M31.

L'appartenance de M33 au sous-groupe de M31 est encore mal défini. Mais il est clair que ces deux galaxies ont eu des interactions dans le passé. L'étude du gaz HI à grand échelle montre une structure complexe de M33 (Grossi et al., 2008). Le milieu interstellaire de M33 est assez bien accessible et présente une grande diversité des structures interstellaires. Elle reste un exemple assez bien indiqué pour la compréhension et l'étude des galaxies plus lointaines, d'où l'intérêt de l'étude de sa cinématique.

1.2 Cinématique des galaxies

L'étude de la cinématique des galaxies, se donne pour objectif de mieux comprendre la distribution de matière dans les galaxies et aussi d'expliquer la morphologie de ces galaxies. La détermination précise des paramètres cinématiques permet de mieux expliquer toutes les observations (les attentes et les anomalies). Plusieurs phénomènes conduisent ou influencent la rotation d'une galaxie. Les principaux sont l'accrétion de matière, la formation d'étoiles et le mouvement du gaz interstellaire.

La rotation dans les galaxies permet de donner une stabilité au disque. En effet, cette rotation tend à compenser la force gravitationnelle en s'opposant à l'effet de la masse qui tend à amener la galaxie à l'effondrement. Une rotation insuffisante engendre une instabilité gravitationnelle appelée instabilité de Jeans. Le critère de Jeans est décrit par une longueur critique λ_J définie par l'équation (1.5).

$$\lambda_J = \sqrt{\frac{\sigma^2}{\pi G \Sigma}} \tag{1.5}$$

Dans cette équation σ désigne la dispersion de vitesse du gaz et Σ la densité surfacique. Une rotation efficace stabilise le disque. Le critère qui permet de décrire la stabilité d'un disque à une longueur L_{rot} est donné par l'équation (1.6) :

$$L > L_{rot} = \sqrt{\frac{\pi G \Sigma}{\kappa^2}} \tag{1.6}$$

où $\kappa^2 = rd\Omega^2/dr + 4\Omega^2$ désigne la fréquence épicyclique d'un point situé à un rayon r dont le mouvement est doté d'une fréquence angulaire Ω. Les instabilités sont mesurables par la dispersion des vitesses σ avec $\sigma^2 = \sigma_{th}^2 + \sigma_{per}^2$. La dispersion $\sigma_{th} = \sqrt{k_B T/m}$ est dérivée des perturbations thermiques et σ_{per} dérive des turbulences macroscopiques. Les instabilités dans le disque des galaxies peuvent entrainer la formation stellaire. Cette formation stellaire peut s'exprimer par le taux de formation stellaire selon l'équation 1.7 (SFR : Star Formation Rate), qui est lié à la densité surfacique de gaz (Kennicutt, 1998).

$$\Sigma_{\rm SFR} = (2.5 \pm 0.7) \times 10^{-4} \left(\frac{\Sigma_{\rm gas}}{1{\rm M}_{\odot}.{\rm pc}^2} \right)^{1.4\pm0.15} {\rm M}_{\odot}{\rm yr}^{-1}{\rm kpc}^{-2} \tag{1.7}$$

La rotation des galaxies révèle une grande particularité des galaxies en tant que corps stable en rotation. Les résultats de Vera Rubin (Rubin & Ford, 1970) sur la rotation de M31, montrèrent une courbe de rotation (CR) plate dans les régions extérieures (figure 1.6) ; donc des vitesses quasi constantes aux grands rayons. Sur cette courbe les carrés pleins sont les données optiques de Rubin & Ford (1970), tandis que les cercles remplis sont les données prises en H I selon l'axe majeur. La courbe de droite de la Figure 1.6 présente également le même type de plateau à grands rayons (r > 16 kpc) dans la rotation de NGC 3198.

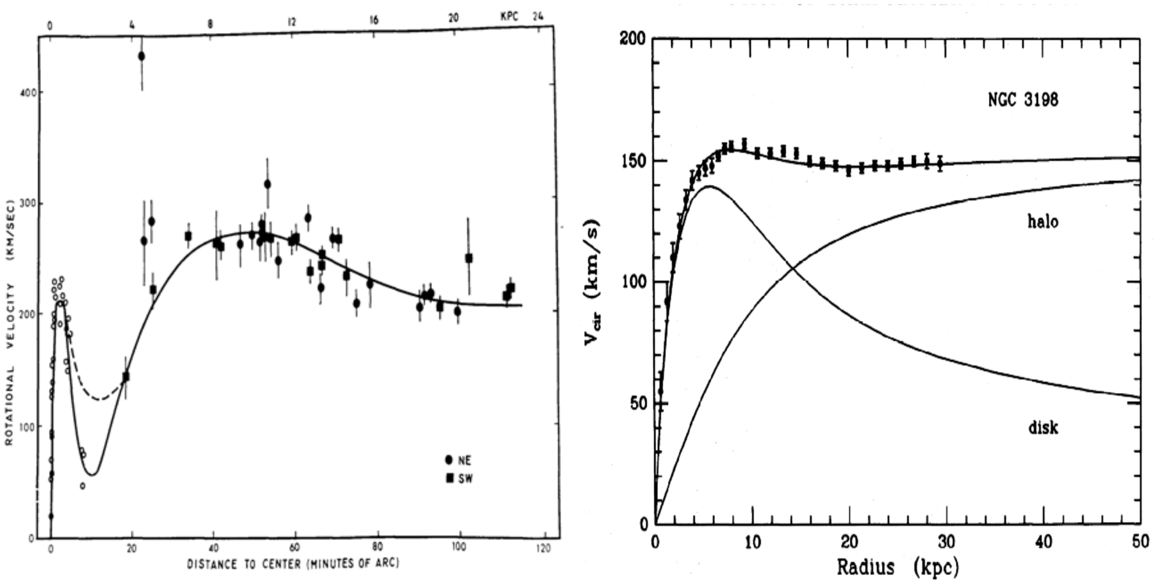

FIGURE 1.6: À gauche la courbe de M31 tirée de Rubin & Ford (1970) et à droite une courbe de rotation de NGC 3198 de van Albada et al. (1985) ; dans les deux cas la courbe de rotation montre une vitesse de rotation constante dans les régions extérieures contrairement aux attentes.

Les observations de Rubin & Ford (1970) décrites dans la Figure 1.6 (à gauche) sont soutenues par celles de Roberts & Whitehurst (1975) ; ces études confirmèrent la présence d'une quantité de masse inattendue dans le halos des galaxies. Dans la Figure 1.6 à droite, van Albada et al. (1985) montrent la nécessité d'une masse supplémentaire dans le halo pour décrire la courbe de rotation observée. Dans ces deux cas, seule une description newtonienne avec $v \propto \sqrt{\frac{GM}{r}}$ du

disque stellaire et du gaz, de la composante visible, ne saurait expliquer sa rotation.
L'idée de masse supplémentaire avait été suggérée par Fritz Zwicky[i] dans ses travaux sur l'amas de la Coma (Zwicky, 1933, 1937). En effet, Zwicky avait appliqué le théorème du viriel à ses observations de l'amas de la Coma et arrivait à la conclusion qu'il existait de la masse supplémentaire non évaluée donc invisible, permettant de justifier l'équilibre des amas (garder les galaxies rattachées à l'amas).

À partir de la dispersion des vitesses, d'une approximation du rayon de l'amas et du théorème du viriel, ils furent en mesure d'estimer la masse totale de l'amas pour ensuite expliquer les vitesses observées de ces galaxies. Le théorème du viriel stipule que l'énergie cinétique (E_c) est reliée à l'énergie potentielle (E_p) selon l'équation (1.8). Dans cette équation v peut être considérée comme la dispersion des vitesses. Le décalage Doppler dans l'observation de raies connues des galaxies est la véritable source d'information dans la détermination des vitesses.

$$E_c \;=\; -\frac{1}{2}E_p = \frac{1}{2}Mv^2 = -\frac{1}{2}\frac{GM^2}{2r} \tag{1.8}$$

Bien connaitre la cinématique d'une galaxie passe par une bonne observation d'un traceur et une bonne instrumentation. Un traceur optique nécessite une instrumentation optique et la construction de chaque instrument est basée sur les propriétés des traceurs.
**L'observation du H*I : L'hydrogène neutre reste le plus important dans les galaxies. Le HI est froid et est détectable à des longueurs d'onde centimétriques. Observer le comportement de ce gaz permet de bien comprendre la cinématique des galaxies à grande échelle. Le HI reste le traceur qui est en mesure de décrire l'enveloppe la plus externe des galaxies et de montrer les interactions entre les galaxies dans un amas. Les télescopes radio, coupole unique ou placés en configuration d'interféromètre, permettent d'étudier cette composante. Une propriété intéressante du HI est qu'il est optiquement mince. Cela permet d'intégrer l'ensemble du flux de la galaxie, le long de la ligne de visée.
**La spectroscopie optique* : Dans le visible, la spectroscopie reste un moyen assez efficace. Il existe plusieurs types de spectrographe. Les différences résident principalement dans le mode d'observation et du type d'instrument. Dans cet instrument l'élément dispersif joue un rôle très important : *longue fente* ; *FTS* ; *Michelson* ; *Fabry Pérot* ; *Multifibre*.

Le HI, le CO (traceur de H_2) et le Hα sont les principaux traceurs de la cinématique des galaxies. L'utilisation de ces traceurs permet de déduire la masse dynamique dans les galaxies.

---

[i] Fritz Zwicky [1898–1974] astronome suisse qui a découvert les étoiles à neutrons et a beaucoup travaillé sur la matière noire

Cette masse permet de déterminer une estimation de la masse totale dans le disque et le halo. La contribution des étoiles vient de la prise en compte des différentes populations stellaires dans la galaxie étudiée. Ces populations laissent des traces dans le spectre des galaxies. Les étoiles jeunes et les plus chaudes, à l'instar des étoiles O et B de la séquence principale, sont celles qui marquent le plus le spectre optique des galaxies. Pour bien modéliser la masse des galaxies, il est important de considérer la rotation du disque, des étoiles, du gaz , du bulbe, du trou noir central s'il y'a lieu et prendre en compte le halo de la galaxie. A défaut de considérer un halo qui dominerait les régions externes il faut modifier les lois de Newton : utiliser le modèle du Modified Newtonian Dynamics (MOND).

1.3 Modèle de masse

Un modèle de masse est l'ensemble constitué par les paramètres permettant d'expliquer la courbe de rotation d'une galaxie. La bonne determination d'une courbe de rotation permet de donner un meilleur modèle.

1.3.1 Vitesse de rotation dans les galaxies

1.3.1.1 Détermination du champ de vitesse

L'équation (1.9) donne le principe de la détermination du moment un. Le moment un M_1 permet de construire la carte de vitesses.

$$\mathrm{M}_1 = \frac{\sum \nu \mathrm{A}(\nu)}{\sum \mathrm{A}(\nu)} \tag{1.9}$$

Les outils comme *GIPSY* :Groningen Image Processing System (Allen et al., 1985; van der Hulst et al., 1992; Vogelaar & Terlouw, 2001), *CASA* : Common Astronomy Software Applications (McMullin et al., 2007), *AIPS* :Astronomical Image Processing System[j], *KARMA* (Gooch, 1996), *MIRIAD* (Sault et al., 1995), ont tous des routines qui permettent de calculer les moments des cubes de données. La carte de moment un est utilisée pour déterminer les courbes de rotation.

---

[j] http ://www.aips.nrao.edu/index.shtml

1.3.1.2 Tilted ring model

La tâche $rotcur$ dans $GIPSY$ permet de déterminer les paramètres cinématiques d'une galaxie à partir de la carte de vitesses. Cette tâche permet de fixer ou de laisser libre les paramètres et de considérer dans la minimalisation, à chaque rayon des valeurs différentes pour les paramètres. *VELFIT* et *Diskfit* sont également des outils qui permettent de trouver les paramètres cinématiques. Dans la détermination de ces paramètres chacun de ces outils utilise le modèle d' ellipses concentriques : "tilted ring model". Cette technique de 'tilted ring' est bien décrite par Begeman (1989). Pour chacun des anneaux concentriques, est défini un angle de position (PA), une inclinaison (i) et une vitesse de rotation (V_{rot}). Dans ce cas la vitesse systémique est maintenue constante. Pour un points (x, y) situé sur un anneau de rayon R du modèle, la vitesse selon la ligne de visée est donnée par l'équation (1.10).

$$V(x, y) = V_{sys} V_{rot}\ sin(i)\ cos(\theta) + V_{exp} sin(i)\ cos(\theta) \tag{1.10}$$

où θ est l'angle de position dans le plan du disque de la galaxie, V_{exp} la vitesse d'expansion. Dans le cas des galaxies dans le voisinage du Groupe Local des galaxies, la vitesse d'expansion est considérée comme nulle. La valeur réelle de l'angle de position PA est liée à θ par les équations (1.13) et (1.12).

$$sin(\theta) = \frac{-(x - x_0) sin(PA) + (y - y_0) cos(PA)}{R} \tag{1.11}$$

$$cos(\theta) = \frac{-(x - x_0) cos(PA) + (y - y_0) cos(PA)}{R sin(i)} \tag{1.12}$$

$$\cos(\theta) = \frac{-(\mathrm{x} - \mathrm{x}_0)\sin(\mathrm{PA}) + (\mathrm{y} - \mathrm{y}_0)\cos(\mathrm{PA})}{\mathrm{R}}, \tag{1.13a}$$

$$\sin(\theta) = \frac{-(\mathrm{x} - \mathrm{x}_0)\cos(\mathrm{PA}) - (\mathrm{y} - \mathrm{y}_0)\sin(\mathrm{PA})}{\mathrm{R}\cos(\mathrm{i})} \tag{1.13b}$$

où (x_0, y_0) sont les coordonnées du centre cinématique. Les relations entre R, θ et le rayon projeté sur le ciel r et l'angle ψ sont :

$$\mathrm{R} = \mathrm{r}\sqrt{\cos^2(\psi) + (\sin(\psi)/\cos(\mathrm{i}))^2} \tag{1.14a}$$

$$\tan(\theta) = \tan(\psi)/\cos(\mathrm{i}) \tag{1.14b}$$

avec $\mathrm{r} = \sqrt{(\mathrm{x}-\mathrm{x}_0)^2 + (\mathrm{y}-\mathrm{y}_0)^2}$.

Autres méthodes

La détermination des paramètres cinématiques peut se faire en utilisant d'autres techniques. Une méthode d'optimisation (Epinat, 2008), donnant des résultats semblables au tilted ring model, à été utilisée dans nos travaux. L'inclinaison photométrique de la galaxie est obtenue par :

$$\sin^2 i = \frac{1 - 10^{2\mathrm{logr}_{25}}}{1 - 10^{2\mathrm{logr}_0}} \tag{1.15}$$

où r_0 est donné par $\mathrm{logr}_0 = 0.43 + 0.053\mathrm{t}$, et t allant de -5 à 7 désigne le type morphologique de de Vaucouleurs. Pour des valeurs de t plus grand que 7, logr_0 est 0.38 (Paturel et al., 1997).

La nature des vitesses de rotation calculées aux grands rayons fait qu'il est nécessaire de considérer soit un halo de matière sombre soit de redéfinir les équations de Newton.

1.3.2 Composante visible : Etoiles et Gaz

La composante visible des étoiles et celle du gaz restent les premières auxquelles on pense quant vient le moment de calculer la masse d'une galaxie. Dans la majorité des galaxies, la composante visible renferme une faible proportion de la masse qui soutient la rotation.

1.3.2.1 Le gaz

La composante gazeuse est principalement représentée par le gaz neutre dans la galaxie. La contribution du gaz est donnée par le profil de densité du gaz. En utilisant les données des observations radio, la tâche $ELLINT$ de $GIPSY$ peut être utilisée pour extraire le profil densité de masse. $ELLINT$ détermine à chaque rayon de la galaxie la valeur de la densité de masse (en $\mathrm{M}_\odot/\mathrm{pc}^2$). Pour une bonne exécution de la tâche, il faut déterminer en premier lieu :

- Les rayons pour lesquels les densités seront déterminées. Ces rayons sont choisis en tenant compte de la taille du faisceau afin d'éviter de sur-échantillonner.
- La masse totale du gaz HI peut se calculer en utilisant l'équation(1.16) :

$$\frac{\mathrm{M}_{\mathrm{HI}}}{\mathrm{M}_\odot} = 2.36 \times 10^4\ \mathrm{D}^2 \int \mathrm{Fdv} \tag{1.16}$$

où F et le flux intégré et dv la résolution de vitesse.

- Son inclinaison aux rayons pour lesquels la densité doit être déterminée.
- Son angle de position à tout rayon.

Le profil de densités de masse donné par $ELLINT$ est utilisé par la tâche $ROTMAS$ de $GIPSY$ pour déterminer la contribution en vitesse du gaz.

1.3.2.2 Les étoiles

La seconde composante du visible dans les galaxies est représentée par les étoiles. Les observations à 3.6 μm donnent une bonne représentation de la composante du disque stellaire. Dans le cas de M33 l'étude à $3.6\mu m$ de $SPITZER$ permet d'aller jusqu'à 30 arcmin. Les données $2MASS$ sont moins sensibles. Les bandes optiques (B,V) ne vont pas à grands rayons et peuvent être affectées par la poussière interstellaire, l'âge et la métalicité. La détermination du rapport Masse/Luminosité dans le visible présenterait beaucoup plus d'incertitudes. Idéalement, toutes les différentes composantes stellaires devraient participer à la détermination de cette densité. Cette densité de masse stellaire se détermine par l'étude de la brillance de surface. Pour une plus grande précision, une étude de la distribution spectrale d'énergie est nécessaire, car elle prendra en compte les différentes composantes stellaires. Nous adoptons une méthode de synthèse de populations avec une seule bande en IR. Cette méthode est décrite par Oh et al. (2008).

La détermination de la brillance de surface $\mu_{3.6\mu m}$ à $3.6\mu m$ dans les galaxies peut se faire en utilisant les données d'archives de $SPITZER$. La brillance de surface est donnée par l'équation (1.17) (Oh et al., 2008).

$$\mu_{3.6\mu\mathrm{m}} = -2.5\,\log\left(\frac{\mathrm{S}_{3.6\mu\mathrm{m}} \times 2.35 \times 10^{-5}}{\mathrm{ZP}_{3.6\mu\mathrm{m}}}\right) \tag{1.17}$$

où $S_{3.6\mu m}$ est la valeur du flux dans la bande de $3.6\mu m$ et exprimée en MJy/sr^{-1}, et $\mathrm{ZP}_{3.6\mu\mathrm{m}}$ est le point zéro en magnitude (280 Jy). La contribution stellaire réelle est liée à la valeur du rapport masse luminosité. Oh et al. (2008) et de Blok et al. (2008a) montrent que le M/L est lié à la couleur de la galaxie. Pour déterminer $\Upsilon_*^{3.6}$, l'équation (2.24) est utilisée.

$$\Upsilon_*^{3.6} = B^{3.6}\ \times\ \Upsilon_*^{K} + A^{3.6} \tag{1.18}$$

Pour trouver la valeur de Υ_*^K l'équation (1.19) donne la relation avec la couleur de la galaxie.

$$\log(\Upsilon_*^{\mathrm{K}}) = \mathrm{b}^{\mathrm{K}}\ \times\ \mathrm{Color}\ +\ \mathrm{a}^{\mathrm{K}} \tag{1.19}$$

Les équations (2.24) et (1.19) donnent ensuite les équations (2.25) et (1.21).

$$\Upsilon_*^{3.6} = 0.92\ \times\ \Upsilon_*^{K} + 0.05 \tag{1.20}$$

$$\log(\Upsilon_*^{\mathrm{K}}) = 1.46(\mathrm{J} - \mathrm{K}) - 1.38 \tag{1.21}$$

La couleur (J-K) est calculée par Jarrett et al. (2003), pour un grand nombre de galaxies. Le M/L et la brillance de surface sont utilisés pour déterminer la densité de masse stellaire définie par l'équation (3.15).

$$\Sigma[\mathrm{M}_\odot pc^{-2}] = \Upsilon_*^{3.6} \times 10^{-0.4\times(\mu_{3.6}-C^{3.6})} \tag{1.22}$$

1.3.3 Contribution d'un halo de matière sombre

1.3.3.1 Vitesse et potentiel gravitationnel d'un halo de matière sombre

Le modèle $\Lambda\mathrm{CDM}$ (pour Lambda Cold Dark Matter) désigne un modèle cosmologique représentant un univers homogène et isotrope ; ayant une courbure spatiale nulle et contenant de la matière sombre, de l'énergie sombre en plus de la matière ordinaire (baryonique). Pour mieux quantifier la distribution de masse dans les galaxies, on définit des modèles de potentiels ou de couples densité-potentiel. Les modèles les plus utilisés prennent en compte le halo de matière sombre prévue par le ΛCDM pour expliquer la rotation des galaxies. La vitesse totale de rotation est dérivée du potentiel de rotation Φ. L'équation (1.23) donne l'expression de ce potentiel.

$$V_{rot}^2 = \frac{r\partial\Phi}{\partial r} \tag{1.23}$$

Le potentiel $\Phi(r)$ lié à cette vitesse est dérivé de l'équation de Poisson bien décrite dans l'équation (1.24).

$$\Delta\Phi(r) = 4\pi G\rho(r). \tag{1.24}$$

Dans l'équation (1.24), Φ est donné par l'expression de l'équation (1.25) :

$$\Phi = \Phi_\star + \Phi_{gaz} + \Phi_{ms} \tag{1.25}$$

où $\Phi_\star$, Φ_{gaz} et Φ_{ms} désignent respectivement les potentiels des étoiles, du gaz et de la matière sombre. La composante Φ_{gaz} représente le potentiel du gaz neutre, celui du gaz moléculaire ou celui du gaz ionisé. Le potentiel décrit dans l'équation (1.25) montre que la vitesse de rotation (équation 3.18) est une somme quadratique des vitesses de toutes les composantes dynamiques de la galaxie.

$$V_{rot}^2 = V_\star^2 + V_{gaz}^2 + V_{ms}^2 \tag{1.26}$$

La méthode utilisée pour modéliser de la distribution de masse consiste dans la majorité des cas, à donner une description de la densité de halo de matière sombre donnant un bon profil de la courbe de rotation de la galaxie. Une généralisation de celle présentée dans Carignan & Freeman (1985) est décrite dans Blais-Ouellette (2000) (Kravtsov et al., 1998) dans l'équation (1.27).

$$\rho(r) = \frac{\rho_0}{[c + (r/r_0)^{\gamma}][1 + (r/r_0)^{\alpha}]^{(\beta-\gamma)/\alpha}} \tag{1.27}$$

Dans cette équation ρ_0 et r_0 représentent respectivement la densité caractéristique et le rayon caractéristique. La densité caractéristique correspond à celle déterminée au centre de la galaxie. L' équation (1.27) prend en compte la composante lumineuse (étoiles et gaz) et la contribution de la composante non-lumineuse, qui peut être représentée par un halo sphérique de matière sombre.

Blais-Ouellette (2000) donne dans l'équation (1.27) un modèle plus général. De cette équation peut se déduire d'autres modèles de profils utilisés. La variation de $(c, \alpha, \beta, \gamma)$ dans l'équation (1.27) peut donner des modèles comme ceux de la sphère pseudo isotherme (ISO) (Zhao, 1996), de Burkert, KKBP (Kravtsov et al., 1998), de Navarro-Frenk-White (NFW) (Navarro et al., 1996a, 1997, 2004)

1.3.3.2 Le model pseudo-Isothermal (ISO), Profil de densité Navarro-Frenk-White (NFW) et Profil de Einasto (EIN)

pseudo-Isothermal (ISO) : En posant des contraintes sur les paramètres $(c, \alpha, \beta, \gamma)$ = (1, $\alpha \neq 0$,2,2) de l'équation (1.27), on obtient le modèle de la sphère pseudo isotherme (ISO) proposé par Begeman (1987) . Ce modèle contraint bien la distribution de masse dans les galaxies.
Dans ce cas, le potentiel décrivant la matière sombre (équation 3.19) est fonction du rayon, de la densité centrale ρ_0 et de R_c le rayon caractéristique. À ce potentiel est lié une vitesse de rotation, $\mathrm{V_{ISO}(R)}$, du halo de la galaxie.

$$\rho_{ISO}(R) = \frac{\rho_0}{1 + (\frac{R}{R_c})^2} \tag{1.28}$$

L'équation (3.20) permet de donner à chaque R du centre de la galaxie la vitesse de rotation liée à la matière sombre.

$$\mathrm{V_{ISO}(R)} = \sqrt{4\pi\ \mathrm{G}\ \rho_0\ \mathrm{R_c^2}(1 - \frac{\mathrm{R}}{\mathrm{R_c}}\ \mathrm{atan}(\frac{\mathrm{R}}{\mathrm{R_c}}))} \tag{1.29}$$

Profil de densité Navarro-Frenk-White : NFW : Le potentiel gravitationnel lié à la densité NFW s'écrit sous la forme de l'équation (1.30).

$$\Phi(r) \propto -\frac{ln(1+r/r_0)}{(r/r_0)} \tag{1.30}$$

Ce potentiel est décrit dans Cole & Lacey (1996) et repris par Łokas & Mamon (2001). Navarro et al. (2004) ont donné à la suite du modèle NFW des profils plus ajustés et meilleurs. Ces profils sont dérivés du modèle de Sersic en 3D avec *n*=6 (équation (1.31)).

$$\rho(r) = \rho_0 \exp(-(r/r_0)^{1/n}) \tag{1.31}$$

Dans l'équation (1.31) *n* détermine la pente du profil de densité. Ce modèle tire son potentiel gravitationnel de Cardone et al. (2005). Le profil de l'équation (3.21) , est dit de Navarro-Frenk-White (Navarro et al., 1996a).

$$\rho_{NFW}(R) = \frac{\rho_i}{\frac{R}{R_S}(1+\frac{R}{R_S})^2} \tag{1.32}$$

R_s désigne ici le rayon caractéristique du halo. La densité ρ_i représente la densité de l'univers pendant l'effondrement du halo de matière non lumineuse. L'équation (3.22) donne la vitesse du halo de matière sombre avec le potentiel NFW.

$$\mathrm{V_{NFW}(R) = V_{200}\sqrt{\frac{\ln(1+cx) - cx/(1+cx)}{x(\ln(1+c) - c/(1+c))]}}} \tag{1.33}$$

Dans cette équation $x = R/R_{200}$, V_{200} la vitesse à $\mathrm{R_{200}}$ et $c = R_{200}/R_s$ désigne le paramètre de concentration. Au rayon R_{200}, le rapport densité du halo et à la densité critique de l'univers dépasse 200. À ce rayon la vitesse est V_{200}.

Profil de Einasto : Le profil de densité de Einasto, du nom de celui qui a suggéré ce type de profil pour la première fois (Einasto, 1969), est décrit dans l'équation (3.23). Ce profil à de grandes similitudes avec le NFW. Les vitesses dans ce cas sont données par l'équation (3.24).

$$\mathrm{\rho_{EIN}(R) = \rho_e \exp(-2\ n[(\frac{R}{R_e})^{\frac{1}{n}} - 1])} \tag{1.34}$$

$$\mathrm{V_{EIN}(R) = \sqrt{4\pi\ G\ R_e^3\ n\ (2n)^{3n} \exp(2n)\ \frac{1}{R}[\gamma(3n) - \gamma(3n, r/Re)]}} \tag{1.35}$$

où $\gamma(3\mathrm{n},\mathrm{x}) = \int_0^{\mathrm{x}} \mathrm{e}^{-\mathrm{t}}\mathrm{t}^{3\mathrm{n}-1}\,\mathrm{dt}$ (Merritt et al., 2006). Ici ρ_e est la densité effective au rayon R_e. R_e défini le rayon à l'intérieur duquel, le halo de matière sombre de la galaxie, possède la moitié de sa masse, n est l'indice de Einasto et défini la pente de la densité du halo.

1.3.3.3 Autres profils

Profil de Burkert : Le profil de densité de Burkert (équation(1.36)) est décrit dans Burkert (1995) et Salucci & Burkert (2000). Pour ce type, la densité et les vitesses sont données par l'équation(1.36) et l'équation(1.37).

$$\rho_{\mathrm{Burk}}(\mathrm{R}) = \frac{\rho_0\mathrm{r}^3}{(\mathrm{r}-\mathrm{r}_0)(\mathrm{r}^2+\mathrm{r}_0^2)} \tag{1.36}$$

$$\mathrm{V}_{\mathrm{Burk}}(\mathrm{R}) = \sqrt{\mathrm{GM}_{\mathrm{b}}(\mathrm{r})/\mathrm{r}} \tag{1.37}$$

où M_{b} est donnée par l'équation(1.38) avec $M_0 = 1.6\ \rho_0\ r_0^3$

$$\mathrm{M}_{\mathrm{b}}(\mathrm{R}) = 4\mathrm{M}_0\{\ln(1+\frac{\mathrm{r}}{\mathrm{r}_0}) + \mathrm{tg}^{-}1(\frac{\mathrm{r}}{\mathrm{r}_0}) + \frac{1}{2}\ln(1+(\frac{\mathrm{r}}{\mathrm{r}_0})^2)\} \tag{1.38}$$

Profil de Hernquist : Hernquist (1990) présente un profil de densité (équation (1.39)), semblable à celui de la sphère isotherme mais avec une décroissance plus rapide (profil du type $r^{1/4}$).

$$\rho_{\mathrm{Hern}}(\mathrm{R}) = \frac{\mathrm{M}_{\mathrm{H}}}{2\pi}\,\frac{\mathrm{R}_{\mathrm{c}}}{\mathrm{r}}\,\frac{1}{(\mathrm{r}+\mathrm{R}_{\mathrm{c}})^3} \tag{1.39}$$

La vitesse de rotation du halo de Hernquist est donnée par l'équation (1.40).

$$\mathrm{V}_{\mathrm{Hern}}(\mathrm{R}) = \sqrt{\mathrm{GM}_{\mathrm{H}}\,\frac{\mathrm{r}}{(\mathrm{r}+\mathrm{R}_{\mathrm{c}})^2}} \tag{1.40}$$

où M_{H} est la masse totale de la galaxie.

Il existe d'autres types de densité décrivant le halo de matière sombre proposées dans la littérature. Nous pouvons noter ceux de KKBP de Kravtsov et al. (1998), ceux décrits dans Fukushige & Makino (1997), Moore et al. (1998), Plummer (1911) et Jaffe (1983) de type $r^{1/4}$) .

L'universalité de loi de Newton et l'introduction de la matière sombre pour expliquer la rotation des galaxies, ne sont pas partagées par tous, d'où l'existence de modèles dans lesquels seuls les composantes observables sont prises en compte.

1.3.4 Modified Newtonian Dynamics : MOND

Mordehai Milgrom en 1983 proposa une alternative à la matière sombre en proposant un modèle, Modifed Newtonian Dynamics (MOND), dans lequel la loi de Newton est modifiée. Cette modification permet d'exprimer la courbe de rotation seulement avec la matière observable : les étoiles et le gaz. Les hypothèses qui soutiennent la théorie de MOND sont principalement :
** L'existence d'une rupture dans les petites accélérations dans le cadre de la dynamique.
** L'accélération gravitationnelle est donnée par $\mu(g/a_0) \times g \sim g_N$. Le paramètre g_N étant l'accélération définie suivant la loi de Newton.
** a_0 est une constante. Elle permet de déterminer le point de transition entre les deux types d'accélération (Newton vs MOND).
Les fonctions d'interpolation décrites ci dessous permettent de donner la forme de la courbe de rotation dans la théorie de MOND. La détermination des vitesses de rotation est bien décrite dans Milgrom (1983a); Zhao & Famaey (2006); Wu et al. (2007) et Swaters et al. (2010). D'une manière générale, les fonctions d'interpolation utilisées répondent aux critères suivants :
$\mu(\mathrm{x}) = 1$ si $\mathrm{x} \ll 1$
$\mu(\mathrm{x}) = \mathrm{x}$ si $\mathrm{x} \gg 1$.
Cette fonction peut se généraliser à l'équation (1.41)

$$\mu(x) = \frac{x}{\sqrt{(1 + x^n)^{1/n}}} \tag{1.41}$$

Deux formes d'interpolation sont utilisées dans le cas des modèles MOND.

1. Interpolation standard : La fonction d'interpolation standard est trouvée en remplaçant dans l'équation (1.41) $n = 2$. C'est ce cas qui a été utilisé par Milgrom.

   $$\mu(x) = \frac{x}{\sqrt{1 + x^2}} \tag{1.42}$$

   Un régime purement de type MOND règne si $x \ll 1$. Dans ce cas $\sqrt{g = g_N a_0}$. Pour $x \gg 1$ le régime newtonien prend le dessus avec $\mu(x = g/a_0)g = g_N$. Avec l'interpolation standard, les vitesses sont données par l'équation (3.27).

   $$V_{rot}^2 = \frac{V_{sum}^2}{\sqrt{2}} \sqrt{1 + \sqrt{(2\,r\,a_0/V_{sum}^2)^2}} \tag{1.43}$$

   où V_{sum} désigne la somme quadratique des vitesses du bulbe (V_b), du disque (V_d), et du gaz (V_g) ($V_{sum}^2 = V_b^2 + V_d^2 + V_g^2$). Pour les galaxies sans bulbe, on a seulement le disque stellaire et le disque gazeux. Des composantes supplémentaires (trou noir, gaz moléculaire) peuvent s'ajouter à la somme quadratique.

2. Interpolation simple : L'interpolation simple est exprimée par la fonction $\mu(x)$ définie dans l'équation (1.44). En se basant sur cette fonction d'interpolation, le carré de la vitesse de rotation est donné par l'équation (3.28). La fonction d'interpolation simple à été adoptée dans les modèles MOND car elle donne un meilleure rapport M/L (Famaey & Binney, 2005).

$$\mu(x) = \frac{x}{1+x} \tag{1.44}$$

$$V_{rot}^2 = \sqrt{V_b^2 + V_d^2 + V_g^2} \; * \; \sqrt{a_0 * r + V_b^2 + V_d^2 + V_g^2} \tag{1.45}$$

Ces modèles ci dessus cités utilisent les éléments du milieu inter-stellaire pour donner une description de la cinématique des galaxies. Le MIS est doté de plusieurs traceurs de la cinématique des galaxies ; le HI, le Hα et le CO sont les plus souvent utilisés car abondants. Des études sur la cinématique du gaz HI de M33 ont été réalisées par plusieurs auteurs (ex :Corbelli (2003); Rubin (2006); Grossi et al. (2008); Putman et al. (2009); Chemin et al. (2009); Braun et al. (2009)). Ces études bien que souvent de faibles résolutions permirent de donner certains détails sur la morphologie, la rotation et de faire une approximation de la masse de la galaxie. Dans le disque optique, la raie Hα est la plus résolue pour la détermination des mouvements dans la galaxie car elle est intense et majoritaire dans les nébuleuses. Cette raie est utilisée pour déterminer la forme et la taille des nuages. Pour étudier M33 Boulesteix & Monnet (1970); Boulesteix et al. (1974) ou Carranza et al. (1968) ont également étudié le gaz ionisé de M33 à très faible résolution. Le gaz moléculaire du disque a également été l'objet de multiples études (e.g : Braine et al. (2010); Tosaki et al. (2011); Gratier et al. (2012) et références associées). Les principaux résultats sur la cinématique Hα de M33, datent de longtemps. Dans les chapitres qui suivent nous donnons plus de détails sur l'étude cinématique de M33 en utilisant le gaz neutre auquel nous associons le gaz ionisé. Dans ces études, la contribution stellaire et le gaz moléculaire sont pris en compte.

Cinématique Hα de M33

Chapitre 2

Cinématique Hα de M33

Sommaire

Résumé

Dans ce chapitre, nous décrivons la technique de la spectroscopie à champ intégral avec l'interféromètre Fabry Perot (FP). Nous donnons des détails sur l'instrument utilisé pour les observations. Nous présentons ensuite les données Hα et notre méthode de réduction. L'article joint à ce chapitre donne les détails de l'analyse de nos observations en Hα à l'Observatoire du Mont Mégantic et les résultats des modèles de masse. Cet article a été accepté pour publication dans la revue Monthly Notices of the Royal Astronomical Society (Kam, Z. S., Carignan, C., Chemin, L., Amram, P. & Epinat, B. 2015, Kinematics and mass modeling of M33 : Hα Observations, MNRAS, 449, 4048).

2.1 Cinématique Hα

La raie Hα se sature très vite à cause du fait que l'hydrogène est la principale composante des nébuleuses. Cette abondance fait qu'elle peut être utilisée efficacement pour déterminer la forme et la taille des nuages, mais elle ne permet pas de connaître exactement la quantité d'hydrogène contenue dans le nuage. Par contre, les molécules, telles le dioxyde de carbone (CO_2), le monoxyde de carbone (CO), le formaldéhyde, l'ammoniac etc..., permettent de déterminer la masse d'un nuage de gaz. Les raies d'émission nous fournissent des informations comme la température, la densité électronique, la dynamique et l'état d'ionisation du milieu. Nous nous sommes intéressés au décalage des raies Hα en vue de déterminer les paramètres cinématiques de la galaxie.

L'observation du Hα présente des avantages mais également des limites :

1. *Bonne résolution dans les parties internes* de la courbe de rotation (CR) qui permet de résoudre le problème de beam-smearing (faible résolution) qui affecte le HI. La partie montante de la courbe de rotation est importante dans la détermination des paramètres du modèle de masse.
2. *Bonne détermination des paramètres d'orientation*. La spectroscopie longue fente donne simplement la vitesse systémique. La spectroscopie Hα avec le FP permet de bien déterminer l'angle de position (PA) cinématique, qui donne une bonne détermination de la CR et permet d'éviter l'utilisation du PA photométrique qui est souvent obtenu en IR et qui peut être différent du PA cinématique.
3. *Observation des mouvements non axisymétriques.*
4. *Observation de galaxies fortement inclinées :* On retient très souvent que le Hα n'est pas en mesure de résoudre une galaxie fortement inclinée, vu que le gaz n'est pas optiquement mince ; mais Hernandez et al. (2005) ont montré qu'avec le Hα, l'étude de la cinématique du disque de NCG 4236 inclinée de 76° est possible. Le problème ne se pose pas pour M33.
5. *Absence possible d'émission aux rayons extérieurs.* Les températures de moins en moins grandes dans les régions externes font que le Hα a un flux faible aux grands rayons. Le HI est alors meilleur pour la détermination des paramètres de la galaxie à ces rayons.

Plus les instruments sont performants, plus les problèmes liés à l'observation du Hα sont résolus. L'observation de cette composante permet de résoudre le problème de résolution spatiale dans les régions proches du centre cinématique. Les instruments utilisant l'interféromètre de Fabry Pérot sont bien adaptés pour la détection des faibles flux Hα dans les régions centrales.

2.2 L'instrumentation

Nous avons utilisé l'Observatoire du Mont Mégantic (OMM) pour la réalisation de nos observations (Figure 2.1). L'OMM a un télescope de 1.6m de type Ritchey-Chrétien[a]. Nous avons utilisé le télescope dans sa configuration f/8 (Figure 2.2). Un réducteur focal, des filtres interférentiels et un étalon de Fabry-Pérot ont été montés au télescope.

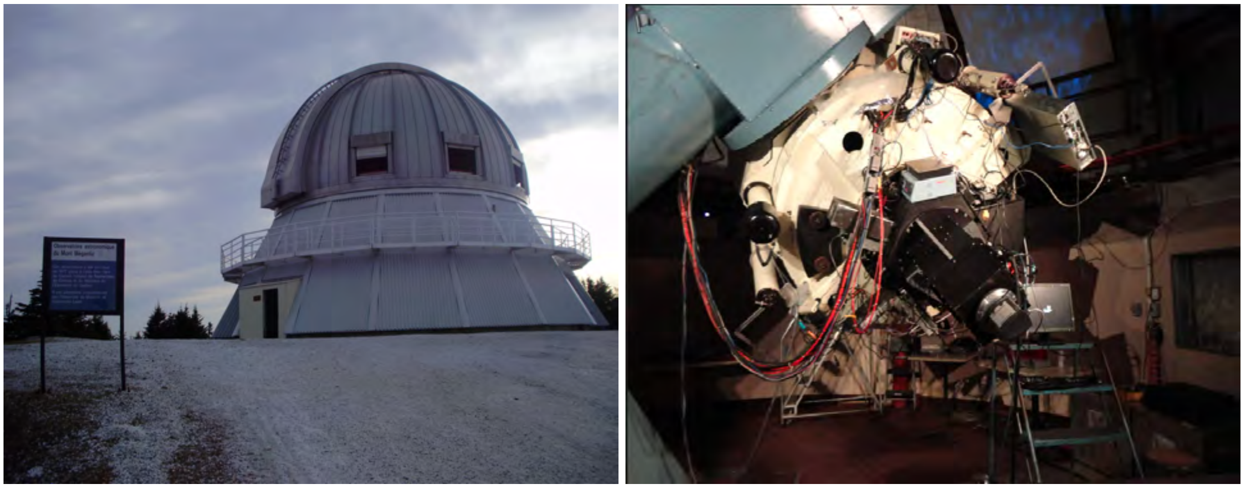

FIGURE 2.1: L'image de gauche montre le dôme du télescope de 1.6 m de l'observatoire du Mont Mégantic. À droite le télescope et le réducteur focal PANORAMIX I sur lequel est monté la camera Andor IXON 888 et le FP d'ordre 765 en Hα.

2.2.1 Le réducteur focal PANORAMIX I de l'OMM

Le réducteur focal permet d'augmenter le flux du signal des objets afin de permettre de meilleures observations. Le réducteur focal est constitué essentiellement de deux blocs de lentilles : la camera et la collimatrice. Ces deux ensembles sont essentiels. La collimatrice rend le faisceau provenant du télescope parallèle à la camera, l'objectif concentre le faisceau sur le détecteur. Un réducteur focal placé au foyer du télescope permet de réduire la distance focale (diminution du rapport d'ouverture f/D) et de ce fait augmente la luminosité des objets observés. Si la distance focale est réduite par z, alors la luminosité est multipliée par z^2. L'image donnée par un réducteur est plus petite que celle formée au foyer du télescope. L'étalon Fabry-Perot est placé dans le faisceau parallèle du réducteur focal juste avant l'objectif. La Figure 2.3 montre le réducteur focal PANORAMIX I utilisé lors de nos observations. PANORAMIX I placé à f/8 du

---

[a] plus de détails sur le télescope et les instruments de l'OMM :http ://www.astro.umontreal.ca/omm/manuel/

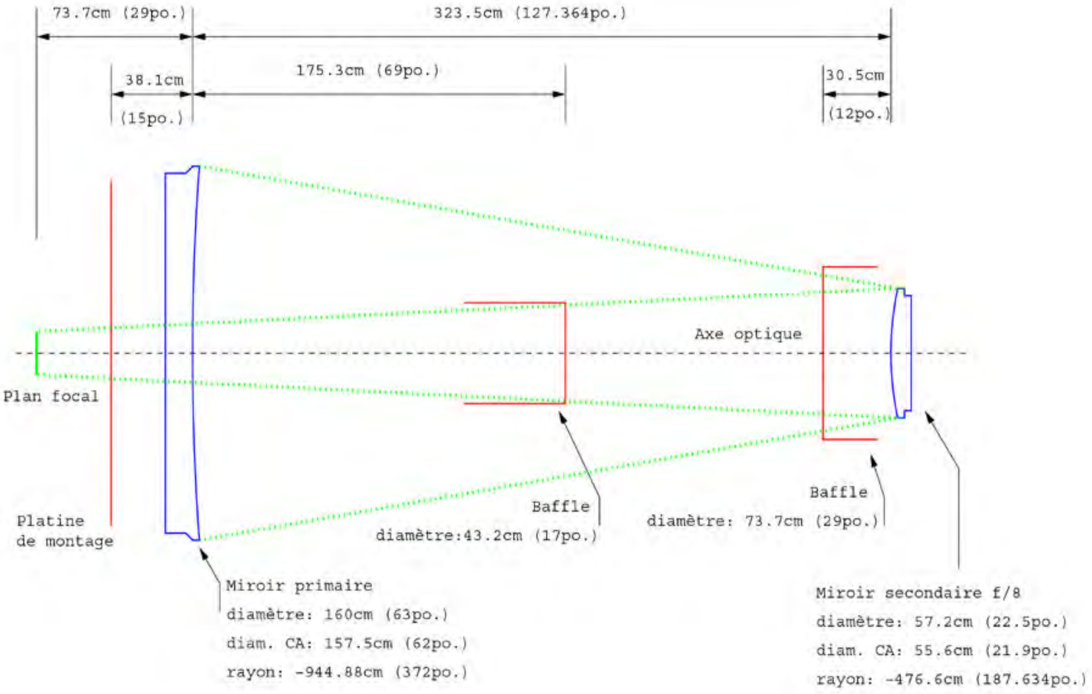

FIGURE 2.2: Configuration f/8 du télescope de 1.6m de l'OMM. Source manuel de l'OMM.

télescope ramène l'ensemble à f/2. Son collimateur a une ouverture de f/7.9 avec une distance focale de 335 mm. Son objectif est à f/2 avec une distance focale de 90 mm. PANORAMIX I est opérationnel dans le domaine spectral de :$\lambda = 4850$ et 6750 Å (Hα de 6550-6750Å avec $\Delta\lambda$=200Å et Hβ de 4850-5050Å avec $\Delta\lambda$=100Å).

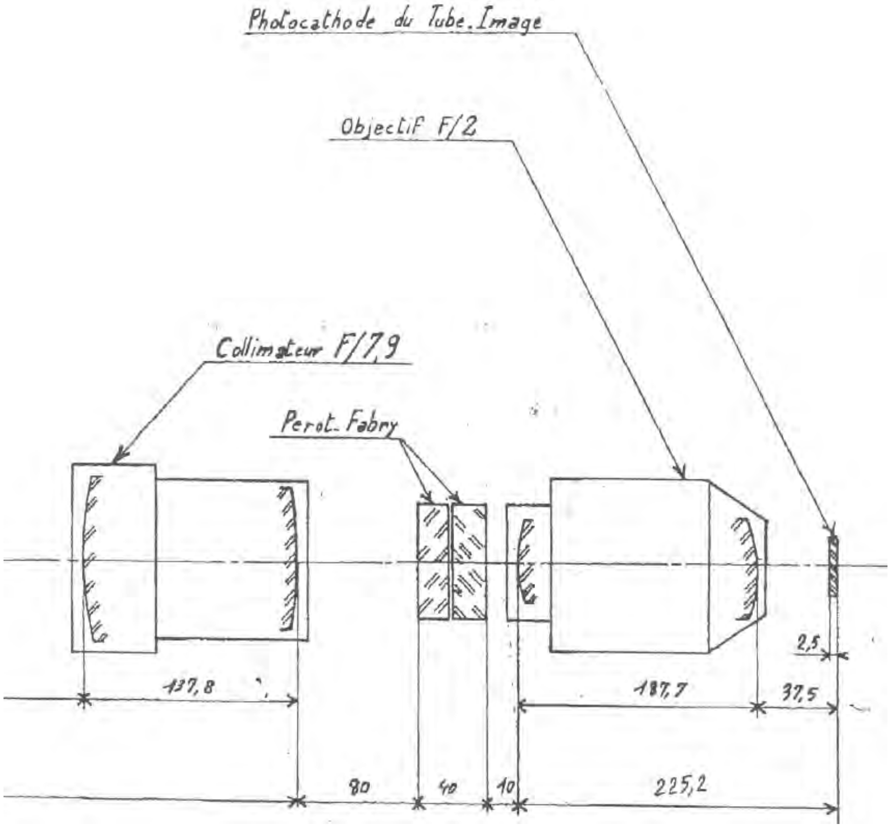

FIGURE 2.3: Schéma de la mécanique/optique du réducteur focal PANORAMIX I (PANO I). (Communication d'Olivier Hernandez, OMM)

2.2.2 Le Fabry-Perot à balayage

L'interféromètre de Fabry-Pérot, appelé simplement Fabry-Pérot (FP), est un outil de mesure mis au point par Alfred Pérot et Charles Fabry. Le FP est un instrument constitué de deux plaques planes et parallèles séparées par une distance e variable. Entre ces deux miroirs, il existe un milieu d'indice de réfraction n tandis qu'à l'extérieur des miroirs, l'indice est supposé égal à 1 lorsque les lames sont sous vide.
Lorsqu'une onde électromagnétique est envoyée sur un FP, elle subit des réflexions multiples entre les deux miroirs. Les ondes peuvent interférer de manière constructive ou destructive suivant leurs déphasages relatifs, déphasages qui dépendent du rapport de l'épaisseur optique du FP à la longueur d'onde de la lumière reçue (McLean, 2008).

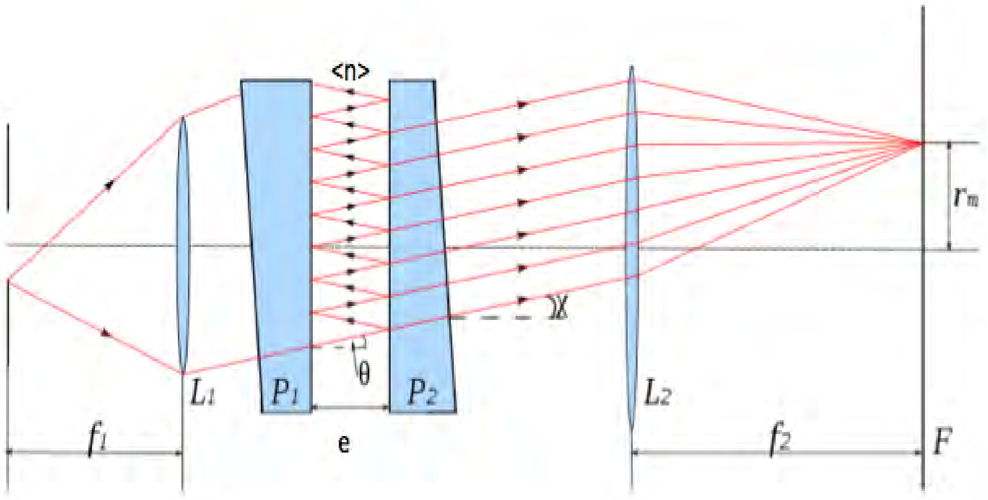

FIGURE 2.4: Description d'un Fabry-Pérot : L'image donne une description théorique du fonctionnement d'un FP. Les lentilles L1 et L2 permettent de focaliser la lumière afin de définir un plan objet de l'ensemble.

FIGURE 2.5: L'image montre un système Fabry-Pérot avec à côté le contrôleur du parallélisme des plaques.

L'image de la Figure 2.4 montre le fonctionnement d'un FP. La lentille L1 joue le rôle d'un collimateur et L2 le rôle d'un objectif. Dans le milieu d'indice $< n >$ situé entre les plaque P1

et P2, un faisceau lumineux subit de nombreuses réflexions avec un angle θ. Lorsque les deux lames sont parallèles, l'image produite par un faisceau, est située à l'infinie. Dans l'exemple de la figure 2.4, la lentille L2 permet de focaliser ce faisceau sur un écran (F). La Figure 2.5 montre l'image d'un FP commercial à balayage (Queensgate/ICOS), avec un contrôleur de piézo-électrique de type CS100.
Cet instrument à été introduit dans les observations astronomiques à l'observatoire de Marseille. De deux lames plates stationnaires ; nous avons aujourd'hui des FP à balayage avec deux plaques mobiles. Le FP est utilisé pour la réalisation des observations dans le visible. Les résultats sont présentés sous forme de "cubes" de données. Un cube de données (figure 2.9), montre un plan dans lequel se trouve la galaxie et une troisième dimension correspondant à différentes longueurs d'onde. La variation de la longueur d'onde est obtenue par la modification contrôlée de l'intervalle e séparant les deux lames du FP. Cette variation fait bouger les anneaux sur le plan du détecteur ce qui permet de construire pour chaque pixel du détecteur un spectre[b] selon la largeur du filtre interférentiel utilisé. La technique d'observation avec le FP est bien décrite par Amram & Georgelin (2000) et dans la thèse de doctorat de Benoît Epinat (Epinat, 2008). Le FP est un interféromètre assez pratique d'utilisation. Chaque FP est caractérisé par sa finesse (F), son intervalle spectral libre (ISL), son ordre d'interférence (*p*) et sa résolution spectrale (*R*).

2.2.2.1 Les principes physiques du FP.

Pour bien caractériser un FP, il faut connaître les coefficients de transmission des deux lames $\tau 1$ et $\tau 2$, leurs coefficients de réflectivité $\rho 1$ et $\rho 2$, l'indice n du milieu inter-plaques (on considère dans le cas des FP à balayage l'indice n=1) et l'écart e entre les lames. Un faisceau incident avec un angle θ sur une face du FP peut être caractérisé comme une onde de fréquence $\omega = 2\pi c\lambda$ et de phase ϕ_0. Le champ électrique de l'onde plane ainsi formé est décrit par (Epinat, 2008) :

$$E(\lambda) = Ue^{-iw+i\phi_0} \tag{2.1}$$

où U représente l'amplitude réelle de l'onde. La différence de marche entre deux rayons émergents, l'un réfléchi une fois de plus dans la cavité que l'autre, est donnée par :

$$\delta = 2necos(\theta) \tag{2.2}$$

Pour un nombre k de réflexions de l'onde à l'intérieur des deux plaques, l'onde incidente

---

[b] le nombre de points du spectre dépend du nombre de canaux balayés par le FP pendant un cycle.

donne à la sortie du FP un champ émergent défini par :

$$E_k(\lambda,\theta) = U\tau_1\tau_2(\rho 1\rho 2)^k e^{-iw+i\phi_1-2i\pi\frac{k\delta}{\lambda}}. \tag{2.3}$$

L'intensité de cette onde émergente est donnée par :

$$I(\lambda,\theta) = \left|\sum_{k=0}^{\infty} E_k(\lambda,\theta)\right|^2. \tag{2.4}$$

Comme dans Epinat (2008), nous posons pour la suite,
$\tau = \tau_1\tau_2;$
$\rho = \rho 1\rho 2;$
$I_0 = \mid U\mid^2 \;\; et$
$\phi = 2\pi\dfrac{2necos(\theta)}{\lambda}$
on peut alors écrire l'équation (2.4) sous la forme de l'équation (2.5)

$$I(\lambda,\theta) = I_0\tau^2\left|\sum_{k=0}^{\infty}(\rho e^{-i\phi})k\right|^2 = I_0\tau^2\frac{1}{|1-\rho e^{-i\phi}|^2} \tag{2.5}$$

La relation $\left|(1-\rho\mathrm{e}^{-\mathrm{i}\phi})\right|^2 = (1-\rho)^2(1+\dfrac{4\rho}{(1-\rho)^2}\sin^2(\phi/2))$ est vérifiée.

Il est possible de poser que :

$$F = \frac{\pi\sqrt{\rho}}{1-\rho} \tag{2.6}$$

L'expression de la fonction d'Airy est donnée par :

$$I(\lambda,\theta) = I_0\left(\frac{\tau}{1-\rho}\right)^2\frac{\pi^2}{\pi^2+4F^2sin^2(\phi/2)} \tag{2.7}$$

L'intensité dans l'equation 2.7 est une fonction 2π périodique en ϕ ; elle est maximale pour les valeurs de $\phi = 0[2\pi]$. La relation exprimant la longueur d'onde à l'ordre p pour un FP d'indice n et d'espacement e ; vu sous un angle θ est donnée par :

$$\lambda_p p = 2necos(\theta) \;\; avec \;\; p \in \aleph \tag{2.8}$$

L'intervalle spectral libre (ISL) d'un FP est l'espacement entre deux pics donnés par la fonction d'Airy. Pour un FP idéal et pour deux ordres d'interférence différents ; l'équation (2.8) est vérifiée.

$$\lambda_p p = \lambda_{p+1}(p+1) \; et \; 2ISL = |\lambda_{p-1} - \lambda_{p+1}| \tag{2.9}$$

Pour un ordre très grand, ISL=$|\lambda_{p+1} - \lambda_p|$ en combinant avec l'équation (2.8) on obtient :

$$ISL = \frac{\lambda}{p} \tag{2.10}$$

l'équation 2.10 vient de $ISL = \frac{\lambda_p p}{p^2 - 1}$, pour p grand.

On peut donc en déduire une expression réduite de la finesse.

$$F = \frac{ISL}{\delta\lambda} \tag{2.11}$$

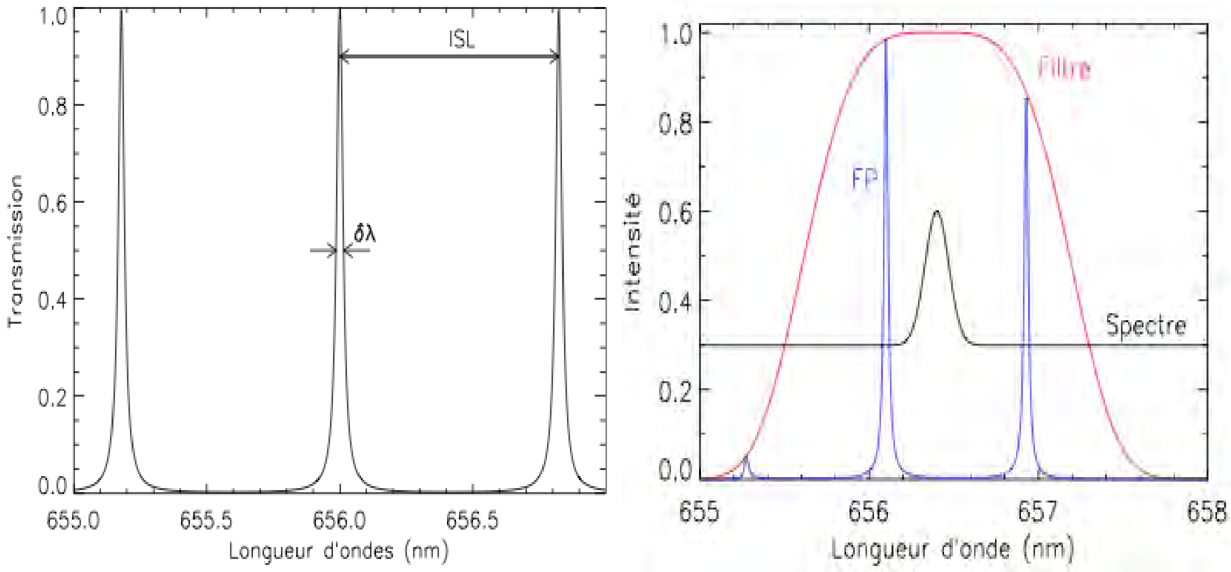

FIGURE 2.6: Les images sont tirées de Epinat (2008) ; celle de gauche indique la transmission d'un Fabry-Perot théorique (fonction d'Airy), possédant un facteur de réflexion de 0.9 et fonctionnant à l'ordre 798 pour la raie Hα (656,3 nm). L'image de droite représente la fonction d'Airy du Fabry-Perot modulée par la réponse du filtre interférentiel. Ainsi, seuls les pics de transmission sur la région du spectre à étudier ont une bonne transmission. La raie est échantillonnée en balayant le spectre avec le Fabry-Perot.

La résolution est définie par :

$$R = \frac{\lambda}{\delta\lambda} \tag{2.12}$$

où $\delta\lambda$ désigne l'élément de résolution ; la largeur à mi-hauteur de la PSF est généralement utilisée. Des expressions (2.10) et (2.11), on peut décrire la résolution du FP comme étant le produit de la Finesse (F) et de son ordre d'interférence (p).

$$R = Fp \tag{2.13}$$

Les équations 2.10, 2.11, 2.12 et 2.13 sont les relations de base de la spectroscopie Fabry-Perot.

2.2.2.2 L' interféromètre Fabry-Perot de l'OMM.

Le FP de l'OMM a un ordre interférentiel de p = 765 à Hα, pour un ISL de 8.58 Å. La finesse permet d'avoir une indication de la qualité de l'information spectrale transmise après de multiples réflexions dans la cavité. Elle donne donc une idée de la résolution (équation (2.11)). La finesse moyenne durant les observations est de l'ordre de 18, ainsi la résolution spectrale de l'étalon est d'environ 0.49 Å($\Delta\lambda$= ISL (Å) / Finesse). Les cibles sont balayées à travers le ISL en 48 canaux, chaque canal ayant une largeur de 0.18 Å. Les 48 canaux sont choisis de manière à voir passer au moins deux fois la bande passante dans l'ISL. Ce choix permet de régler le problème de fréquences d'échantillonnage. Avec 40 canaux le problème de l'échantillonnage est résolu. Nous avons utilisé 48 canaux.

2.2.3 Les filtres interférentiels

L'utilisation des filtres interférentiels est essentielle dans les observations FP. À l'OMM nous avons utilisé deux filtres pour ce projet. Le premier filtre (M4) centré à $\lambda = 6598$ Å permet d'isoler la raie de Néon (NE) à $\lambda = 6598.95$ Å pour l'étalonnage en longueur d'onde (calibration). Le second filtre (M1) est centré à $\lambda = 6564$ Å et permet d'isoler la raie Hα de la galaxie. L'utilisation de ces filtres permet de diminuer les perturbations dues aux longueurs d'onde parasites provenant des ordres d'interférence non désirés. Cela est possible grâce à la bande étroite de fréquences permises par ces filtres. La Figure 2.7 donne la transmission de ces deux filtres en fonction de la longueur d'onde et la variation du maximum transmis en fonction de l'inclinaison.

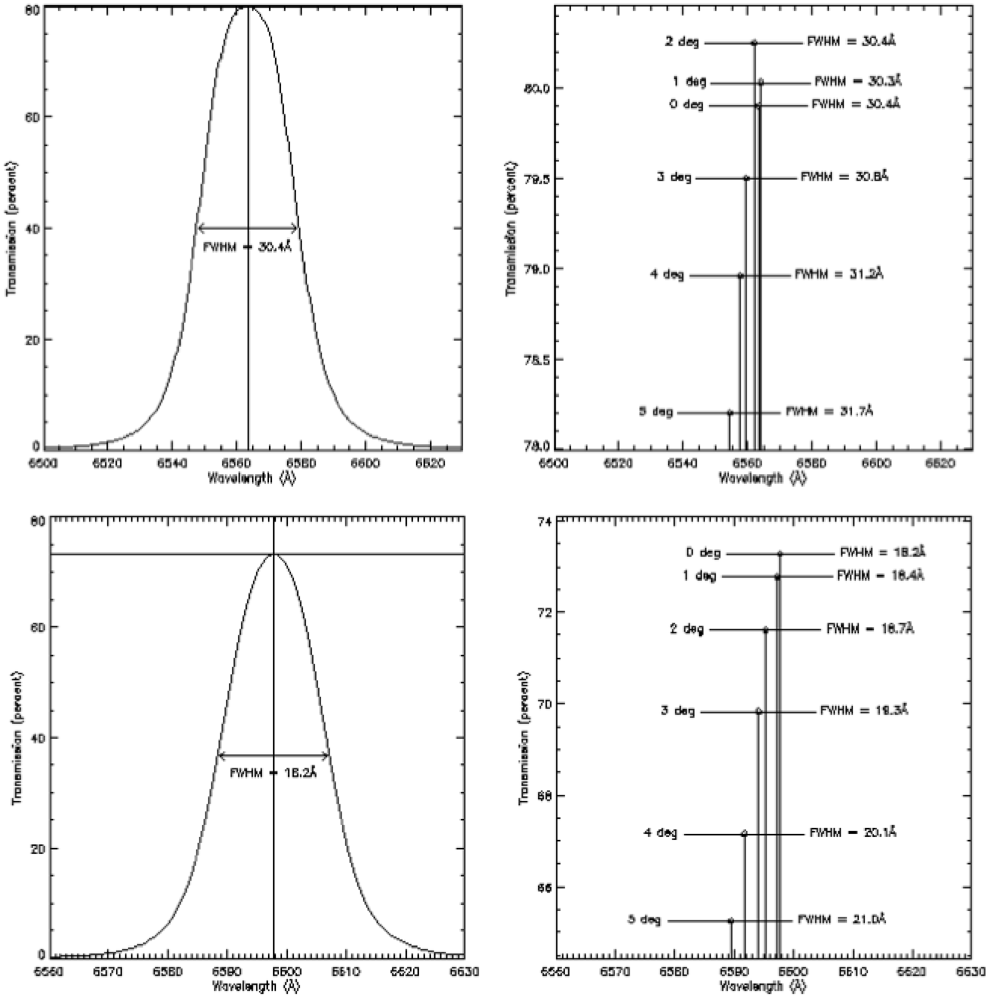

FIGURE 2.7: Transmission des filtres M1 et M4 en fonction de la longueur d'onde. Les images du haut donnent les caractéristiques de M1 et les graphes de bas celles de M4. Les graphes de gauche montrent les courbes de transmission dans les conditions idéales. Les courbes de droite donnent les variations du pic de transmission en longueur d'onde en fonction de l'angle d'inclinaison.

2.2.4 Les détecteurs pour le comptage de photons à l'OMM

Les détecteurs utilisés ces dernières années pour le comptage de photons à l'OMM sont des EMCCD (electron multiplying charge-coupled device) à lecture rapide. Ils ont des rendements quantiques généralement supérieurs à 90% en Hα. Dans le but d'observer de faibles flux, les détecteurs de l'OMM sont dotés de contrôleurs leur permettant de mieux réduire les bruits

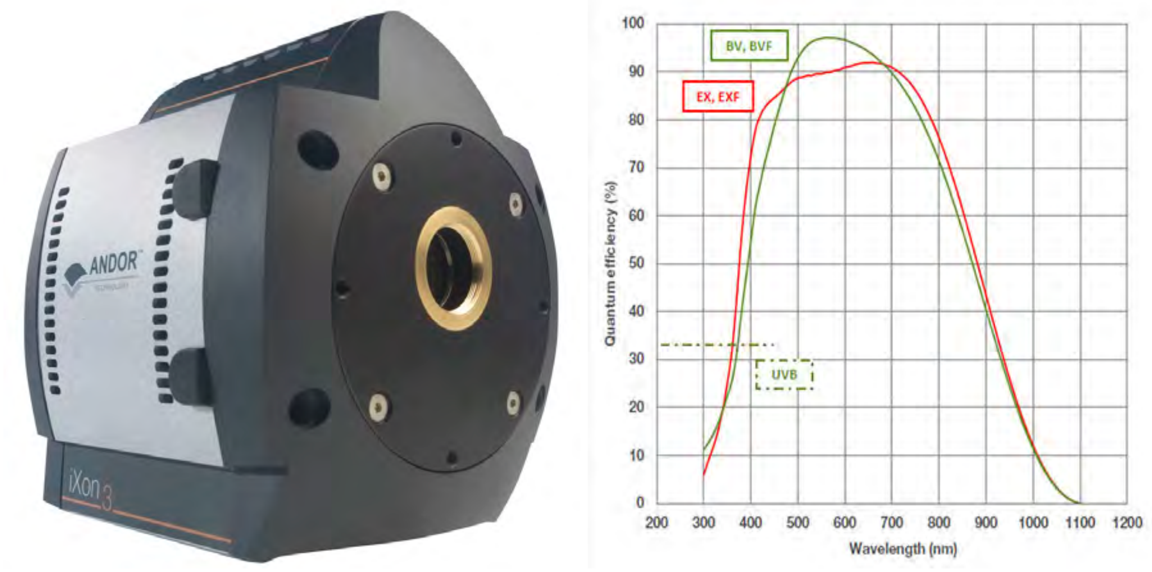

FIGURE 2.8: Andor : Image d'une camera Andor iXon3 EMCCD - 888 à gauche et la courbe de son efficacité quantique à droite (source Andor technologie).

parasites. Contrairement à la camera FaNTOmM[c], ces contrôleurs, pilotent les CCDs permettant d'observer sans une photocathode (tube intensificateur d'image). À l'image de CCCP[d] (CCD Controller for Counting Photons), prototype des contrôleurs pour nüvü caméras[e] (Daigle et al., 2008, 2009a), les cameras Andor utilisées à l'OMM ont des gains variables et aussi des charges induites réduites permettant d'augmenter l'efficacité de transfert de charge (ETC).
La camera Andor iXon888 a été utilisée pour les observations Hα présentées dans cette thèse (cf. Figure 2.8). C'est un produit de la compagnie Andor[f] doté d'un détecteur de grade scientifique de type CCD97 EMCCD de l'entreprise $e2v$ qui offre un grand champ de vue avec son détecteur de 1024 x 1024 pixels d'une taille de 13μm chacun.

2.3 Les observations Fabry-Pérot à L'OMM

Des images prises après la variation de l'espace entre les plaques d'un Fabry-Pérot permettent de former un cube à l'image du schéma de la figure 2.9. Cette figure montre comment se construit un cube de données en utilisant un FP. La variation de l'espace inter-plaques permet de varier la

---

[c] Fabry-Perot de Nouvelle Technologie pour l'Observatoire du mont Mégantic, est l'ancien spectro imageur à champ intégral de l'OMM

[d] CCCP est un contrôleur construit au Laboratoire d'Astrophysique Expérimental (LAE) de l'Université de Montréal. Nous avons commencé nos observations avec ce prototype. Les données obtenues ne sont pas présentées ici.

[e] http ://www.nuvucameras.com/

[f] http ://www.andor.com/

longueur d'onde transmise, ce qui permet de constituer la troisième dimension (direction z). Le plan (x,y) de la figure est le plan donné par l'image dans le plan du ciel.

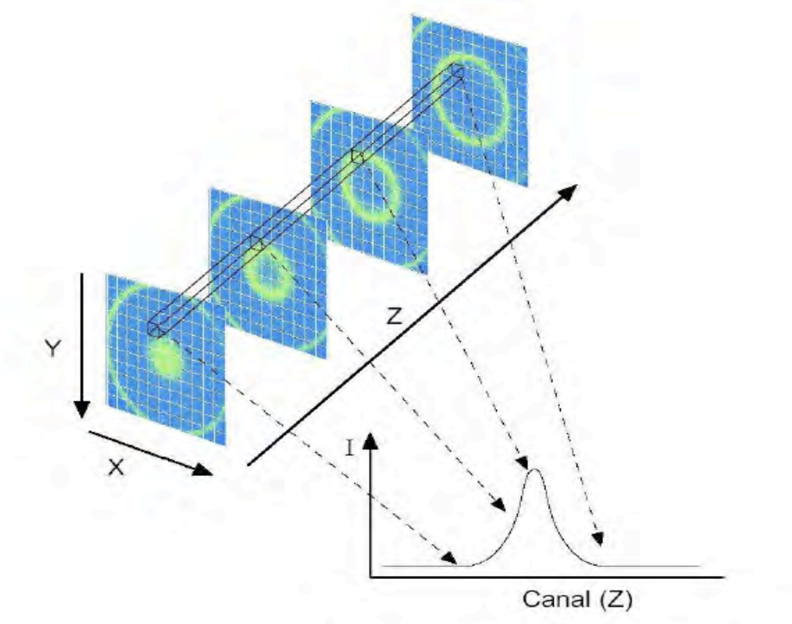

FIGURE 2.9: Cube 3D en FP : l'image montre le balayage du champ par les anneaux du FP pour la réalisation d'un cube de données à intégral de champ.

Une des phases les plus importantes des observations en FP reste sans conteste la calibration. Plus une calibration est bonne en longueur d'onde et en phase plus la qualité des données, principalement la définition des raies, est bonne.

2.3.1 La calibration des détecteurs

La réponse du détecteur dépend de son régime de fonctionnement. Pour avoir une réponse bien calibrée, il faut réaliser les observations suivantes :
Bruit : permet de déterminer le courant sombre du détecteur. Même sans aucune illumination, il y a des détections parasites sur tout détecteur sensible à faible flux. Ces observations permettent de corriger cet effet. Un minimum de 50 images est nécessaire pour un bonne détermination.
Gain : L'amplification en gain n'est pas linéaire. La détermination du gain réel est alors nécessaire. Un minimum de 200 images est nécessaire pour un bonne détermination.
Courant sombre : Permet de trouver l'effet exact du gain pour un temps d'observation donné. Il faut au moins 50 images au même temps d'observation et au même gain que dans le cas de la galaxie.

Plage uniforme : permet de donner un poids à chaque pixel pour que la surface du détecteur ait une réponse uniforme si elle est éclairée par une lumière monochromatique.

Nous opérons les caméras dans un régime ou le gain n'est pas un facteur augmentant le bruit. La Table 2.1 donne les différentes options disponibles pendant l'utilisation de la camera Andor. Il est important de maintenir la température à une valeur faible et stable. Selon le type d'exposition, la fréquence de lecture peut varier de même que les amplifications et temps de transfert pour une observation optimisée.

TABLE 2.1: Configurations de la Camera Andor

Paramètres	Options	Configuration
Output amplifier	Conventional - EM	EM
Read-out resolution	16-14 bits	14 bits
Read-out speed	10-5-3-1 MHz	10 MHz
Preamp gain	1x-2x-3x-4x	4x
Vclock speed	0.3-0.5-0.9-3.3 μs	0.5 μs
Vclock amplitude		Normal
Post processing	Analogic, PC*	Analogic
Température	≥ -95	-85

*Photon Counting

2.3.2 Calibration en longueurs d'onde

La calibration en longueur d'onde est faite par l'observation d'une lampe de néon (NE) utilisant la raie à 6598.95 Å. Les observations FP doivent être calibrées en longueur d'onde afin d'établir une relation entre la longueur d'onde variable et la position d'un pixel dans le cube. La calibration permettra de connaître avec précision la longueur d'onde transmise sur chaque pixel et pour chacun des espacements des lames, autrement dit, permet de savoir à quel canal une longueur donnée est transmise (Figure 2.10). La correction de la phase est nécessaire car la phase brute est décrite par une fonction parabolique repliée. Cette correction donne la phase parabolique pour la calibration en longueur d'onde (Figure 2.10).

Pour deux angles d'incidence distincts (0 et θ), la même longueur λ_0 est transmise à des espacements différents. En considérant le même ordre d'interférence p on peut écrire $\lambda_0\mathrm{p} = 2\mathrm{ne}_0\cos(0) = 2\mathrm{ne}_\theta\cos(\theta)$ autrement :

$$e_\theta = \frac{e_0}{cos(\theta)}. \tag{2.14}$$

Par la suite on trouve [g] :

$$e_\theta - e_0 = e_0\frac{\theta^2}{2} \tag{2.15}$$

alors la forme de l'équation de phase est parabolique. La calibration permettra enfin de réaligner les longueurs d'ondes de manière à ramener au centre du cube la longueur d'onde d'observation de la galaxie. Cette procédure est bien détaillée dans Epinat (2008).

2.3.3 Observations Hα de la galaxie M33

Un bilan des observations Hα publiées de M33 indique qu'il y a peu d'observation Hα. De plus, un grand nombre de ces études souffre d'un manque de résolution dans les régions internes. Ce manque influence la détermination des paramètres cinématiques des galaxies ; aussi bien pour les galaxies lointaines que celles voisines de la Voie Lactée comme M33. Plus d'observations Hα sont nécessaires pour mieux contraindre les modèles, surtout dans les parties intérieures de la courbe de rotation. Cette étude permettra de confirmer ou non la rotation rapide du gaz ionisé. A l'oeil nu, la galaxie M33 apparait comme un petit nuage dans le ciel d'automne à l'Observatoire du Mont Mégantic (OMM).

La proximité de M33 permet de sonder véritablement le gaz ionisé dans les régions internes, l'étude de ce gaz donnant une bonne approximation de la partie montante de la courbe de rotation. Cette proximité permet d'avoir une bonne résolution des régions HII. En plus de la contribution dans l'étude de la cinématique de M33, l'observation des régions HII donne plus de détails sur la dispersion des vitesses dans les régions de formation stellaire ayant diverses formes.

Nous avons réalisé la cartographie de la galaxie M33 à l'OMM en utilisant le réducteur focal PANORAMIX I (Pano I). Dans ce document nous présentons les données obtenues avec un champ de vue $\sim 13\ \mathrm{arcmin}^2$ pour chacun des champs. Nous réalisons des recoupements de manière à reconstruire la carte de la galaxie par superposition des champs. La figure 2.11 donne un aperçu de notre plan d'observation pour M33.

---

[g] $e_\theta = \frac{e_0}{cos(\theta)}$ peut s'écrire comme $e_\theta - e_0 = e_0\left(\frac{1}{cos(\theta)} - 1\right)$,
avec l'approximation $cos(\theta) = 1 - \frac{\theta^2}{2} + \frac{\theta^4}{4!} + \varepsilon(\theta^6)$ on obtient l'équation 2.15 .

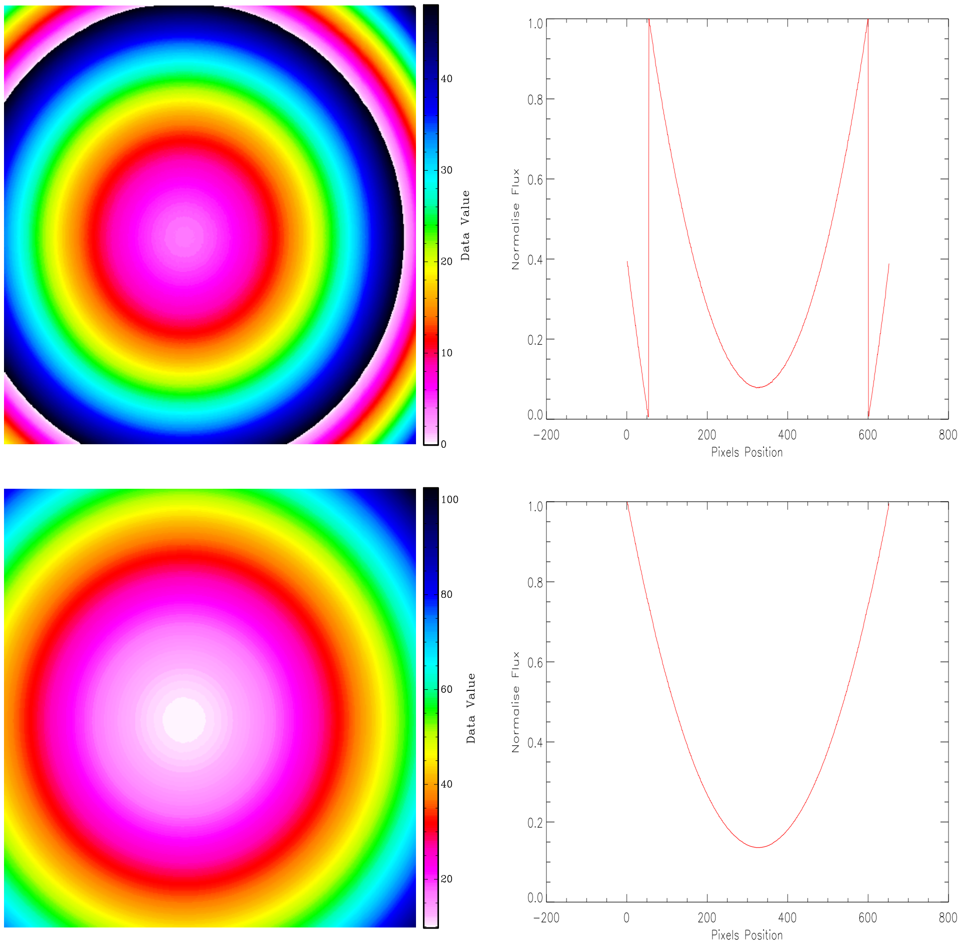

FIGURE 2.10: Calibration : L'image en haut à gauche montre une carte de phase brute, celle en bas à gauche montre la carte de la phase parabolique correspondante. Les images de droite indiquent les courbes correspondantes aux cartes de phase à gauche. La courbe dans le coin droit en bas, montre la transformation de la phase brute en phase parabolique.

Il existe plusieurs instruments utilisant un interféromètre Fabry-Perot et qui réalisent des observations en comptage de photons (Figure 2.2). Les trois premiers instruments présentés dans la Table 2.2 n'utilisent pas de EMCCD. Dans le dispositif utilisé à l'OMM, la sensibilité et la performance des détecteurs EMCCD sont des avantages qui nous permettent de faire du comptage de photons. La capacité du EMCCD à faire du comptage de photons a été bien montrée par Daigle et al. (2009a) et Daigle et al. (2008). La grandeur de notre détecteur par rapport à celui de FaNTOMM, nous a permis de réduire le temps de télescope tout en observant profondément les champs définis dans la figure 2.11. Il a permis de réduire d'un facteur ~ 4 les temps d'acquisition sur la galaxie. Avec la camera Andor, dix champs seulement ont été nécessaires pour couvrir M33.

TABLE 2.2: Instruments utilisant le Fabry-Perot pour la cinématique des galaxies.

Instruments	GHASP [1]	FaNTOMM [2]	GHαFaS [3]	3D-NTT [4]
Mise en service	2000	2002	2007	–
Diamètre (m)	1.96	1.6	4.2	3.6
Nombre de pixels	512×512	1024×1024	1024×1024	1600×1600 & 4096×4096
Champ circulaire(″)	8.2	27.4	4.9	9 12 & 23
Finesse des FP	12	≥15	12	10&50
Domaine deλ (nm)	500-750	500-750	500-750	350-800
Résolution spectrale	∼10000	∼10000	∼10000	30000-5000-100

[1] Epinat (2008)

[2] Hernandez et al. (2003)

[3] Carignan et al. (2008)

[4] Marcelin et al. (2008)

Les observations ont été étendues sur les régions extérieures pour mieux étudier certaines régions HII individuellement. La profondeur des champs dans ces cartographies sera utile pour des études statistiques à grande échelle. Nous disposons actuellement de la cinématique de plusieurs centaines de régions HII de M33.

L'image de la figure 2.12 montre une faible variation de la masse d'air moyenne entre les champs pendant nos observations. Dans cette figure, le panneau du bas montre le facteur de correction pour les différents champs ; la correction moyenne est de l'ordre de 1.02 ± 0.05. Toutes ces observations couvrent les longueurs d'onde de 6556.5Å à 6560.6Å. Le pic d'émission Hα observé sur chaque pixel, apparait dans les régions HII du côté Nord-Est puis progressivement dans celles du côté Sud-Ouest, preuve de la différence de vitesse entre ces deux côtés.
Le détail de ces observations est donné dans l'article joint à ce chapitre.

2.4 Réduction des données Fabry-Perot

2.4.1 Étapes importantes de la réduction des données FP.

Les grandes lignes de la réduction des données sont décrites dans les thèses de Philippe Amram, Benoit Epinat et Olivier Daigle (Amram, 1991; Daigle, 2005; Epinat, 2008). La réduction des données se fait en prenant en compte les étapes suivantes :

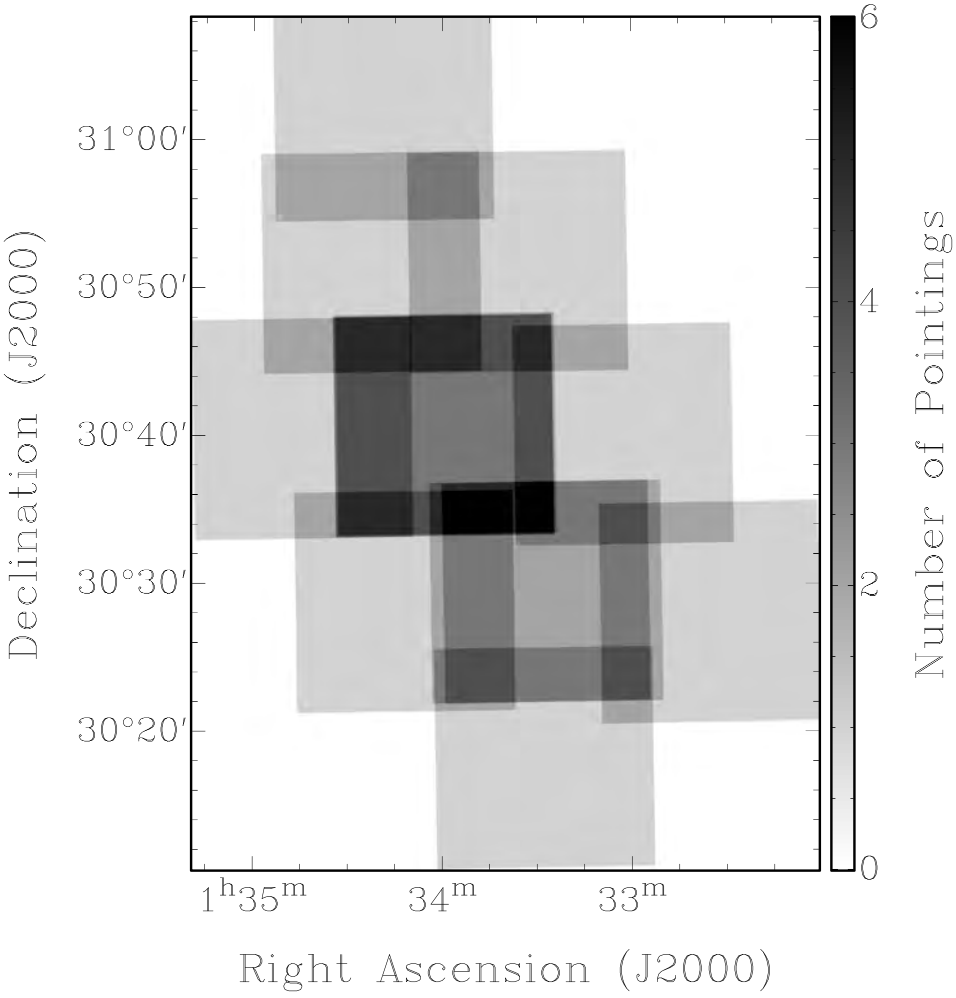

FIGURE 2.11: Champs observés avec le réducteur focal Pano I et la caméra Andor iXon888 à l'OMM. Dans l'image, les grands rectangles désignent la grandeur du champ du détecteur. L'image fait un bilan des observations et celui des superpositions des champs observés. Le nombre maximal de superpositions est six.

- La vérification des canaux intégrés et construction d'un cube brute ;
- La construction du fichier de phase à partir d'un ou des fichiers de calibration ;
- L'application de la phase parabolique aux données brutes d'observation ;
- Le lissage spectral du cube de données ;
- La correction spectrale du cube de données en utilisant le spectre du ciel nocturne contenu dans le cube de données ;
- La soustraction du spectre du ciel nocturne du cube de données ;
- Le lissage adaptatif du cube de données ;
- L'extraction des cartes de vitesse radiale, flux monochromatique, continu et des largeurs

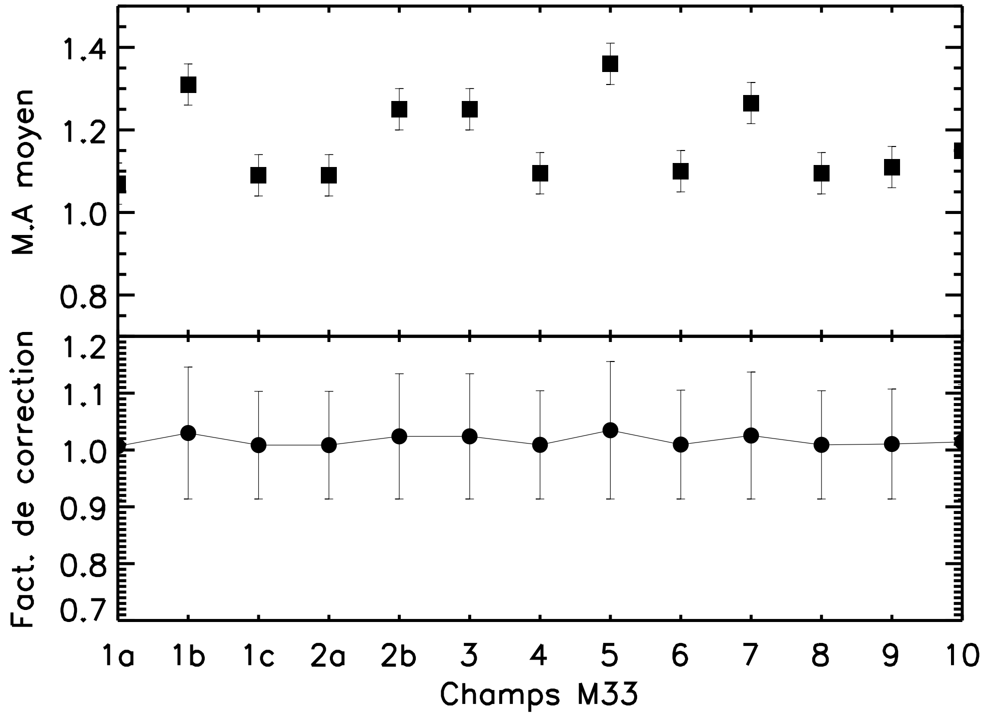

FIGURE 2.12: Cette image montre la variation de la masse d'air moyenne (X) de tous les champs observés. Les données du cadran supérieur, donnent la masse d'air d'une observation tandis que la courbe du cadran en bas indique la correction à appliquer afin de corriger les comptes.

des raies d'émission ;

- La recherche automatique des raies d'émission dans les régions à très faible flux monochromatique, corrélées aux plus fortes raies d'émission environnantes ;
- L'ajustement automatique du cube de données en fonction des vitesses radiales.
- La calibration en flux a été réalisée avec les sources extraites de Relaño et al. (2013)

Le programme computeeverything décrit dans les annexes (cf. Annexe C), est un programme IDL interactif, qui permet de réaliser ces étapes de la réduction. Pour les données EMCCD, la particularité/différence réside dans l'intégration des fichiers d'observation et la formation du cube calibré en longueur d'onde. Le programme reducl3fp (cf. Annexe B) permet de produire les cubes calibrés en longueur d'onde prêt pour l'analyse.

2.4.2 Résultats

La réduction des données Hα permet de trouver pour chaque pixel du détecteur, un spectre. Le flux Hα n'est pas transmis à la même longueur d'onde à chaque point. Il est donc nécessaire d'avoir une bonne correction du guidage et de la pointée du télescope. L'image de la figure 2.13, montre les spectres bruts, combinés sur 10x10 pixels, observés sur une région HII de M33. Cela montre d'autre part la complexité du spectre dans les régions de forte émission Hα.

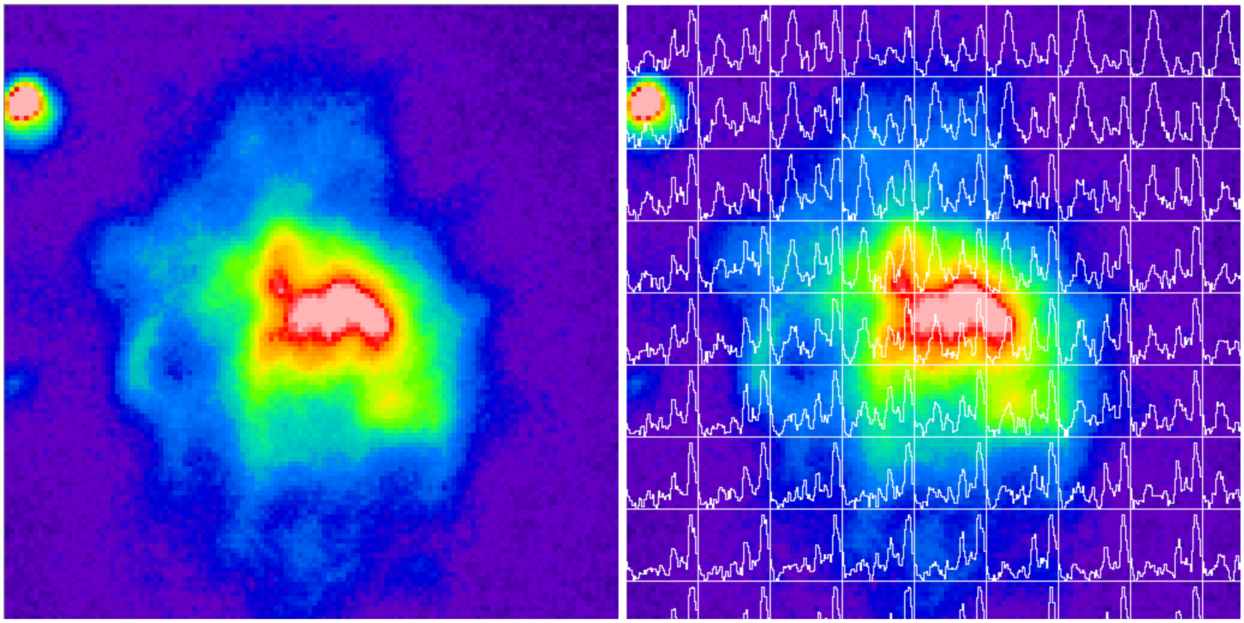

FIGURE 2.13: Spectroscopie à champ intégral avec l'interféromètre Fabry-Pérot. L'image présente la région NGC604 avec une superposition de profils Hα binés sur plusieurs pixels.

Des observations réalisées à l'OMM, il est possible de montrer à la fois les régions compactes où le Hα est dense et les régions où le Hα semble plus diffus. La figure 2.14 est une représentation des deux cas. Dans le cas de cette figure, une limite de 55 comptes Hα a été fixée entre les régions denses et diffuses présentes autour.

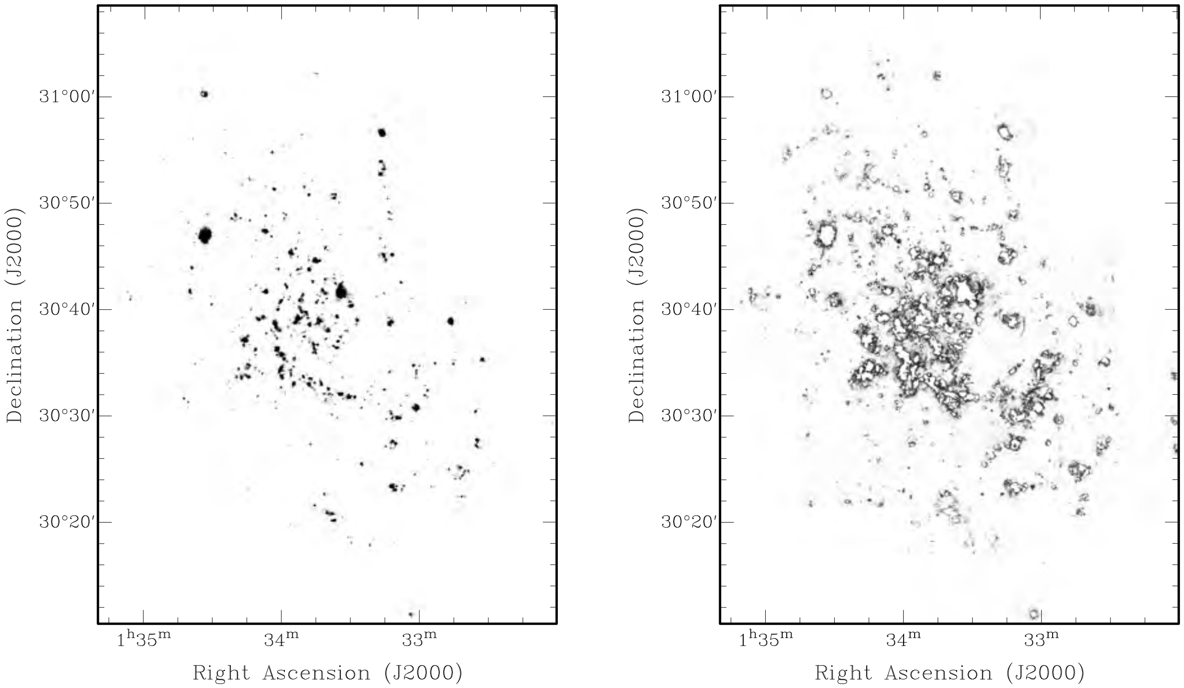

FIGURE 2.14: L'image de gauche donne les régions HII compactes de M33 et l'image de droite montre le Hα diffus autour de ces régions.

Détermination des paramètres initiaux

Les paramètres cinématiques sont ceux qui donnent la meilleure représentation de la carte de vitesses. Les paramètres les plus importants sont : le centre de rotation (x_0, y_0), la vitesse systémique (V_{sys}), l'inclinaison (i) et l'angle de position de l'axe majeur (PA). Pour minimiser l'influence et les erreurs de déprojection près de l'axe mineur, les données autour d'un angle de $\sim 30^{\circ}$ autour de l'axe sont excluses.

Il est bien connu que la vitesse systémique et la position du centre de rotation sont corrélées. Ces deux paramètres sont alors déterminés simultanément en fixant l'angle de position et l'inclinaison aux valeurs optiques. Les paramètres initiaux sont déterminés à quelques minutes d'arcs autour du centre optique. Le meilleur centre de rotation (x_0, y_0) est obtenu avec un léger décalage de (-8 , 15.5) arcsec du centre optique et $V_{sys} = -180. \pm 2.7$ km.s^{-1}. La Figure 2.15 montre la variation de la vitesse systémique et du centre de rotation dans la partie centrale de la galaxie.

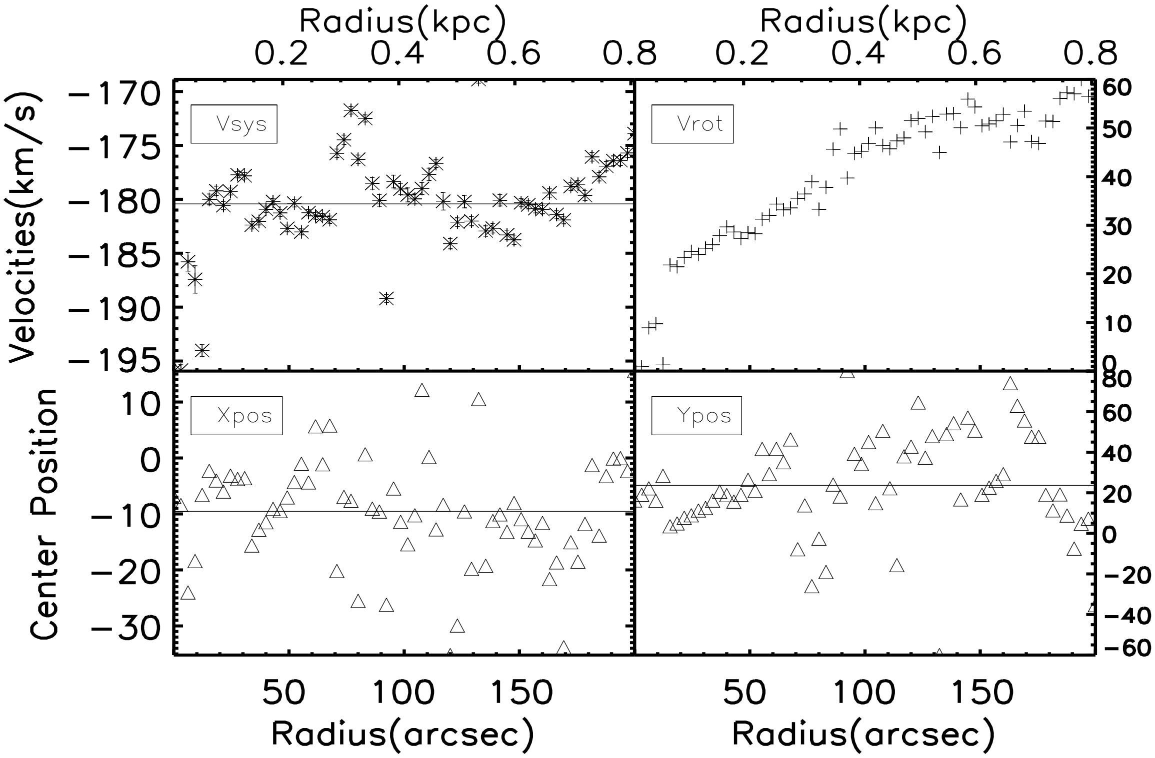

FIGURE 2.15: Determination des paramètres cinématiques initiaux. En haut à gauche V_{sys}, en haut à droite V_{rot}, en bas à gauche X_{pos} et en bas à droite Y_{pos}. Les lignes horizontales montrent les valeurs moyennes.

Dans la figure 2.16, les données en rouge montrent la CR pour le coté qui s'éloigne, en bleu pour le coté qui s'approche et en noir la valeur déterminée pour les deux côtés simultanément. Dans la figure du milieu qui donne le PA et du bas l'inclinaison, la ligne verte montre la valeur moyenne du paramètre.

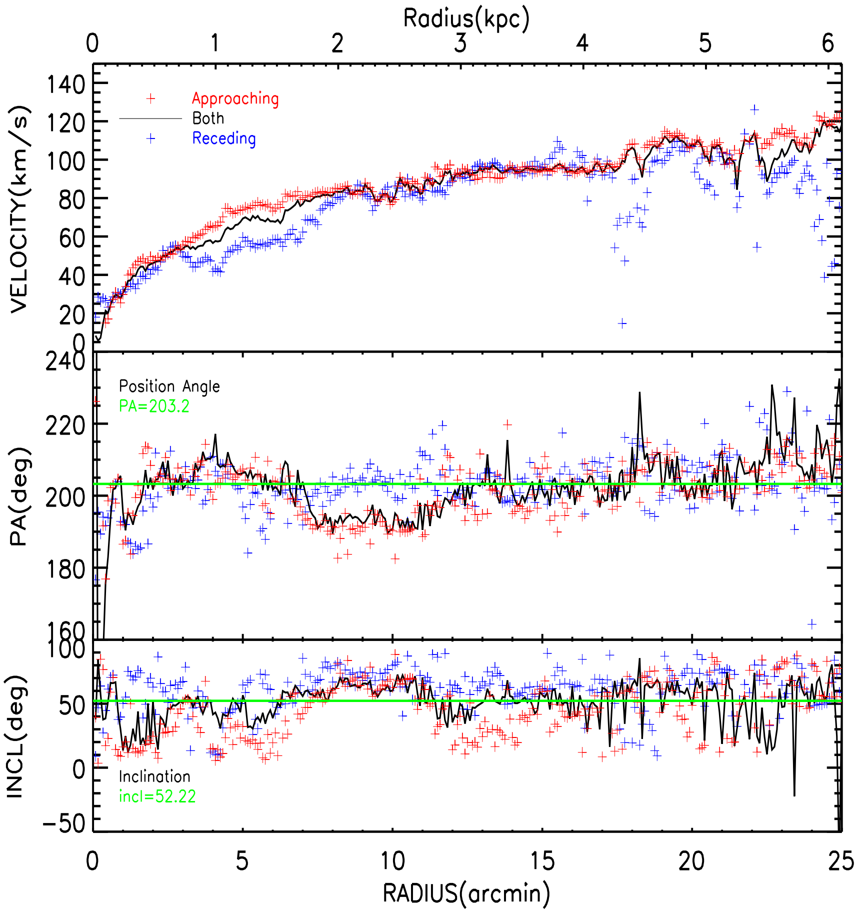

FIGURE 2.16: Les graphes donnent les valeurs initiales obtenues par le tilted-ring model implementé dans GIPSY. Du haut vers le bas : la courbe de rotation, le PA, et l'inclinaison déterminés avec le centre et le V_{sys} constants.

Une description plus détaillée des paramètres est donnée dans l'article ci joint, publié dans MNRAS.

2.5 Kinematics and Mass Modeling of M33 : Hα Observations

Kam, Z. S.[1,2,3], Carignan, C.[1,2,3], Chemin, L.[4], Amram, P.[5] & Epinat, B.[5]
[1]Laboratoire d'Astrophysique Expérimentale, Département de physique,
Université de Montréal, C.P. 6128, Succ. centre-ville, Montréal, Québec, Canada, H3C 3J7
[2]Observatoire d'Astrophysique de l'Université de Ouagadougou, BP 7021, Ouagadougou 03, Burkina Faso
[3]Department of Astronomy, University of Cape Town, Private Bag X3, Rondebosch 7701, South Africa
[4]Université de Bordeaux & CNRS, LAB, UMR 5804, F-33270, Floirac, France
[5] Université Aix Marseille , CNRS, LAM (Laboratoire d'Astrophysique de Marseille), 13388, Marseille, France

ABSTRACT

As part of a long-term project to revisit the kinematics and dynamics of the large disc galaxies of the Local Group, we present the first deep, wide-field ($\sim 42' \times 56'$) 3D-spectroscopic survey of the ionized gas disc of Messier 33. Fabry-Perot interferometry has been used to map its Hα distribution and kinematics at unprecedented angular resolution ($\lesssim$3″) and resolving power (~ 12600), with the 1.6 m telescope at the Observatoire du Mont Mégantic. The ionized gas distribution follows a complex, large-scale spiral structure, unsurprisingly coincident with the already-known spiral structures of the neutral and molecular gas discs. The kinematical analysis of the velocity field shows that the rotation center of the Hα disc is distant from the photometric center by ~ 168 pc (sky projected distance) and that the kinematical major-axis position angle and disc inclination are in excellent agreement with photometric values. The Hα rotation curve agrees very well with the HI rotation curves for $0 < R < 6.5$ kpc, but the Hα velocities are $10 - 20$ km.s^{-1} higher for $R >$ 6.5 kpc. The reason for this discrepancy is not well understood. The velocity dispersion profile is relatively flat around 16 km.s^{-1}, which is at the low end of velocity dispersions of nearby star-forming galactic discs. A strong relation is also found between the Hα velocity dispersion and the Hα intensity. Mass models were obtained using the Hα rotation curve but, as expected, the dark matter halo's parameters are not very well constrained since the optical rotation curve only extends out to 8 kpc.

Keywords

techniques : interferometric, integral field, Fabry-Perot – galaxies : individual : M33 – galaxies :

kinematics and dynamics – galaxies : ISM : Bubbles, HII regions – cosmology : dark matter

2.5.1 Introduction

Late-type spiral and dwarf irregular (dIrr) galaxies present an extended HI emission. The HI emission usually extends to larger radii than the optical emission. This makes of HI a powerful tool for probing the dark matter (DM) dominated regions and for characterizing the parameters of the flat part of the rotation curves (RCs). However, it is the rising inner part of the RCs that constrains the parameters of the mass models (see e.g. Blais-Ouellette et al., 1999). Two-dimensional Hα observations are ideally suited to give more accurate velocities in the inner parts of galaxies having a better spatial resolution than the HI (Amram et al., 1992, 1994; Swaters et al., 2000). The ideal approach is then to combine high spatial resolution Hα observations in the inner parts and sensitive lower spatial resolution HI observations in the outer parts to derive the most accurate mass models for the luminous disk and the dark halo. The objective of this project is to perform a new mass distribution model of Messier 33 (M33), combining high-sensitivity Hα and HI interferometric data. In particular, this article presents the first Hα survey devoted to the large-scale distribution and kinematics of the M33 ionized gas disk.

M33 is the second most luminous spiral (SA(s)cd) galaxy in our neighborhood after M31. With an absolute magnitude of $M_V \sim$-19.3, it presents several arms (Sandage & Humphreys, 1980). Although two main arms are well known, M33 has not a clearly defined grand-design pattern. A system of seven spiral arms is pointed out by Ivanov & Kunchev (1985). In the optical bands, it could be considered as a flocculent spiral galaxy, but UV and IR observations show more prominent arms. The M33 profile presents a small bulge-like component in the IR bands. Its bulge and nucleus are the subject of numerous studies (e.g. : McLean & Liu 1996; Lauer et al. 1998; Gordon et al. 1999; Corbelli & Walterbos 2007). The optical parameters of M33 are given in Table 3.3.

In the literature, one can find distances to M33 varying from 700 to 940 kpc. Table 2.4 gives recent distance measurements for M33. The adopted distance for this study is D = 0.84 Mpc (scale $1'$ = 244 pc). It is the mean distance estimated by using resolved sources techniques such as Cepheids, Planetary Nebulae Luminosity Function (PNLF) and Tip of the Red Giant Branch (TRGB). The optical disk of M33 has a scale length of $\sim$9.2$'$ (2.25 kpc) in the V band (Kent, 1987; Guidoni et al., 1981) and its optical radius is R_{25} = 35.4$'$ (RC3). A cutoff in the radial surface brightness profile appears at $\sim 36'$ (~ 9 kpc) in the I band (Ferguson et al., 2007).

TABLE 2.3: Optical parameters of M 33.

Parameter	Value	Source
Morphological type	SA(s)cd	RC3
R.A. (2000)	$01^{\mathrm{h}}\ 33^{\mathrm{m}}\ 33.1^{\mathrm{s}}$	RC3
Dec. (2000)	$+30^{o}\ 39^{'}\ 18^{''}$	RC3
Optical inclination, i	$52^{\circ}\pm3^{\circ}$	WW
Optical major axis, PA	$22.5^{\circ}\pm1^{\circ}$	WW
Apparent magnitude, m_V	5.28	RC3
Absolute magnitude, M_V	-19.34	
(J-K)	0.89	JTH
Optical radius, R_{25} (′)	35.4 ± 1.0	RC3
Systemic velocity, V_{sys}	-179 ±3 $\mathrm{km.s}^{-1}$	RC3

References :WW : Warner et al. (1973), RC3 : de Vaucouleurs et al. (1991), JTH : Jarrett et al. (2003)

TABLE 2.4: Distances for M 33.

Method (indicator)	Distance Modulus m-M [mag]	Distance [Mpc]	Source
TRGB	24.54 ± 0.06	0.81	(1)
TRGB	24.75 ± 0.10	0.89	(2)
TRGB	24.64 ± 0.15	0.85	(3)
PNLF	24.62 ± 0.25	0.84	(4)
Cepheids	24.64 ± 0.06	0.85	(5)
Cepheids	24.70 ± 0.13	0.87	(6)
Cepheids	24.52 ± 0.14	0.80	(7)
Cepheids	24.55 ± 0.28	0.81	(8)
Cepheids	24.58 ± 0.10	0.84	(9)
Cepheids	24.62 ± 0.01	0.84	(10)
Mean adopted distance		0.84 ±0.04	
		$1'' \equiv 4$ pc	

References : (1) McConnachie et al. (2005), (2) Stonkutė et al. (2008), (3) Galleti et al. (2004), (4) Magrini et al. (2000), (5) Saha et al. (2006), (6) Paturel et al. (2002), (7) McConnachie et al. (2004), (8) An et al. (2007), (9) Freedman et al. (2001), (10) Gieren et al. (2013)

Mapping the environment of the Local Group galaxies, as is done by the "Pan-Andromeda Archaeological Survey" (PAndAS) (McConnachie et al., 2009), confirms that there was many mergers and interactions between them. The discovery of dwarf galaxies around the Milky Way and M31 and the tidal streams between M31 and M33 (PAnDAS) confirm our ideas about galaxy formation. The particular structure (star streams) seen in M33 could be associated with this history of mergers and interactions. In fact, many of the structures presented in McConnachie et al. (2009, 2010); Cockcroft et al. (2013) and Wolfe et al. (2013) around M31 and M33 can only be explained by these interactions. Deep Hα observations of M33 reveal the presence of low density HII regions outside the optical disk (Hoopes et al., 2001). This suggests recent star formation activity, possibly due to recent interactions.

Studying the kinematics of such a galaxy will provide a better understanding of the contribution of dark matter and of the best functional form describing its distribution. Still today, the cusp–core problem remains as one compares observations to predictions, especially for dwarf systems and this, despite the numerous studies on the DM distribution in galaxies in the last 30 years. While, on large scales, N-body cosmological simulations reproduce well the observations, it is more problematic at galaxy scales. The NFW profile, derived from those simulations, predicts a cuspy distribution in the central parts of the DM halos (e.g. Fukushige & Makino 1997; Moore et al. 1999; Navarro et al. 1997, 2010; Ishiyama et al. 2013), while observations especially of dwarf systems show more a core distribution (Oh et al., 2011). Those results can be explained by the gravitational potential related to the gas in those simulations, since the gas, which is important in the inner parts, is not accurately introduced in those simulations. Phenomena such as stellar feedbacks, galactic winds or massive clumps are not often well handled and reproduced (Goerdt et al., 2010; Inoue & Saitoh, 2011; Ogiya & Mori, 2011; Pontzen & Governato, 2012; Teyssier et al., 2013).

Several studies of the kinematics of M33 exist (e.g. Corbelli & Salucci 2000; Corbelli 2003; Putman et al. 2009; Corbelli et al. 2014), mainly based on HI. It appears from those studies that M33 is dark matter dominated (the dark matter mass is $>$ 10 times larger than the mass of the stellar disk) and that its HI disk is strongly warped. The gas in the disk of M33 is estimated $\sim$1.4-3$\times 10^9$ M$_\odot$ (Corbelli, 2003; Putman et al., 2009). In the mass model derived by Corbelli (2003), the stellar mass is estimated at $\sim 3 - 6 \times 10^9$ M$_\odot$ and the dark halo mass at $\sim$5$\times 10^{10}$ M$_\odot$. Most of the M33 kinematical studies use HI or CO (H$_2$), with a probable beam smearing impact on the innermost parts of the RC due to the lower spatial resolution of the HI data. Among the few Hα (optical) studies, the results presented by Carranza et al. (1968) show small velocity dispersions from 5 km.s^{-1} to 9 km.s^{-1} in the disk. However, they argue that these values could even be lower if taking into account the instrumental corrections. The mass-to-light ratio is an important parameter in the determination of the dark matter halo shape. In M33, Boulesteix & Monnet (1970) show very low values of M/L in the central ($< 50'$) part of the galaxy and increasing in the outer parts of the disk. The kinematics of the inner regions was studied using the warm gas (Hα) (Boulesteix & Monnet, 1970; Boulesteix et al., 1974; Zaritsky et al., 1989) and the cold molecular gas (H_2 via CO) (Wilson & Scoville, 1989; Gratier et al., 2010, 2012; Kramer et al., 2013; Druard et al., 2014).

The precise determination of the rising parts of RCs with high resolution data and a better estimate of the M/L ratio for the stellar disk could define more accurately the shape of its dark matter halo. High resolution optical observations of a nearby galaxy such as M33 is complex in view of the large size of the galaxy compared to the small field of view of high resolution integral field spectroscopic instruments. For M33, there is a lack of high resolution optical data available for the kinematical study. An exception is the study by Corbelli & Walterbos (2007) on the central $5'$ using the gas and stellar kinematics obtained by long-slit spectroscopy.

Mass models are sensitive to the rising part of the RCs (see, e.g Amram et al. 1996, Swaters et al. 1999, Blais-Ouellette et al. 1999). High resolution Hα RCs give a more accurate determination of the kinematical parameters for the derivation of the RCs and subsequently a more accurate determination of the mass model parameters . The high resolution Fabry-Perot (FP) integral field observations at Hα with a resolution $\gtrsim 10000$ give optimal kinematical data for the optical disk. The Hα RC can be used to test the shape of the DM halo allowing us to compare the derived DM distribution with CDM predictions.

To address these problems, this study presents Fabry-Perot (FP) mapping of M33 obtained at the Observatoire du mont Mégantic (OMM). Relaño et al. (2013) have studied the Spectral Energy Distribution (SED) of the HII regions of M33 and the star formation rate (SFR) and star formation efficiency (SFE) have been investigated by Gardan et al. (2007) and Kramer et al. (2011). More than 1000 HII regions can be resolved by the Hα observations ; Courtes et al. (1987) gave a catalogue of 748 HII regions. Observing those regions allows us to derive the ionised gas (optical) kinematics of M33. Determination of the M33 kinematics with a spatial resolution $\lesssim 3''$ (~ 12 pc) using the Hα velocity field and the derivation of an accurate RC in the inner parts are the main goals of this paper. The 3D data will be used to derive mass models with a dark halo component (ISO and NFW).

Section 2.5.2 describes the data acquisition and the instrumentation used while section 2.5.3 discusses the data reduction techniques. Section 2.5.4 details the kinematical analysis and

TABLE 2.5: Photon counting cameras at OMM.

Cameras	IXON888 [a]
Pixels size	$0.84'' \times 0.84''$
Active Pixels	1024×1024
Quantum Efficiency (QE)	$\gtrsim 90\%$
Cooling	-85 °C
Max. Readout Speed	10 MHz
RON	$< 1\ e^-$ with EM gain
Detectors	CCD201-20[b]
CIC[c] levels	$5 - 8 \times 10^{-3d}$

$1'' \equiv 4$ pc, $0.8'' \equiv 3.3$ pc at a distance of 0.84 Mpc

[a] http ://www.andor.com

[b] http ://www.e2v.com/products-and-services

[c] Clock-induced charges per pixel per frame

[d] Daigle et al. (2009b)

RON : Read-Out Noise given per pixel per frame

section 2.5.5 gives the details of the mass models analysis. A discussion of the M33 velocity dispersion, a comparison with other studies and the results from the mass modeling can be found in Section 3.4.5. Finally, a summary and the general conclusions are given in section 3.4.6 .

2.5.2 Fabry-Perot observations

2.5.2.1 Telescope and instrument configuration

The observations took place at the 1.6-m telescope of the Observatoire du mont Mégantic (OMM, Québec), in September 2012. A scanning Fabry-Perot (FP) etalon interferometer has been used during the observations with the device IXON888, a commercial Andor EM-CCD camera of 1024×1024 pixels . The details of this camera, based on e2v chips, are given in Table 2.5.

The IXON888 camera provides a large field-of-view (FOV) and was set to Electron Multiplying (EM) mode, 14 bits read-out resolution and its detector was cooled to -85 K during the observations. The camera clocks, gains and read-out speeds were adjusted in order to reduce the noise.

The order-sorter filter is a narrow band interference filter, centered at λ_c = 6557Å (nearly at the systemic velocity ~ -180 km.s^{-1}) with a FWHM of 30Å. Its maximum transmission is ~80%. The interference order of the FP interferometer is $p = 765$ at Hα. The FP has a Free Spectral Range (FSR) of 8.16Å (~373 km.s^{-1}), which has been scanned through 48 channels, corresponding to a spectral sampling of $\sim$ 0.17Å (7.8 km.s^{-1}). The finesse f of the Fabry-Perot etalon provides the spectral resolution $\Delta\lambda = FSR/f$. Our observations were done with a mean finesse of $f = 16.5$, as determined from datacubes of a Neon calibration lamp. The FWHM spectral resolution is thus $\Delta\lambda_{max}$ ~0.53Å (resolving power of ~ 12620 at Hα). This corresponds to a FWHM instrumental broadening of 23 km.s^{-1} (dispersion of ~ 10 km.s^{-1}) at the scanning wavelength of the observation of 6558.8 Å.

2.5.2.2 Data acquisition

The wide field-of-view of ~14′ ×14′ allows to map the bright inner disk regions of Messier 33 with only ten pointings. The different pointings overlap by a few arcseconds to allow the derivation of one final large mosaic with no gaps (§2.5.3.3). Figure 2.17 shows those pointings, whose centre coordinates are listed in Table 2.6. Notice that the central field has been observed more than once to yield very deep Hα data for the innermost regions of Messier 33. A region of the sky, free from apparent HII regions from Messier 33, has been observed before and after each galaxy pointing whose duration was larger than 30 minutes. Those acquisitions were done with the same interference filter as the one used for the galaxy, in order to perform the subtraction of the night-sky emission lines.

The data were obtained by operating the camera at two seconds exposure per frame. A gap of 0.4s between two consecutive channels was necessary to move the reflective plates of the FP etalon in order to avoid overlapping frames during the fast transfer.

Dark current, gain, flat field and noise calibration observations have been acquired at the beginning and the end of each night. The “Dark” observation consisted in a series of at least fifty images during which the detector is exposed for two seconds without light, and the gain is set to its largest amplitude, like during the observations of every sky/galaxy fields-of-view. The “Gain” observations consisted of about 200 frames, again acquired with the largest gain value. The “Noise” observations consisted in an integration of zero second, with the lowest gain value. A minimum of fifty frames were collected in order to calculate the read out noise of the CCDs. The noise, gain and dark were observed in off-light mode in the dome.

The total exposure time performed for each field is listed in Table 2.6. In total, the time spent to integrate on the Messier 33 fields was >30 hours. The seeing of the observations was $\lesssim 3''$. To

TABLE 2.6: Characteristics of the observations

Fields ID (1)	RA (2)	DEC (3)	T (4)	S (5)	am (6)	V_h (7)
M33_01a	1 :33 :59	+30 :40 :48.54	2.0	2.7	1.1	19.6
M33_01b	1 :33 :59	+30 :40 :48.54	1.4	2.2	1.3	17.5
M33_01c	1 :33 :59	+30 :40 :48.54	2.0	2.2	1.1	17.5
M33_02a	1 :33 :22	+30 :29 :22.27	1.4	2.8	1.1	17.0
M33_02b	1 :33 :22	+30 :29 :22.27	2.7	2.5	1.3	17.0
M33_03	1 :34 :29	+30 :51 :52.41	2.4	2.4	1.3	19.3
M33_04	1 :33 :06	+30 :40 :16.96	2.5	2.4	1.1	19.2
M33_05	1 :34 :50	+30 :40 :30.72	2.5	2.3	1.4	18.9
M33_06	1 :34 :15	+30 :28 :52.98	3.0	2.3	1.1	19.0
M33_07	1 :33 :35	+30 :52 :04.25	2.6	2.1	1.3	18.5
M33_08	1 :32 :33	+30 :28 :16.19	2.7	2.1	1.1	18.5
M33_09	1 :33 :26	+30 :18 :26.23	2.4	2.2	1.1	17.4
M33_10	1 :34 :18	+31 :02 :01.11	2.6	2.5	1.1	17.2
Sky	1 :32 :14	+31 :00 :09.48	0.2			17.5
Dark			0.1			
Noise			0.1			
Gain			0.1			
Flat	Dome	Dome	0.1			

Columns notes : (1) Identification of the field. (2) and (3) Coordinates of the field center (J2000). Each field-of-view is $14' \times 14'$. Observations presented in this paper have been taken in September 2012. (4) Exposure time in hours, (5) Seeing FWHM during observations. (6) Air mass correction factor. (7) V_h is the heliocentric velocity correction (km.s^{-1}).

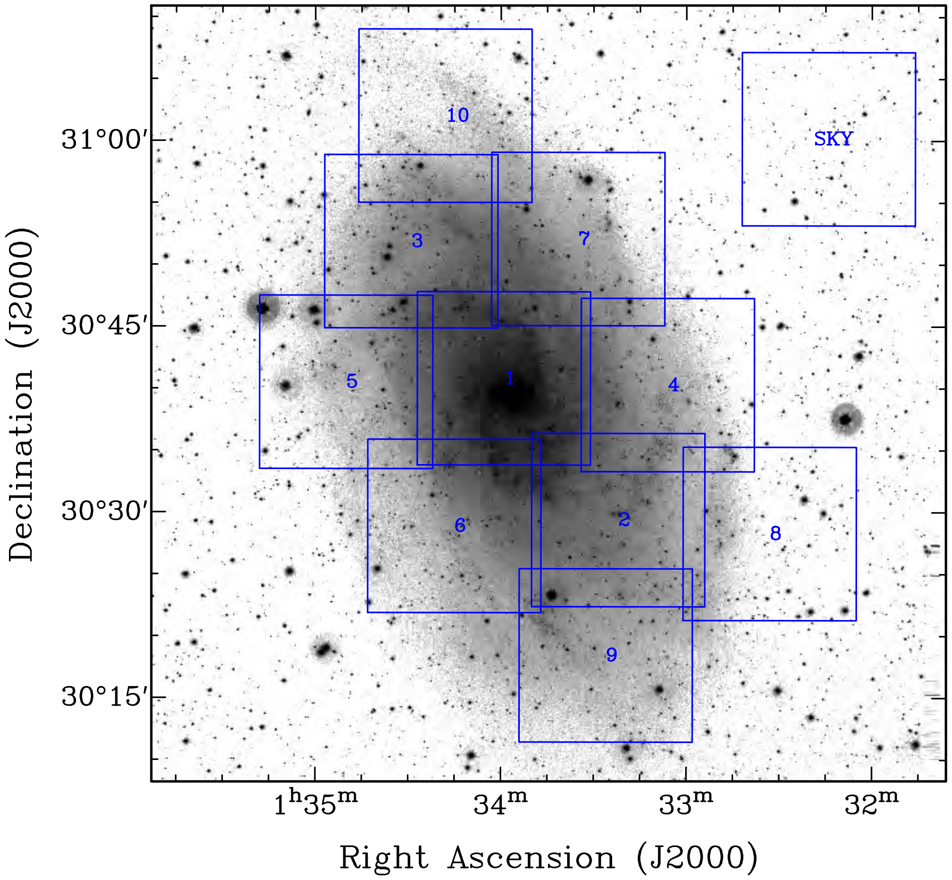

FIGURE 2.17: Mosaic of the 10 Fabry-Perot pointings in the direction of M33, shown with the sky field to the NW. The FOV of each field is $\sim 14' \times 14'$, with an overlap of $\sim 5''$. The background image is a R band archive image from KPNO (Hoopes et al., 2001).

perform the wavelength calibration, the system (filter+lenses+FP+camera) has been illuminated by a Neon (Ne) lamp. A narrow band filter centered on 6598Å and of FWHM=16.3Å was used to isolate the Ne line at λ=6598.95Å.

2.5.3 Data Reduction

2.5.3.1 Wavelength calibration, spectral smoothing

The raw frames of the observations contain interferograms giving the information on the number of photons per frame per channel and per cycle. We used Interactive Data Language (IDL) routines to integrate raw 2D files into a 3D datacube. A phase correction consisting in shifting every pixels such that they are at the same wavelength across the field has been applied to the raw datacubes to yield wavelength-calibrated datacubes. For that purpose, a phase map has been derived from a Ne line calibration observation. Datacubes are then wavelength-sorted and corrected for guiding shifts and cosmic rays. The "Noise", "Dark" and "Gain" observations (§2.5.2.2) were then used to correct and calibrate the detector response.

A Hanning filter with a width of three channels has then been applied to the spectra to increase the sensitivity. This reduction step is the same as the one applied to the Virgo Cluster, GHASP or SINGS samples (Chemin et al., 2006; Epinat et al., 2008a,b; Daigle et al., 2006; Dicaire et al., 2008). The same process is used for the sky observations, whose datacubes have been subtracted of all the other fields to produce M33-only Hα emission line datacubes. For pointings having more than one observation, all night-sky corrected and wavelength calibrated datacubes have been combined into a single datacube, to increase the sensitvity.

2.5.3.2 Airmass and ghosts corrections

Because the center of the interference rings of the observations is near the center of the detector, there are some reflections about the optical axis, called ghosts. The size and the intensity of the ghost depend on the shape of the region which produces the effect. We have used the method described in Epinat (2008) to reduce the number of pixels dominated by those ghosts. The typical residuals after ghost removal are about 10% of the initial ghosts flux.

Then, an airmass correction has to be applied. Indeed, differences in airmass during the multiple sessions of observations can affect the number of counts received by the detector, which implies field-to-field sensitivity variations. In Table 2.6, we give the airmass correction factor (AM) which has to be applied to each field in order to get the counts equivalent to an airmass of 1.0. Starting from the observed counts $\mathrm{C_{obs}}$ at a given airmass, the true value of the counts $\mathrm{C_{true}}$ is given by :

$$\mathrm{C_{true}} = 10^{-0.4\mathrm{AX}} \times \mathrm{C_{obs}} \tag{2.16}$$

The parameter A represents the Hα extinction coefficient. Our Fabry-Perot system has already been used by Hlavacek-Larrondo (2009) to determine the value of that coefficient. We used their value of 1.03. The X quantity is given by $\mathrm{X} = \mathrm{AM} - 1.0$, with the airmass correction factors AM listed in Tab. 2.6.

2.5.3.3 Mosaicing and binning the datacubes

Due to the large angular size of Messier 33, there are two possibilities to generate the final set of moment maps (Hα integrated emission, line-of-sight velocity and velocity dispersion maps, continuum map). A first one is to compute for each of the ten pointings its own moment maps, and combine all the maps to produce a single field-of-view moment map. The second approach is first to combine all datacubes into a mosaic datacube, and then generate moment maps. The first approach is easier to do, but it introduces more errors in radial velocities in regions of overlap. Instead, we think it is better to combine and correct the Hα spectra directly, than radial velocities or velocity dispersions. We thus chose the second approach, which is a more powerful process, though less straightforward to implement. Combining the data cubes increases the signal to noise per pixel, which results in increasing the numbers of pixels for which we can measure a line. To minimize the errors in the overlap regions, astrometry information have been added in each single cube headers. The different steps in the process are :

1. White light image (sum of all channels)
2. Accurate astrometry on the white light image
3. Field positioning from astrometry
4. Generation of an exposure map with the sum of exposures
5. Accurate spectral calibration, taking into account heliocentric correction
6. Generation for each channel of a mosaic
7. Weighting of each channel by the exposure map
8. Combination of all channels to generate the mosaic cube

In order to process projections and make an accurate mosaic, some parts of the Montage packages from IPAC (Infrared Processing and Analysis Center) have been used to develop our tools.

Once the mosaic datacube has been obtained, an adaptive spatial binning has been performed. That adaptive spatial binning is based on Voronoi 3D binning (e.g. Daigle et al., 2006; Chemin et al., 2006; Dicaire et al., 2008). The Voronoi technique consists in combining pixels to larger bins up to a given value of S/N (signal-to-noise ratio) or more. The pixels/bins with a S/N lower than the threshold S/N are combined with the neighbouring pixels until the threshold S/N value is reached. A S/N of 7 has been targeted for this study. This particularly allows to preserve the angular resolution where the S/N is high.

Figure 2.18 gives the channel maps of the data cube used to determine the kinematical parameters of M33. The detections plotted in Figure 2.18 are those above 3 sigmas. It represents the wavelength variation from 6556.5Å to 6560.6Å (from channel 11 to channel 35 in our data) where the channels width is 0.18 Å. The HII regions appear progressively from the North East side to the South-West side.

2.5.3.4 Moment maps derivation

The integrated emission field is the 0-th moment map derived from the spectra and the velocity field the first moment map. Radial velocities are given in the heliocentric rest frame. Making the assumption that the PSF has a gaussian profile, the velocity dispersion field is the second moment map :

$$\sigma_{corr} = \sqrt{\frac{\sum_{\mathrm{i}} \lambda_{\mathrm{i}}^2 \mathrm{F}(\lambda_{\mathrm{i}})}{\sum_{\mathrm{i}} \mathrm{F}(\lambda_{\mathrm{i}})} - \Lambda^2 - \sigma_{\mathrm{PSF}}^2} \tag{2.17}$$

where $\mathrm{F}(\lambda_{\mathrm{i}})$ is the flux corrected for the continuum level at wavelength λ_i, Λ is the barycenter of the emission line, and σ_{PSF} is the instrumental dispersion. Velocity dispersions have not been corrected for thermal broadening of the medium, nor for the natural width of the Hα line. While the natural width of the Hα line remains negligible (~3 km.s^{-1}), the reason for not correcting for the thermal dispersion of the gas was that the temperature of the ionized interstellar medium of Messier 33 is not known accurately. A typical broadening of ~ 10 km.s^{-1} is often given in the literature, for a temperature of $\sim 10^4$ K for the ionized gas. However, we have observed many bins of dispersion (after instrumental broadening correction) lower than this usual value of ~ 10 km.s^{-1}, implying that a typical temperature of $\sim 10^4$ K cannot be valid everywhere.

Finally, the moment maps have been cleaned to get rid of all possible unrealistic patterns, like those from reflection, noise and background emission residuals. For that purpose, we have masked all pixels with data values lower than twenty counts. We are left with maps having 546941 independent bins.

2.5.3.5 Flux calibration

The flux calibration that turns Fabry-Perot data counts into surface brightness (in $\mathrm{erg/s/cm^2/arcsec^2}$) is given by :

$$\mathrm{SB} = \mathrm{Cst} \times \mathrm{SB_{fp}} \tag{2.18}$$

Here, Cst is a calibration constant, SB is the corresponding surface brightness value. and SB$_{\mathrm{fp}}$ is the calibrated value of FP count/pixel/s. The FP fluxes calibration using a Hα map is a linear relation. We have used the catalog of HII regions of Relaño et al. (2013) as reference

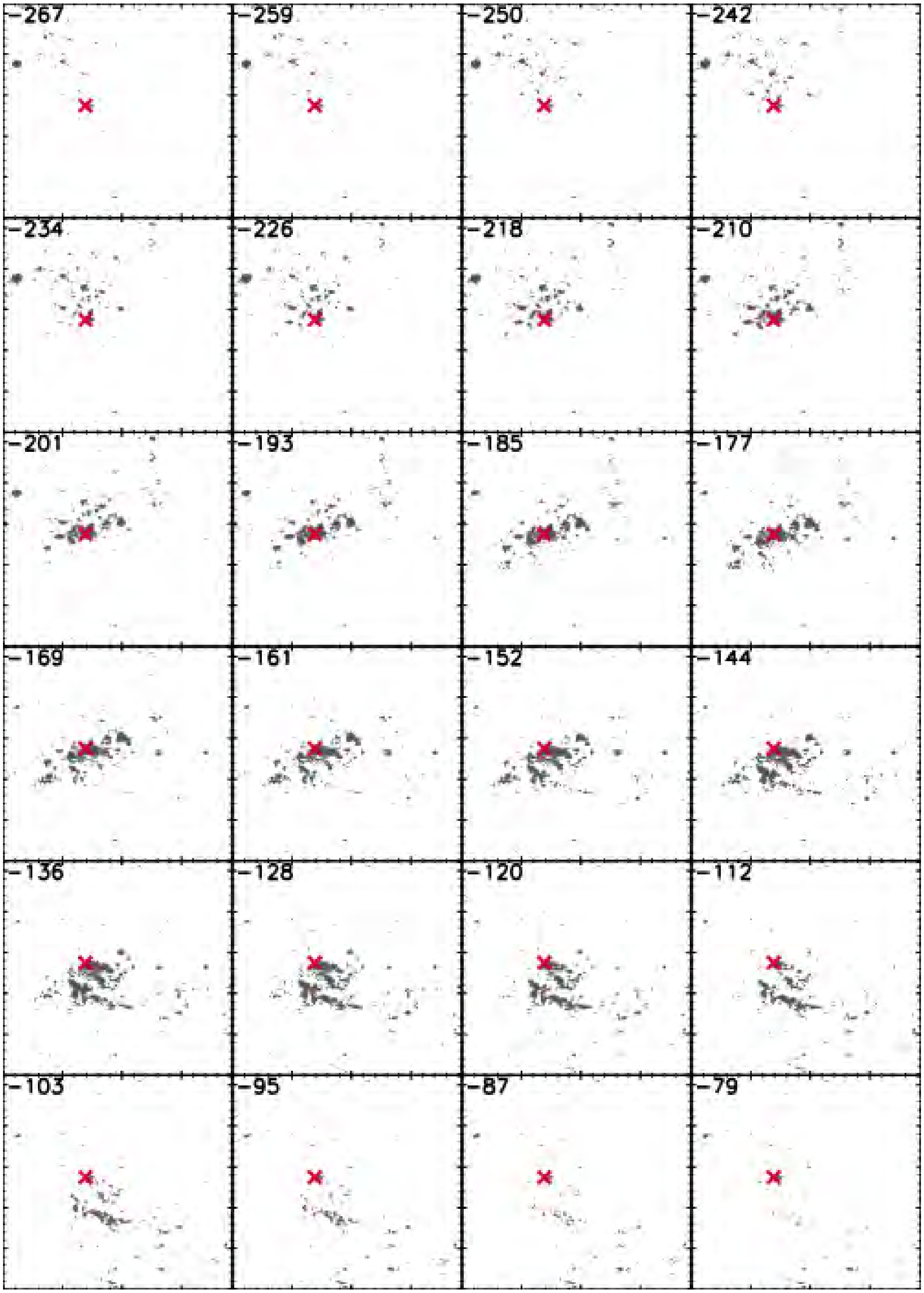

FIGURE 2.18: Hα channel maps. The radial velocity (km.s^{-1}) is indicated in the upper left corner of each channel and the cross indicate the kinematical center.

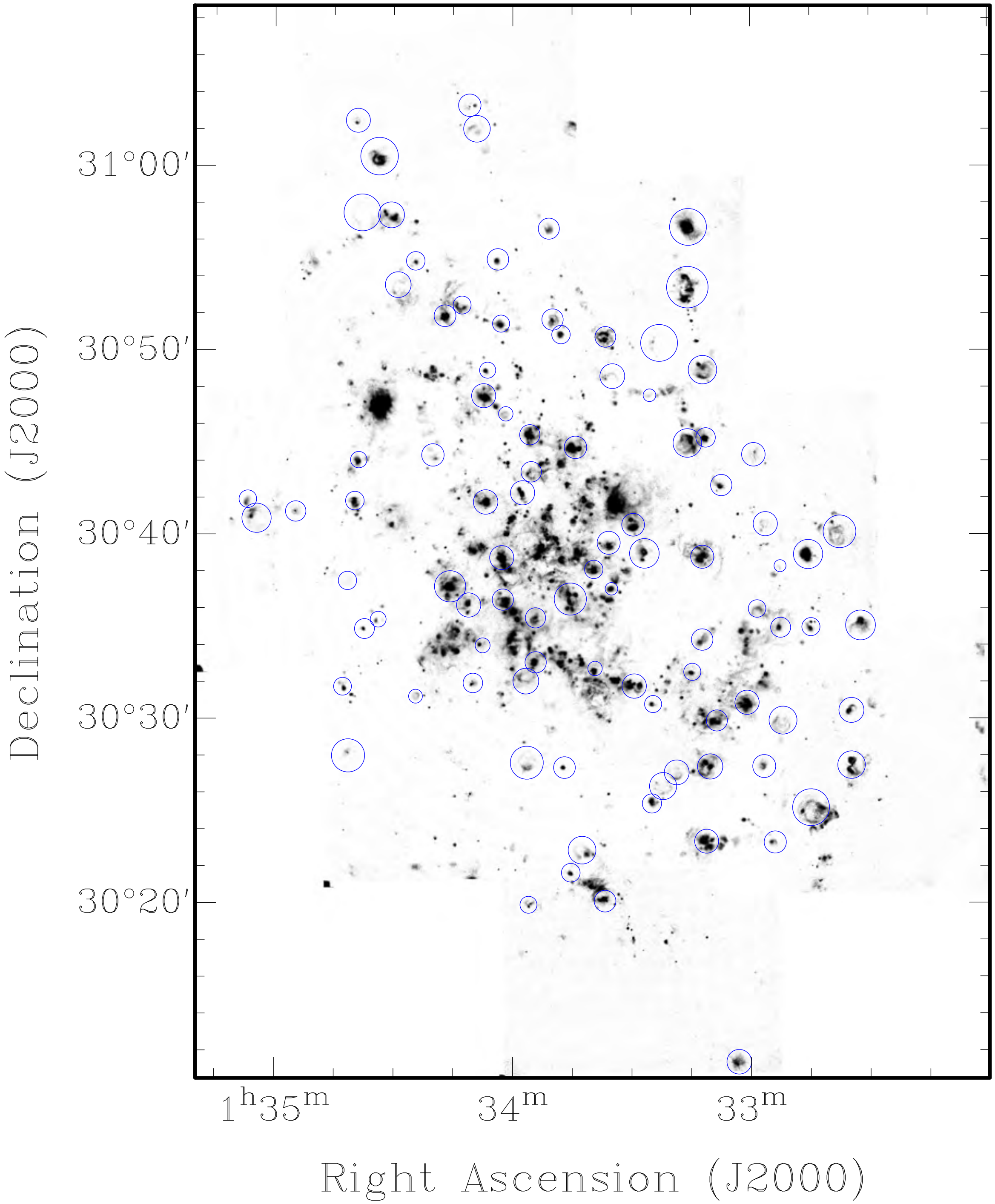

FIGURE 2.19: Selected HII regions for the Hα flux calibration over-plotted on the Hα line flux map obtained from our set of observations. The aperture size around each region is the same as in Relaño et al. (2013).

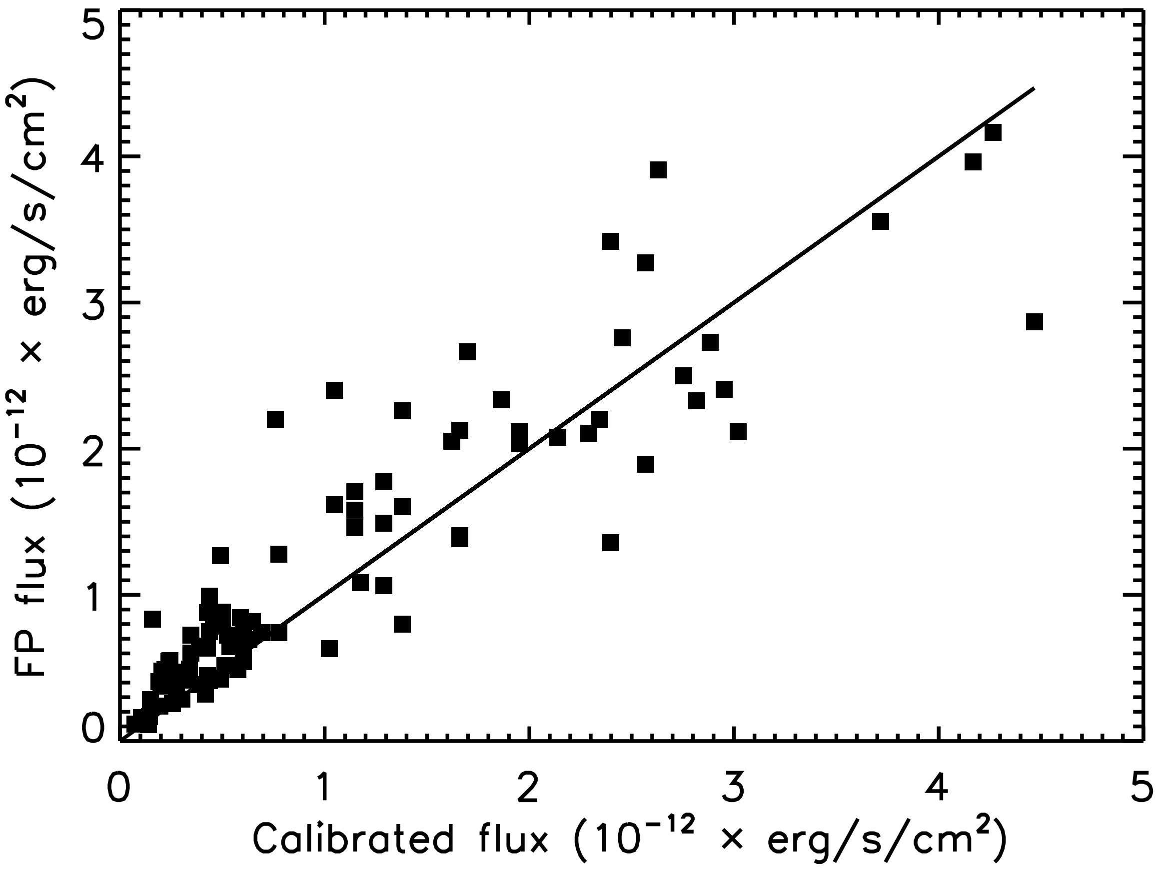

FIGURE 2.20: Comparison between the derived Fabry-Perot Hα fluxes and the reference Hα fluxes of Relaño et al. (2013) used for the FP flux calibration. Square symbols represent data from individual HII regions (Fig. 2.19) and the solid line is the linear fit to the data.

fluxes to calibrate our interferometric data. Figure 2.19 shows the selected regions and their associated aperture size used to integrate the Hα counts. For each region the total integrated flux is computed using the counts and the mean exposure time.

The calibration constant for the M33 Hα FP image is given by $1 \text{ count/pixel/s} = 2.45 \pm 0.03 \times 10^{-17} \text{erg/s/cm}^2/\text{arcsec}^2$. The typical error that can be noticed on the flux determination at an aperture used, is $\sim 2.4 \times 10^{-16} \text{erg/s/cm}^2/\text{arcsec}^2$. It takes into account the errors on the Hα flux provided in Relaño et al. (2013) and the dispersion of the fit. Figure 2.20 shows the comparison bewteen our Fabry-Perot calibrated data, and the Relaño et al. (2013) data in units of flux, $erg/s/cm^2$.

2.5.4 Hα distribution and kinematics

2.5.4.1 Hα maps

The observations obtained at the OMM give 13 cubes on ten fields. Those cubes were used to build a mosaic cube as described in section 2.5.3.3. Figure 2.21 shows the Hα emission of M33 in the $\sim 42' \times 56'$ field. The contours are from HI and CO emission. We can see that while the Hα emission follows roughly the HI emission, it is even more so for the CO emission. The HI and CO structures seem to follow the arms described by the HII regions. The final cube was produced with the same FSR and same spectral resolution as the small cubes observed. The Hα monochromatic image (moment zero map) is presented at the top right of Figure 2.22 and can be compared to the WISE I NIR image on the left. The discrete HII regions have different sizes and shapes, filled and clear shell regions as described by Relaño et al. (2013). Two main strong arms are clearly defined along with the multi arms structure as presented by Boulesteix et al. (1974).

The velocity field (first moment map) at the bottom left of Figure 2.22 was obtained by using the zeroth moment map as a mask. The bins of the voronoi binning with data values greater than 20 counts are shown. This criteria was chosen in order to avoid all probable unreal pattern introduced by ghosts of strong Hα regions, noise and/or background. The velocity dispersion map (second moment) is shown in the bottom right of Figure 2.22.

For this study, the data will be used mainly to derive the overall kinematics and derive the optical rotation curve. Figure 2.23 shows that the resolution of this data set ($\sim 3''$) could be used to study the detailed kinematics of HII regions, shells, cavities, bubbles, filaments, loops, outflows and ring-like structures. This will be done in another publication. Except within such local features, the large-scale Hα velocity field of M33 seems regular, typical of nearby disk galaxies, without significant apparent twist of the major axis, and with mild streamings inherent to spiral arms (see sect. 2.5.4.2.4).

Figure 2.24 provides a zoom of the $\sim 8' \times 8'$ central regions of M33. When compared to the WISE I NIR image to the lop left, it can be seen clearly that emission is detected all the way to the very center of the galaxy. The velocity dispersion map shows that brighter HII regions exhibit larger dispersion (20-30 km.s^{-1}), though the largest dispersions (up to 60 km/s) are only seen in bins with the faintest Hα emission. The map also shows that the inner regions exhibit smaller dispersion (see Section 6 for more details).

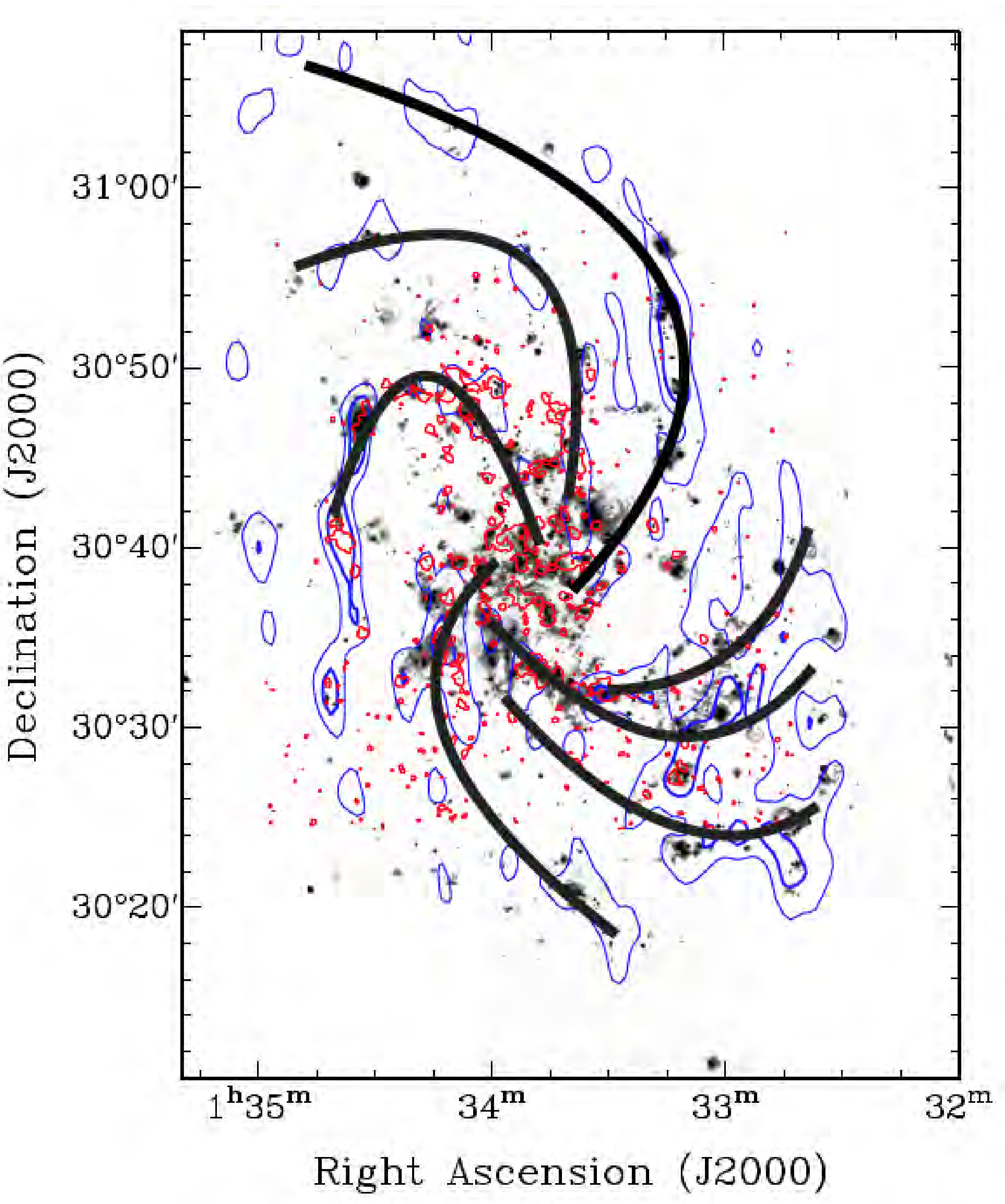

FIGURE 2.21: Hα map of M33 derived from our Fabry-Perot data. The CO peak contours are in red (120 K km/s) from Tosaki et al. (2011) and the HI peak contours are in blue (9500 and 1200 K km/s) from Chemin et al. (2012). The black sketchs are drawn to follow the HII regions and trace the multi arms profile of M33. These arms are close to those shown in Li & Henning (2011) or Boulesteix et al. (1974).

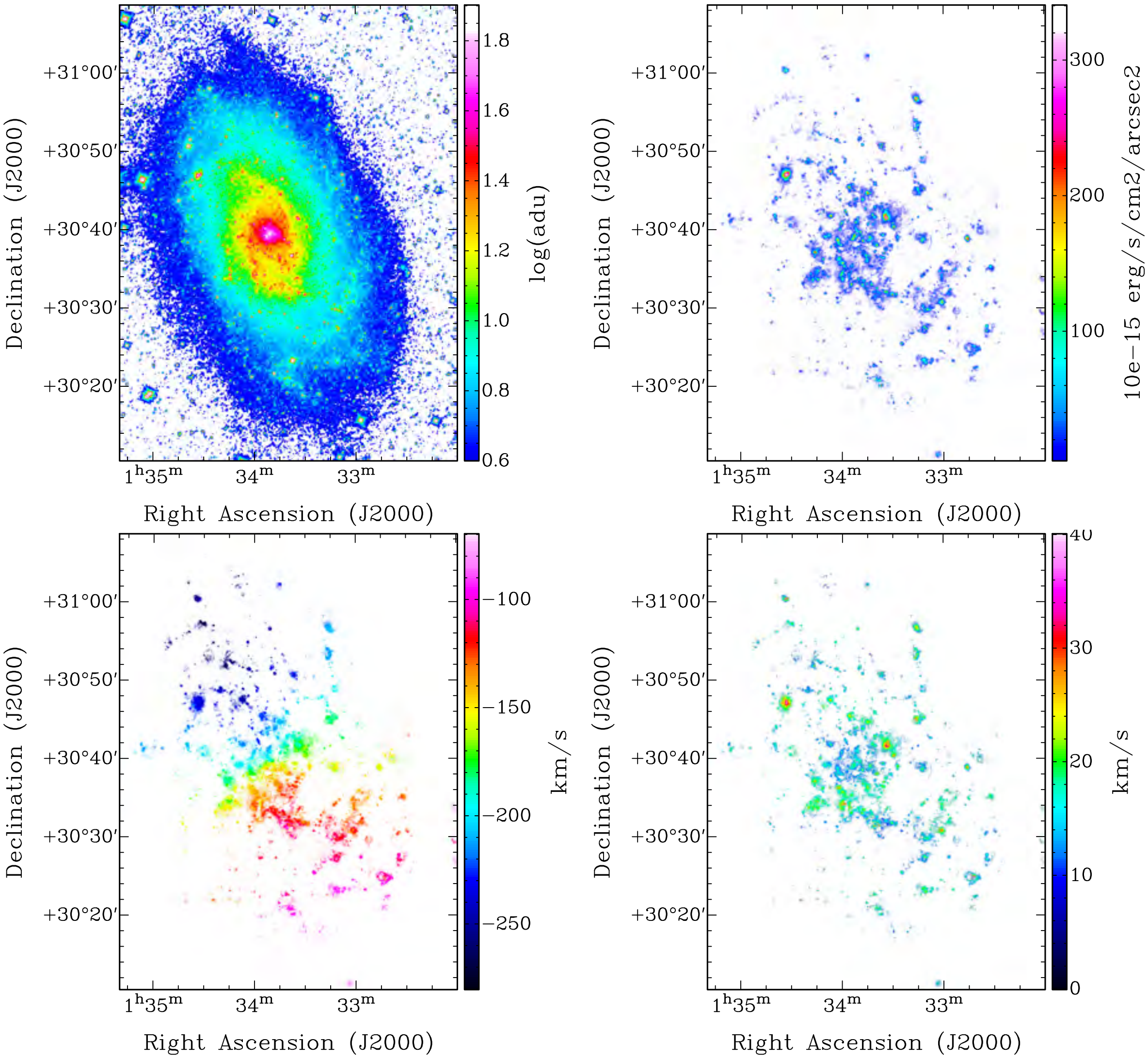

FIGURE 2.22: 3.4 μm and narrow-band Hα maps of Messier 33. The NIR image from WISE I (top-left) is shown with a logarithmic stretch. The Fabry-Perot interferometry images are the Hα integrated emission map, velocity field and velocity dispersion field (top-right, bottom-left and bottom-right, respectively).

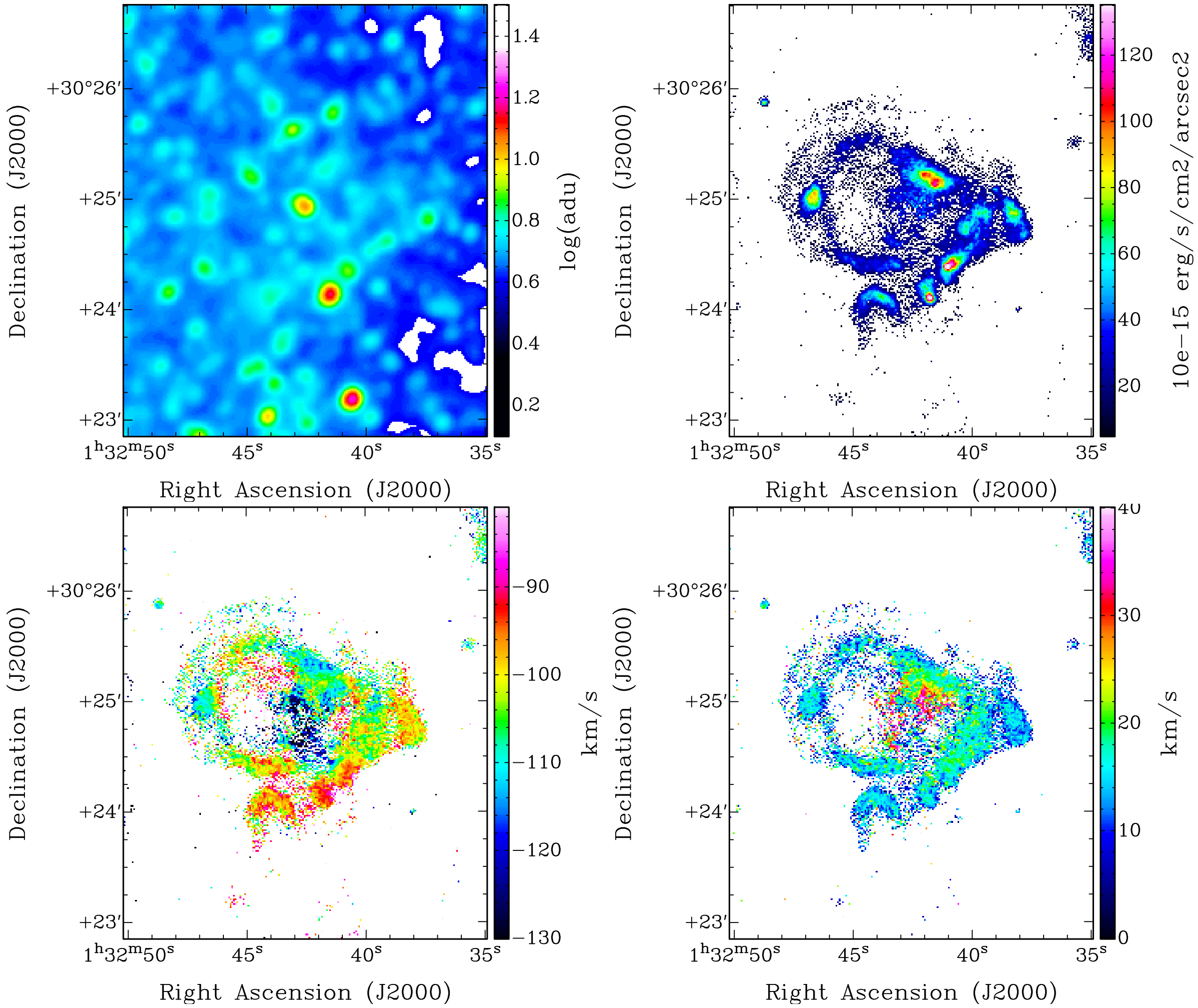

FIGURE 2.23: Same as in Figure 2.22, zoomed on the star forming region located at α=01h32m43s, δ=30°24′57″.

2.5.4.2 Kinematics

We performed a kinematical analysis in order to recover the set of kinematical parameters and the best possible rotation curve with meaningful uncertainties.

2.5.4.2.1 Initial parameters

The ROTCUR algorithm implemented in the reduction package GIPSY (Groningen Image Processing System ; Vogelaar & Terlouw 2001) has first been used to find the mean initial values of the kinematical parameters, and to verify that no significant warp of the ionized gas disc exists. ROTCUR is based on the tilted-ring model described in Begeman (1987). Starting from initial values of i = 51° and PA = 200° , V_{sys} and the rotation center (x_0, y_0) are first determined.

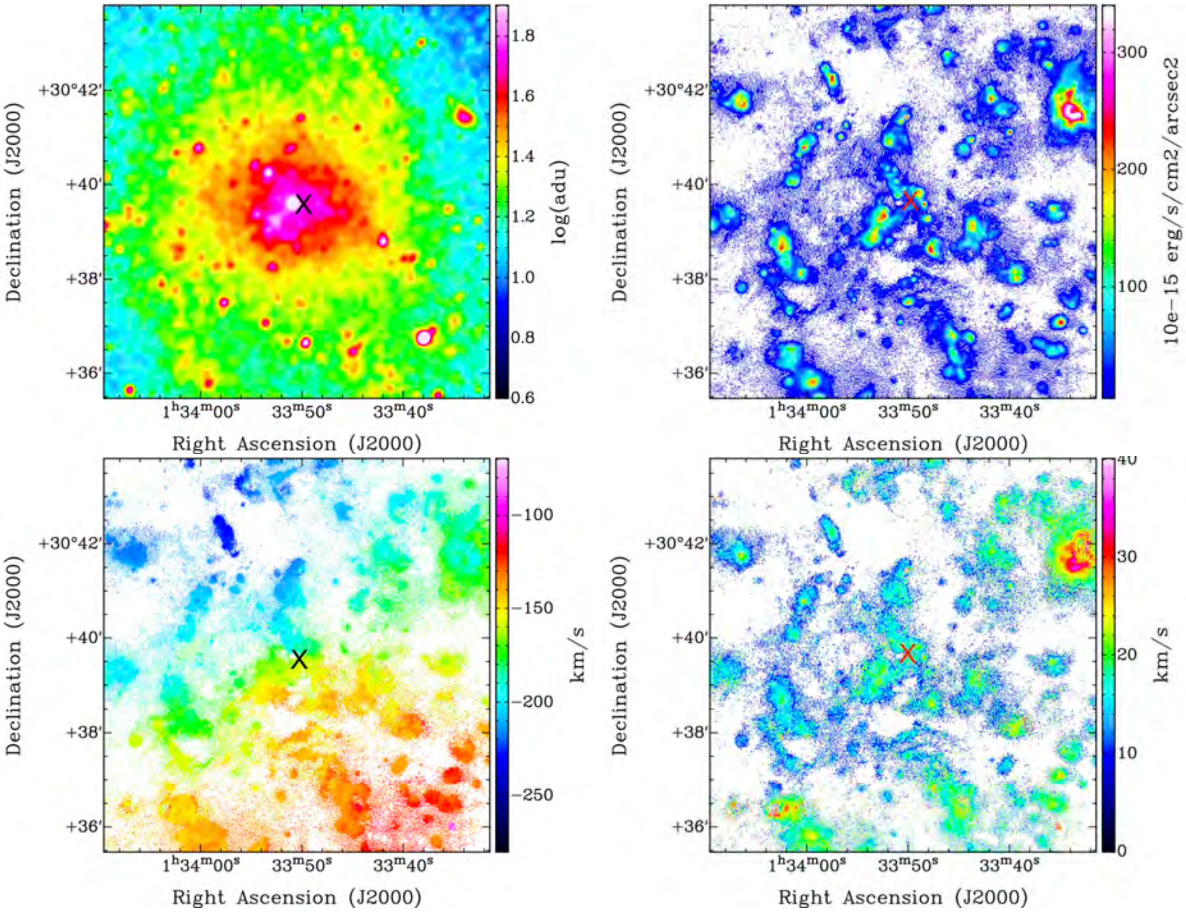

FIGURE 2.24: M33 central ∼8′ field - same caption as in Figure 2.22. The datapoints presented are the barycenter after an adaptive binning with S/N=7. The cross indicate the kinematical center.

A second run allowed us to derive the inclination and PA profiles. From those profiles, we measured an inclination i = 52° ± 2°, and a PA = 202°±2°, both values being very close to the optical morphological values (see Table 3.3). In both cases, the errors are determined using the deviation around the mean values. No trend has been detected in the inclination and position angle profiles, and the small standard deviations are clear indications that no significant warp of the Hα disk exists (at least in the regions covered by our observations), as is usually the case for the optical disks (warps are mainly seen in the extended HI disks).

2.5.4.2.2 Rotating disk model

Since no warp is detected in the Hα disc using ROTCUR (tilted ring model), we used a model in which the gas is supposed to lie in a unique plane in order to derive the kinematical parameters and the rotation curve. Thus we use the whole 2D information to derive the projection parameters and their uncertainties. The model is explained in Epinat et al. (2008b) and was used

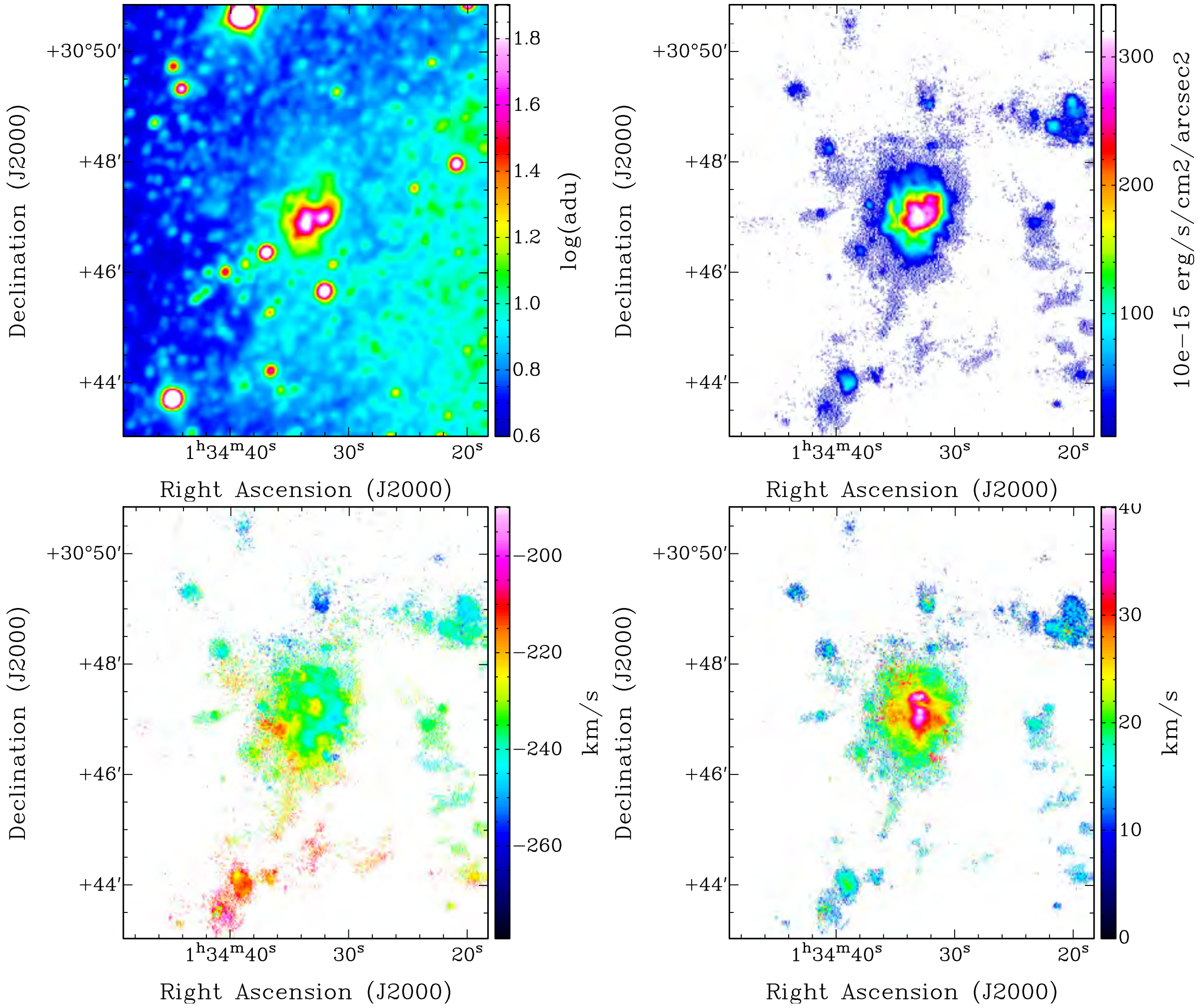

FIGURE 2.25: Same as in Fig. 2.23, zoomed on the star forming region NGC 604

for the $GHASP$ sample data analysis. When the vertical motion velocities are not considered, the observed line-of-sight velocities are expressed as :

$$\mathrm{V_{obs}} = \mathrm{V_{sys}} + (\mathrm{V_{rot}}(\mathrm{R})\cos(\theta) + \mathrm{V_{exp}}(\mathrm{R})\sin(\theta))\sin(\mathrm{i}); \tag{2.19}$$

where R and θ are the polar coordinates in the plane of the galaxy, i is the disk inclination, $\mathrm{V_{rot}}(\mathrm{R})$ is the azimuthal velocity (i.e. the rotation curve) and $\mathrm{V_{exp}}(\mathrm{R})$ is the radial velocity in the galaxy plane (often referred to as the expansion velocity). Defining the kinematical position angle PA as the anticlockwise angle between the North and the direction of the receding side, the azimuthal angle θ can be deduced at each position (more details in the annexes of Epinat et al., 2008b).

With the hypothesis that the radial velocities of the ionized gas are negligible with respect to the azimuthal rotation, the observed velocities become $\mathrm{V_{obs}} = \mathrm{V_{sys}} + \mathrm{V_{rot}}(\mathrm{R})\cos(\theta)\sin(\mathrm{i})$. We therefore build a 2D model with a set of projection parameters (center, position angle and inclination) and a set of kinematics parameters describing the rotation curve and the motion of the galaxy with respect to the Earth (systemic velocity). All these parameters have no dependency with radius, contrary to what is done in tilted ring models (e.g. Begeman, 1987).

The rotation curve we used in our model is described by the Zhao function (Kravtsov et al., 1998) with reduced parameters :

$$\mathrm{V_{rot}} = \mathrm{V_t}\frac{(\mathrm{R/r_t})^{\mathrm{g}}}{1 + (\mathrm{R/r_t})^{\mathrm{a}}}; \tag{2.20}$$

where $\mathrm{r_t}$ and $\mathrm{V_t}$ define the transition ("turnover") radius and velocity, a and g describe the sharpness of this transition and the shape before and after the transition. Therefore, the 2D model is described by a set of 9 parameters (i, PA, X_{cen}, Y_{cen}, V_{sys}, V_t, r_t, g, a). The optimization starts with the initial parameters i, PA, Vsys and the rotation center previously found using ROTCUR, which are compatible with morphological parameters. The method uses a χ^2 minimization calling the IDL LMFIT routine based on the Levenberg-Marquardt method in order to find the best fit model. The uncertainties on the parameters are derived using a Monte Carlo method based on the power spectrum of the residual velocity map (see Epinat et al., 2008b for details).

2.5.4.2.3 Derived kinematical parameters

With thousands of degrees of freedom, the optimized model converges rapidly towards a stable solution. The optimized center is found at R.A. = 01^{h} 33^{m} 54.1^{s}, DEC. = $30°39'42''$. That location is $\sim 42''$ (168 pc) from the photometric centre (sky projected distance), towards the NE direction, with an angle of 60° with respect to the semi-major axis of the approaching side. This offset corresponds to a deprojected distance of $63''$ (252 pc) in the galaxy plane of Messier 33. As a comparison, sky-projected offsets between photometric and kinematical centres of bright spirals in the Virgo cluster of galaxies have been found between 70 and 800 pc (Chemin et al., 2006). The offset we find for Messier 33 is thus comparable with other spirals, at the low end of the distribution for other galaxies.

The derived systemic velocity is $\mathrm{V_{sys}} = -178 \pm 3$ km.s^{-1}, the position angle $\mathrm{PA} = 202 \pm 4°$ and the disc inclination $i = 52 \pm 2°$. These parameters are in excellent agreement with those found with ROTCUR, and with literature values. The values for the other parameters are $g = 1.2 \pm 0.7$ and $a = 1.01 \pm 0.6$; those parameters being in good agreement with best fits parameters range of rotating discs described by Kravtsov et al. (1998). Rotation can be approximated to a linear function of radius in the inner parts where $R < r_t = 1.1'$and velocities $\mathrm{V} < \mathrm{V_t}$ = 50 km.s^{-1}.

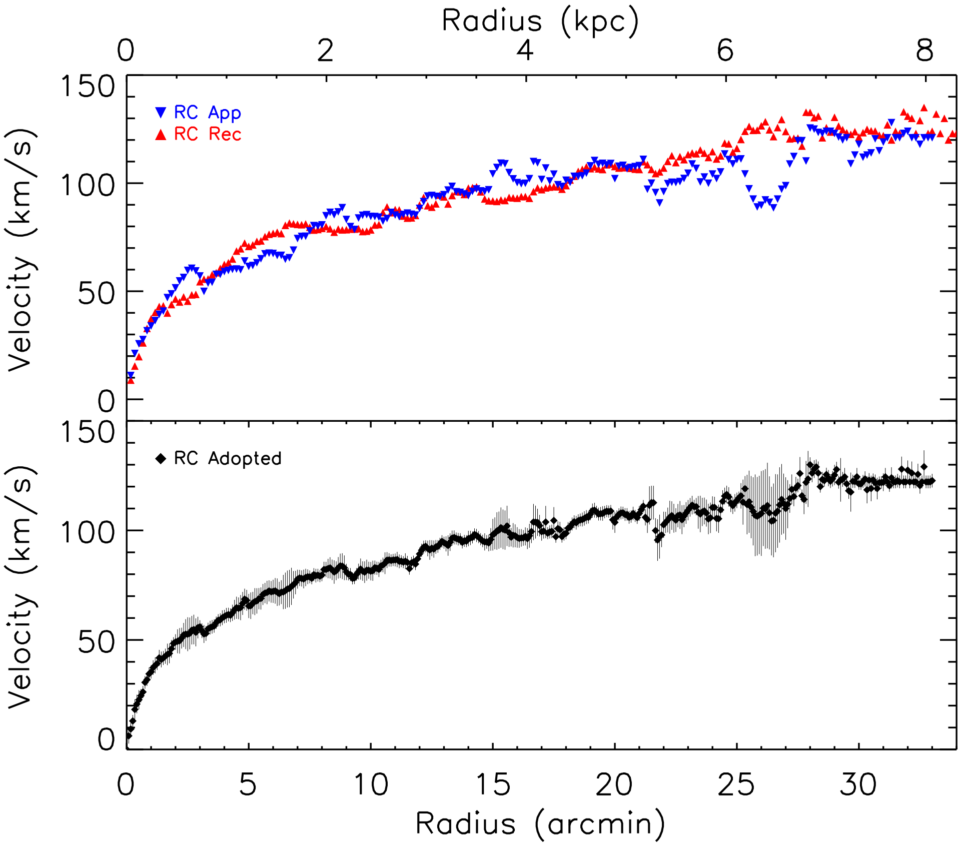

FIGURE 2.26: Hα rotation curve of Messier 33. The top panel shows the curves for the approaching and receding disk sides (blue downward triangles and red upward triangles, respectively). The adopted rotation curve of M33 is shown in the bottom panel.

2.5.4.2.4 Rotation curve

Rotation curves for the entire disk, and for the separate approaching and receding sides of the disk have been extracted using the projection parameters obtained from the model fitting described above. As detailed in Epinat et al. (2008b), the rotation curve is extracted in rings whose width is optimized by gathering a minimum of fifteen velocity measurements in the velocity field within each ring. Because the velocity field contains more than 500000 independent pixels, it was very easy to define rings with such a number of pixels. As a result, the rotation curves were incredibly resolved, with thousands of rings for $0 < R < 35'$. Therefore, for practical reasons we decided to rebin the resulting curves at radii regularly spaced by 5″, and of 5″ width. The top panel of Figure 2.26 shows the Hα rotation curves for the approaching and receding sides, while the bottom panel shows the global rotation curve, as fitted using both sides of the disk simultaneously. The adopted rotation curve is given in Table 2.7 with the associated velocity errors ΔV. The adopted rotation velocity uncertainty is given by $\Delta \mathrm{V} = \sqrt{\epsilon^2 + |\mathrm{V_a} - \mathrm{V_r}|^2/4}$.

TABLE 2.7: Sample of the Hα rotation curve of M33. Full table available online.

Rad (1)	V (2)	ΔV (3)	σ (4)	$\Delta\sigma$ (5)	Rad (6)	V (7)	ΔV (8)	σ (9)	$\Delta\sigma$ (10)	Rad (11)	V (12)	ΔV (13)	σ (14)	$\Delta\sigma$ (15)
0.08	6	4	14	10	11.08	87	4	16	5	22.08	104	5	17	7
0.17	9	4	12	6	11.17	86	3	16	5	22.17	105	6	17	7
0.25	13	3	12	4	11.25	86	3	16	6	22.25	106	8	18	7
0.33	18	5	14	5	11.33	86	3	16	6	22.33	107	7	19	8
0.42	21	4	15	4	11.42	86	4	15	6	22.42	106	7	18	8
0.50	23	4	16	4	11.50	85	3	15	6	22.50	105	5	17	7
0.58	25	3	15	4	11.58	83	3	15	6	22.58	107	5	16	7
0.67	26	3	16	5	11.67	85	3	16	6	22.67	107	6	17	8
0.75	31	3	16	5	11.75	86	3	16	6	22.75	105	7	16	7
0.83	32	3	15	5	11.83	85	3	16	6	22.83	107	5	15	7
0.92	35	3	15	4	11.92	87	3	16	6	22.92	108	5	16	7
1.00	35	3	15	4	12.00	89	3	17	7	23.00	109	5	15	6
2.00	49	4	14	4	13.00	94	3	18	8	24.00	110	5	17	8
3.00	56	3	14	5	14.00	96	4	16	6	25.00	114	4	16	7
4.00	61	3	15	5	15.00	98	7	15	7	26.00	108	19	17	7
5.00	65	6	16	5	16.00	97	5	16	6	27.00	110	14	14	8
6.00	72	5	17	5	17.00	99	4	17	6	28.00	130	3	19	12
7.00	78	4	17	6	18.00	99	3	17	7	29.00	125	5	19	9
8.00	80	3	17	6	19.00	107	3	17	7	30.00	121	3	14	10
9.00	81	4	17	6	20.00	104	5	16	6	31.00	122	4	15	11
10.0	81	4	15	6	21.00	108	3	15	8	32.00	128	4	22	21

Notes : Column (1) : radius in arcmin, (2) the rotation velocities in km.s^{-1}, (3) errors on V (4) : σ (velocity dispersion) profile and (5) errors on the velocity dispersion. The following columns (up to 15) have the same definitions as the previous columns

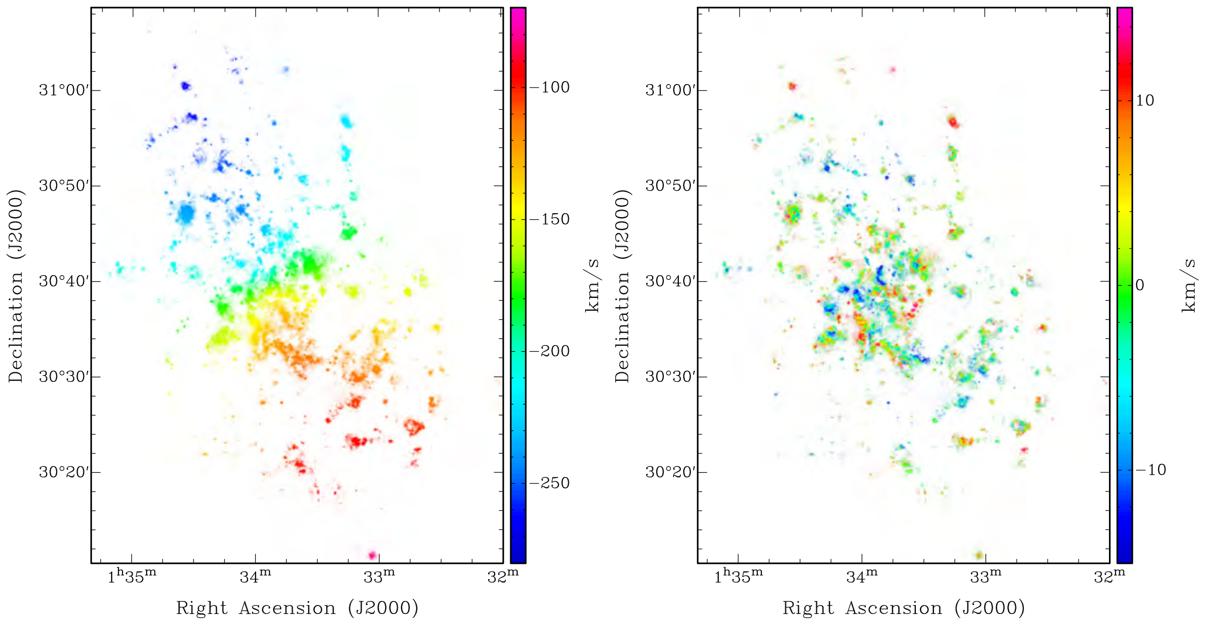

FIGURE 2.27: The left image gives the axisymmetric model obtained with the kinematical parameters obtained with the Zhao model (See Sect. 2.5.4.2.2). The map was masked with the Hα monochromatic map (top right map in figure 2.22). The right image gives the residual map (observed-model).

The term ϵ is the dispersion around the mean value within each ring (statistical error for the both sides velocity calculation). The second part $|\mathrm{V_a} - \mathrm{V_r}|/2$ is the systematic uncertainty that expresses the asymmetry between rotation velocities for the approaching ($\mathrm{V_a}$) and receding ($\mathrm{V_r}$) disk halves. The formal statistical error is usually smaller than the systematic error. The RC used for the mass models is the adopted RC of Figure 2.26 (bottom panel). Only the points where data are present on both sides are used. As shown in Figure 2.26 (top panel), the RC on the approaching side goes out to ≥ 8.5 kpc and only out to ~ 8.1 kpc on the approaching side. So, the adopted RC stops at ~ 8.1 kpc. The RC was smoothed at a binning of 5″to get constant step in the mass modeling. The Hα rotation curve exhibits a regular rising gradient within the inner $R = 8$ kpc, reaching a maximum velocity of ~ 125 km.s^{-1} at the last data points. Many wiggles are obviously seen, as probable consequences of the crossing of the spiral arms of Messier 33 or due to co-rotation effects. The axisymmetry of the rotation is very good. Indeed, the most significant differences (~ 35 km.s^{-1}) between $\mathrm{V_a}$ and $\mathrm{V_r}$ are only observed in a narrow range around $R = 6.5$ kpc. The axisymmetric velocity field model, as deduced from the adopted rotation curve with all kinematical parameters kept constant with radius, and its subtraction to the observed velocity field are shown in Fig. 2.27. The distribution of residuals is centered on 0 km.s^{-1}, with a standard deviation of 8 km.s^{-1}, implying a very accurate kinematical model for most of the disk. We note that locally, bright Hα emission in spiral arms can exhibit larger velocity differences. For instance, the star forming region at R.A. = $01^{\rm h}$ $33^{\rm m}$ $15.4^{\rm s}$, DEC. = $30°56'48''$ has an average residual of ~ 10 km.s^{-1}. This likely shows the limit of the axisymmetric rotation model at those angular resolution ($5''$, i.e 20 pc). Our observations are indeed sensitive to very local, non-axisymmetric motions inherent to such star forming regions (expanding shell, etc.), which cannot be modeled correctly by the large-scale rotation of the galaxy. Notice also that larger residuals in spiral arms indicate the presence of asymmetric or streaming motions. Such motions are often observed in disk galaxies, but cannot be modeled by the axisymmetric rotation. Finally, larger residuals at the outskirts of the Hα disk could indicate that some HII regions may not necessarily lie in the main equatorial plane of inclination i = 52°, so that deprojection of their velocities has not been performed correctly.

2.5.4.2.5 Velocity dispersions

The velocity dispersion profile has been derived by azimuthally averaging the velocity dispersions σ in annuli of $5''$ width, in $5''$ steps (Figure 2.28). Annuli have been computed using the projection parameters determined from the kinematical model (sect. 2.5.4.2.3) The σ profile is almost consistent with a flat profile. The mean dispersion is 16 km.s^{-1}. Like for the rotation curve, wiggles are detected. They are likely caused by increased dispersion when crossing the spiral arms. They are nonetheless not significant to make a noticeable increase of the scatter. We measure a standard deviation of the disperion profile of 2 km.s^{-1}. The profile marginally decreases from R=1.5 kpc towards the centre. From $R \sim 7.5$ kpc, the velocity dispersions increase to $\sim 20-25$ km.s^{-1}. This radius is the location of the beginning of the warp of the HI disk where the twist of the position angle starts (Corbelli & Salucci, 2000). However, it would be interesting to have Hα data with good SNR beyond these radius to better understand the Hα dispersions behaviour in regions where the HI disk warp is more pronounced.

2.5.5 Mass modeling

The Hα rotation curve describes accurately the velocity gradient in the center of galaxies, usually better than any other kinematical tracer. Such optical high-resolution is crucial to test different inner shapes of dark matter haloes, like cuspy or shallow models. This section only focuses on the modelling of the mass distribution of Messier 33 within the inner 8 kpc from our newly derived Hα rotation curve. However, with a RC only derived out to 8 kpc, we do

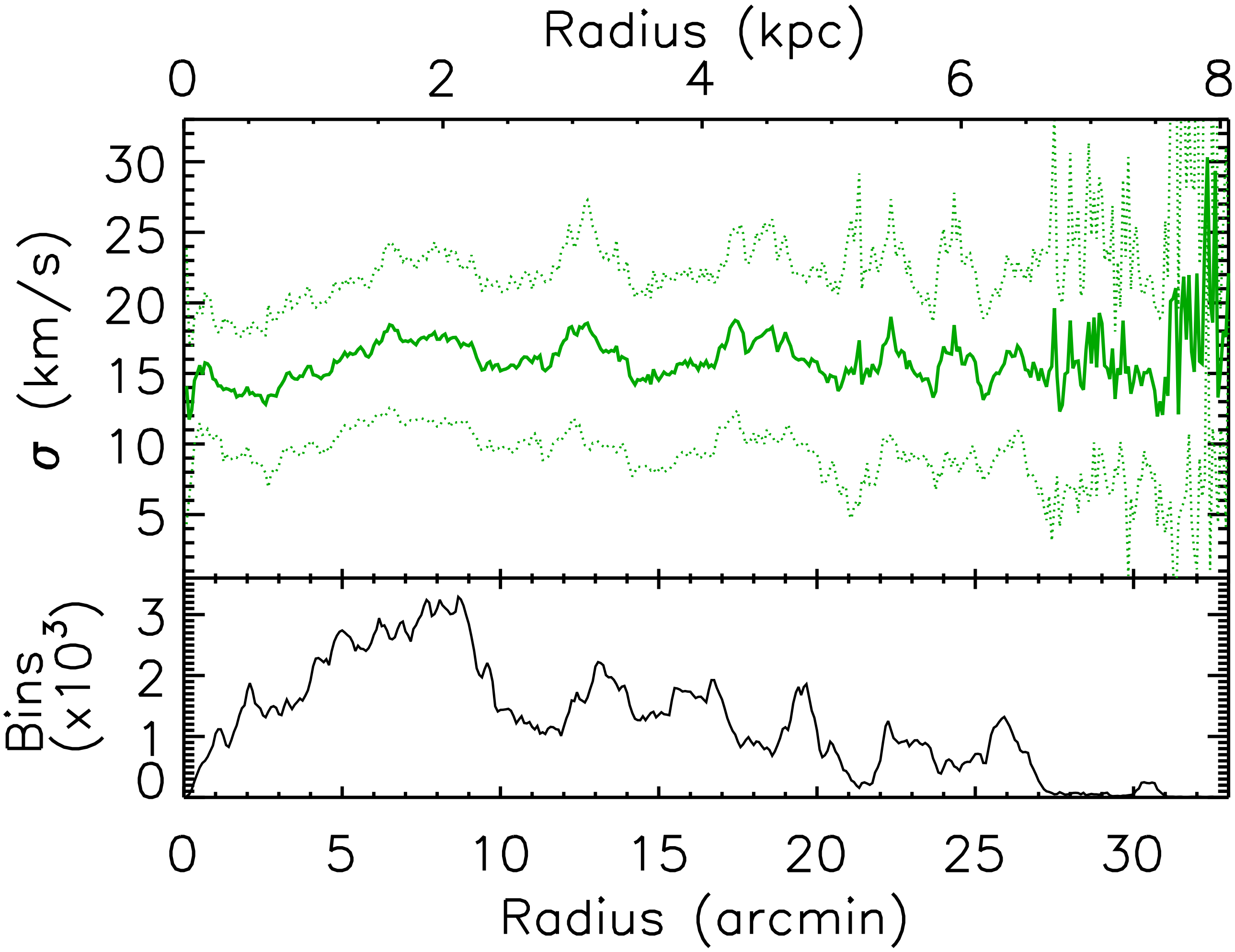

FIGURE 2.28: Hα velocity dispersion profile of M33. Dotted lines display values at +/- one standard deviation derived in each radial bin. The bottom panel shows the number of independent bins used to calculate the dispersion.

not expect strong constraints on the halo's parameters. We postpone to a forthcoming article a more complete modelling of the mass distribution from a more extended rotation curve that will merge our inner Hα rotation curve with a new HI rotation curve for the outer regions of Messier 33 (Kam et al., in preparation).

2.5.5.1 Luminous mass components

2.5.5.1.1 The neutral gaseous disc

Provisional data on the HI gas component have been presented in Chemin et al. (2012). Those observations will be fully described in a future Kam et al.'s paper. Figure 2.29 presents (left-hand

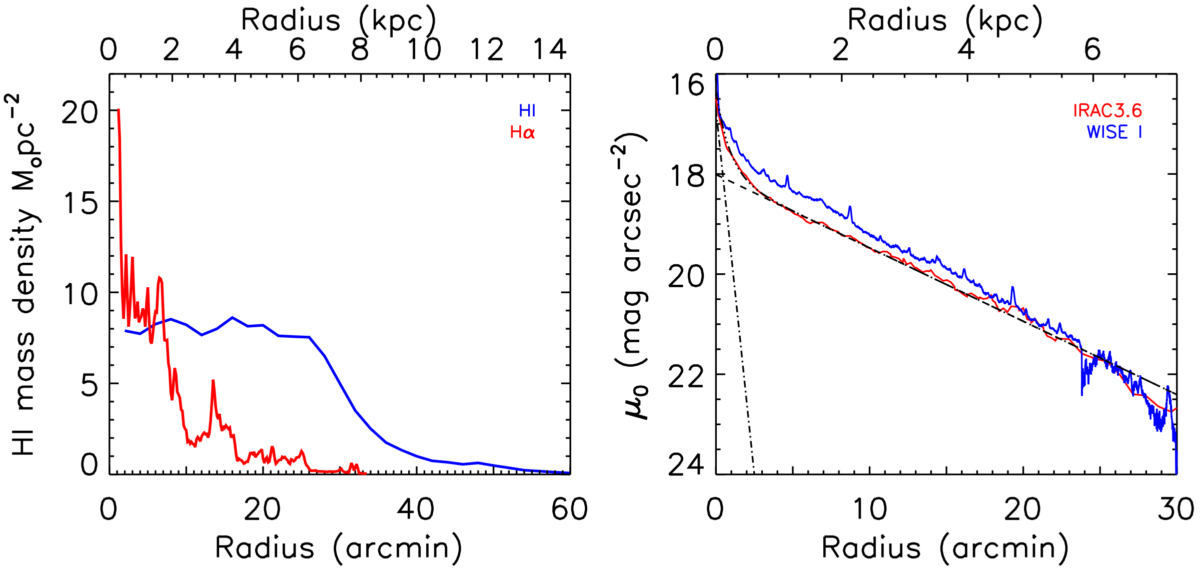

FIGURE 2.29: Left panel : HI surface density profile (blue line) and Hα brightness profile (red line, in arbitrary units). Right panel : in red the M33 surface brightness profile using the Spitzer/IRAC $3.6\mu m$ and in blue using the WISE I (Tom Jarrett, private communication) data. The dashed-dotted line is the bulge component, the dashed line is the disk component, the other line is the contribution of both components.

panel) the HI mass density profile overlaid on the ionized gas brightness profile (in arbitrary units). Both profiles have been derived with the task *ELLINT* in GIPSY. The HI disc mass is $\sim 2 \times 10^9$ M$_\odot$. The surface density only slightly varies around 8 M$_\odot$ pc^{-2} within $R = 7$ kpc, then decreases at larger radii.

2.5.5.1.2 The bulge-disk decomposition

For the stellar contribution, the surface brightness profile is derived from the Spitzer/IRAC $3.6\mu m$ data. The archive mosaic file from guaranteed time observations of Robert Gehrz, Observer Program ID 5 was used (Gehrz & Willner, 2004). After removing the stars and the background, the CHANDRA's CIAO[h] tools have been used to derive the profile of Figure 2.29. The Spitzer/IRAC 3.6 μm profile is compared to the WISE I (3.4 μm) data. The profile presented in the right-hand panel of Figure 2.29 (red), reaches a surface brightness of $\mu_{3.6} \sim 21.0\ \mathrm{mag.arcsec}^{-2}$ at a radius of 21 arcmin (~5 kpc), which is similar to the WISE I profile (blue). The surface brightness

---

[h] http ://cxc.harvard.edu/ciao/

μ_{cor}, corrected for the inclination and dust, is obtained by :

$$\mu_{\rm cor} = \mu_{\rm obs} + {\rm A}_\lambda + 2.5 \times {\rm b}_\lambda \log(\cos({\rm i})) \tag{2.21}$$

where the correction parameters A_λ and b_λ are tabulated in Graham & Worley (2008). The mean inclination of 52° is used for the density correction. In this correction, the influence of PAH at $3.3\ \mu m$ is considered as very weak and the maximum dust correction used in the IR comes from the J band (Graham & Worley, 2008). In the right panel of Figure 2.29, the central 3 arcmin shows a small spheroidal component in the $3.6\ \mu m$ band. This small central bulge has been discussed by many authors (Regan & Vogel, 1994; Gebhardt et al., 2001; Minniti et al., 1994; Seigar, 2011). Kent (1987) found that the nucleus in M33 is similar to a point source and the rising inner $3'$ part of the surface brightness profile suggests the presence of a small bulge. Corbelli & Salucci (2007) found for M33 a bulge component extending up to 1.7 kpc and Seigar (2011) only to 0.39 kpc. In view of those different results, it is clear that a disk-bulge decomposition has to be done using the IR profile from this study.

The best fit of the bulge-disk decomposition, shown in Figure 2.29, is obtained using an exponential disk with a Sersic model for the bulge. The black dot-dot-dot-dash line gives the best fit of the sum of the decomposition. The disk is described by :

$$\mu(r) = \mu_0 + 1.10857\, \frac{R}{R_d} \tag{2.22}$$

where μ_0 is the central surface brightness and R_d the scale-length of the disk. The disk parameters found are $R_d = 1.82 \pm 0.02$ kpc (slightly smaller than the scale-length in the optical) and $\mu_0 = 18.01 \pm 0.03\ {\rm mag.arcsec}^{-2}$. As seen in Figure 2.29, the Wise I profile has a slightly shorter scale-length. The disk parameters found for the Wise I profile are R_d = 1.70 kpc and $\mu_0 = 17.60\ {\rm mag.arcsec}^{-2}$.

The bulge is described by :

$$\mu(r) = \mu_e + 2.5\, b_n \left[\left(\frac{R}{R_e} \right)^{1/n} + 1 \right] \tag{2.23}$$

where, μ_e is the effective surface brightness at R_e, the effective radius. R_e defines the radius that contains half of the total light. The parameter n determines the "curvature" of the luminosity profile. b_n is defined as $b_n = 1.9992n - 0.3271$ for $0.5 < n < 10$ (Capaccioli, 1989). The best fit in Figure 2.29 gives $\mu_e = 20.8 \pm 0.3\ {\rm mag.arcsec}^{-2}$, $n = 1.12 \pm 0.1$ and an effective radius $R_e = 0.35 \pm 0.05$ kpc for the IRAC profile and $\mu_e = 21.5 \pm 0.4\ {\rm mag.arcsec}^{-2}$, $n = 1.20 \pm 0.05$ and an effective radius $R_e = 0.40 \pm 0.05$ kpc for the Wise profile. With these values, our study leads to a bulge-to-disk ratio of B/D=0.04 ± 0.012 that is in agreement with B/D=0.03 obtained by Seigar (2011) with IRAC data at 3.6 μm. The bulge component is subtracted from the total profile in order to get the disk contribution.

Stars in a disk have a vertical thickness. For the vertical distribution of the stellar component, we adopted a $sech^2(z/z_0)$ law (van der Kruit & Searle, 1981). We used a vertical scale height of ∼ 365 pc, which is ∼20% of the stellar disk scale length.

2.5.5.1.3 The mass-to-light ratio

With such a small bulge-to-disk ratio (and consequently Re), M33 can be considered as nearly a pure disk galaxy. In this paper, both cases are considered ; the pure disk case and the disk + small bulge case. However, with such a small bulge, they should be fairly similar. The color mass-to-light ratios (M/L) are defined separately for the bulge and the disk and are used to obtain the actual total stellar mass contribution using the method described in **?** :

$$\Upsilon_*^{3.6} = B^{3.6} \ \times \ \Upsilon_*^K + A^{3.6} \tag{2.24}$$

where $\Upsilon_*^{3.6}$ is the M/L at $3.6\mu m$, Υ_*^K, the M/L in the K band and $B^{3.6}$ and $A^{3.6}$ the correction coefficients. For the K band M/L, we used the relation $\log(\Upsilon_*^{\rm K}) = 1.46({\rm J}-{\rm K}) - 1.38$ taken from de Blok et al. (2008a), obtained by using an extrapolation of Bell & de Jong (2001), where the stellar mass synthesis uses a Salpeter initial mass function (IMF). The $\Upsilon_*^{3.6}$ for nearby galaxies is obtained using Υ_*^K (de Blok et al., 2008a) :

$$\Upsilon_*^{3.6} = 0.92 \ \times \ \Upsilon_*^K - 0.05 \tag{2.25}$$

The K band M/L is obtained using the 2MASS (J-K) color computed by Jarrett et al. (2003). The (J-K) color has been computed separately for the bulge in the inner part and for the disk in the outer parts. The first data points (J-K) are used for the bulge. For the pure disk case, the mean color from 65 to 570 arcsec has been used. The (J-K) decomposition gives for the bulge and disk 0.94 ± 0.03 and 0.86 ± 0.03 respectively. However, it is quite likely that the bulge color is underestimated, being contaminated by disk light. Those values give the mean M/L in the $3.6\mu m$ band : $\Upsilon_d^{3.6} = 0.72 \pm 0.1$ for the disk and $\Upsilon_b^{3.6} = 0.80 \pm 0.1$ for the bulge. The effective mass density profile is obtained by (**?**) :

$$\Sigma[{\rm M}_\odot pc^{-2}] = \Upsilon_*^{3.6} \times 10^{-0.4\times(\mu_{3.6}-24.8).} \tag{2.26}$$

where $\Upsilon_*^{3.6}$ is the mass-to-light ratio in the *Spitzer*/IRAC 3.6 micron band. The density profile is used in $GIPSY$ to compute the contribution of the stellar component.

2.5.5.2 Dark matter halo density profile

The total rotation velocity is given by :

$$\mathrm{V}^2_{\mathrm{rot}} = \mathrm{V}^2_{\star} + \mathrm{V}^2_{\mathrm{gas}} + \mathrm{V}^2_{\mathrm{DM}} \tag{2.27}$$

where $\mathrm{V}^2_{\star}$ is the contribution of the stars, $\mathrm{V}^2_{\mathrm{gas}}$ the contribution of the gas component and $\mathrm{V}^2_{\mathrm{DM}}$ the contribution of the dark matter halo. The dark matter contribution is required to explain the outermost flat part of the rotation curves in galaxies (Bosma, 1978; Carignan & Freeman, 1985). The dark matter distribution can be defined by different types of density profile. We will limit this study to the most commonly used halo density profiles, the pseudo-isothermal (ISO) and the Navarro, Frenk and White (NFW) halo distributions, which show the largest differences in the inner parts, where the RC is well defined by the Hα data.

2.5.5.2.1 ISO density profile

The pseudo-isothermal (ISO) dark matter halo is a core-dominated type of halo. The ISO density profile is given by :

$$\rho_{ISO}(R) = \frac{\rho_0}{1 + (\frac{R}{R_c})^2} \tag{2.28}$$

where ρ_0 is the central density and R_c the core radius of the halo. The velocity contribution of a ISO halo is given by :

$$\mathrm{V}_{\mathrm{ISO}}(\mathrm{R}) = \sqrt{4\pi\ \mathrm{G}\ \rho_0\ \mathrm{R}_c^2(1 - \frac{\mathrm{R_c}}{\mathrm{R}}\ \mathrm{atan}(\frac{\mathrm{R}}{\mathrm{R_c}}))} \tag{2.29}$$

2.5.5.2.2 NFW density profile

The NFW model is derived from ΛCDM simulations (Navarro et al., 1996b, 1997). This density profile (so-called "universal halo") is known as the cuspy type and follows an R^{-1} law (de Blok, 2010) in the innermost regions. The NFW halo density profile is described by :

$$\rho_{NFW}(R) = \frac{\rho_i}{\frac{R}{R_S}(1 + \frac{R}{R_S})^2} \tag{2.30}$$

where $\rho_i \approx 3H_0^2/(8\pi G)$ is the critical density for closure of the universe and R_S is a scale radius. The velocity contribution corresponding to this halo is given by :

$$\mathrm{V}_{\mathrm{NFW}}(\mathrm{R}) = \mathrm{V}_{200}\sqrt{\frac{\ln(1+\mathrm{cx}) - \mathrm{cx}/(1+\mathrm{cx})}{\mathrm{x}(\ln(1+\mathrm{c}) - \mathrm{c}/(1+\mathrm{c}))]}} \tag{2.31}$$

where $\mathrm{V_{200}}$ is the velocity at the virial radius $\mathrm{R_{200}}$, $\mathrm{c = R_{200}/R_S}$ gives the concentration parameter of the halo and x is defined as $\mathrm{R/R_S}$. The relation betwen $\mathrm{V_{200}}$ and $\mathrm{R_{200}}$ is given by :

$$\mathrm{V_{200}} = \frac{\mathrm{R_{200} \times H_0}}{100} \tag{2.32}$$

where $\mathrm{H_0}$ is the Hubble constant taken as $\mathrm{H_0 \ = \ 72}$ km.s$^{-1}\mathrm{Mpc}^{-1}$ (Hinshaw et al., 2009).

2.5.5.2.3 Results

The Hα rotation curve of Figure 2.26 (bottom panel) will be used for the mass modeling. Figure 2.30 shows the models using the ISO (top) and the NFW (bottom) DM distributions for the pure disk case and Figure 2.31 for the bulge-disk decomposition. The left panels of the figures give the best fit models and the right panels, the models with the mass-to-light ratio constrained by the IR color and population synthesis models (**?**). Both fits use Levenberg-Marquardt least-squares fitting techniques. At the bottom of each model, the mean residuals (observation - model) are represented by a black line with the same error bars as the velocity errors of the top panels. The part colored in pink gives the dispersion of the residuals around the black regression line.

Table 2.8 and Table 2.9 give the results of the mass models : column (1) gives the type of halo density profile used ; column (2) gives the parameters of the halo. In the tables, Υ gives the mass-to-light ratios obtained from the fits and χ^2_r the goodness of the fit. Column (3) shows the results using the best fits and column(4) the results when the mass-to-light ratios are kept fixed at the value obtained using the (J-K) color and population synthesis models. In Table 2.9, the parameter for the bulge mass-to-light ratio is given by Υ_b. The results of the mass models will be discussed in the next section.

2.5.6 Discussion

2.5.6.1 M33 velocity dispersion

Our new dataset is ideal to study the internal velocity dispersion of HII regions in M33, and the mean velocity disperion of the galaxy. In Figure 2.32, we compare the mean velocity dispersion of M33 to a subsample of 151 nearby star-forming galacitc disks from the GHASP survey (Epinat et al., 2008b) studied in Epinat et al. (2010) It is obvious how the ionized interstellar medium of Messier 33 appears dynamically colder (lower velocity dispersion) than in other galaxies. We have divided the sample into three classes of size : small galaxies with $\mathrm{R_{25}} < 7.5$ kpc, intermediate size galaxies with $7.5 < \mathrm{R_{25}} < 11.5$ kpc and large galaxies with $\mathrm{R_{25}} > 11.5$ kpc.

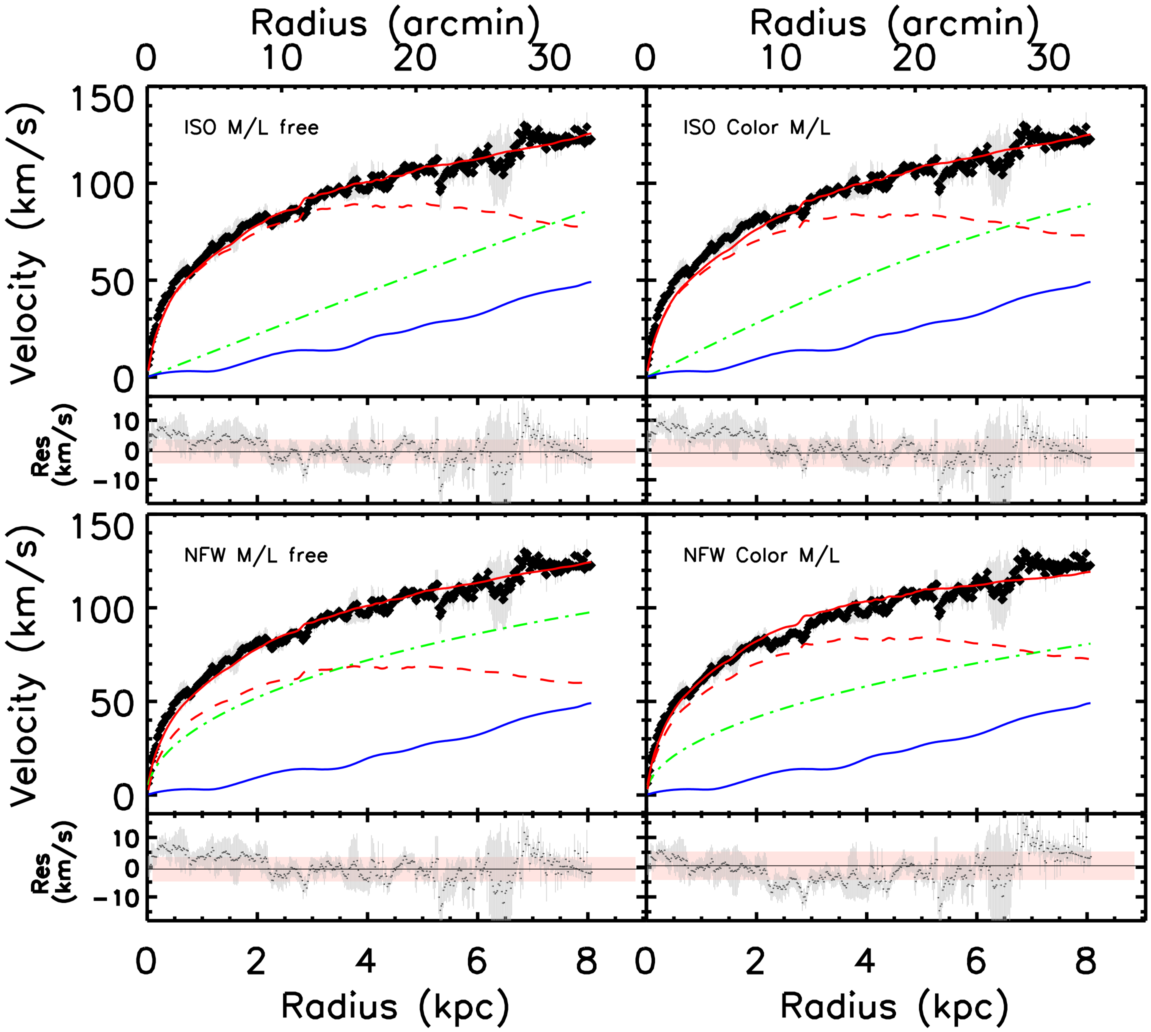

FIGURE 2.30: M33 mass models with a DM halo for the pure disk case. Models on the left are best fits while models on the right have a fixed M/L determined by the IR color (see sec. 2.5.5.1). The top panels represent the models with the ISO and the bottom panels those with the NFW density distributions. The stellar disk contribution is in broken red, the HI contribution in blue, the halo contribution in broken green and the sum of the 3 components is shown as a continuous red line. At the bottom of each model the mean residuals (observation - model) are presented.

TABLE 2.8: Hα mass model results with DM halos for the pure disk case.

Halo Model	Params	Best Fit	Color M/L*
(1)	(2)	(3)	(4)
ISO	ρ_0	6.75 ± 0.57	7.46 ± 0.43
	R_c	24.23 ± 17.02	11.13 ± 0.40
	Υ	0.81 ± 0.01	0.72
	χ_r^2	0.88	1.16
NFW	R_{200}	240.00 ± 188.34	300.26 ± 106.55
	c	4.41 ± 4.15	2.37 ± 0.91
	Υ	0.48 ± 0.11	0.72
	χ_r^2	0.87	1.56

*M/L fixed by the color of the disk ;
ρ_0, the central DM density, is given in units of 10^{-3} M$_\odot/pc^3$;
R_c and R_{200} are in kpc.

Though being within the class of intermediate galaxy size, Messier 33 curiously behaves like smaller galaxies that have lower mass and absolute magnitude.

Giant extragalactic HII regions seen in gas-rich spiral and dIrr galaxies are regions of strong star formation with a size ranging between 0.1 and 1 kpc, a Hα luminosity of $10^{39} - 10^{40}$ erg/s, a mean density of $1 - 10$ cm^{-3} and an ionized mass of $10^4 - 10^5$ M$_\odot$, which embeds a population of $100 - 200$ ionizing stars (Kennicutt et al., 1984; Kennicutt, 1984). In addition, the velocity dispersion of the gas presents distinct kinematics with subsonic and supersonic emission-line widths (Smith & Weedman, 1970, 1971). Uniform expansion of HII regions into a medium of constant density results in subsonic expansion velocities (Spitzer & Tomasko, 1968). Supersonic motions are inferred for velocity dispersion typically larger than (kT/$m)^{0.5} \sim 10 - 13$ km.s^{-1}, where k is the Boltzmann constant, m the typical hydrogen mass weighted by the molecular content and T = 10^4K, the characteristic temperature of the HII region. Supersonic velocity dispersions ranging from 15 to 40 km.s^{-1} are observed and give rise to different interpretations (see discussion in Bordalo & Telles (2010). In the "champagne" model (Tenorio-Tagle, 1979), the expanding HII bubble bursts thought the surface of the surrounding molecular cloud where the sharp gas density discontinuity generates a shock wave that accelerates the gas to supersonic speeds. Density gradient within the HII regions may generate supersonic motions prior to their

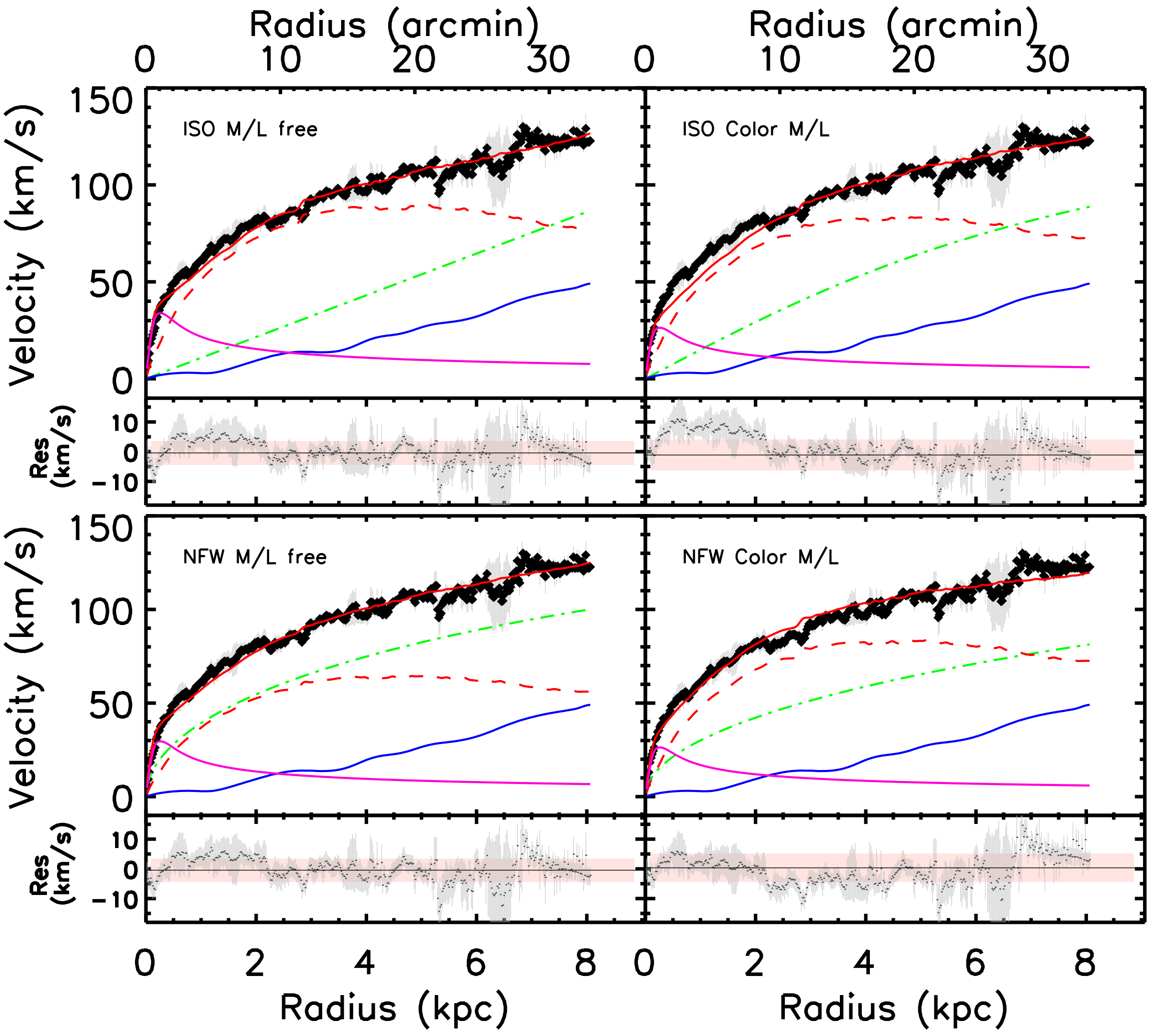

FIGURE 2.31: Same as in Figure 2.30 but with the bulge contribution (in cyan)

acceleration through the surface of the cloud (Mazurek, 1982).

Our data confirm that the region NGC 604 (Figure 2.25), like many other giant HII regions, displays both single Gaussian and complex line profiles (Munoz-Tunon et al., 1996; Yang et al., 1996). Single Gaussian profiles essentially come from the bright regions and show the broadening mechanics due to self-gravitation. More complex lines come from faint regions and emanate from the wind-driven mechanical energy injection due to massive stars that produce expanding shells, cavities and bubbles, filaments and outflows, loops and ring-like regions.

A velocity dispersion versus intensity ($\sigma - I$) diagram provides diagnostics used to separate the main broadening mechanisms detected in the emission lines of giant HII regions, such as differentiating the broadening produced by virial motions resulting from the total gravitational potential and that resulting from the superposition of shells and loops generated by massive

TABLE 2.9: Hα mass model results with DM halos, using the bulge-disk decomposition.

Halo Model	Params	Best Fit	Color M/L*
(1)	(2)	(3)	(4)
ISO	ρ_0	6.41 ± 0.60	12.52 ± 0.53
	R_c	$119.50 \pm \gtrsim 200$	6.32 ± 0.40
	Υ_d	0.82 ± 0.01	0.72
	Υ_b	1.32 ± 0.06	0.80
	χ_r^2	0.85	1.34
NFW	R_{200}	211.55 ± 0.72	2.78 ± 0.78
	c	8.67 ± 0.12	0.76 ± 0.45
	Υ_d	0.43 ± 0.01	0.72
	Υ_b	1.01 ± 0.11	0.80
	χ_r^2	0.75	1.43

*M/L fixed by the color of the disk and of the bulge ;
ρ_0, the central DM density is given in units of 10^{-3} M$_\odot/pc^3$;
R_c and R_{200} are in kpc.

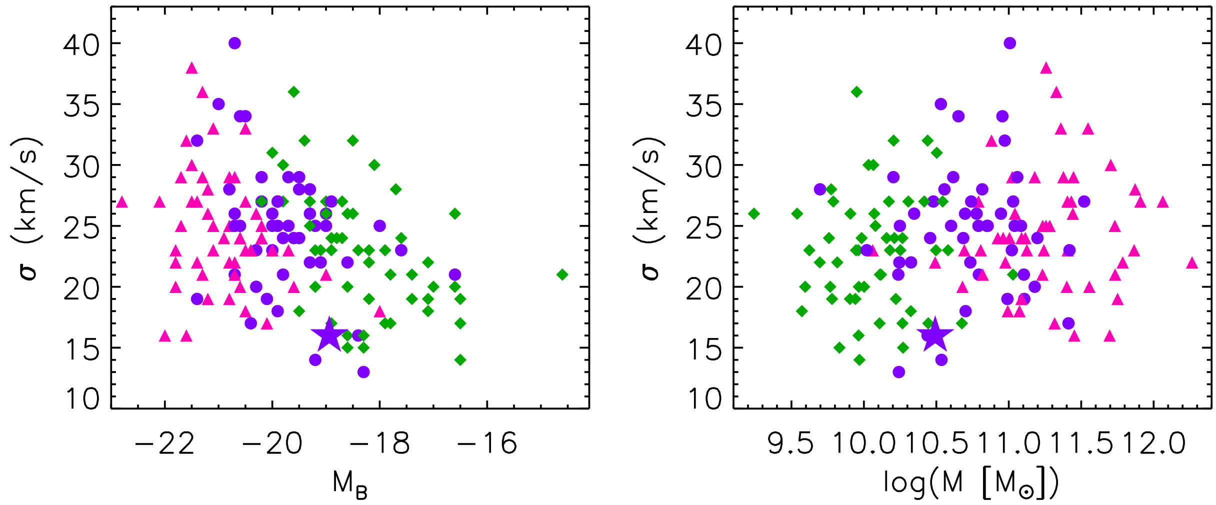

FIGURE 2.32: Mean velocity dispersion of Messier 33 (star) and of other nearby star-forming disc galaxies from Epinat et al. (2010). On the right, the mass is given by $\mathrm{M} = \mathrm{V}_{\mathrm{max}}^2 \mathrm{R}_{25}/\mathrm{G}$, where $\mathrm{V}_{\mathrm{max}}$ is the maximum velocity of each Hα rotation curve.

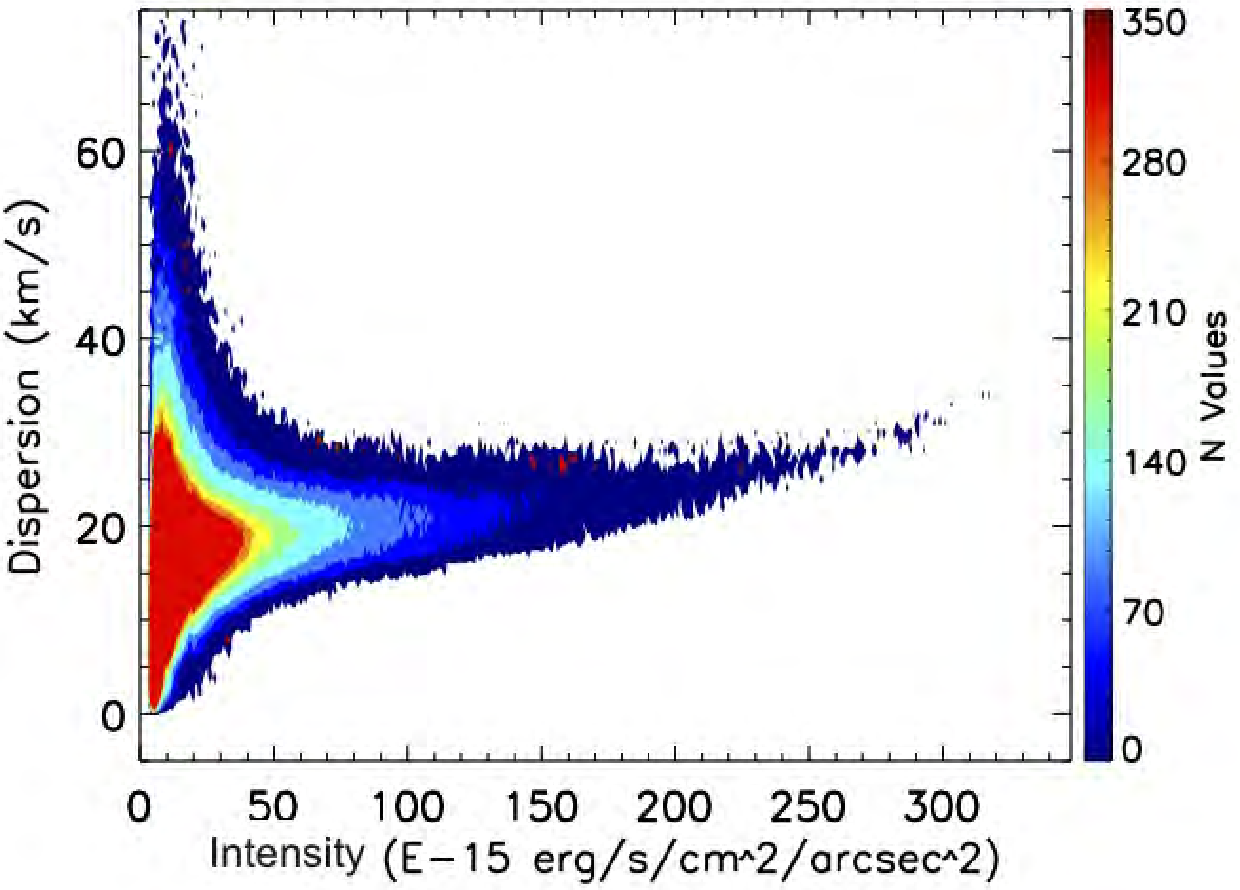

FIGURE 2.33: Corrected velocity dispersion ($\sigma_{cor}^2 = \sigma_{obs}^2 - \sigma_{PSF}^2$), computed using a single Gaussian, vs integrated line intensity for the whole field-of-view of M33. The number of pixels having a given intensity and dispersion is given by the color scale.

stars, which ends up dispersing the parent clouds (Munoz-Tunon et al., 1996; Yang et al., 1996; Martínez-Delgado et al., 2007; Moiseev & Lozinskaya, 2012). Such a diagram is given for the whole disk of the galaxy in Figure 2.33. We used the total intensity in the line rather than the intensity peak because the total intensity is independent from the spectral resolution (which is not the case of the intensity peak). In the following, we use intensity to refer to the total line intensity. Figure 2.33 shows the strong relation between the Hα velocity dispersion and the Hα intensity. Only low intensity regions show a broad range of velocity dispersions. In other words, the range of velocity dispersions decreases when intensity increases. Regions showing larger velocity dispersions arise from diffuse emitting areas rather than from intense HII regions. Subsonic dispersions are only observed in low intensity regions, whereas supersonic motions are both observed in the low surface brightness medium and the brightest star forming regions. These latter have a roughly constant velocity dispersion (20-30 km.s^{-1}), while the largest supersonic dispersions (40-60 km.s^{-1}) are only seen among the lowest intensities.

As described in Munoz-Tunon et al. (1996), in the frame of the CSM for stellar cluster formation (Tenorio-Tagle et al., 1993), the gravitational collapse fragments the gas clouds and first forms the low-mass stars. The bow shocks and wakes caused by their stellar winds suspend the collapse of the cloud and communicate the stellar velocity dispersion to the surrounding gas. The core of the cloud is thus virialized and the supersonic gas velocity dispersion traces its gravitational potential, despite dissipation. Massive stars form later in a cloud at equilibrium in which the velocity dispersion of the gas is constant and does not depend on the intensity of the newly formed giant HII regions. In the $\sigma - I$ diagram, this corresponds to the horizontal area (with the almost constant velocity dispersion of 20 ± 3 km.s^{-1}) displaying a broad range of intensities.

As massive stars evolve, strong mechanical energy sweeps the ISM into shells displaying supersonic velocities higher than the ambient stellar velocity dispersion. The velocity dispersion of these shells decreases with age while their luminosity increases : young and faint shells produce a large range of velocity dispersions and low intensities while older and bright shells display a narrower velocity dispersion amplitude and higher intensities. If the shells are embedded in the virialized core, their velocities cannot be lower than the stellar velocity dispersion but, if the shells are outside the core, their velocities can decrease to lower values, down to subsonic velocities. In the $\sigma - I$ diagram, these shell phases, ages and locations are found within the broad range of velocity dispersions at low intensities. To fully understand how this last area of the $\sigma - I$ diagram is filled by expanding shells, this zone should be understood as the result of different projection effects.

On the one hand, emission from a line-of-sight passing across the center of an expanding spherical shell of gas will present the largest velocity difference across the shell due to the large distance separating its two edges and an intermediate intensity. On the other hand, a line-of-sight going through the inner-edge of the shell will present a lower velocity difference but a very high intensity due to the large quantity of gas integrated along the line-of-sight. Finally, a line-of-sight running through the outer-edge of the shell will display even a much lower velocity difference and a very low intensity due to the small quantity of gas integrated along the line-of-sight. In addition to these shells that cannot be distinguished individually on this plot, this area of the $\sigma - I$ diagram mainly corresponds to diffuse Hα emission.

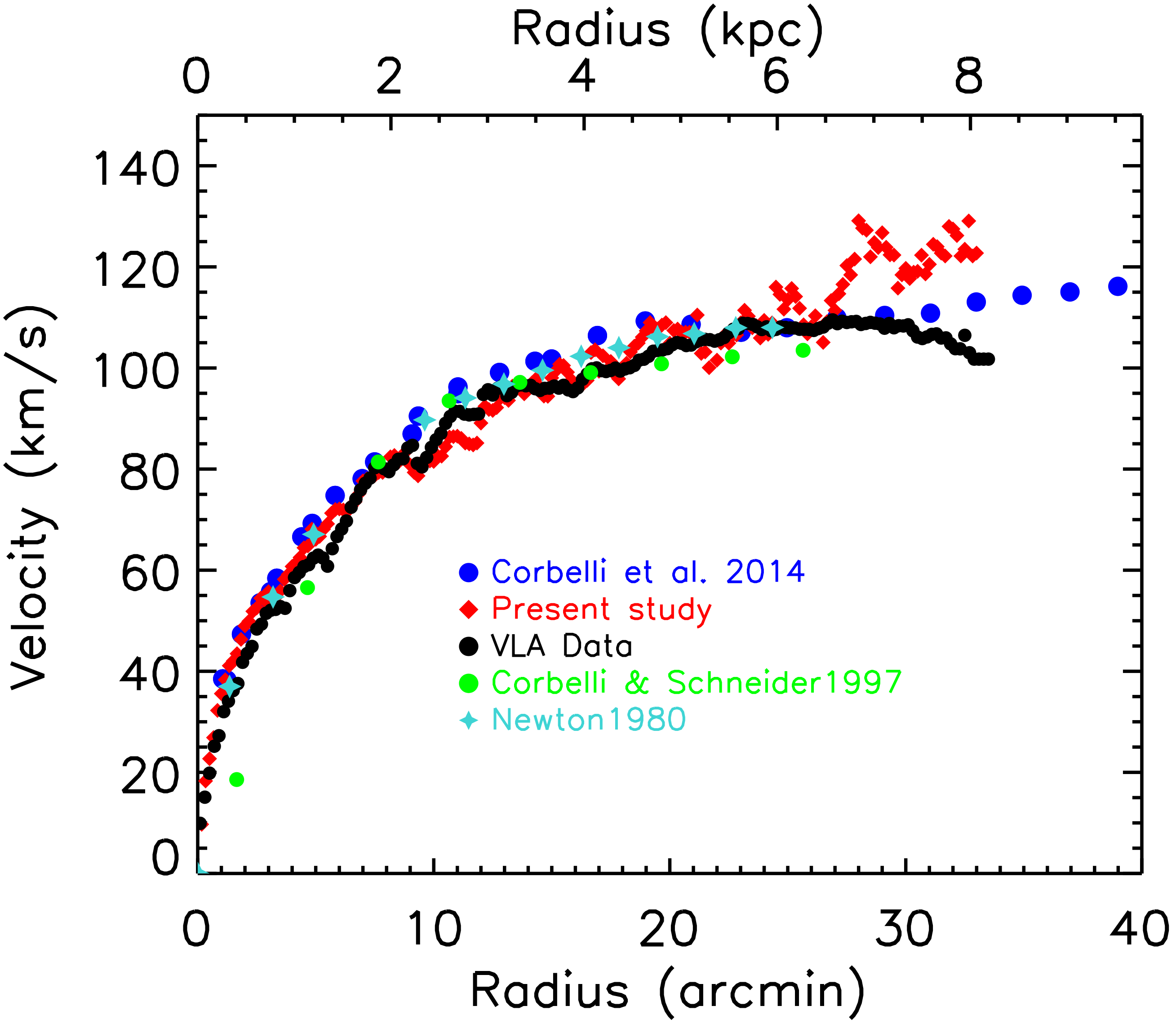

FIGURE 2.34: Comparison of Hα and HI rotation curves. Blue represents the HI (squares) RC from Corbelli et al. (2014) ; black is for Gratier et al. (2010) VLA data ; green circles are for Corbelli & Schneider (1997) data ; green crosses for Newton (1980) data and red symbols are for our Hα RC.

2.5.6.2 Comparison of the Hα kinematics with HI results

In this section, a comparison of our Hα kinematical results is done with previous HI studies. Normally, our 5″ binning Hα RC should give the optimal representation of the kinematics in the inner parts of M33, without suffering from e.g. the beam smearing that may affect earlier HI data. Figure 3.22 compares the HI RC derived by Corbelli et al. (2014), as well as older HI studies by Corbelli & Schneider (1997) and Newton (1980) and recent VLA data at 12″ resolution (Gratier et al., 2010) with the Hα RC obtained in this study. It is not surprising that the Arecibo data of Corbelli & Schneider (1997) suffer from beam smearing in the inner kpc and underestimate the rotational velocities while the 1.5′x 3.0′ resolution Newton (1980) data are quite consistent with the 12″ resolution ($\sim$ 48 pc) HI data and our 5″ step ($\sim$ 20 pc) Hα data, at least out to 6.5 kpc. Comparing our Hα data to the HI for R > 6.5 kpc seems to suggest that we may overestimate the RC in the outer parts. Since the difference occurs at radii with the lowest number of independent bins (see bottom panel of Fig. 2.28), it could simply reflect the difficulty to derive accurate Hα rotation velocities by our fitting procedure within these regions. However it should be noted that the 2010 VLA data of Gratier et al. (2010) have lower velocities than Corbelli et al. (2014) in those same outer parts.

2.5.6.3 Mass modeling results

The extent of the spheroidal component shown in the surface brightness profile is very small $r \leq 1.5$ arcmin (≤ 350 pc) ; with a bulge-to-disk ratio of only $\sim$0.04, large differences between the mass models with and without a bulge component are not expected. In each case, a best-fit model and a fixed M/L model are explored. The reduced chi-square χ_r^2 is used to determine the goodness of the fit.

In the pure disk case (Figure 2.30), the two DM best-fit models (ISO and NFW) give very similar good fits as shown by the values of the χ_r^2 in Table 2.8. The redisuals (bottom panels) shows that the only discrepancy is in the very inner parts. When using the fixed M/L value of the disk, it can be seen that ISO gives a better fit (χ_r^2 = 1.16 vs 1.56), despite the fact that it still slightly underestimates the velocities for R < 2 kpc. This may points out that the method used to derive the M/L may underestimates it slightly (0.72 vs 0.83). This could also point out that an additional mass component (a small bar or nuclear disk) is missing in our models in the innermost parts of the disk.

As expected, in the bulge-disk case, it is clear that the addition of a bulge component does not bring anything more than the disk only model due to its very small Re and the extra uncertainty coming from the M/L of the bulge. Looking at Figure 2.31 and Table 2.9, the conclusions are that both functional forms (ISO and NFW) yields very similar results. Because in the bulge+disk case, we add one free parameter (Υ_b of the bulge) and because the uncertainty on that parameter is large since the IR color used to derive it is polluted by disk light with the result of underestimating the IR color and thus the Υ_b of the bulge, we favor the results of the disk-only models.

We conclude, that the pure-disk ISO models (best-fit and/or fixed M/L) give a slightly better representation of the mass distribution using the Hα rotation curve that is derived out to ~8 kpc with a M/L for the luminous disk $\sim 0.72 - 0.82$, a core radius $\sim 12 - 24$ kpc and a central density $\rho_0 \sim 0.007 - 0.008$ M$_\odot$.pc^{-3} for the dark isothermal halo. It is clear that when we will combine those Hα data to more extended HI kinematics, we should be able to constrain much better the parameters of the mass distribution.

2.5.7 Summary and conclusions

New Hα Fabry-Perot mapping of the nearby galaxy M33 has been presented. The data were obtained on the 1.6 m telescope of the Observatoire du Mont Mégantic (OMM) using a high resolution FP etalon (p = 765) and a very sensitive photon counting EMCCD camera (QE$\sim 90\%$). The ten fields observed cover a field of $\sim 42' \times 56'$ (10 kpc×13.5 kpc) with a spatial resolution ~3″. The HII regions inside this area are well defined spatially and spectrally. This study provides for the whole field, as well as for each HII regions and nebulae (e.g : NGC 604, NGC 595, NGC 588, IC 137, IC 136) velocity and dispersion maps. The data was flux calibrated using Relaño et al. (2013) data.

Looking at the velocity dispersion σ profile as a function of radius, we found that it is essentially flat at an average value of 16 ± 2 km.s^{-1}. From $R \sim 7.5$ kpc, the velocity dispersions increase to $\sim 20 - 25$ km.s^{-1}. This radius is the location of the beginning of the warp of the HI disk where the twist of the position angle starts. The mean velocity dispersion of M33 was found to be small when compared to a sample of nearby star-forming galactic discs (GHASP sample) which have σ varying from 15 to 35 km.s^{-1}. Finally, a velocity dispersion versus intensity ($\sigma - I$) diagram shows clearly a strong relation between the Hα velocity dispersion and the Hα intensity.

The main aim of this study was to derive a high spatial resolution Hα RC for M33 in order to try to constrain the best functional form representing the dark matter distribution between the cored ISO models and the cosmologically motivated cuspy NFW models. The rotation center found is very close to the optical center. The other kinematical parameters found are $V_{sys} = -178 \pm 3$ km.s^{-1}, PA = 202°±4°and $i = 52° \pm 2°$. The RC was derived separately for the approaching, receding and for both sides. The rotation curve was computed using a constant 5″ step to perform the mass modeling. Besides the intrinsic error in each ring, we added an error to represent the asymmetry of both sides since this RC will be compared to axisymmetric mass models. After a steep rise in the inner 1 kpc, the RC rises slowly to its maximum value of $\sim$123±3 km.s^{-1} at the last point (33′).

Comparing our adopted RC to HI rotation curves in the literature, we found that our Hα data agree very well with the HI from the center out to $\sim$ 6.5 kpc. The only exception is the first inner point of Corbelli & Schneider (1997), which may a bit suffer from beam smearing due to the large Arecibo beam. With our high resolution data we bring more data points in the inner part of the RC, which is very useful for the mass modeling. On the other hand, for R $>$ 6.5 kpc, this comparison suggests that our Hα data may overestimate the velocities in the outer parts.

For the mass model analysis, the Spitzer/IRAC $3.6\mu m$ profile was used to represent the stellar disk mass contribution. The disk parameters found are a scale length $R_d = 1.82 \pm 0.02$ kpc and an extrapolated surface brightness $\mu_0 = 18.01 \pm 0.03$ mag.arcsec^{-2}. A bulge–disk decomposition was also done even if it will not alter significantly the results of the mass models with a bulge to disk ratio of only 0.04. Besides best-fit models, models with fixed M/L based on IR colors and population synthesis models, following the method used by **?** and de Blok et al. (2008a) are also explored.

For the mass models, we decided to favor the disk-only models because of the extra uncertainties introduced by adding a bulge which contributes very little (B/D = 0.04) to the luminous mass. In this case, the ISO models give a better fit despite the fact that they seem to underestimate the velocities in the inner 2 kpc (see the residual curves at the bottom of Figure 2.30). This may point out to the fact that the determination of the M/L values using the IR colors and population synthesis models slightly underestimates the M/L ratio of the disk or that an inner mass component has been omitted in the modeling.

An ideal RC using our high spatial resolution Hα RC in the inner 6.5 kpc and a high sensitivity but low spatial resolution HI RC in the outer parts should allow to constrain much better the parameters of the mass models. This should be done in a subsequent study presenting new deep HI observations.

Acknowledgment

SZK's work was supported by a grant of the CIOSPB of Burkina Faso, CC's Discovery grant of the Natural Sciences and Engineering Research Council of Canada and CC's South African Research Chairs Initiative (SARChI) grant of the Department of Science and Technology (DST), the SKA SA and the National Research Foundation (NRF). L.C. acknowledges a financial support from CNES. We would like to thank Tom Jarrett for providing the WISE I data, the staff of the OMM for their support and Yacouba Djabo for observing with us at OMM. A part of the montage package of IPAC have been used in the process of our reduction. The optical image in blue band comes from the Digitized Sky Surveys (DSS images). The IR archives images are from the Spitzer and WISE Space Telescopes.

Data for the rotation curve and the Hα dispersion profile : online

TABLE 2.10: The Hα rotation curve of M33

Rad	V	ΔV	σ	$\Delta\sigma$	Rad	V	ΔV	σ	$\Delta\sigma$	Rad	V	ΔV	σ	$\Delta\sigma$
(1)	(2)	(3)	(4)	(5)	(6)	(7)	(8)	(9)	(10)	(11)	(12)	(13)	(14)	(15)
0.08	6	4	14	10	11.08	87	4	16	5	22.08	104	5	17	7
0.17	9	4	12	6	11.17	86	3	16	5	22.17	105	6	17	7
0.25	13	3	12	4	11.25	86	3	16	6	22.25	106	8	18	7
0.33	18	5	14	5	11.33	86	3	16	6	22.33	107	7	19	8
0.42	21	4	15	4	11.42	86	4	15	6	22.42	106	7	18	8
0.50	23	4	16	4	11.50	85	3	15	6	22.50	105	5	17	7
0.58	25	3	15	4	11.58	83	3	15	6	22.58	107	5	16	7
0.67	26	3	16	5	11.67	85	3	16	6	22.67	107	6	17	8
0.75	31	3	16	5	11.75	86	3	16	6	22.75	105	7	16	7
0.83	32	3	15	5	11.83	85	3	16	6	22.83	107	5	15	7
0.92	35	3	15	4	11.92	87	3	16	6	22.92	108	5	16	7
1.00	35	3	15	4	12.00	89	3	17	7	23.00	109	5	15	6
1.08	37	3	14	4	12.08	91	3	17	7	23.08	111	4	15	6
1.17	38	4	14	4	12.17	92	3	17	7	23.17	112	4	15	6
1.25	39	3	14	5	12.25	93	3	18	7	23.25	111	3	15	6
1.33	42	4	14	5	12.33	92	4	18	7	23.33	111	4	15	5

Continued on next page

Table 2.10 Continued

Rad	V	ΔV	σ	$\Delta\sigma$	Rad	V	ΔV	σ	$\Delta\sigma$	Rad	V	ΔV	σ	$\Delta\sigma$
(1)	(2)	(3)	(4)	(5)	(6)	(7)	(8)	(9)	(10)	(11)	(12)	(13)	(14)	(15)
1.42	41	4	14	5	12.42	91	4	18	6	23.42	108	7	15	5
1.50	42	3	14	5	12.50	92	4	18	7	23.50	108	8	15	6
1.58	43	3	14	5	12.58	91	4	18	7	23.58	108	6	14	5
1.67	43	5	13	4	12.67	92	3	18	8	23.67	109	6	13	5
1.75	44	5	13	4	12.75	93	3	18	9	23.75	108	6	14	7
1.83	46	4	13	4	12.83	94	3	19	9	23.83	105	7	15	7
1.92	48	3	14	5	12.92	95	3	18	8	23.92	106	7	16	8
2.00	49	4	14	4	13.00	94	3	18	8	24.00	110	5	17	8
2.08	49	5	14	4	13.08	94	3	18	8	24.08	111	5	16	7
2.17	50	6	14	5	13.17	93	5	17	7	24.17	105	6	16	7
2.25	51	5	13	5	13.25	95	4	17	7	24.25	105	6	16	8
2.33	52	5	13	5	13.33	96	3	17	7	24.33	109	3	18	9
2.42	53	7	13	5	13.42	97	3	17	7	24.42	113	5	17	8
2.50	53	8	13	5	13.50	96	3	17	7	24.50	116	4	17	9
2.58	53	7	13	5	13.58	96	3	17	7	24.58	116	4	16	7
2.67	54	7	13	6	13.67	96	3	17	7	24.67	115	4	16	7
2.75	55	7	13	6	13.75	95	3	17	8	24.75	113	4	16	7
2.83	53	6	13	5	13.83	95	3	16	6	24.83	111	4	16	7
2.92	56	5	13	5	13.92	95	3	16	6	24.92	113	4	16	6
3.00	56	3	14	5	14.00	96	4	16	6	25.00	114	4	16	7
3.08	54	3	14	5	14.08	97	3	16	7	25.08	115	3	14	6
3.17	53	4	15	5	14.17	97	3	15	6	25.17	116	6	14	6
3.25	53	3	15	5	14.25	98	3	14	7	25.25	113	10	13	6
3.33	55	3	15	6	14.33	98	3	14	6	25.33	119	6	14	6
3.42	56	3	15	5	14.42	97	3	15	6	25.42	112	14	14	6
3.50	56	3	15	5	14.50	96	3	15	6	25.50	113	14	14	6
3.58	56	3	15	5	14.58	95	3	15	6	25.58	111	14	15	6
3.67	58	3	15	6	14.67	95	4	14	6	25.67	109	16	15	6
3.75	59	3	15	6	14.75	95	3	15	6	25.75	107	19	15	5
3.83	59	3	15	5	14.83	94	4	14	6	25.83	106	18	15	6

Continued on next page

Table 2.10 Continued

Rad	V	ΔV	σ	$\Delta\sigma$	Rad	V	ΔV	σ	$\Delta\sigma$	Rad	V	ΔV	σ	$\Delta\sigma$
(1)	(2)	(3)	(4)	(5)	(6)	(7)	(8)	(9)	(10)	(11)	(12)	(13)	(14)	(15)
3.92	60	3	15	6	14.92	96	5	15	7	25.92	107	18	16	6
4.00	61	3	15	5	15.00	98	7	15	7	26.00	108	19	17	7
4.08	61	3	15	5	15.08	99	7	15	6	26.08	110	17	17	6
4.17	62	3	15	5	15.17	100	9	15	6	26.17	110	18	16	6
4.25	61	3	15	5	15.25	100	9	15	7	26.25	111	20	16	6
4.33	62	4	15	5	15.33	101	9	15	7	26.33	108	17	17	6
4.42	64	5	15	5	15.42	100	9	15	7	26.42	104	16	17	6
4.50	65	5	15	5	15.50	100	9	15	7	26.50	105	17	16	6
4.58	64	5	15	5	15.58	102	9	15	7	26.58	108	18	15	6
4.67	65	6	15	5	15.67	99	6	16	7	26.67	109	17	15	7
4.75	67	5	16	6	15.75	97	4	16	6	26.75	112	17	15	7
4.83	69	5	16	5	15.83	98	6	16	6	26.83	114	16	16	8
4.92	68	5	16	5	15.92	98	5	16	6	26.92	112	14	15	8
5.00	65	6	16	5	16.00	97	5	16	6	27.00	110	14	14	8
5.08	66	6	16	5	16.08	96	4	16	7	27.08	112	11	15	8
5.17	67	5	16	5	16.17	97	4	16	6	27.17	115	7	15	9
5.25	67	6	16	5	16.25	97	4	16	6	27.25	119	7	14	9
5.33	68	6	16	5	16.33	97	4	15	6	27.33	116	4	15	9
5.42	69	5	16	5	16.42	96	5	16	7	27.42	119	5	15	12
5.50	69	5	17	5	16.50	98	5	16	6	27.50	121	3	20	14
5.58	71	5	17	5	16.58	100	5	16	7	27.58	126	8	15	7
5.67	71	5	17	5	16.67	104	8	15	6	27.67	116	3	12	8
5.75	72	5	16	5	16.75	104	8	16	7	27.75	114	7	13	7
5.83	72	5	16	5	16.83	104	6	15	6	27.83	122	10	15	8
5.92	72	5	16	5	16.92	102	5	16	5	27.92	124	13	15	8
6.00	72	5	17	5	17.00	99	4	17	6	28.00	130	3	19	12
6.08	72	6	17	5	17.08	100	3	17	6	28.08	126	4	15	9
6.17	72	6	17	5	17.17	104	7	17	6	28.17	128	4	16	9
6.25	71	5	17	5	17.25	99	3	17	6	28.25	129	3	16	11
6.33	72	5	18	6	17.33	99	3	18	7	28.33	126	5	14	6

Continued on next page

Table 2.10 Continued

Rad	V	ΔV	σ	$\Delta\sigma$	Rad	V	ΔV	σ	$\Delta\sigma$	Rad	V	ΔV	σ	$\Delta\sigma$
(1)	(2)	(3)	(4)	(5)	(6)	(7)	(8)	(9)	(10)	(11)	(12)	(13)	(14)	(15)
6.42	72	8	18	6	17.42	100	3	19	7	28.42	120	3	14	7
6.50	72	8	18	6	17.50	105	6	19	7	28.50	123	3	17	10
6.58	73	8	18	6	17.58	97	3	19	6	28.58	123	3	19	13
6.67	73	9	18	6	17.67	101	3	18	7	28.67	126	3	16	9
6.75	74	8	18	6	17.75	100	4	18	7	28.75	124	4	19	9
6.83	75	6	17	6	17.83	97	3	16	6	28.83	123	3	15	9
6.92	76	5	17	6	17.92	98	3	17	6	28.92	124	4	19	10
7.00	78	4	17	6	18.00	99	3	17	7	29.00	125	5	19	9
7.08	78	4	17	6	18.08	101	3	17	7	29.08	128	3	16	7
7.17	78	4	17	6	18.17	102	3	17	7	29.17	122	3	15	8
7.25	78	4	17	6	18.25	103	3	18	7	29.25	123	10	15	8
7.33	79	4	17	5	18.33	104	3	18	7	29.33	123	3	17	10
7.42	79	3	17	6	18.42	104	3	18	8	29.42	124	4	13	5
7.50	79	3	18	6	18.50	104	3	18	7	29.50	121	3	15	8
7.58	78	3	18	6	18.58	105	3	18	7	29.58	118	4	15	5
7.67	80	3	17	6	18.67	105	3	18	8	29.67	118	9	19	10
7.75	79	3	18	6	18.75	105	3	17	7	29.75	122	3	15	8
7.83	80	3	18	6	18.83	106	3	17	6	29.83	122	3	15	15
7.92	79	3	18	6	18.92	106	3	17	7	29.92	124	4	14	7
8.00	80	3	17	6	19.00	107	3	17	7	30.00	121	3	14	10
8.08	82	4	17	6	19.08	109	3	18	7	30.08	121	3	16	10
8.17	82	3	18	6	19.17	109	3	17	6	30.17	122	3	15	7
8.25	83	4	18	6	19.25	108	3	17	6	30.25	124	3	14	7
8.33	83	5	17	6	19.33	107	3	16	6	30.33	119	6	15	6
8.42	82	5	17	6	19.42	108	3	16	6	30.42	123	3	15	7
8.50	81	5	18	6	19.50	108	3	16	6	30.50	119	6	15	7
8.58	82	4	18	6	19.58	108	3	16	6	30.58	123	3	15	7
8.67	83	5	17	6	19.67	109	3	16	6	30.67	122	4	14	6
8.75	84	6	17	5	19.75	109	3	16	6	30.75	119	5	12	8
8.83	84	6	17	5	19.83	109	3	16	6	30.83	122	3	13	6

Continued on next page

Table 2.10 Continued

Rad	V	ΔV	σ	$\Delta\sigma$	Rad	V	ΔV	σ	$\Delta\sigma$	Rad	V	ΔV	σ	$\Delta\sigma$
(1)	(2)	(3)	(4)	(5)	(6)	(7)	(8)	(9)	(10)	(11)	(12)	(13)	(14)	(15)
8.92	83	6	17	5	19.92	105	4	16	7	30.92	122	3	12	7
9.00	81	4	17	6	20.00	104	5	16	6	31.00	122	4	15	11
9.08	80	3	17	6	20.08	106	3	16	7	31.08	124	4	13	8
9.17	80	3	17	6	20.17	107	3	15	6	31.17	122	3	20	14
9.25	78	3	16	6	20.25	108	3	15	8	31.25	120	3	20	19
9.33	78	3	16	6	20.33	108	3	15	8	31.33	124	5	21	23
9.42	80	3	15	6	20.42	107	3	14	7	31.42	122	3	12	7
9.50	81	4	15	6	20.50	107	3	15	7	31.50	122	3	19	14
9.58	82	5	16	6	20.58	106	3	15	6	31.58	123	3	22	16
9.67	81	4	16	6	20.67	106	3	15	7	31.67	122	3	17	11
9.75	81	5	15	6	20.75	108	3	14	7	31.75	128	6	22	11
9.83	82	5	16	6	20.83	107	3	14	8	31.83	122	3	17	12
9.92	82	4	16	6	20.92	106	3	15	8	31.92	122	3	15	13
10.00	81	4	15	6	21.00	108	3	15	8	32.00	128	4	22	21
10.08	82	5	15	5	21.08	109	3	15	10	32.08	122	3	16	7
10.17	83	3	15	6	21.17	111	3	15	11	32.17	126	5	16	9
10.25	83	3	15	6	21.25	106	4	15	9	32.25	122	3	25	17
10.33	82	3	16	6	21.33	105	6	16	10	32.33	122	3	30	3
10.42	84	3	16	6	21.42	111	9	17	12	32.42	126	5	20	19
10.50	84	3	15	6	21.50	113	8	14	7	32.50	121	4	19	7
10.58	85	5	16	5	21.58	113	8	15	8	32.58	122	3	29	20
10.67	86	4	16	6	21.67	100	6	15	7	32.67	129	8	13	9
10.75	87	3	16	6	21.75	96	10	15	8	32.75	122	3	15	4
10.83	86	3	16	6	21.83	97	10	16	8	32.83	122	3	18	8
10.92	87	3	16	6	21.92	98	6	15	8	32.92	122	3	18	13
11.00	87	3	16	5	22.00	103	6	15	7	33.00	123	3	22	3

Suppléments Figures :

Les figures ci dessous sont des reprises de certaines figures de l'article ci dessus dans l'optique d'une plus grande visibilité.

- Une carte monochromatique Hα.
- Une carte Hα avec une superposition des contours HI en bleu et CO en rouge puis une approximation des bras spiraux en noir.
- Une carte de vitesse de M33 en Hα.

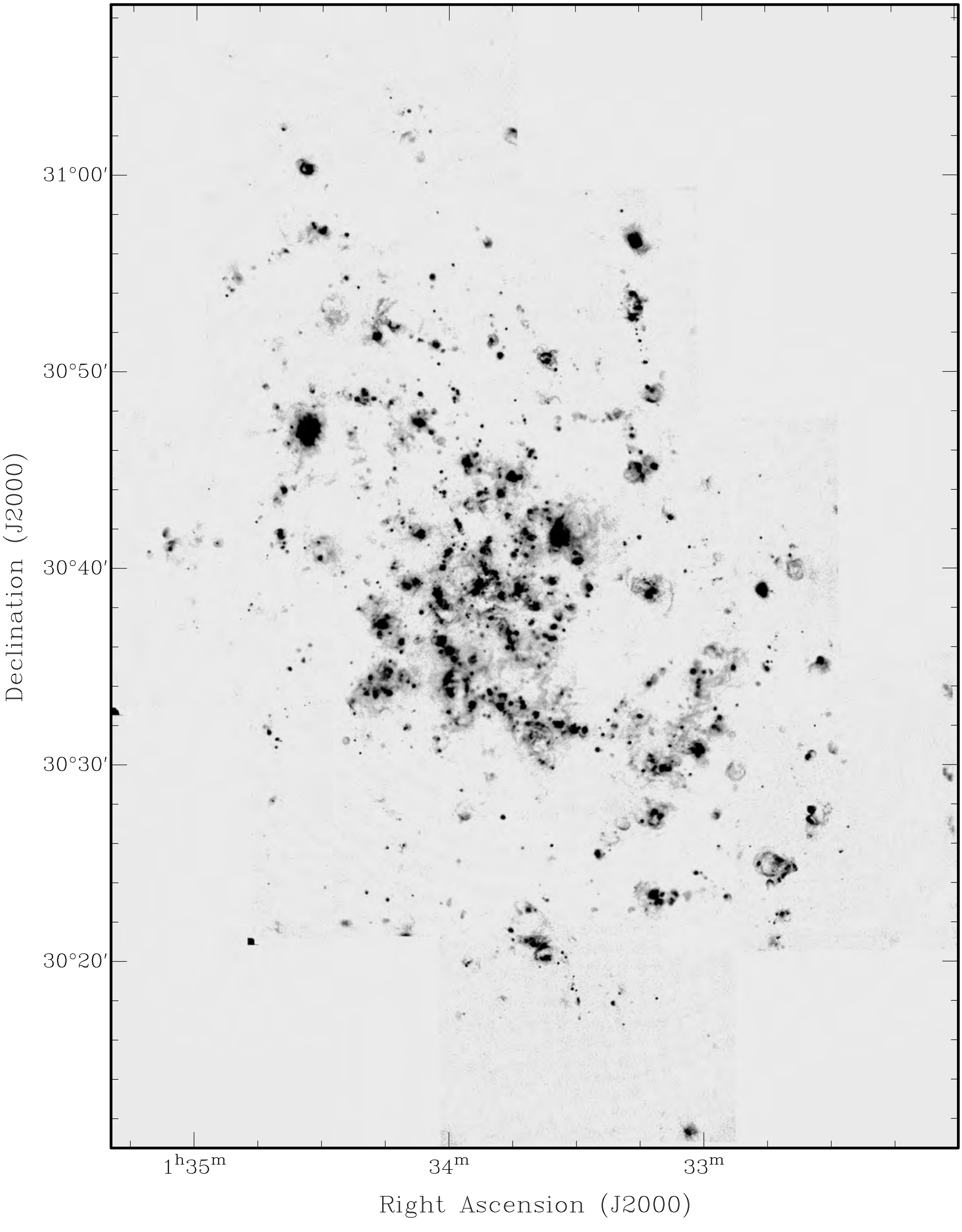
31°00′
30°50′
30°40′
30°30′
30°20′
Declination (J2000)
1h35m
34m
33m
Right Ascension (J2000)

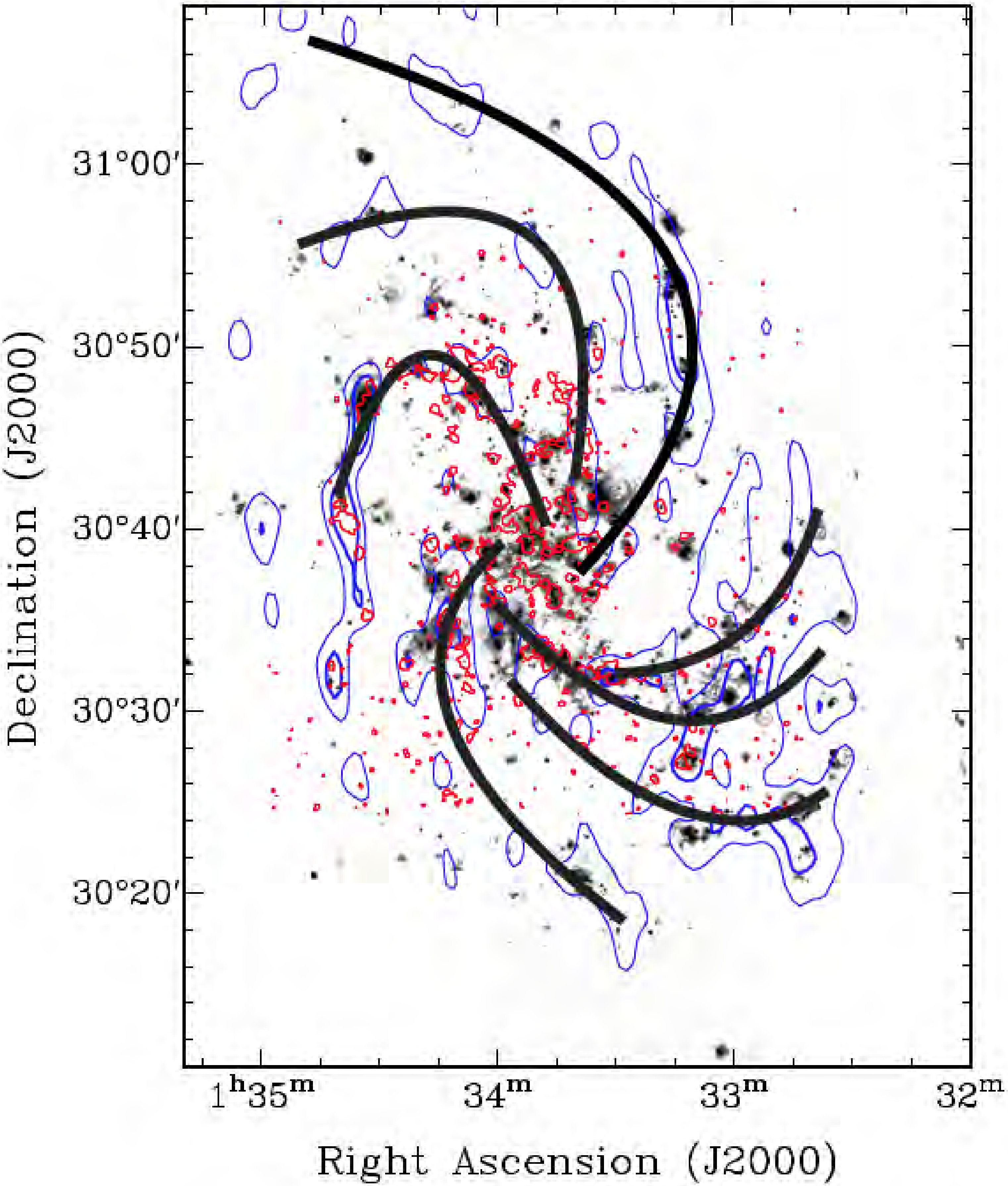
31°00′
30°50′
30°40′
30°30′
30°20′
Declination (J2000)
1h35m
34m
33m
32m
Right Ascension (J2000)

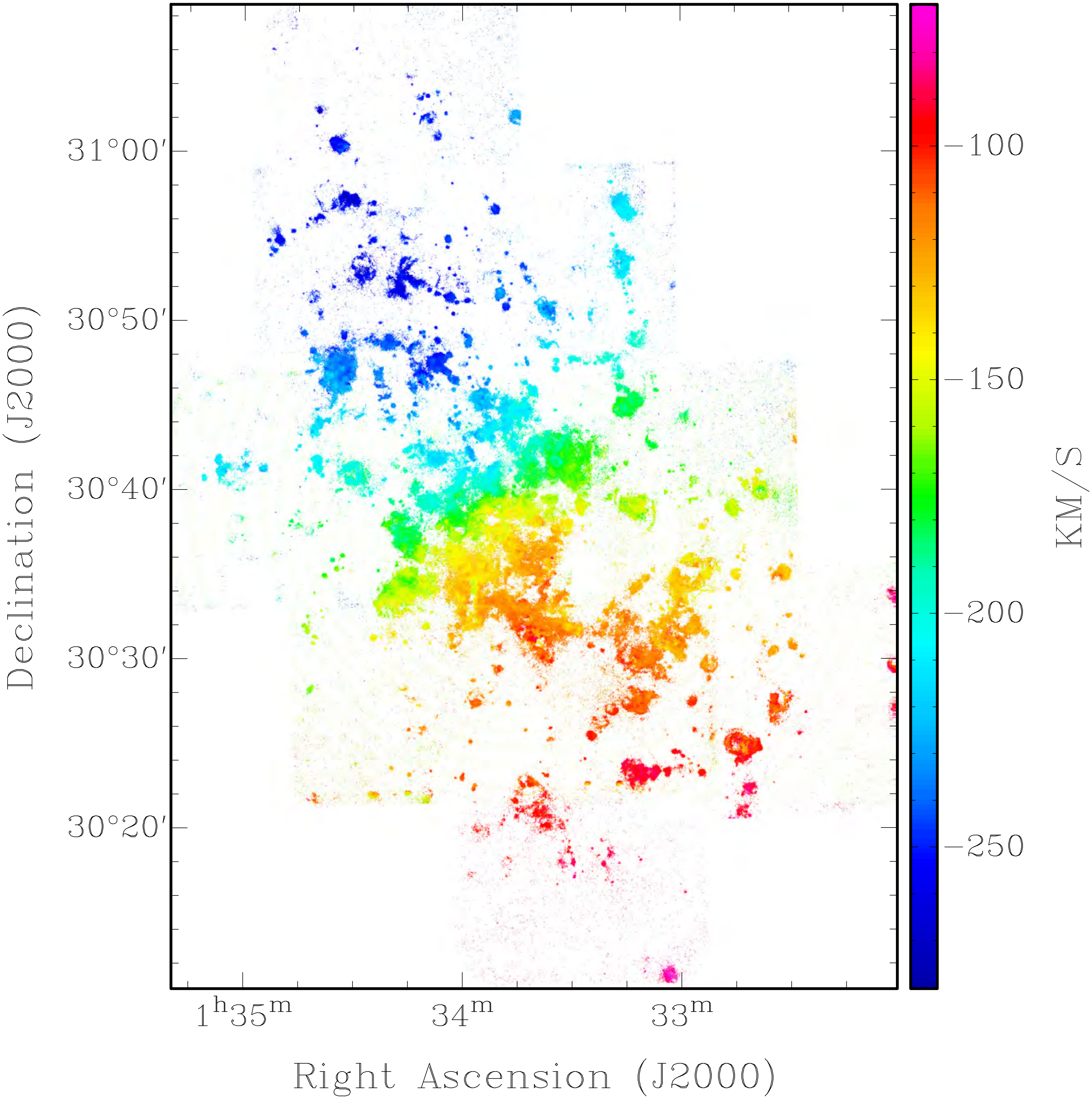
31°00′
30°50′
30°40′
30°30′
30°20′
Declination (J2000)
1h35m
34m
33m
Right Ascension (J2000)
−100
−150
−200
−250
KM/S

Cinématique HI de M33

Chapitre 3

Cinématique HI de M33

Sommaire

Résumé

Nous présentons dans cette partie les analyses sur la cinématique de M33 en utilisant les données HI combinées de DRAO et Arecibo dans le domaine radio. Nous présentons également les modèles de masse avec les profils HI et une contribution du Hα dans les régions internes. Les résultats sont présentés dans l'article ci joint.

3.1 Les dispositifs pour l'obtention des données HI

La gaz HI décrit dans la section 1.1.1.2 est observable à grand échelle dans les galaxies. Il renseigne efficacement de l'activité dans les objets allant des galaxies aux amas de galaxies. Les récepteurs utilisés pour l'observation de cette composante sont installés sur des télescopes à coupole unique ou sur des interféromètres.

3.1.1 Télescope à parabole unique

Les principales composantes

Un radiotélescope à coupole unique est un télescope utilisant une seule surface collectrice réfléchissante. La table 3.1 donne des exemples de radiotélescopes à coupole unique.

TABLE 3.1: Quelques radiotélescopes à parabole unique.

Noms	Diamètres (m)	Fréquences	Site	En fonction
Jodrell Bank	76	1.4 GHz	UK	1957
Parkes	64	Jusqu'à 5 GHz	Australie	1961
Effelsberg	100	0.4 - 86 GHz	Allemagne	1970
Arecibo	305	1- 10 GHz	Puerto Rico	1970
GBT	100	0.290 -100 GHz	USA	2000

On peut aussi ajouter les radio-télescopes spatiaux comme Odin, WMAP et Planck.

Lorsque la surface réfléchissante est en grille, la longueur d'onde détectable est de l'ordre de la grandeur des mailles de la grille. Le récepteur est placé au foyer (primaire, Cassegrain, Naysmith ...) de la parabole. Les ondes reçues sont amplifiées pour faciliter les détections. Le récepteur est à l'image d'un radiomètre et est constitué d'amplificateurs, de filtres passe-haut et passe-bas, de trieurs de bandes passantes, d'atténuateurs, de mixeurs et de détecteurs. Les données arrivant du récepteur sont des tensions ; elles renseignent sur les températures de surface après correction de la phase et du flux. Certains télescopes ont des multi récepteurs leur permettant d'opérer simultanément sur plusieurs gammes de fréquences. Le télescope d'Arecibo dans la figure (3.1) couvre les fréquences de 1-10 GHz.

FIGURE 3.1: Radio télescope de 305 m situé à Arecibo, Puerto Rico (Source : www.nsf.gov/news).

L'exploration de faibles fréquences nécessite l'utilisation de télescopes à grand diamètre (D) de surface collectrice, pour obtenir des images avec une résolution comparable à une image optique. Dans un cas parfait, la résolution angulaire pour une observation à la longueur d'onde λ, est considérée équivalent à la largeur à mi hauteur du lobe principal ($\theta = 1.22\ \lambda/D$). La grandeur du diamètre devient ainsi un facteur important dans l'observation haute résolution du gaz H I dans les galaxies. L'interférométrie est l'option utilisée pour palier au problème que peut poser la construction de télescopes de très grand diamètre.

Le fonctionnement

L'image 3.2 montre une simplification du fonctionnement d'un télescope radio ayant une seule antenne. Dans ce type de configuration très courant, un secondaire généralement convexe renvoie les ondes radio vers la base de la parabole où sont placés les cornets-détecteurs (stabilisateur d'ondes). Le signal électromagnétique, convergeant vers le récepteur radio, est converti en signal électrique. Des récepteurs très performants sont utilisés afin de dissocier facilement les bruits parasites qui sont à des longueurs d'onde assez proches de celles des sources. Un circuit complexe d'amplification et d'échantillonnage de l'onde est nécessaire pour obtenir de manière distincte la longueur d'onde observée. La réduction du signal permet ensuite de produire les images radio.

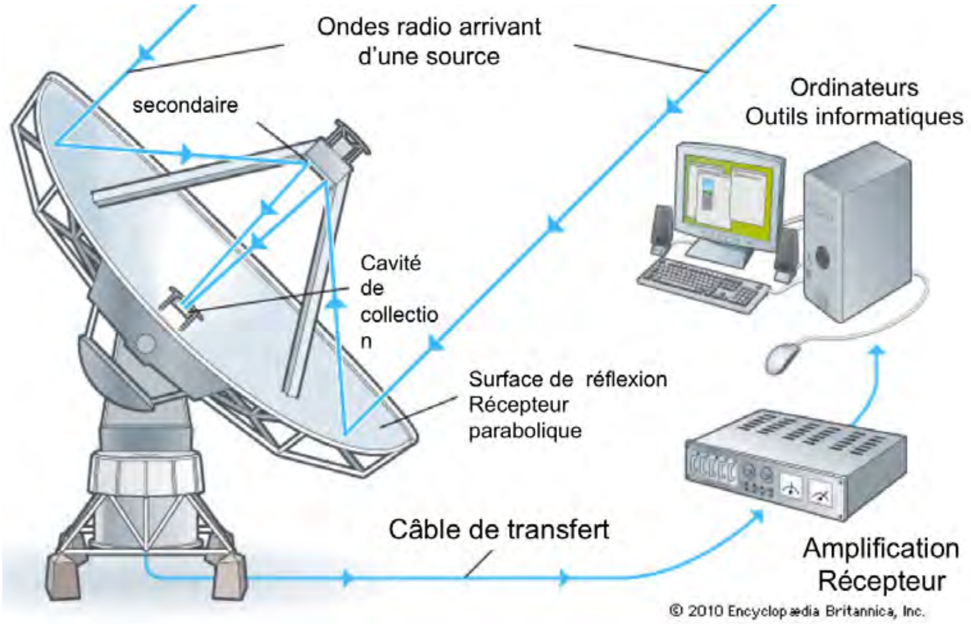

FIGURE 3.2: Principe de fonctionnement d'un radiotélescope à foyer Cassegrain (Image original de britannica.com).

3.1.2 L' interférométrie en radio

Les principales composantes

La combinaison de plusieurs radiotélescopes à parabole unique donne un interféromètre qui permet d'obtenir une plus grande sensibilité dans la détection. L'interférométrie donne l'avantage de pouvoir observer de petites structures radio (compactes) très distantes. En effet, la grande étendue du champ de télescope produit un faisceau plus petit, propice à l'observation des structures de petites tailles. La résolution angulaire d'un interféromètre ayant d comme sa plus grande ligne de base vaut λ/d. Le faisceau d'un tel interféromètre formé de télescopes de diamètre D, est de l'ordre de $(D/d)^2$ fois plus petit que celui d'une seule antenne. L'image de la figure 3.3 montre l'exemple d'un interféromètre radio : le Very Large Array (VLA). Comme indiqué dans la table 3.2, le VLA est constitué de 27 antennes.

TABLE 3.2: Quelques interféromètres radio.

Nom	Diamètre (m)	N Antennes	Base max	Fréquence	Site	En fonction
DRAO	9	7	600 m	0.40-1.4 GHz	Canada	1960
WSRT	25	14	2.7 km	0.12-8.3 GHz	Netherlands	1970
VLA	25	27	36 km	0.074-50 GHz	USA	1980
VLBA	10	25	8000 km	0.3-95 GHz	USA	1993
KAT7	7	12	185 m	1.20-1.95 GHz	SA	2010
ALMA	7-12	66	14.5 km	5-900 GHz	Chili	2013
SKA	12-15	3000	3000 km	0.07-10 GHz	SA	—

FIGURE 3.3: Very Large Array Télescope radio de 27 antennes situé à Soccoro à New Mexico. *Crédit : NRAO*

Le fonctionnement

Dans les interféromètres radio chaque paire d'antennes constitue une base. Pour un nombre N d'antennes on distingue $N(N-1)/2$ bases. La distance de base est donnée par la distance entre les antennes. La figure 3.4 donne le principe de fonctionnement des interféromètres radio. Chaque antenne constitue un récepteur en elle même. Les ondes arrivent sur les antennes avec une différence de marche équivalent à $d.cos(\theta)$. Pour une onde monochromatique de fréquence $\nu = \omega/2\pi$ arrivant sur les deux antennes ; selon le schéma de la figure 3.4, les tensions $V_A \ et \ V_B$ des antennes A et B (antennes identiques) sont données par :

$$V_A = Vcos(\omega t) \quad V_B = Vcos(\omega t - \tau_g) \tag{3.1}$$

où $\tau_g = d.cos(\theta)/c$, t désigne le temps.

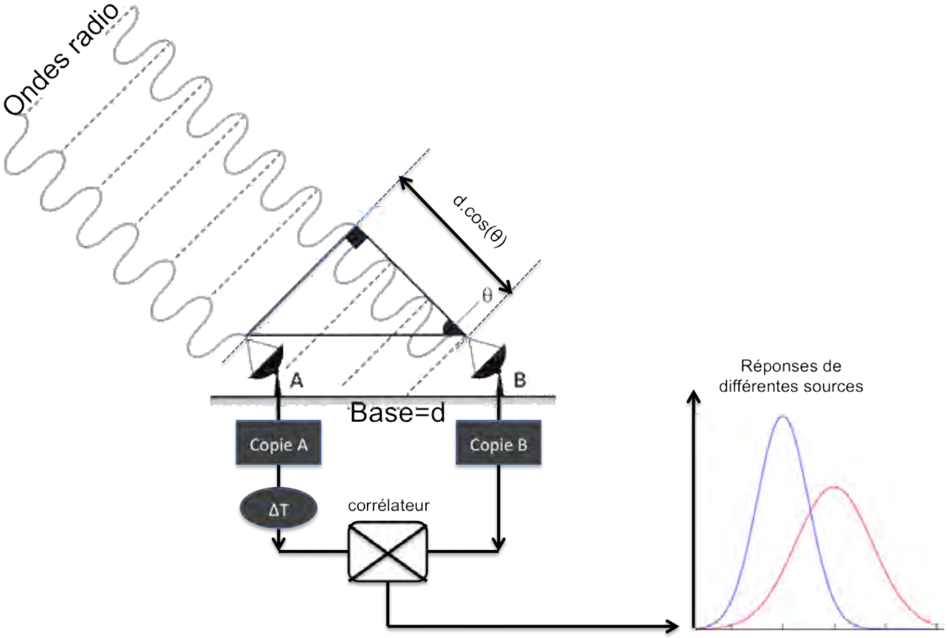

FIGURE 3.4: Principe de fonctionnement d'un interféromètre radio à deux antennes.

La tension résultante donnée par le corrélateur dans la figure 3.4 est celle exprimée dans l'équation (3.2).

$$R =< V_A V_B > \frac{V^2}{2} cos(\omega\tau_g) \tag{3.2}$$

La réponse du corrélateur est donc une fonction sinusoïdale dont la phase est $\phi = \omega\tau_g$. La phase change énormément avec l'angle θ associée à la position de l'objet et est également fonction de ω donc fonction de la longueur d'onde λ. Le bruit d'un corrélateur est $\sqrt{2}$ fois plus faible que celle $\sqrt{signal}$ d'une antenne.

Le plan uv

Lorsque les observations sont réalisées avec un interféromètre, le repère associé aux données recueillies est celui formé par le plan (uv) des antennes et la direction antennes-source. Le plan (uv) est décrit par les lignes de base des télescopes qui sont fixes. Avec la rotation de la terre, au bout de 12 heures, ces lignes forment dans le plan (uv) des ellipses concentriques si le nombre d'antennes vaut au moins trois. u désigne la composante Est-Ouest et v la composante Nord-Sud. Les deux composantes dépendent fortement de la déclinaison de l'objet. Pour obtenir les images, une transformée de fourrier est réalisée sur les données de l'espace (uv).

3.1.3 Les relations fondamentales

Les relations [a] ci-dessous sont importantes dans l'analyse des observations du gaz HI.

Conversion des flux

Les valeurs des observations peuvent se présenter en mJy (milli Jansky) ou en K (température Kelvin). L'équation (3.3) donne une correspondance entre ces deux unités.

$$T_B = \frac{\lambda^2 S}{2k_B \Omega} = \frac{1.36\lambda^2 S}{a \times b} = \frac{1.36\lambda^2 S}{\theta^2} \tag{3.3}$$

Dans cette équation S désigne la densité de flux en mJy et Ω l'angle solide représentant le faisceau du télescope. Le faisceau est défini par ses axes, majeur et mineur, dont les valeurs sont $a\ et\ b$ données en seconde d'arc. Pour un faisceau circulaire on $a = b = \theta$; k_B est la constante de Boltzmann. La dernière partie de l'équation est donnée pour $\lambda = 21\ cm$.

La sensibilité

Une antenne ou un ensemble d'antennes est caractérisée par sa sensibilité. Les équations (3.4), (3.5) et (3.6) permettent de calculer de manière théorique le seuil de sensibilité. Dans ces trois équations σ_s désigne la sensibilité, T_{sys} le bruit du système en température. On pose $A_{\text{eff}} = 2k\Delta T/S$ où S est la densité de flux, ΔT la température d'antenne. $\Delta\nu_{RF}$ est l'intervalle de radio fréquence dans lequel les donnée sont prises. τ est le temps d'intégration sur la cible.

L'équation (3.4) donne l'expression de la sensibilité d'une coupole.

$$\sigma_{\text{s}} = \frac{2\ \text{k}\ \text{T}_{\text{sys}}}{\text{A}_{\text{eff}}\sqrt{(\Delta\nu_{\text{RF}}\tau)}} \tag{3.4}$$

---

[a] www.atnf.csiro.au/people/Tobias.Westmeier/ www.cv.nrao.edu/course/astr534/ERA.shtml

L'équation (3.5) donne l'expression de la sensibilité de deux coupoles associées.

$$\sigma_{\rm s} = \frac{2^{1/2}\ \rm k\ T_{sys}}{\rm A_{eff}\sqrt{(\Delta\nu_{RF}\tau)}} \tag{3.5}$$

L'équation (3.6) donne l'expression de la sensibilité d'un interféromètre constitué de N coupoles associées.

$$\sigma_{\rm S} = \frac{2\ \rm k\ T_{sys}}{\rm A_{eff}\sqrt{N(N-1)(\Delta\nu_{RF}\tau)}} \tag{3.6}$$

Racine carrée de la moyenne des carrés (rms) : σ_T
est une quantité qui est fonction de l'angle solide du faisceau.

$$\sigma_{\rm T} = \frac{\sigma_{\rm s}\ \lambda^2}{2\ \rm k\ \ \Omega_\theta} \tag{3.7}$$

Dans l'équation (3.7) $\Omega_\theta = \dfrac{\pi\ \theta_0^2}{4\ln(2)}$, où θ désigne la largeur à mi-hauteur du faisceau et σ_S la sensibilité d'une source ponctuelle comme définie dans l'équation (3.4)

Densité de colonne $N_{H\rm I}$
La densité de colonne du gaz HI ($\rm N_{HI}$) est déterminée par l'équation (3.8). Cette densité de colonne $\rm N_{HI}$ du gaz HI est obtenue en supposant que le gaz est optiquement mince. Dans l'équation (3.8), elle est calculée pour une profondeur optique de 1. La densité $\rm N_{HI}$ est définie en cm^{-2} et T_B la température de surface en K.

$$N_{H\rm I} = 1.832\times 10^{18}\int \frac{T_B(\nu)}{[K]}\frac{d\nu}{[km\ s{-}1]} \tag{3.8}$$

*Masse du gas H*I
Dans l'équation (3.9), $\rm S_{int}$ désigne le flux intégré de la galaxie en $[\rm mJy\ km\ s^{-1}]$. Il est en général considéré pour les régions où le flux est supérieur au bruit. Il est courant de considérer à chaque fréquence un seuil de détection lié à la valeur du bruit et à une intensité minimale de détection. La variable d donne la distance de l'objet en $[\rm Mpc]$. La masse ainsi calculée est en unité de masse solaire.

$$\frac{M_{H\rm I}}{[M_\odot]} = 236\times\frac{\rm S_{int}}{[\rm mJy\ km\ s^{-1}]}\times(\frac{d}{[Mpc]})^2 \tag{3.9}$$

Le moment zéro : Flux
Dans l'équation (3.10), $A(\nu)$ représente l'intensité du flux à la vitesse ν. $\Delta\nu$ est le pas entre deux

vitesses (fréquences) consécutives. La carte de moment zéro donne le flux intégré du spectre sur tout point de l'objet.

$$\mathrm{M}_0 = \Delta\nu \sum \mathrm{A}(\nu) \tag{3.10}$$

Le moment un : Vitesse

Le moment un défini la vitesse en chaque point de la source. L'équation (3.11) représente l' "intensity-weighted velocity" du spectre et représente bien la vitesse moyenne du gaz.

$$\mathrm{M}_1 = \frac{\sum \nu \mathrm{A}(\nu)}{\sum \mathrm{A}(\nu)} \tag{3.11}$$

Le moment deux : dispersion des vitesses (σ)

La carte de moment deux décrit dans l'équation (3.12), donne la carte de dispersion (σ) de la raie (spectre HI). Pour une vitesse V mesurée en un point la dispersion en ce point est définie par $\sigma = \sqrt{(< V.V > - < V >< V >)}$ et donne la largeur de la raie en ce point. La dispersion mesurée est une somme quadratique de la dispersion réelle et de la dispersion instrumentale. En se basant sur l'intensité mesurée, le moment deux est obtenu par :

$$\mathrm{M}_2 = \sqrt{\frac{\sum (\nu - \mathrm{M}_1)^2 \mathrm{A}(\nu)}{\sum \mathrm{A}(\nu)}} \tag{3.12}$$

3.2 Les observations HI

La séquence des observations HI comporte en plus de la source, l'observation des sources étalons. Deux types d'étalonnages sont réalisés en radio : l'étalonnage de flux et la calibration en phase. L'observation d'une source est une alternance d'observations entre la source et les étalons. La source étalon de la phase des antennes doit être très bien suivie pendant les observations, car la phase varie énormément avec la position de l'objet dans le ciel. Pour calibrer le flux, deux observations à des périodes différentes (de préférence au début et à la fin) peuvent suffire.

3.2.1 Les interférences de fréquences radio (RFI)

Les observations radio sont très sensibles aux interférences radio. Les principales sources de pollution des données sont les satellites en orbites, les appareils téléphoniques, les postes radios de communication, les fours microondes et bien d'autres. Dans le processus de réduction des données, les fréquences contaminées sont identifiées ('flaguées') et corrigées.

3.2.2 La calibration en phase

La calibration en phase permet de connaître la réponse en phase du télescope à une position donnée dans le ciel. Les étalons utilisés sont très bien étudiés. Pendant l'observation d'une source, plusieurs étalons de phase peuvent servir étant donné que leur réponse est bien connue. Ces étalons sont au préalable bien étudiés sur le site d'observation. Pour une bonne correction en phase, il faut alterner les observations de la source avec celles de l'étalon de phase.

3.2.3 La calibration en flux

En radio comme dans plusieurs autres types d'observations en astrophysique, la connaissance du flux réel est importante. Pour calibrer les observations en flux, il est important d'observer des sources étalon, idéalement, au même moment que les observations. Mais dans les observatoires, plusieurs étalons de flux sont bien définis à différentes masses d'air dans le ciel. Alors il est possible de réduire le nombre d'acquisitions sur l'étalon et d'observer seulement deux fois à deux positions différentes.

3.3 Résultats des observations HI de M33

L'étude de la cinématique HI de M33 qui suit, a été réalisée avec les observations de deux télescopes radio : le télescope à coupole unique d'Arecibo (305 m de diamètre) et l'interféromètre radio de DRAO. Cet article fait :

- une présentation des données obtenues ;
- une présentation des paramètres cinématiques et
- une étude des modèles de masse avec et sans présence de matière sombre.

Les modèles de Navaro-Frenk-White, Einasto, de la sphère isotherme et les formalismes de MOND ont été testés dans cette étude.

L'article a été soumis à la revue MNRAS.

3.4 Kinematics and mass modelling of M33 : H I Observations

Kam, Z. S.[1,2,3], Chemin, L.[4], Carignan, C.[1,2,3], Foster, T.[5,6]
[1]Laboratoire d'Astrophysique Expérimentale, Département de physique,
Université de Montréal, C.P. 6128, Succ. centre-ville, Montréal, Québec, H3C 3J7, Canada
[2]Observatoire d'Astrophysique de l'Université de Ouagadougou, BP 7021, Ouagadougou 03, Burkina Faso
[3]Department of Astronomy, University of Cape Town, Private Bag X3, Rondebosch 7701, South Africa
[4]Univ. Bordeaux and CNRS, LAB, UMR 5804, F-33270, Floirac, France
[5]Department of Physics and Astronomy, Brandon University, 270-18th Street, Brandon, MB, R7A 6A9, Canada
[6]National Research Council Canada, Dominion Radio Astrophysical Observatory, P.O. Box 248, Penticton, British Columbia, V2A 6J9, Canada

ABSTRACT

A new large scale study of the H I kinematics and mass distribution of Messier 33 is presented, based on observations obtained with the Dominion Radio Astrophysical Observatory interferometer, combined with data from the Arecibo 305 m single dish telescope. An area larger than $2^\circ \times 2^\circ$ is surveyed, with a final spatial resolution of $2'$. Mass models using Modified Newtonian Dynamics (MOND) and three different functional forms of dark matter (DM) halo (the pseudo-isothermal sphere, the Navarro-Frenk-White and the Einasto models) are fitted to a hybrid Hα-H I rotation curve of M33. There is no way to get a satisfying MOND model, even when allowing the constant a_0 and/or the mass-to-light ratio of the disk to vary, or using different interpolation functions. The DM models show that while both cuspy and shallow inner density profiles give comparable good fits to the rotation curve, haloes with steep inner density profiles are highly unrealistic. The density slope derived at a radius of 41 pc, the radius of the innermost velocity point of the rotation curve, is consistent with a core-dominated halo, in disagreement with other recent mass models favouring a cosmological cusp. The inferred stellar and total masses inside 22 kpc are $\sim 9 \times 10^9$ M$_\odot$ and $\sim 10^{11}$ M$_\odot$, respectively. At the virial radius of 180 kpc, a total mass of $\sim 7 \times 10^{11}$ M$_\odot$ is found for M33, about 1.4 times less massive than its companion M31.

Keywords

techniques : interferometric – galaxies : individual : M 33 – galaxies : kinematics and dynamics – galaxies : haloes – cosmology : dark matter

3.4.1 Introduction

With the Milky Way and Andromeda, the Triangulum galaxy (Messier 33, the third most massive disk of the Local Group) has long been among the most studied nearby galaxies to scrutinize the chemical, dynamical and structural properties of the stellar populations and the interstellar medium. In particular, as it is a prototype of gas-rich spiral of moderate inclination (Tab. 3.3) it is very appropriate to study the relationships of the atomic and molecular gas content with the star formation inside the disk. Since it is now well admitted that M33 has undergone a tidal encounter with a massive galaxy as its close environment is perturbed (very likely Andromeda, Braun & Thilker, 2004; McConnachie et al., 2010), it is expected that gas expelled during that interaction is currently returning into the M33 disk, fueling the active star formation (Putman et al., 2009).

The implied important population of HII regions (e.g. Boulesteix et al., 1974; Zaritsky et al., 1989; Relaño et al., 2013) has thus been a motivation for us to present the first large-scale, arcsec-resolution, 3D spectroscopic survey of the disk of Messier 33 in the Hα emission line (Kam et al., 2015, hereafter Kam15). On one hand, the objectives of this survey was to study the internal kinematics of the HII regions. For instance, Kam15 pointed out the complex relation between the velocity dispersion and the integrated intensity of the Hα line, underlying the physical processes occurring in the brightest regions and in the diffuse interstellar medium. The catalog of HII regions that will follow from this survey will be essential to study the relationships with other tracers of star formation in M33 at an unprecedented level of details. On the other hand, the Hα mapping has been a unique opportunity to determine for the first time the most extended Hα velocity field of M33. The modelling of the velocity field led Kam15 to conclude that the kinematical parameters of the ionized gas disk are very consistent with those of the stellar disk, and that the positional difference of the dynamical centre from the photometric centre is typical of what is observed in many nearby galaxies (about one hundred parsecs in projection). Maybe the most important result of Kam15 is the determination of the Hα rotation curve out to 8 kpc. That curve perfectly traces the velocity gradient in the inner disk, and presents many wiggles characteristic of spiral arms perturbations, but that have been barely showed in previous HI and CO observations. These irregularities however do not prevent the Hα, HI or CO rotation velocities to remain in good agreement.

The derivation of the Hα rotation curve actually constitutes the first pillar of a broader project devoted to revisit the modelling of the mass distribution of M33. The other pillar inherent to such modelling is to get the HI rotation curve to cover as far as possible the outer disk, ensuring as much degrees of freedom as possible to perform accurate fits of dark matter parameters, or of alternate dynamics like MOND.

Existing HI studies of M33 attest to which extent the tidal interaction with Andromeda has not been without consequences on the gas distribution in the disk outskirts, revealing perturbed features like a warp, arc-like structures or diffuse and discrete gas around the disk (Corbelli & Schneider, 1997; Putman et al., 2009; Lockman et al., 2012). Recently, Corbelli et al. (2014) used VLA+GBT observations to model the HI warp and rotation curve. They have presented a new, flat rotation curve that extends about 5 kpc further than previously known. They have also shown that the distribution of dark matter in Messier 33 is consistent with a model for which the mass density steeply decreases in the centre of the halo (the cosmological cusp à la Navarro-Frenk-White, see Navarro et al., 1997). Comparable results have been obtained by Hague & Wilkinson (2015), but from a lower resolution HI curve derived earlier by Corbelli & Salucci (2000). They concluded that models with density slopes < 0.9 at $R \sim 0.5$ kpc (the first velocity point of their rotation curve) with 3.6-μm mass-to-light ratios < 2 are ruled out in M33.

In this context, we have performed an HI survey of Messier 33 at the Dominion Radio Astrophysical Observatory (DRAO). This arcminute-resolution survey is a good intermediate between VLA and Arecibo or GBT measurements. The objectives of this article are first to present the survey, the gas content and distribution of M33, a new tilted-ring model of the HI velocity field and the HI rotation curve. We also want to examine the shape and amplitude of the outer rotation curve, at radii beyond $R = 17$ kpc where Corbelli et al. (2014) presented new velocities. The second objective of the article is to benefit from the high-resolution survey of Kam15 and perform accurate mass distribution models from an hybrid Hα-HI rotation curve. In particular we want to test the Modified Newtonian Dynamics model, determine the best-fit slope of the density profile of the dark matter halo at the first point of the rotation curve ($R = 41$ pc) and infer the total mass of M33.

Throughout the article, we have adopted a Hubble constant of 72 km.s^{-1}Mpc^{-1} (Hinshaw et al., 2009) and a distance to Messier 33 of 0.84 Mpc (see Kam15 and references therein). The basic optical parameters of M33 are summarized in Table 3.3. The observations and the reduction of the HI data are presented in section 3.4.2. Section 3.4.3 presents the HI kinematics, the tilted-ring

TABLE 3.3: Optical parameters of M 33.

Parameters	Value	Source
Morphological type	SA(s)cd	RC3
R.A. (2000)	$01^{h}\ 33^{m}\ 33.1^{s}$	RC3
Dec. (2000)	$+30^{\circ}\ 39'\ 18''$	RC3
Optical inclination, i	$52^{\circ}\pm3^{\circ}$	W73
Optical major axis, PA	$22.5^{\circ}\pm1^{\circ}$	W73
Apparent magnitude, m_V	5.28	RC3
Absolute magnitude, M_V	-19.34	
(J-K)	0.89	TJ03
Optical radius, $D_{25}/2$	$35\farcm4 \pm 1\farcm0$	RC3
Systemic Velocity	-179 ± 3 km.s^{-1}	RC3

RC3 : de Vaucouleurs et al. (1991), W73 : Warner et al. (1973), TJ03= Jarrett et al. (2003)

model, the HI rotation curve and the adopted combined Hα-HI rotation curve. The modelling of the mass distribution is done in Section 3.4.4. Section 3.4.5 presents a discussion of the results, and conclusions are given in Section 3.4.6.

3.4.2 HI line study

3.4.2.1 Observations and data reduction

The primary observations for this study were made in the 21 cm line of neutral hydrogen HI with the synthesis telescope of the DRAO. This telescope is an East-West interferometer consisting of seven (~9 m diameter) dishes spaced along a maximum baseline of 617.2 m. This longest baseline achieves a synthesized half-power beamwidth of 49″(EW) by 49″/sin δ(NS) with uniform weighting although, in the HI line, we chose natural weighting (a Gaussian taper in the u, v plane) to increase the sensitivity at the slight expense of resolution (58″×58″/sinδ) Further specifications and capabilities of the DRAO telescope can be found in Landecker et al. (2000) and Kothes et al. (2010). Other frequencies were also observed with a 30 MHz continuum band centred at 1420 MHz (λ21 cm), and a 2 MHz band at 408 MHz (λ74 cm), although these data are not presented here.

For the HI line observations of M33, the spectrometer was set to a 2 MHz-wide band with 256 channels, each spaced by ΔV = 1.65 km s^{-1} . The band was centred on a heliocentric velocity

TABLE 3.4: Summary of the six 21 cm HI line synthesis fields centred on and surrounding M33, observed with the DRAO synthesis telescope in 2008.

Date	Field Centre (RA, DEC)(J2000.0)	Beam Parameters beam, angle(CCW E)
Sep. 29	$1^{\rm h}33^{\rm m}50.9^{\rm s}$, $+30°39'36''$	$1'.90\times0'.97$, $-89.69°$
Sep. 29	$1^{\rm h}36^{\rm m}10.2^{\rm s}$, $+31°50'34''$	$1'.85\times0'.97$, $-89.82°$
Nov. 05	$1^{\rm h}31^{\rm m}38.2^{\rm s}$, $+29°28'12''$	$1'.98\times0'.97$, $-89.91°$
Nov. 05	$1^{\rm h}34^{\rm m}45.8^{\rm s}$, $+31°08'13''$	$1'.86\times0'.97$, $-90.11°$
Dec. 04	$1^{\rm h}32^{\rm m}56.4^{\rm s}$, $+30°11'01''$	$1'.94\times0'.97$, $-90.30°$
Dec. 04	$1^{\rm h}33^{\rm m}50.9^{\rm s}$, $+30°39'36''$	$1'.91\times0'.97$, $-90.49°$

The beam is given as $\theta_{maj} \times \theta_{min}$

of $V_{\rm HEL} = -180$ km s^{-1}. The typical RMS noise in each (empty) channel is $1.2 - 1.4$ K. To increase the sensitivity to the faint outermost HI disk of M33, a total of 6 full-synthesis pointings on and around the galaxy were observed and mosaiced together, each having a field-of-view equal to the half-power width of the primary beam of the individual antenna ($107'.2$). Table 3.4 lists the field centres for the six individual fields (in J2000.0 coordinates). Two fields are centred precisely on M33, and four others are positioned along the galaxy's major axis (position angle ∼100° CCW from E) with two inner ones spaced $31'$ from the central ones, and two outer fields $46'.5$ from the two inner ones. The integration time for each field was 288 hours for a total integration time of $6 \times 288 = 1728$ hours, equivalent to 144 half days of observation (24/field).

Data processing and mosaic-making steps are identical to those described in Chemin et al. (2009) for the M31 observations using the DRAO telescope. However, for M33, we merge single-dish data obtained from the Turn-On GALFA Survey (TOGS) portion of the GALFA-HI survey done at Arecibo. These data have been previously published by Putman et al. (2009) and have an angular resolution of $3'.4$, providing exceptional spatial-frequency overlap with the DRAO synthesis data (which are missing spatial structures larger than about one degree). TOGS HI data were added to the calibrated interferometer-only mosaic in the same manner as in Chemin et al. (2009) after converting them to the same spatial and velocity resolutions and grid. To gain further sensitivity, the final datacube was smoothed to a velocity resolution of 10.5 km s^{-1} (from 2.64 km s^{-1}). The measured 1σ noise at the pointing centre of the final short-spacings-added and velocity-smoothed mosaic is ≃180 mK per (empty) channel for the full resolution of $115''\times58''$. A velocity-collapsed map of the resulting final mosaic (sum of channels with $-46 \leq v_{\rm HEL} \leq -320$ km s^{-1}) is shown in Figure 3.5. It shows an extended HI disk beyond the

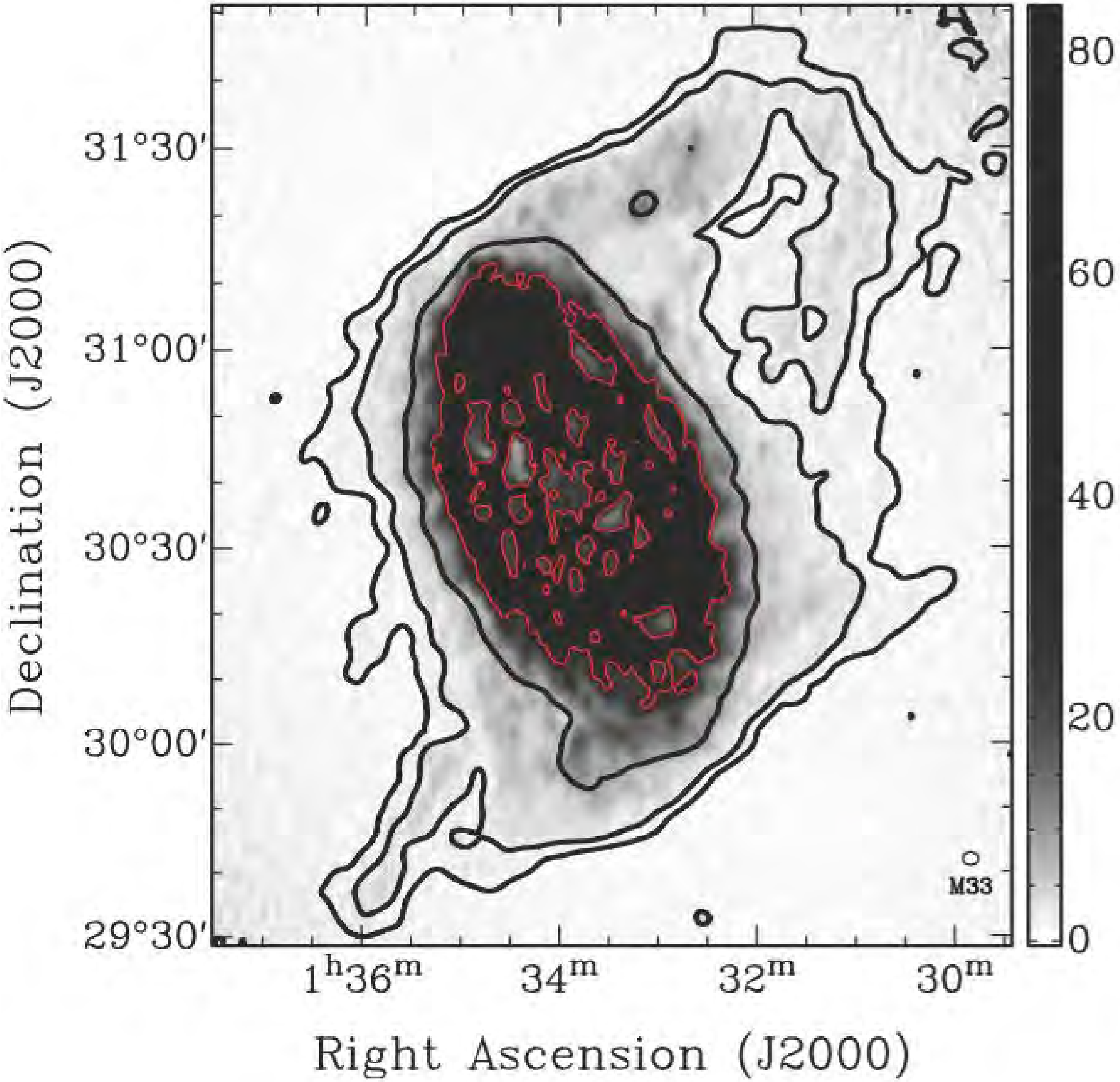

FIGURE 3.5: HI-peak final HI mosaic of M33. T_B contours (red) are at 1.2, 2 and 10 Kelvin. The outermost extent of the warped HI disk of M33 (black), is also visible in the individual channels of the high-resolution cube. The beam, showed at the bottom right corner, is 2′, corresponding to $\sim$ 500 pc using the adopted distance of M33.

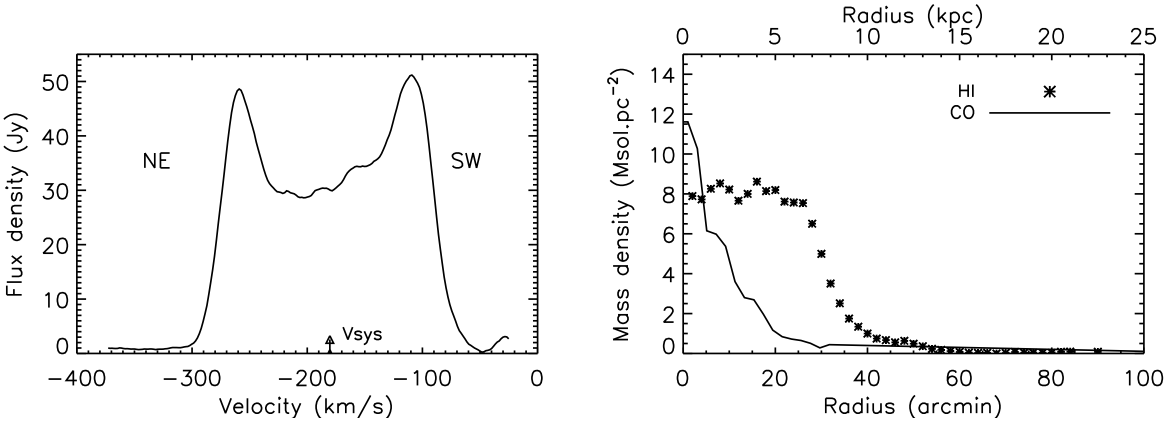

FIGURE 3.6: HI integrated emission profile of M33 (left panel). HI mass surface density profile (right panel). The molecular gas density profile of Druard et al. (2014) is overlaid (solid line).

optical disk and the warp in the outer parts.

3.4.2.2 HI global profile and HI mass

The HI global profile derived from the datacube is shown in Figure 3.6. The profile can be corrected for various effects such as e.g. auto absorption (Haynes & Giovanelli, 1984). If we were to correct for auto absorption according to the model proposed by Haynes & Giovanelli (1984), the fluxes would increase by $\gtrsim$8%.

A spatial smoothing on the 115″×58″ data cube is done in order to get a circular beam at 120″×120″. The RMS noise at 1σ in the new data is $\sim$ 2 mJy/beam using the empty channels. One can notice that the spatial smoothing of the data cube increases the noise but the HI fluxes are conserved. Using the smoothed cube, the Galactic emission appears strong in channels around -25 to -50 km.s^{-1}. Figure 3.6 shows clearly that, channels with velocities ≥ -50 km.s^{-1} are affected by galactic HI.

There is slightly more flux on the SW side than on the NE side. The maximum flux is considered as the mean of the two maxima. The intensity weighted systemic velocity is -180.3 ± 2.3 km.s^{-1} using the fluxes $\geq$ 10% of the maximum to avoid the Galactic HI emission. The width of the HI profile at 50% of the mean maximum, is $\Delta V_{50} = -182.8$ km.s^{-1}. At this height, the mid point velocity is -180.4 ± 3.5 km.s^{-1}, similar to the intensity weighted value. The arrow at the bottom axis of Figure 3.6 (left) indicates this mid point velocity. At the 20% level, the mid point velocity is -179.7 ± 3.5 km.s^{-1} and the width $\Delta V_{20} = 200$ km.s^{-1}. The total HI mass is $1.95 \pm 0.36 \times 10^9$ M$_\odot$. While the HI is detected up to $\gtrsim$ 90′, the mass density profile shows that most of the H I mass of M33 is within 40′, so roughly within the optical radius (∼35′).

Figure 3.7 presents the channel maps. The variation of the contours in this figure shows the variation of the PA of the galaxy (warp), especially in the channels between -136 to -208 km.s^{-1}. Details on the variations of the disk inclination and position angle (PA) of the major axis are presented in Section 3.4.3.1.

3.4.2.3 Warp of the H I disk of M33

Figure 3.8 shows a model of the warp of the H I disk that takes into account the variations of PA and inclination presented in section 3.4.3. Rings are separated by 240″ from each other. Within the region of the inner (optical) disk, the line-of-sight should, according to the model, cross the disk only once. Then the region of the warp should be crossed twice, and finally, once in the outermost regions of the H I disk.

This tilted-ring geometry is totally confirmed by the analysis of the H I profiles. Single peak profiles are seen within the inner disk (positions A and B). Multiple peaks or larger profiles are observed where the tilted rings overlap (positions C and D). Finally, single peak profiles (positions E and F) are observed in the outermost regions. A more detailed analysis of those multiple component profiles, and their spectral decomposition, as in Chemin et al. (2012), will be presented in a following paper.

3.4.3 H I rotation curve

3.4.3.1 Velocity field and kinematical parameters

The task MOMENTS in GIPSY has been used to compute the moment maps using the data cube smoothed at $120'' \times 120''$. Figure 3.9 show the 0th, 1st and 2nd moment maps.

The twist of the iso velocity contours, due to the warp, are clearly visible. The velocity dispersion are small and nearly constant in the central regions of the galaxy and increase when crossing holes or spiral arms in the inner parts. The mean dispersion in the disk is ∼11 km.s^{-1}. The dispersion is getting higher in the outer parts of the disk where the PA starts changing due to the warp. This is due to crossing the disk more than once with the result of generating double peaks or wider profiles.

The outermost feature, the South-Western Cloud, well described by Putman et al. (2009) (see also Grossi et al. 2008), have been removed from the velocity map before deriving the RC.

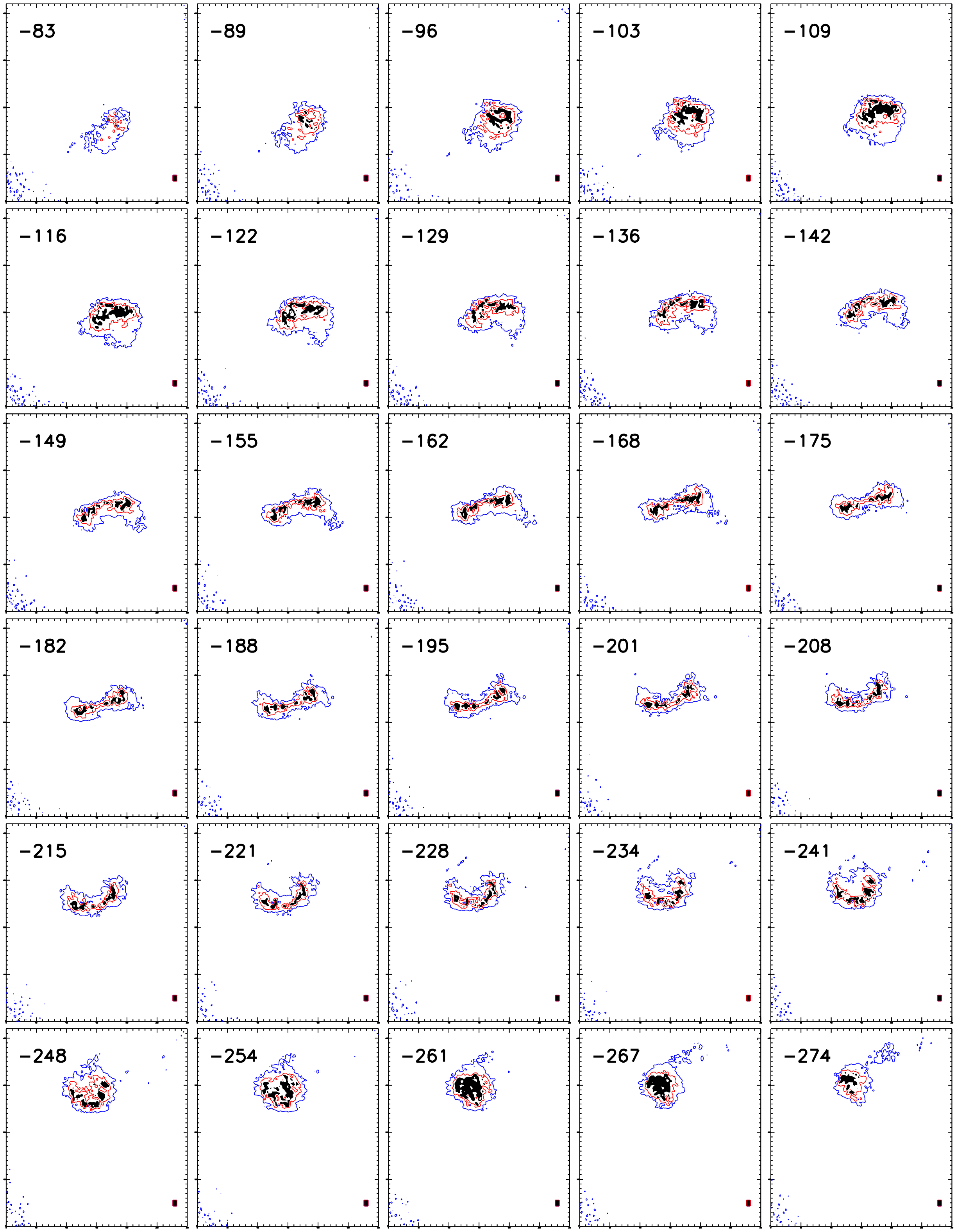

FIGURE 3.7: HI channels maps of M33 for the combined DRAO and Arecibo data. The contour levels are at 2.5 in blue, 8 in red and the filled grey regions represent the levels higher than 15 K. The velocity is noted at the upper left corner of each map. The beam is shown in the bottom right corner.

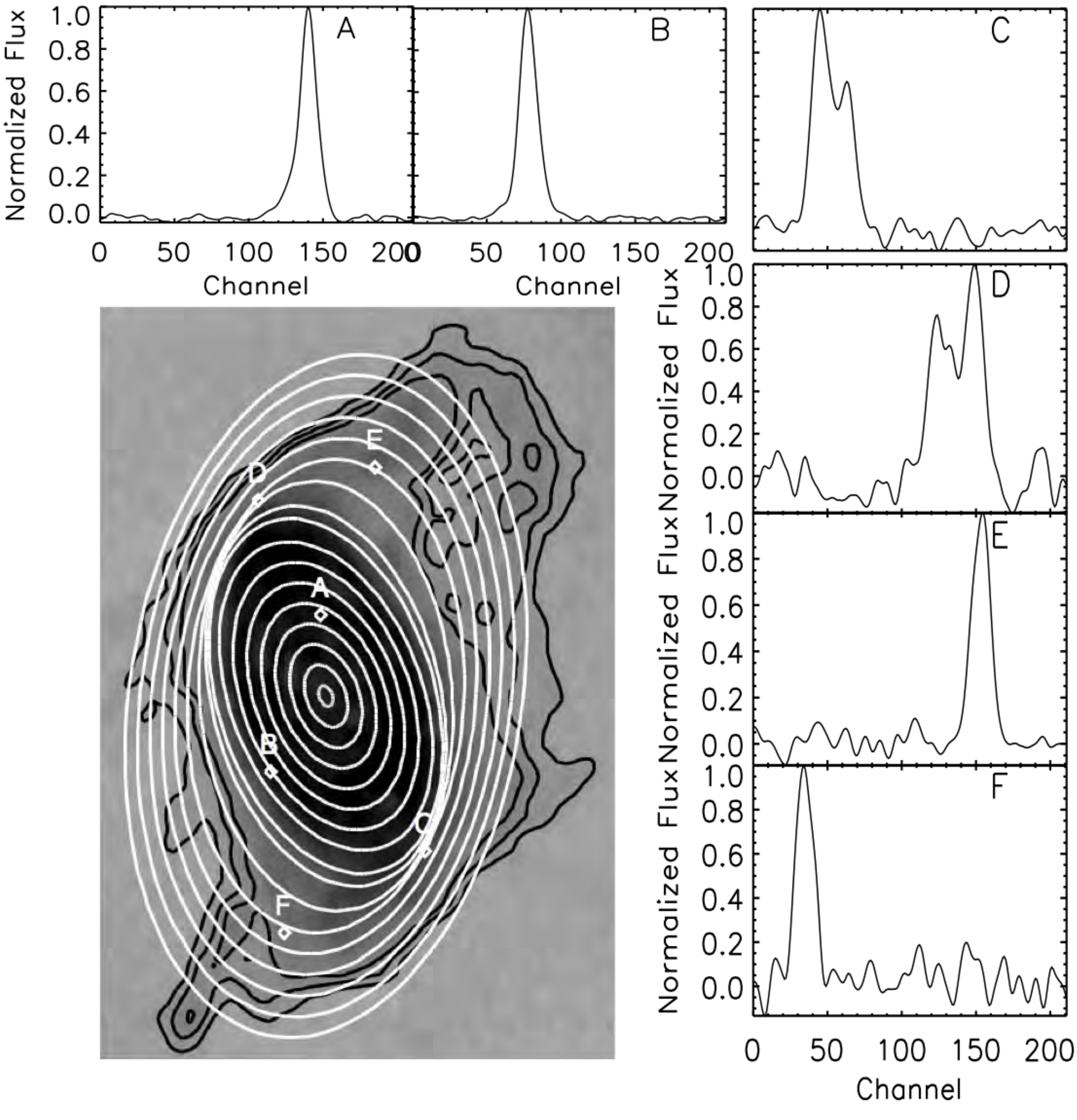

FIGURE 3.8: HI profiles given at several locations in the galaxy. The positions are indicated by the letters A, B, C , D, E, F. The ellipses show the results of the tilted-ring model of M33.

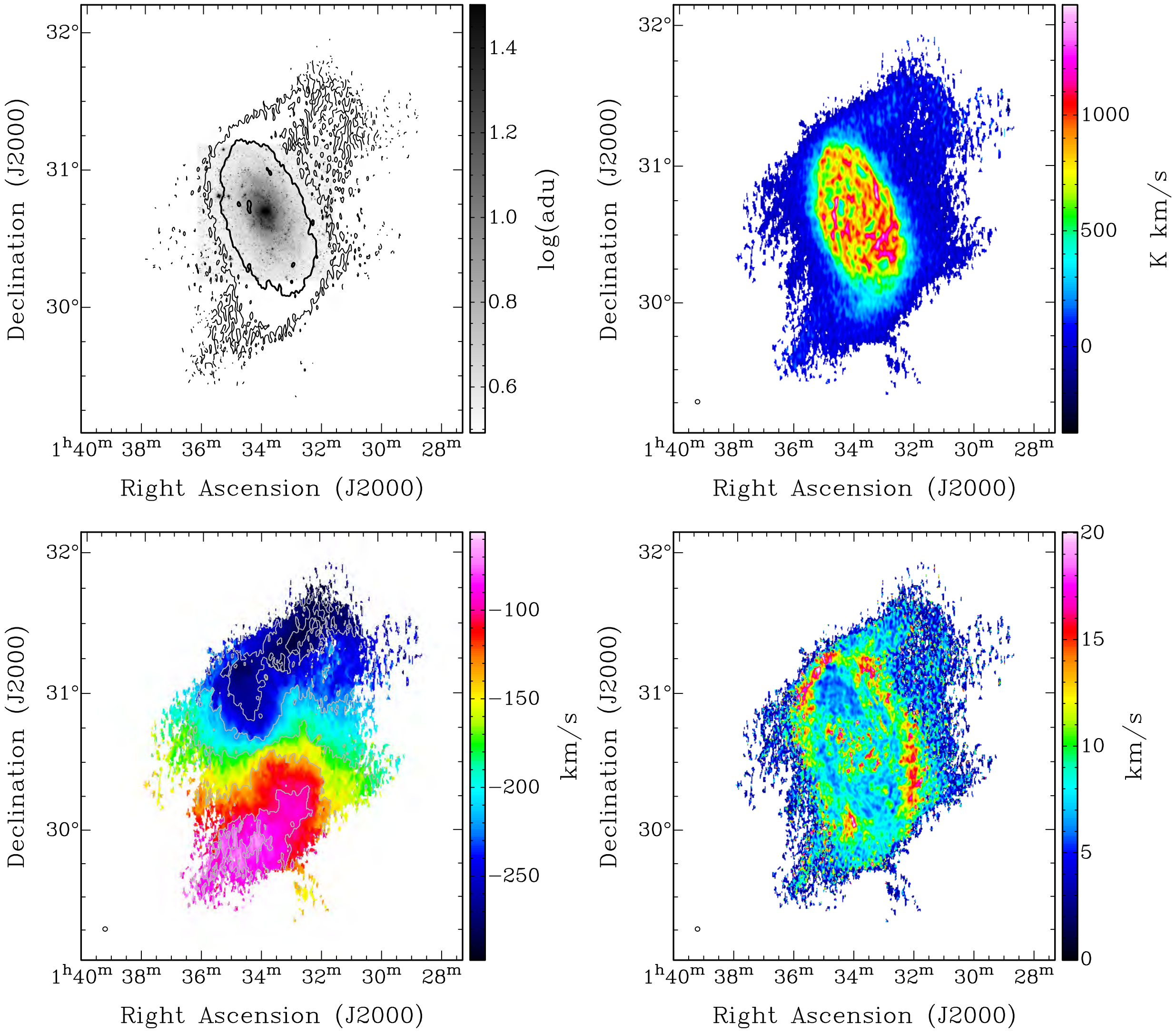

FIGURE 3.9: (top left) Wise w1-band image of M33 with overlaid HI integrated emission contours at 1.2, 3 and 10 K km.s^{-1}. (top-right) Integrated emission map (0-th moment) (bottom-left) HI velocity field (1-st moment). The grey contours are for -280, -260, -220, -180, -140, -100, -80 km.s^{-1}. (bottom-right) HI velocity dispersion map (2nd moment). The 2′ size of the synthesized beam is shown at the bottom left of the moment maps.

This cloud can be seen in green-yellow at the bottom right corner of the velocity field image of Figure 3.9. Only the features having a good agreement with the global velocity pattern have been considered. Several smoothing have been tried to see how far the HI disk can be extended. The map at $120'' \times 120''$ resolution was adopted in order to keep a good spatial resolution for the RC. The velocity map was clipped for observed velocities outside the range -290 km.s^{-1} to -60 km.s^{-1}. The bottom cut-off keep us away from galactic emission (see Figure 3.6).

The task ROTCUR in GIPSY has been used to derive the kinematical parameters and the rotation curve. Assuming negligible radial (expansion) velocity, the tilted-ring model fits the expression :

$$V_{obs} = V_{sys} + V_{rot}(R)cos(\theta)sin(i); \tag{3.13}$$

to the HI velocity field, where R and θ are the polar coordinates in the plane of the galaxy and i the inclination. The position angle of the major axis (PA) is defined as the counterclockwise angle in the plane of the sky from the North to the receding side semi-major axis. In a first run, the position of the rotation centre, and of the systemic velocity $\mathrm{V_{sys}}$ were free to vary, using fixed inclination and PA at the optical values (52° and 202°, respectively). We find a systemic velocity of $\mathrm{V_{sys}} \sim -183$ km.s^{-1}, and a centre at $(\alpha, \delta)_{\mathrm{J2000}} = (01h33m50.9s, +30°40'19.8'')$. Since the positional difference with respect to the photometric centre is much less than the beam size, we decided to fix the kinematical centre at the position of the photometric centre. Also, because the inferred systemic velocity is in agreement with the mean value determined from the global profile (section 3.4.2.1), we adopted $\mathrm{V_{sys}} = -180$ km.s^{-1}. A second run allows us to fit the inclination and PA using fixed centre and systemic velocity given by the adopted values. The results for the approaching and receding disk halves are shown in Figure 3.10.

3.4.3.2 Adopted Rotation Curve

3.4.3.2.1 HI rotation curve

The final HI rotation curve is then derived adopting fixed values of the centre, systemic velocity, inclination and PA. The adopted radial profiles of PA and inclination are modelled from the *both sides* solution and are shown by solid lines in Fig 3.10). Figure 3.10 also shows the obtained HI RC curve for the receding, approaching and both sides. The total velocity errors $\Delta\mathrm{V}_{rot}$ are defined by :

$$\Delta V_{rot} = \sqrt{\epsilon^2 + \frac{|V_a - V_r|^2}{4}} \tag{3.14}$$

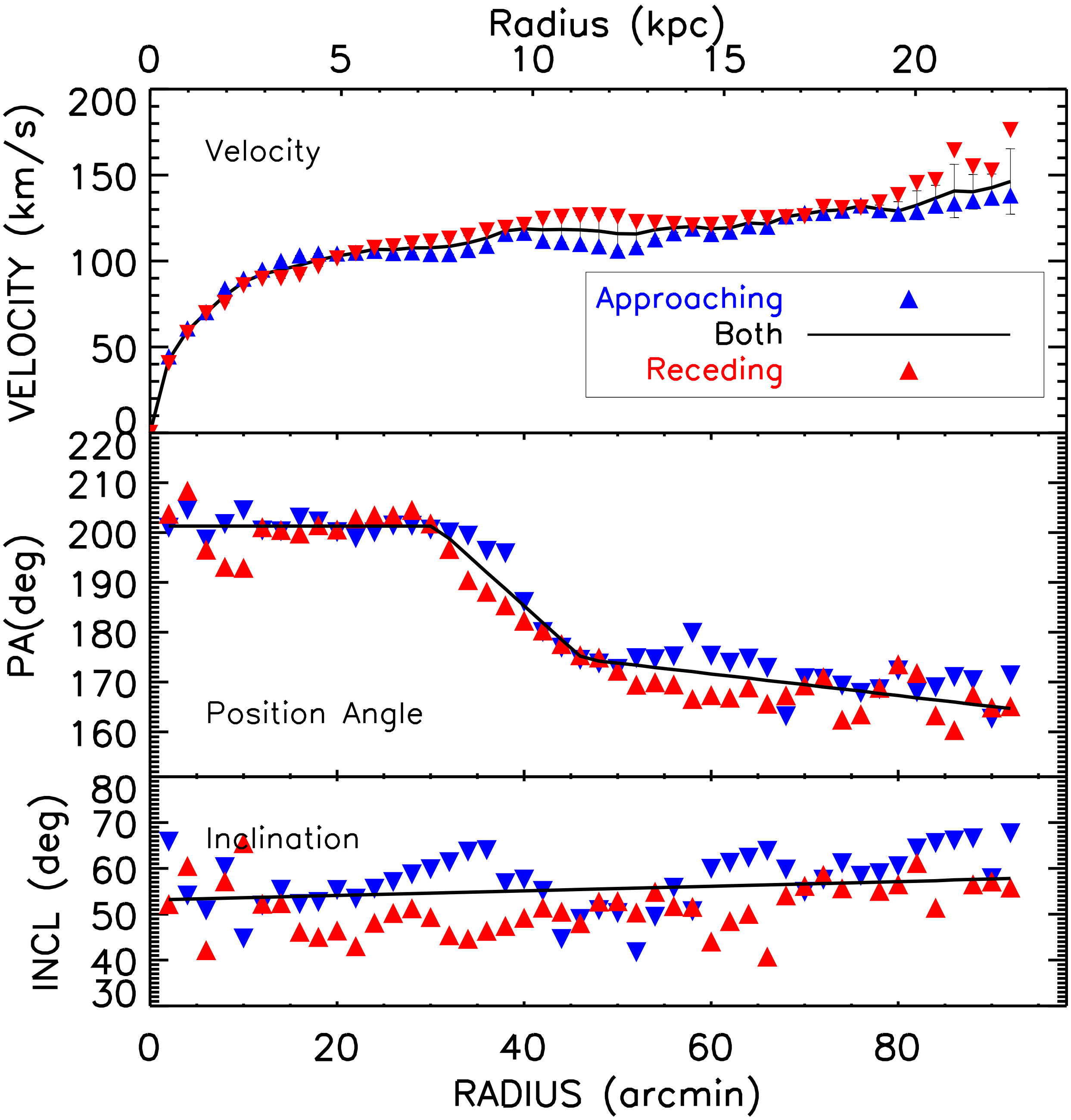

FIGURE 3.10: Determination of the rotation curve, PA and inclination for the HI disk of M33. The top panel gives the rotation velocities, the middle panel the variation of PA and the bottom panel the variation of inclination. The red upward triangles give the results for the receding side and the blue downward triangles for the approaching side. The solid lines give the adopted solutions for both sides.

where, V_a and V_r are the approaching and the receding sides velocities, and ϵ is the formal RMS error of the fits for both sides. The dominant error of the total uncertainty is the systematic difference between the two sides. The approaching and receding sides are in good agreement below ~ 10 kpc and between 14 to 19 kpc. The errors are larger where the warp starts (between 10 and 14 kpc), and increase again beyond R=19 kpc, where the S/N and the number of points in the tilted-rings get lower.

Table 3.5 gives the adopted kinematical parameters and the RC. Column (1) gives the radii. Those radii were chosen to avoid oversampling the data. The smoothed circular beam used is $120'' \times 120''$, then the width used for the sampling is the beam size. Column (2) gives the HI velocities obtained for both sides using the tilted ring model. Column (3) gives the errors on the velocities using equation 3.14. Column (4) presents the position angle defined from the North to the receding side and column (5) presents the inclination at each radius, Columns 6 to 10 are similar to columns 1 to 5.

3.4.3.2.2 Comparison of the adopted RC with the major axis kinematics

Figure 3.11 gives two Position-Velocity (PV) diagrams at PA=202° and at PA = 165°. Since the PA varies by nearly 40° from the optical disk to the outermost warped disk, the positions used are the extreme values of PA used for the RC determination. Figures 3.11 (top) shows the good agreement between the HI (red and blue) and Hα (green) kinematics along the major axis in the inner parts. On the top PV diagram notice the beard-like fainter contours, which suggests the presence of lagging HI in the M33's halo (Fraternali et al., 2001; Oosterloo et al., 2007).

The modelled velocity field and the residual velocity map (defined as the model minus the observation) are presented in Figure 3.12. No systematic velocity asymmetry is found, implying the goodness of the model. The higher residuals are noticed at the boundaries of the optical disc ($\sim \pm 15 - \pm 22$ km.s^{-1}), where the PA changes by ∼20 ° between $10-15$ kpc. Notice that the velocity dispersions (Fig. 3.9) are larger in regions of large residuals.

3.4.3.2.3 Hα kinematics and adopted RC

HI has a poorer spatial resolution in the central regions, where the gradient of the RC is the greatest. Because of this, Hα is a better tracer of the internal kinematics. High resolution Hα Fabry Perot data of M33, obtained at the Observatoire du Mont Mégantic, gives a good description of the kinematics of the central parts (Kam15). Figure 3.11 shows the good agreement

TABLE 3.5: The HI rotation curve of M33.

Rad	V_{rot}	ΔV_{rot}	PA	i	Rad	V_{rot}	ΔV_{rot}	PA	i
(′)	(km/s)	(km/s)	(^{o})	(^{o})	(′)	(km/s)	(km/s)	(^{o})	(^{o})
(1)	(2)	(3)	(4)	(5)	(6)	(7)	(8)	(9)	(10)
2	42.6	2.1	201.3	52.2	48	117.4	9.0	174.2	54.5
4	59.5	1.4	201.3	52.3	50	115.9	9.9	173.8	54.6
6	69.9	0.5	201.3	52.4	52	115.7	7.3	173.4	54.7
08	79.8	4.2	201.3	52.5	54	118.2	4.9	172.9	54.8
10	87.8	2.0	201.3	52.6	56	119.4	2.7	172.5	54.9
12	92.3	2.7	201.3	52.7	58	120.0	1.0	172.1	55.0
14	94.9	5.1	201.3	52.8	60	118.8	2.7	171.6	55.1
16	97.6	5.6	201.3	52.9	62	119.3	2.5	171.2	55.2
18	100.6	3.7	201.3	53.0	64	122.1	2.5	170.8	55.3
20	102.9	1.5	201.3	53.1	66	121.6	2.5	170.3	55.4
22	104.7	0.3	201.3	53.2	68	125.8	0.5	169.9	55.5
24	106.8	0.9	201.3	53.3	70	127.4	1.0	169.5	55.6
26	106.6	2.0	201.3	53.4	72	129.2	1.8	169.0	55.7
28	107.6	2.6	201.3	53.5	74	129.8	0.8	168.6	55.8
30	107.7	3.6	201.3	53.6	76	132.1	0.8	168.2	55.9
32	108.5	4.5	198.8	53.7	78	132.3	7.1	167.7	56.0
34	110.2	3.5	195.4	53.8	80	134.3	5.9	167.3	56.1
36	112.7	3.4	192.0	53.9	82	132.4	7.3	166.8	56.2
38	117.2	1.7	188.7	54.0	84	131.1	6.2	166.4	56.3
40	118.7	2.3	185.3	54.1	86	134.9	5.0	166.0	56.5
42	118.2	6.4	181.9	54.2	88	140.3	10.1	165.5	56.6
44	118.4	7.3	178.5	54.3	90	142.7	7.9	165.1	56.7
46	118.1	8.3	174.2	54.4	92	146.3	19.0	164.7	56.8

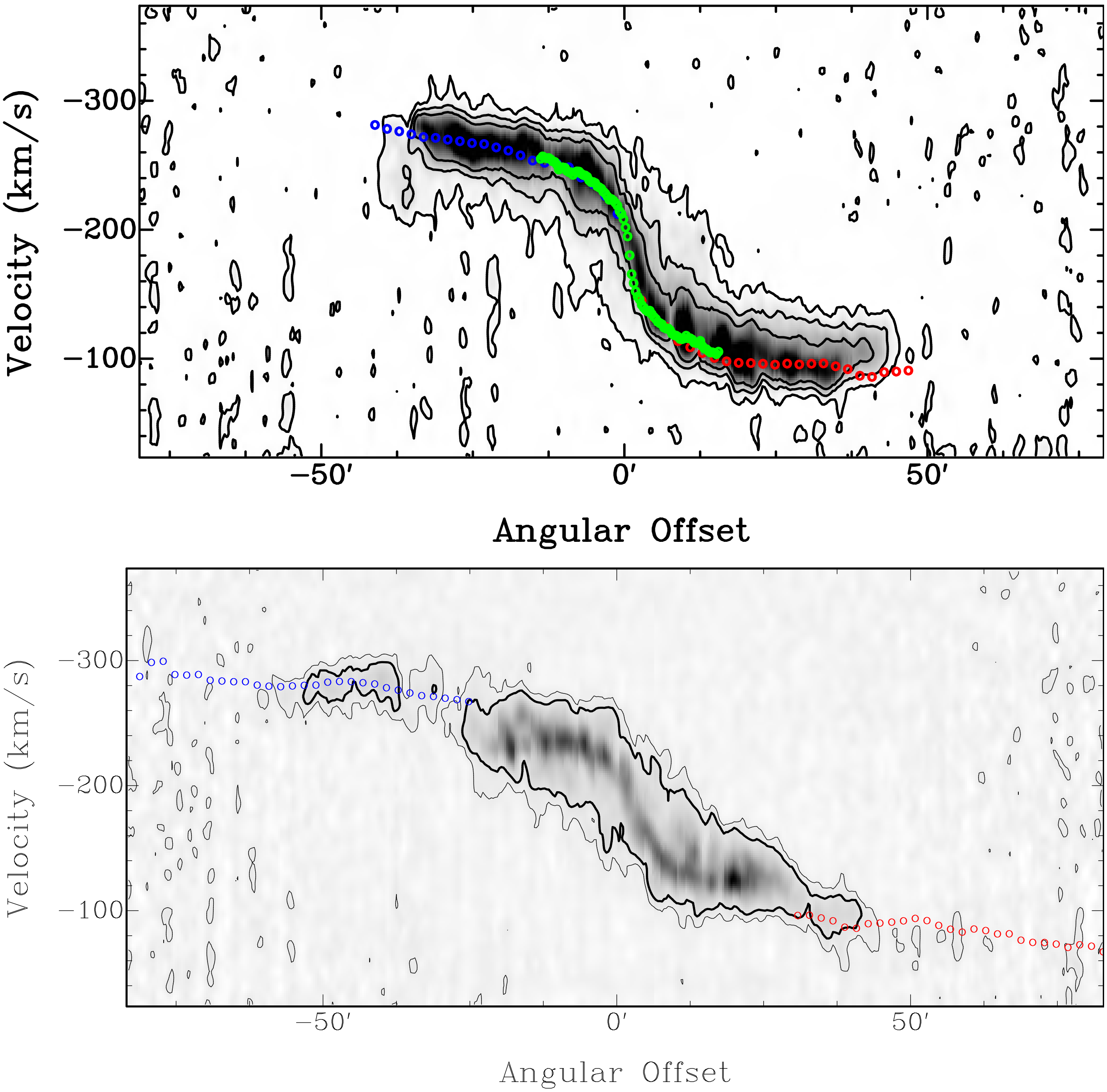

FIGURE 3.11: The top image represents the PV diagram along the major axis at PA=202°. The red and blue squares represent the solutions for the approaching and receding sides and the green ones show the Hα RC (Kam15) at 30″ resolution. The bottom image is at PA=165° without the Hα data and shows the outer warped region.

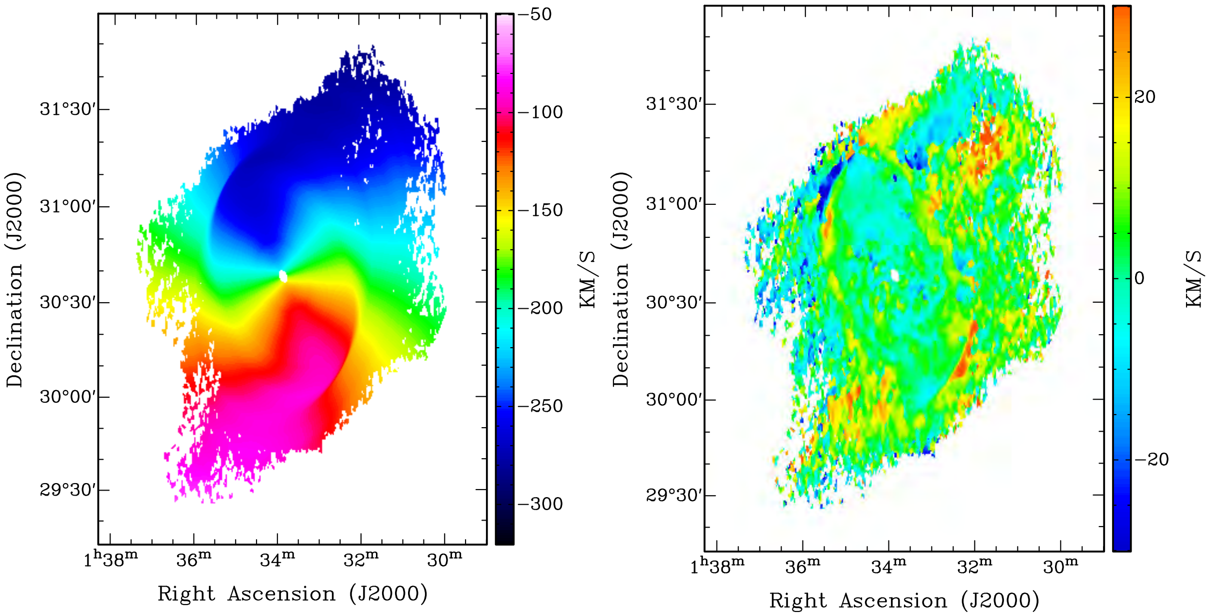

FIGURE 3.12: The left image give the model using the kinematical parameters presented in Figures 3.10, and Table 3.5. The right image is the residual map (model − observations) .

of the Hα RC with the HI data. Taking advantage of the Hα high spatial resolution ($\lesssim 5''$), the outer parts of the HI RC is combined to the Hα RC within 6.5 kpc for the mass models. Figure 3.13 gives the final adopted RC of Messier 33 for the mass modelling. The Hα RC and associated errors have been derived following exactly the same process as for the HI RC. Notice that the average Hα uncertainty for R<6.5 kpc is about twice the average HI uncertainty for $R > 6.5$ kpc. This error inhomogeneity is often seen when combining arcsec resolution Hα data to lower resolution HI data. We have verified that it has no consequences on the mass model results described below.

3.4.4 Mass distribution models of Messier 33

To construct mass distribution models, one needs to take into account, as best as possible, all the mass components. For the stellar component, it is well known that IR data give the best representation of the old disk population, which contributes most of the stellar mass. We use 3.6μm data from *Spitzer*/IRAC. The only uncertainty left is the mass-to-light ratios $\Upsilon_\star$ of the disk and the bulge, which can be constrained using IR colours and population synthesis models. Mass distribution models with fixed and free mass-to-light ratios have thus been performed. Two types of models have been fitted to the hybrid Hα-HI rotation. We have first considered models with dark matter (DM) using three different functional forms for the DM halo : the

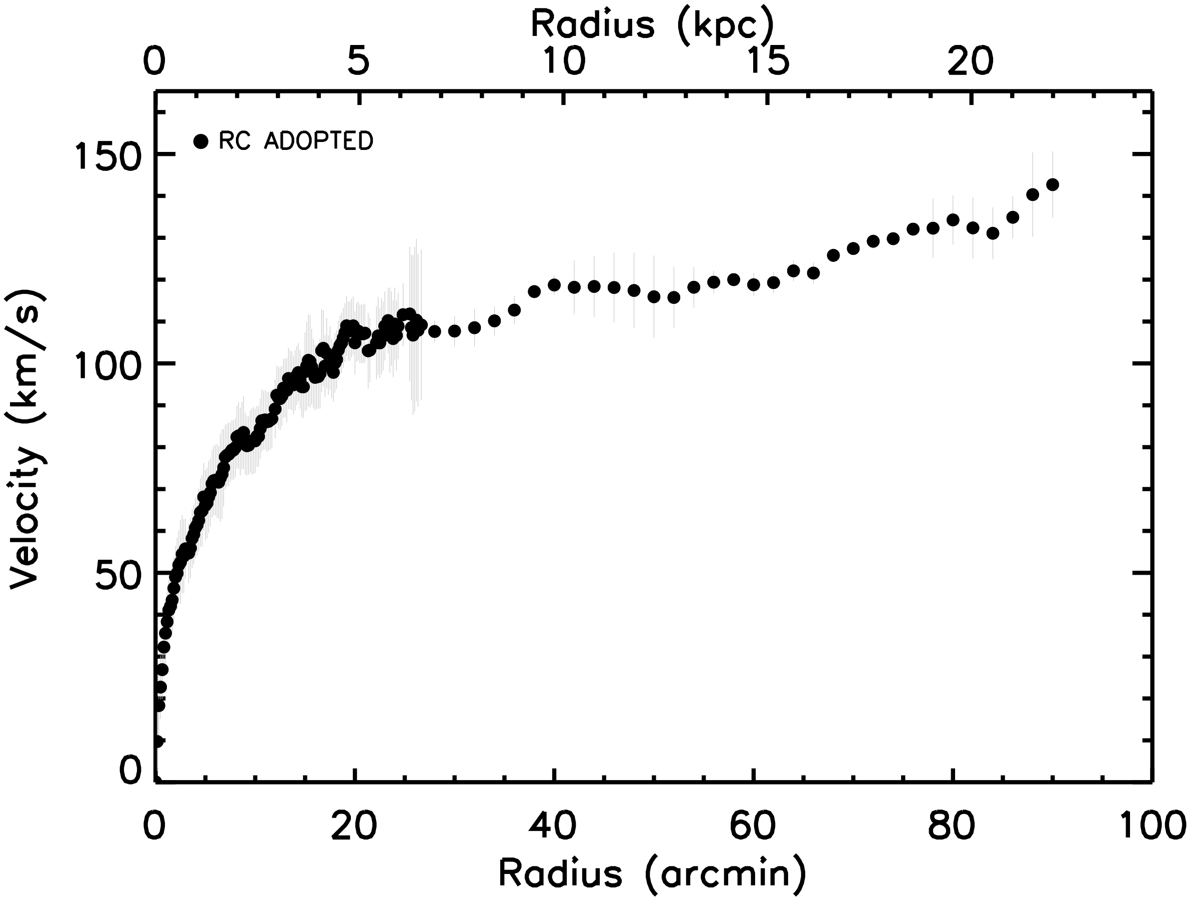

FIGURE 3.13: Final rotation curve of Messier 33 combining Hα velocities from Kam15 for $R < 6.5$ kpc, and our new derived HI rotation curve for the outer parts.

pseudo-isothermal sphere (ISO), the Navarro-Frenk-White (NFW), and the Einasto (EIN) model. We have then performed models using the Modified Newtonian Dynamics (MOND) prescription. A description of those models is given hereafter.

3.4.4.1 Stellar component

Kam15 derived the surface brightness profile of M33 from the 3.6μm data of *Spitzer*/IRAC, where contaminating bright stars have been removed. More complete details on the derivation of the surface brightness profile are given in Kam15. The mass-to-light ratios $\Upsilon_{\rm bulge}$ and $\Upsilon_{\rm disk}$ of the bulge and disk have been estimated from infrared colours and results of population synthesis models given by **?** and de Blok et al. (2008b) :

$$\Sigma[\mathrm{M}_\odot\ \mathrm{pc}^{-2}] = \Upsilon_*^{3.6} \times 10^{-0.4\times(\mu_{3.6}-C^{3.6})} \tag{3.15}$$

where $\Upsilon_*^{3.6}$ is given in the *Spitzer*/IRAC 3.6μm band, $\mu_{3.6}$ is the surface brightness and $C^{3.6} = 24.8$ is a correction value, as given in **?**. Using the $J-K$ colour index from Jarrett et al. (2003), Kam15 derived $\Upsilon_{\mathrm{bulge}} = 0.80$ and $\Upsilon_{\mathrm{disk}} = 0.72$.

An exponential profile has been fitted to the 3.6μm band surface density profile of the disk component using the equation :

$$\mu(R) = \mu_0 + 1.10857\,\frac{R}{h} \tag{3.16}$$

where h defines the disk scale length and μ_0 the disk central surface brightness. The bulge component is described by a Sersic law :

$$\mu_(R) = \mu_e + 2.5\,b_n \left[\left(\frac{R}{R_e}\right)^{1/n} + 1\right] \tag{3.17}$$

where b_n is defined as $b_n = 1.9992n - 0.3271$ for $0.5 < n < 10$ (Capaccioli, 1989) and μ_e the equivalent surface brightness of the bulge. The parameters found by Kam15 for the stellar components are : $h = 1.8$ kpc, $\mu_0 = 18.0$ mag.arcsec^{-2} for the disk and $n = 1.2$, $R_e = 0.40$ kpc and $\mu_e = 20.8$ mag.arcsec^{-2} for the bulge. With a bulge-to-disk ratio of 0.04, large differences are not expected between pure disk and bulge+disk models, as found in Kam15 from a modelling of the Hα rotation curve in the inner $R = 8$ kpc. A $\mathrm{sech}^2(\mathrm{z}/\mathrm{z}_0)$ law has been adopted for the vertical density distribution of the stellar disk, with a scale-height of ~ 400 pc (∼20% of the disk scale length). The velocity contributions have been derived with the task ROTMOD from the GIPSY package (van der Hulst et al., 1992).

3.4.4.2 Atomic and molecular gas components

The contribution from the neutral gas comes from our deep DRAO+Arecibo dataset. The surface densities from Fig. 3.6, which were multiplied by a factor of ∼1.3 to take into account the contribution from Helium, have been used to infer the velocity contribution of the atomic gas disk. The molecular gas contribution, traced by the CO line, is mainly concentrated in the innermost kpcs. Molecular gas in M33 has been observed by Tosaki et al. (2011) with the Nobeyama Radio Observatory at 19″ resolution, and by Gratier et al. (2010) and Druard et al. (2014) with the IRAM 30-m dish at a resolution of $\sim 15''$. Tosaki et al. (2011) report that the HI peaks and CO are not always correlated and that the density of the atomic gas is higher than that of the molecular gas in the inner parts, while Gratier et al. (2010) showed that the molecular gas density is higher than HI. Using a conversion factor of $\mathrm{N(H_2)/I_{CO(1\rightarrow 0)}} = 4\times10^{20}\mathrm{cm}^{-2}$/(K km.s^{-1}), twice the value found for the Milky Way (M33 as half the solar metallicity), they measured an average density of $\Sigma_{H_2} = 8.5 \pm 0.2$ M$_\odot$ pc^{-2} for the central kpc, and a total molecular gas mass of $\sim 3.3 \times 10^8$ M$_\odot$ for the entire M33 disk. We used the H$_2$ density profile of Druard et al. (2014), scaled by a factor of ~ 1.3 to infer the velocity contribution of the total molecular gas component.

3.4.4.3 Dark Matter mass models

The rotation velocities are defined as :

$$V_{rot}^2 = V_\star^2 + V_{\mathrm{gas}}^2 + V_{DM}^2 \tag{3.18}$$

where $V_\star^2 = V_{\mathrm{bulge}}^2 + V_{\mathrm{disk}}^2$ is the velocity contribution from the total stellar component, $V_{\mathrm{gas}}^2 = V_{\mathrm{atom}}^2 + V_{\mathrm{molec}}^2$ is the one from the total gaseous component, and V_{DM} the contribution from the DM mass component.

The ISO and NFW models are the most commonly DM halo profiles used (e.g. de Blok & Bosma, 2002), while it is only recently that the EIN model has been shown to be a good description of the DM mass (Chemin et al., 2011) in disk galaxies.

3.4.4.3.1 The pseudo-isothermal sphere model

The pseudo-isothermal dark matter halo is a core-dominated type of halo, as the density remains constant in the centre. The density profile is given by :

$$\rho_{\mathrm{ISO}}(\mathrm{R}) = \frac{\rho_0}{1+(\frac{\mathrm{R}}{\mathrm{R_c}})^2} \tag{3.19}$$

where ρ_0 is the central density and R_c the core radius of the halo. The corresponding circular velocity is :

$$\mathrm{V_{ISO}(R)} = \sqrt{4\pi\ \mathrm{G}\ \rho_0\ \mathrm{R_c^2}(1-\frac{\mathrm{R}}{\mathrm{R_c}}\ \arctan(\frac{\mathrm{R}}{\mathrm{R_c}}))} \tag{3.20}$$

3.4.4.3.2 The Navarro-Frenk-White model

The NFW model – the so-called 'universal halo' – is deduced from Cold Dark Matter simulations (Navarro et al., 1997). The density profile is cuspy, following a $\rho \propto R^{-1}$ law in the center, and is given by :

$$\rho_{NFW}(R) = \frac{\rho_i}{\frac{R}{R_s}(1+\frac{R}{R_s})^2} \tag{3.21}$$

where $\rho_i \approx 3H_0^2/(8\pi G)$ is the critical density for closure of the Universe and R_S is a scale radius. The velocity contribution corresponding to this halo is given by :

$$\mathrm{V_{NFW}(R) = V_{200}\sqrt{\frac{\ln(1+cx) - cx/(1+cx)}{x(\ln(1+c) - c/(1+c))]}}} \tag{3.22}$$

where $\mathrm{V_{200}}$ is the velocity at the virial radius $\mathrm{R_{200}}$, $\mathrm{c = R_{200}/R_s}$ gives the concentration parameter of the halo and x is $\mathrm{R/R_s}$. The relation between $\mathrm{V_{200}}$ and $\mathrm{R_{200}}$ is $V_{200} = 0.01.H_0.R_{200}$, where we used $\mathrm{H_0} = 72$ km.s$^{-1}\mathrm{Mpc}^{-1}$ for the Hubble constant (Hinshaw et al., 2009).

3.4.4.3.3 The Einasto model

Chemin et al. (2011) analyzed a large sample of nearby disk galaxies and found that the EIN model is a good candidate for being a standard DM halo. The EIN model also comes from cosmological simulations (e.g. Navarro et al., 2004), and its mass density is given by :

$$\rho_{\mathrm{EIN}}(\mathrm{R}) = \rho_{-2}\exp\left(\mathrm{f(n)}\left[\left(\frac{\mathrm{R}}{\mathrm{R_{-2}}}\right)^{\frac{1}{\mathrm{n}}} - 1\right]\right), \tag{3.23}$$

Here, n is the Einasto index that shapes the density profile, $f(n) = -2n$ ($n > 0$), R_{-2} is the radius where the density slope $\alpha = -2(R/R_{-2})^{1/n}$ is -2, and ρ_{-2} is the characteristic density at this radius. The differences with the ISO or NFW models are thus that the density decreases exponentially, and that α decreases continuously with radius, while the slopes of the two other models are constant at small and large radii. The velocity contribution of the EIN halo is then :

$$\mathrm{V_{EIN}(R) = R^{-1/2}\sqrt{4\pi G n R_{-2}^3 \rho_{-2}\ e^{2n}\ (2n)^{-3n}\gamma\,(3n, y)}} \tag{3.24}$$

where $\gamma(3\mathrm{n}, \mathrm{y}) = \int_0^{\mathrm{y}} \mathrm{e^{-t}t^{3n-1}}\ \mathrm{dt}$ is the incomplete gamma function and $y = -\alpha$. The inner slope of the density profile depends on both the scale radius R_{-2} and the index. Disks with $R_{-2} \propto 10$ kpc have central cusps when $n \sim 5-7$, as seen in cosmological simulations (Navarro et al., 2004), and shallower density profiles when $n \sim 1$, as found by Chemin et al. (2011) from a modelling of rotation curves using the same stellar population synthesis model as the one we use here. We have thus fitted EIN models at free index, as well as constrained models at fixed index $n = 1.4$ (the average value from Chemin et al. (2011)) and $n = 6$.

TABLE 3.6: Results of the DM models.

Disk-only		Best-fit	Colour $\Upsilon_\star^{3.6}$	**Bulge+disk**		Bestf-fit	Colour $\Upsilon_\star^{3.6}$
Halo model				Halo model			
ISO	ρ_0	5.0 ± 0.2	7.8 ± 0.3	ISO	ρ_0	5.0 ± 0.2	8.7 ± 0.4
	R_c	12.0 ± 0.5	8.3 ± 0.3		R_c	12.3 ± 0.6	8.1 ± 0.3
	Υ_d	0.86 ± 0.01	0.72		Υ_d	0.87 ± 0.02	0.72
	Υ_b	–	–		Υ_b	0.98 ± 0.10	0.80
	χ^2_r	0.30	0.55		χ^2_r	0.33	0.65
NFW	V_{200}	525 ± 300	598 ± 308	NFW	V_{200}	339 ± 88	556 ± 249
	c	0.63 ± 0.60	0.52 ± 0.50		c	1.40 ± 0.3	0.61 ± 0.5
	Υ_d	0.66 ± 0.02	0.72		Υ_d	0.65 ± 0.02	0.72
	Υ_b	–	–		Υ_b	0.88 ± 0.10	0.80
	χ^2_r	0.27	0.34		χ^2_r	0.31	0.34
EIN	ρ_{-2}	0.56 ± 0.03	0.83 ± 0.04	EIN	ρ_{-2}	0.54 ± 0.03	0.89 ± 0.04
$n = 1.4$	R_{-2}	35 ± 2	24 ± 1	$n = 1.4$	R_{-2}	37 ± 2.40	23 ± 1
	Υ_d	0.83 ± 0.01	0.72		Υ_d	0.86 ± 0.01	0.72
	Υ_b	–	–		Υ_b	1.04 ± 0.10	0.80
	χ^2_r	0.29	0.45		χ^2_r	0.33	0.60
EIN	ρ_{-2}	0.003 ± 0.001	0.006 ± 0.001	EIN	ρ_{-2}	0.003 ± 0.001	0.008 ± 0.001
$n = 6$	R_{-2}	1413 ± 345	758 ± 83	$n = 6$	R_{-2}	1409 ± 386	591 ± 66
	Υ_d	0.77 ± 0.02	0.72		Υ_d	0.79 ± 0.02	0.72
	Υ_b	–	–		Υ_b	1.05 ± 0.10	0.80
	χ^2_r	0.29	0.30		χ^2_r	0.32	0.36
EIN	ρ_{-2}	0.23 ± 0.37	0.002 ± 0.005	EIN	ρ_{-2}	0.02 ± 0.23	0.001 ± 0.005
free index	R_{-2}	66 ± 77	1756 ± 3657	free index	R_{-2}	341 ± 2330	1819 ± 4282
	n	2.2 ± 1.4	7.1 ± 2.7		n	4.2 ± 8.7	7.66 ± 3.03
	Υ_d	0.81 ± 0.03	0.72		Υ_d	0.80 ± 0.10	0.72
	Υ_b	–	–		Υ_b	1.06 ± 0.10	0.80
	χ^2_r	0.28	0.30		χ^2_r	0.32	0.35

Comments : Mass-to-light ratios $\Upsilon_\star^{3.6}$ are fixed by stellar population synthesis models, in $M_\odot/L_\odot$; ρ_0 and ρ_{-2} are in 10^{-3} $M_\odot$ pc^{-3}, R_c and R_{-2} in kpc and V_{200} in km.s^{-1}.

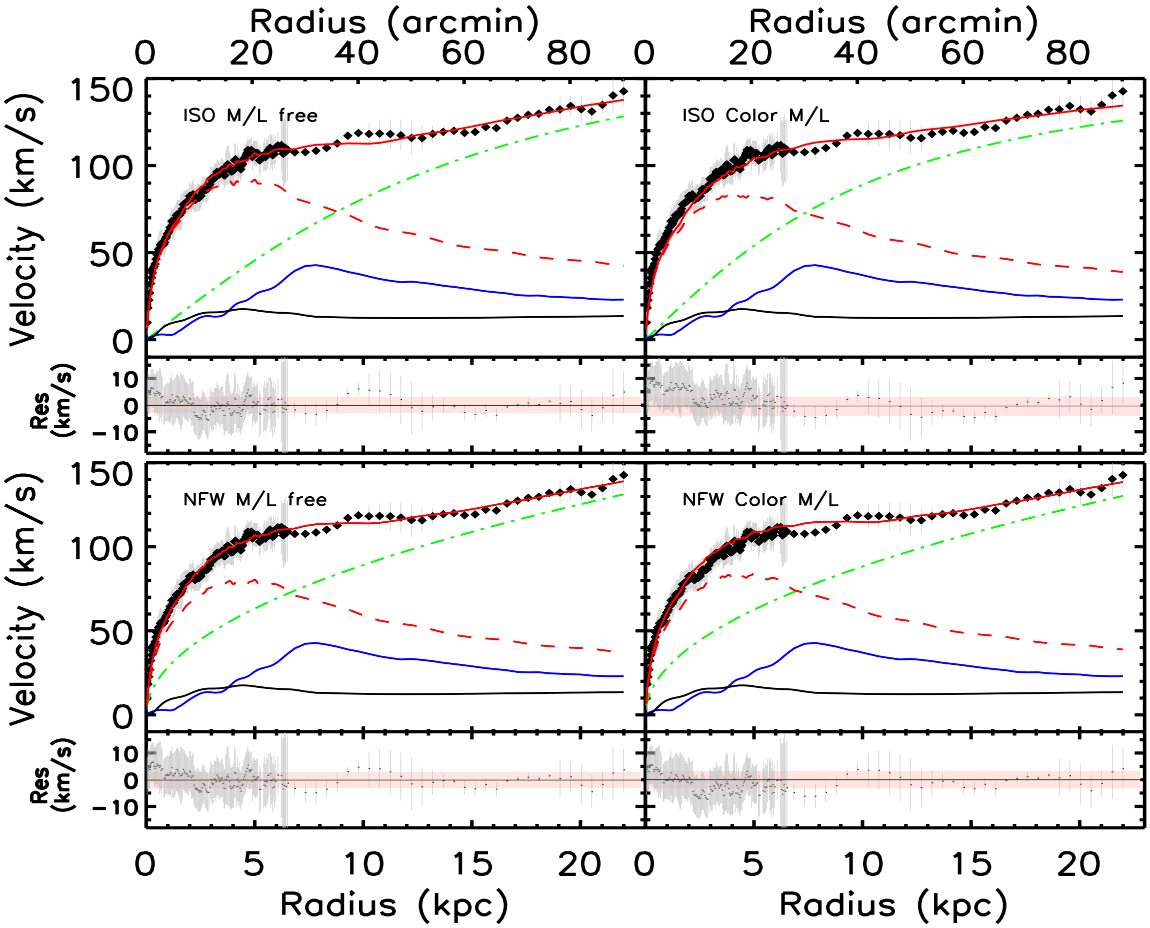

FIGURE 3.14: Pure disk ISO (top) and NFW (bottom) mass models. The panels on the left give the best-fit models and those on the right the models with a fixed mass-to-light ratio, derived from IR colours and population synthesis models. The filled diamonds with error bars represent the RC, The stellar disc contribution is in broken red, the HI contribution in blue, the H_2 contribution in black, the halo contribution in broken green and the sum of the three components is shown as a continuous red line. At the bottom of each model, the mean residuals (observations − model) are represented by a black line with the same error bars as the velocity errors of the top panels. The part coloured in pink gives the dispersion of the residuals around the black regression line.

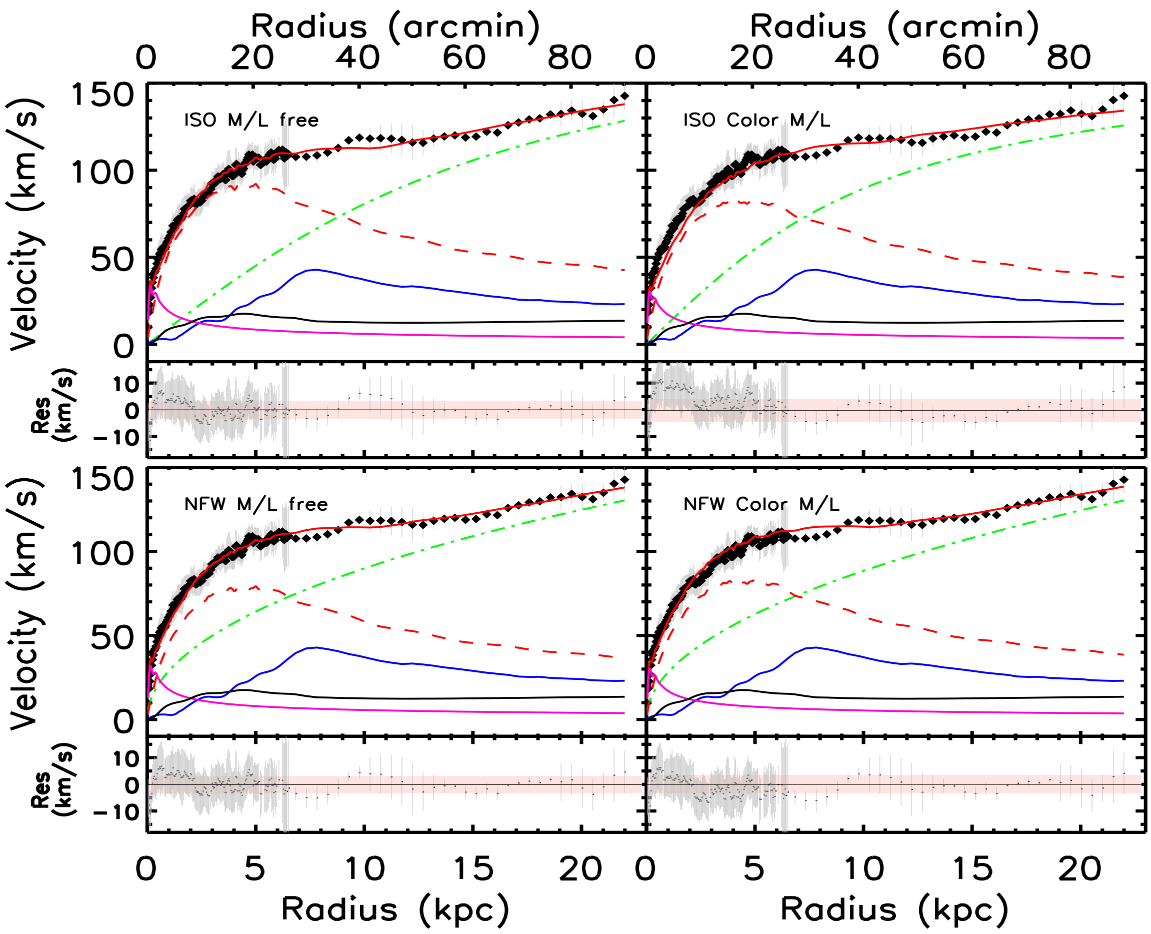

FIGURE 3.15: Same as Fig.3.14 but with the contribution of the bulge presented in magenta..

3.4.4.4 Modified Newtonian Dynamics mass models

An alternative to dark matter to explain the missing mass problem is MOdified Newtonian Dynamics (Milgrom, 1983a,b). MOND has been successful to reproduce correctly galaxy rotation curves (e.g. Sanders & Verheijen, 1998; Gentile et al., 2010). It postulates that in regimes of acceleration much smaller than a universal, constant acceleration a_0, the classical Newtonian dynamics is no more valid, and the law of gravity is modified.

In the MOND framework, the gravitational acceleration of a test particle is given by :

$$\mu(x = g/a_0)g = g_N \tag{3.25}$$

where g is the gravitational acceleration, g_N the Newtonian acceleration and $\mu(x)$ is an interpolating function that must satisfy :

$$\mu(\mathrm{x}) = \begin{cases} 1 & \text{if } x \gg 1 \\ x & \text{if } x \ll 1 \end{cases}$$

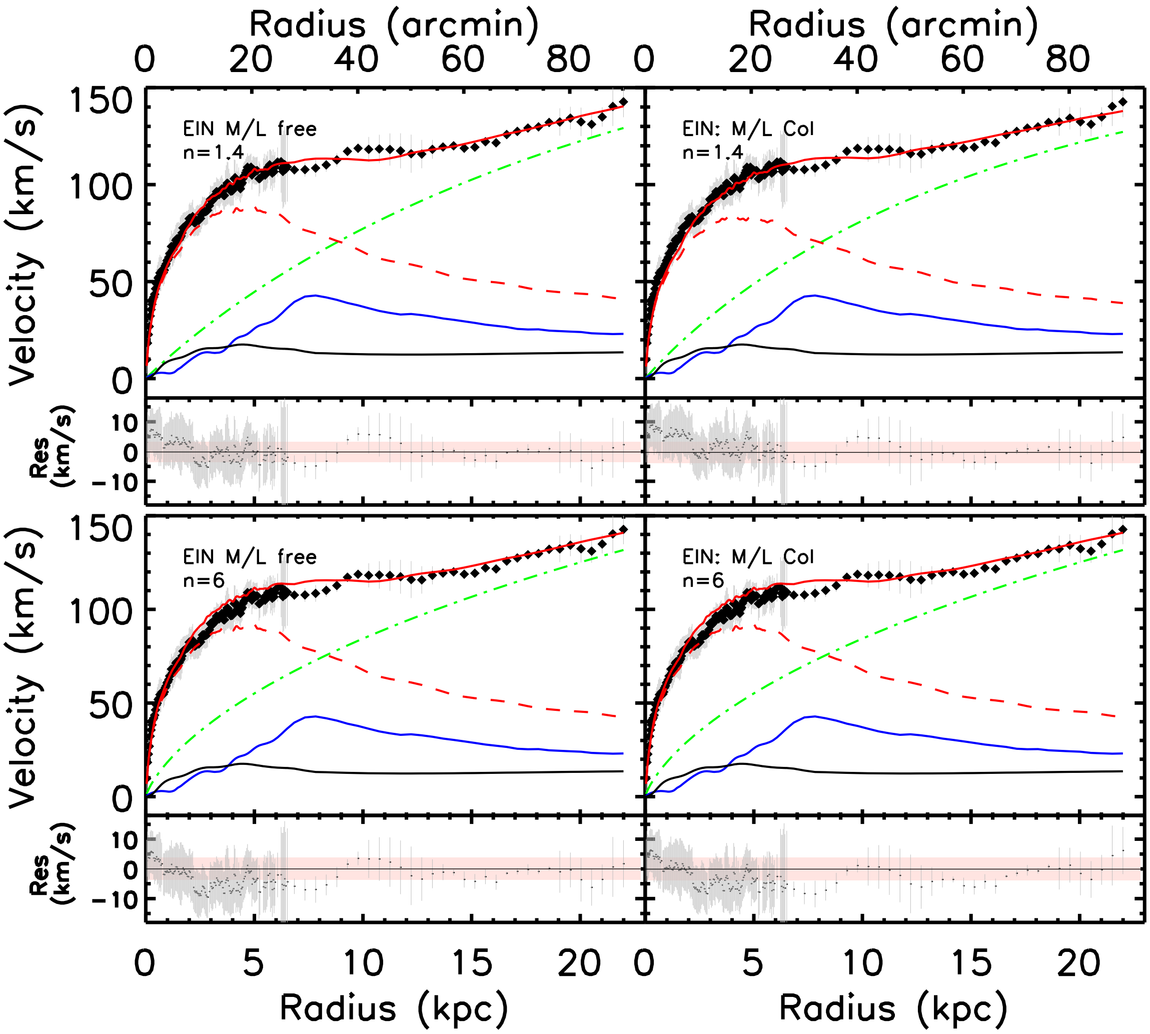

FIGURE 3.16: Pure disk EIN mass models with n=1.4 (top) and n=6 (bottom). The panels on the left give the best-fit models and those on the right the models with a fixed mass-to-light ratio, derived from IR colors and population synthesis models. The colour codes are the same as in Fig.3.14.

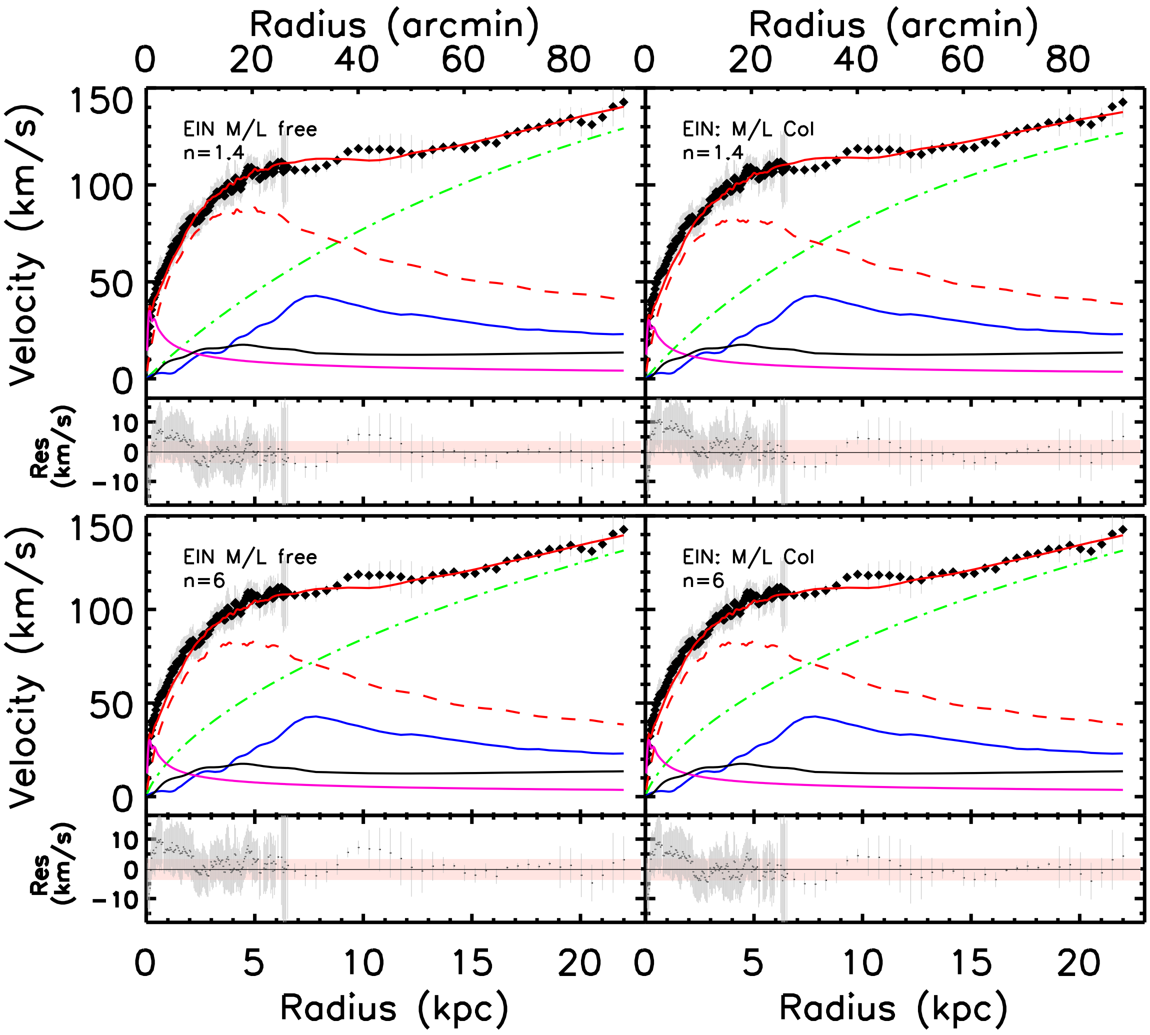

FIGURE 3.17: Same as Fig.3.16 but with the contribution of the bulge presented in magenta..

The shape of the predicted MOND RCs depends on the shape of $\mu(x)$. The 'standard' μ-function proposed by Milgrom (1983a) is :

$$\mu(x) = \frac{x}{(1+x^n)^{1/n}} \tag{3.26}$$

with $n = 2$. Using that form, the total velocity is written as :

$$V_{rot}^2 = \frac{V_{lum}^2}{\sqrt{2}} \sqrt{1 + \sqrt{(2\, R\, a_0/V_{lum}^2)^2}} \tag{3.27}$$

with $V_{lum}^2 = V_\star^2 + V_{\rm gas}^2$, $V_\star$ and $V_{\rm gas}$ being as in Eq. 3.18.

Famaey & Binney (2005) found that the 'simple' interpolation function with $n = 1$ yields a better fit to the rotation curve of the Milky Way than $n = 2$. That 'simple' form is also appropriate to other galaxy rotation curves (see Famaey & McGaugh, 2012, and references therein). Here, the total velocity is obtained by :

$$V_{rot}^2 = V_{lum}\sqrt{a_0 R + V_{lum}^2} \tag{3.28}$$

3.4.4.5 Results of the mass models

Least-square fits to the rotation curve have been performed, using a normal weighting function set to the inverse of the squared velocity uncertainties. For each mass model, we have considered a pure disk case (without bulge) and a disk+bulge case for the stellar contribution. The mass-to-light ratio of the bulge and disk are either fixed at the value inferred by the color indices and stellar population models ('color $\Upsilon_\star^{3.6}$'), or left free ('best-fit'). The fits for the ISO, NFW and constrained EIN ($n = 1.4$ and $n = 6$) models have thus 2 to 4 free parameters, while the fits of the unconstrained EIN have the index n as additional free parameter. For MOND, fits have been performed with a_0 left fixed or free, yielding 1 to 3 free parameters. The 'simple' and 'standard' interpolation functions have been tested. Tables 3.6 and 3.7 give the fitted parameters for DM and MOND models, respectively, and Figures 3.14 to 3.21 show the resulting mass models. The results for the EIN model at free index are not shown, but only reported in Tab. 3.6. The fits are excellent ($\chi_r^2 < 1$) for dark matter halo models, while they are of very poor quality for MOND ($\chi_r^2 >> 1$). The detailed analysis of the mass modelling results is done in Section 3.4.5.

3.4.5 Discussion

3.4.5.1 Distribution and kinematics of the neutral hydrogen gas

Our combined DRAO and Arecibo HI distribution is in very good agreement with recent HI maps of Messier 33, such as the VLA-GBT mosaic of Corbelli et al. (2014). While HI is detected at $R > 90'$, most of the HI is within the optical radius of 35′, which is the region where the disk is more regular, showing many prominent spiral arms. A strong warp starts beyond 35′. The irregular gaseous tails observed to the North-East and South-West of the disk are part of that warp. A numerical modelling of these outer features shows that gas is likely being accreted in the disk (Putman et al., 2009). Our mosaic reaches sensitivities down to $\sim 5 \times 10^{18}$ cm^{-2} in the warped disk regions, which is much lower than in the inner disk.

At that level, a slice along the major axis seem to point out some lagging HI (see the example of NGC 2403 Fraternali et al., 2001), which suggests the presence of "anomalous" extraplanar gas

TABLE 3.7: Results of the MOND models

Disk-only case MOND model		Best-fit	Colour $\Upsilon_\star^{3.6}$	**Bulge+disk case** MOND model		Bestf-fit	Colour $\Upsilon_\star^{3.6}$
Stand'ard	a_0	1.21	1.21	Standard	a_0	1.21	1.21
fixed a_0	Υ_d	0.68 ± 0.03	0.72	fixed a_0	Υ_d	0.88 ± 0.02	0.72
	Υ_b	–	–		Υ_b	0.42 ± 0.37	0.80
	χ_r^2	24.41	25.00		χ_r^2	5.92	7.53
Standard	a_0	3.24 ± 0.21	1.27 ± 0.05	Standard	a_0	3.46 ± 0.21	1.50 ± 0.05
free a_0	Υ_d	0.19 ± 0.02	0.72	free a_0	Υ_d	0.16 ± 0.02	0.72
	Υ_b	–	–		Υ_b	0.87 ± 0.24	0.80
	χ_r^2	7.65	24.11		χ_r^2	2.68	4.71
Simple	a_0	1.21	1.21	Simple	a_0	1.21	1.21
fixed a_0	Υ_d	0.61 ± 0.02	0.72	fixed a_0	Υ_d	0.32 ± 0.30	0.72
	Υ_b	–	–		Υ_b	0.81 ± 0.02	0.80
	χ_r^2	30.40	35.40		χ_r^2	7.41	8.13
Simple	a_0	3.31 ± 0.20	1.17 ± 0.06	Simple	a_0	3.56 ± 0.20	1.46 ± 0.03
free a_0	Υ_d	0.18 ± 0.02	0.72	free a_0	Υ_d	0.15 ± 0.02	0.72
	Υ_b	–	–		Υ_b	0.78 ± 0.21	0.80
	χ_r^2	7.90	35.72		χ_r^2	2.77	6.07

Comment : a_0 is given in units of 10^{-8} cm.s^{-2}. Standard is the model with the standard interpolation function (Eq. 3.27), Simple is the model with the simple interpolation function (Eq. 3.28).

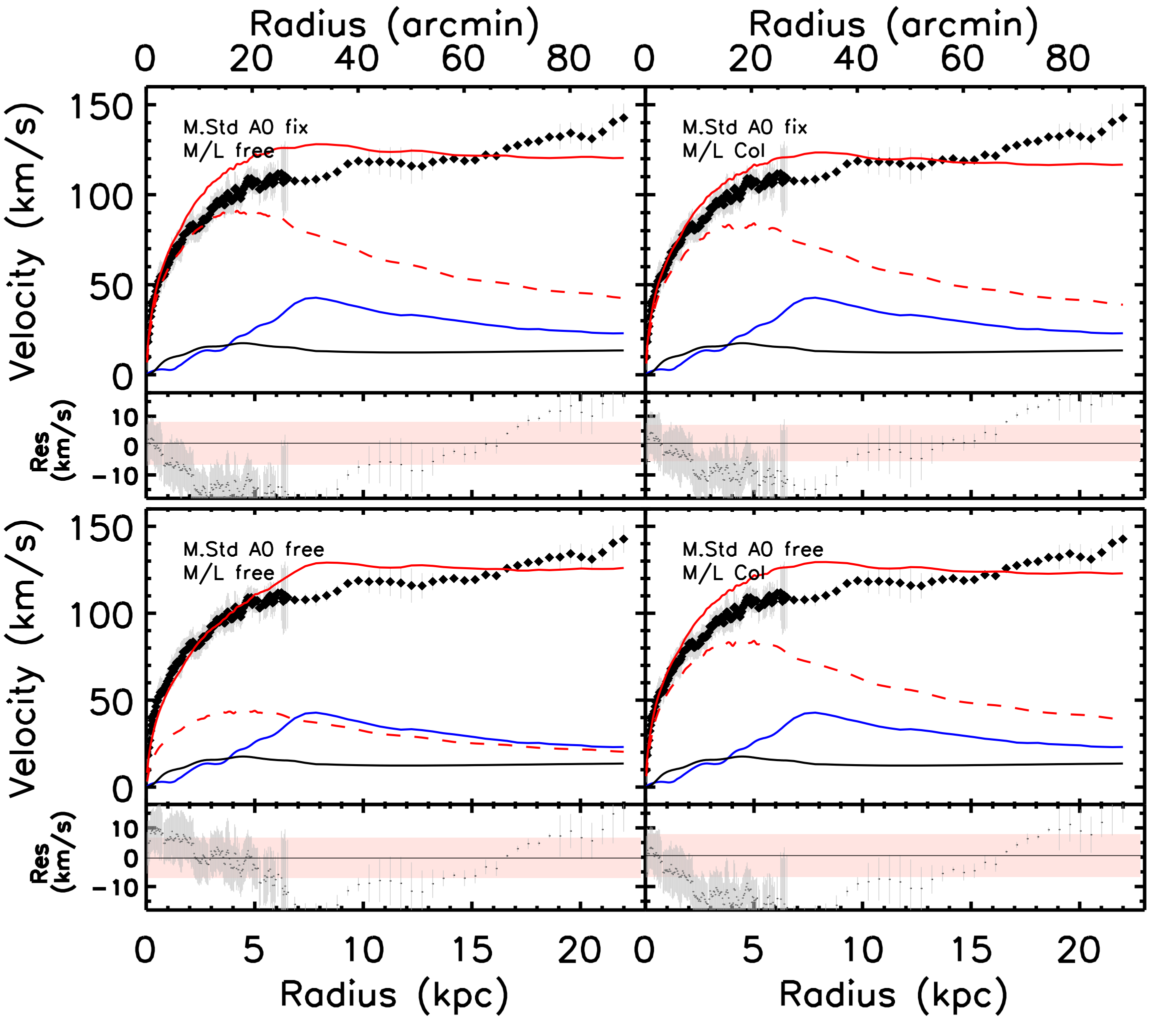

FIGURE 3.18: Pure disk MOND models with the standard interpolation function. The colour codes are the same as in Fig.3.14.

that, due to the 52° inclination of the disk, can just be noticed kinematically since spatially it is superposed to the disk along our line-of-sight. This gas is apparent in the lowest contours of the cut shown in (Figure 3.11). Especially for the receding half of the galaxy, the PV diagram clearly highlights the presence of an anomalous HI component spanning a range of radial velocities that is offset from the high-intensity emission of the main disk, towards the systemic velocity of the system.

We find a total HI mass of $1.95 \pm 0.36 \times 10^9$ $M_\odot$, in agreement with Corbelli (2003), Putman et al. (2009) or Corbelli et al. (2014). Compared with the molecular gas mass of $\sim 3.3 \times 10^8$ $M_\odot$ (Gratier et al., 2010), the total neutral gas mass is thus about six times larger than the molecular content (would be larger if the MW conversion factor was used). Naturally, H_2 is much more

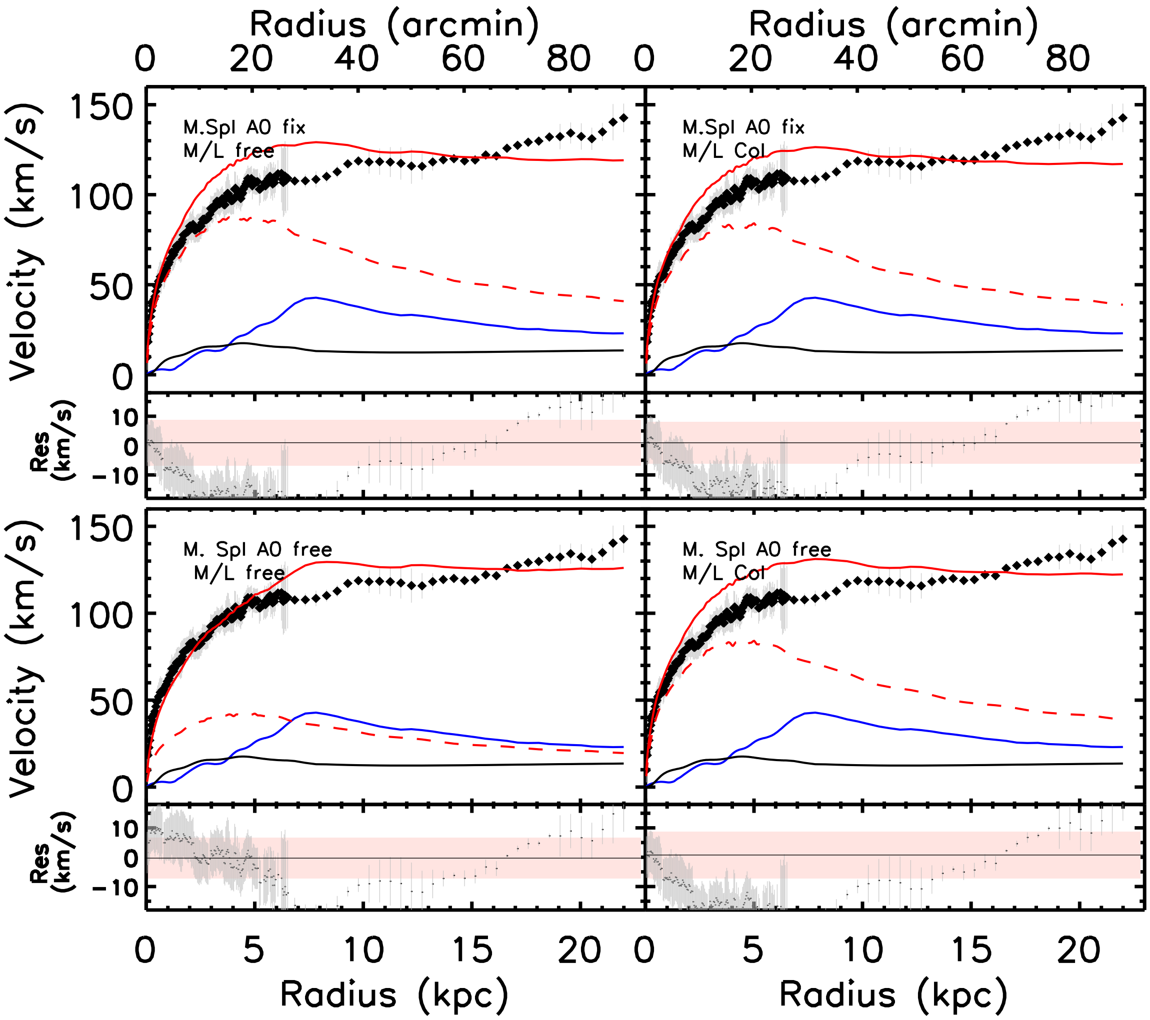

FIGURE 3.19: Pure disk MOND models with the simple interpolation function.

concentrated in the centre than the HI, both reaching central surface densities ~10 $M_\odot$ pc^{-2}.

The warp of Messier 33 is clearly seen in the tilted-ring model of the HI velocity field, that shows a variation of the position angle from ∼ 202° to ∼ 165°. The variation of the inclination seems less spectacular, as it smoothly increases by about 5° from the centre to the disk outskirts. The physical geometry of the HI disk, implied by our model, is confirmed by the presence of double peaks in the HI datacube (see also Chemin et al., 2012). Here, we naturally expect the gas orbits crossing the line-of-sight twice, or more. The other effect is the observed increase of the velocity dispersion in the transition region. It is thought that the HI warp is likely due to an interaction with the nearby massive companion, the Andromeda galaxy (e.g. Putman et al., 2009). M33 is also surrounded by a prominent stellar structure that provides additional evidence of the encounter with M31 (McConnachie et al., 2009), or at least of recent gravitational interaction.

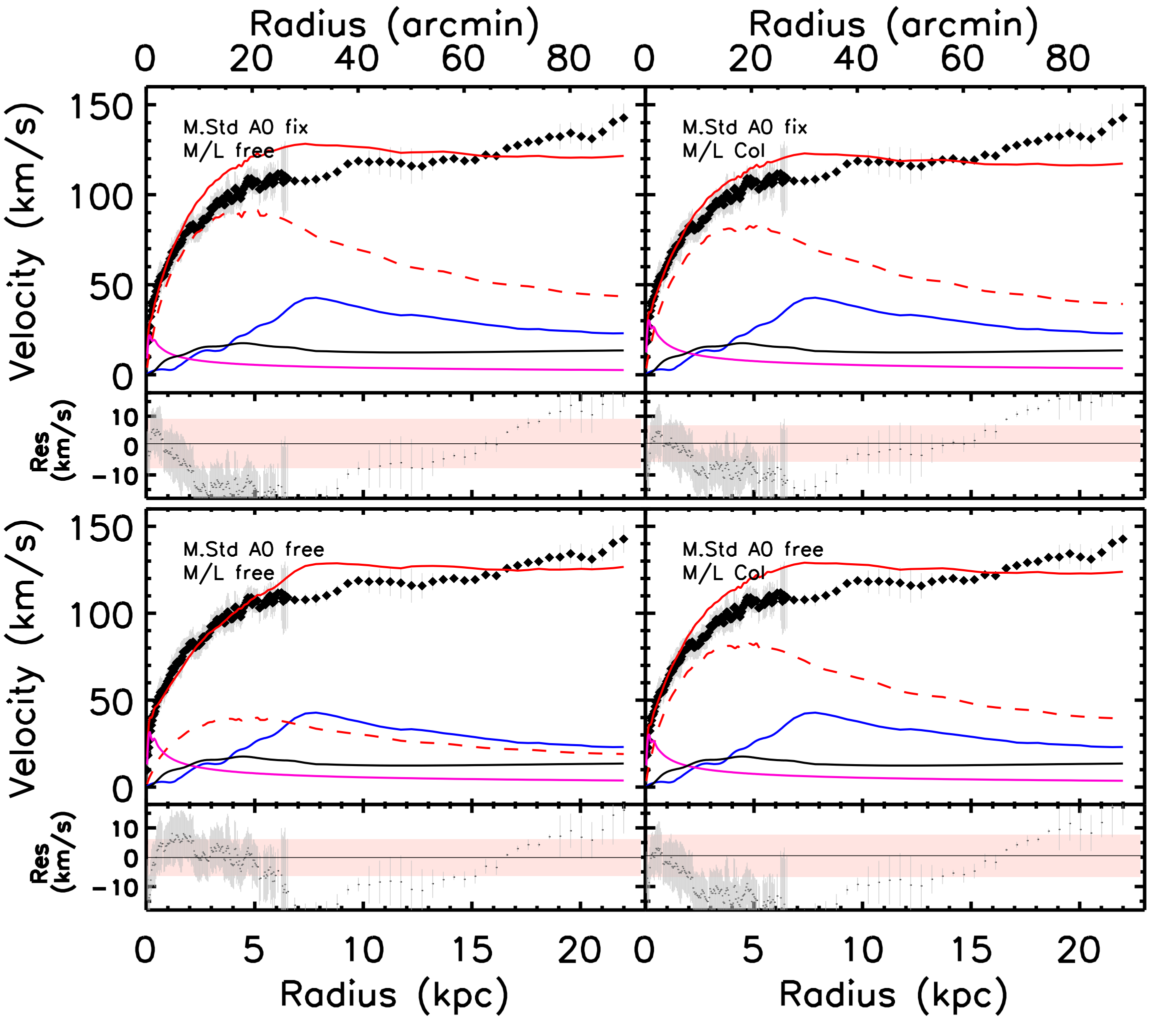

FIGURE 3.20: Same as in Figure 3.18 with the contribution of the bulge presented in magenta.

This stellar structure extends ∼2° (30 kpc in projection) to the North-West towards M31, nearly three times farther out than the size of the optical disk of M33, and thus farther than the HI gas in the warp.

We find a perfect agreement of the systemic velocity, dynamical centre, position angle and inclination of the HI disk with the Hα parameters found in Kam15, within the optical disk. The tilted-ring model is also very consistent with previous HI studies (Corbelli & Schneider, 1997; Corbelli et al., 2014), except the inclination profile that differs from the slightly declining one of Corbelli et al. (2014) for $R > 8$ kpc. The difference between the rotation curve of the approaching and receding sides are small (~ 4 km.s^{-1} on average). Only the transition region ∼35-55′ presents larger differences (~ 20 km.s^{-1}), as well as the outermost points, as likely due to lower quality fits at those radii and a genuine stronger asymmetry between opposite sides of

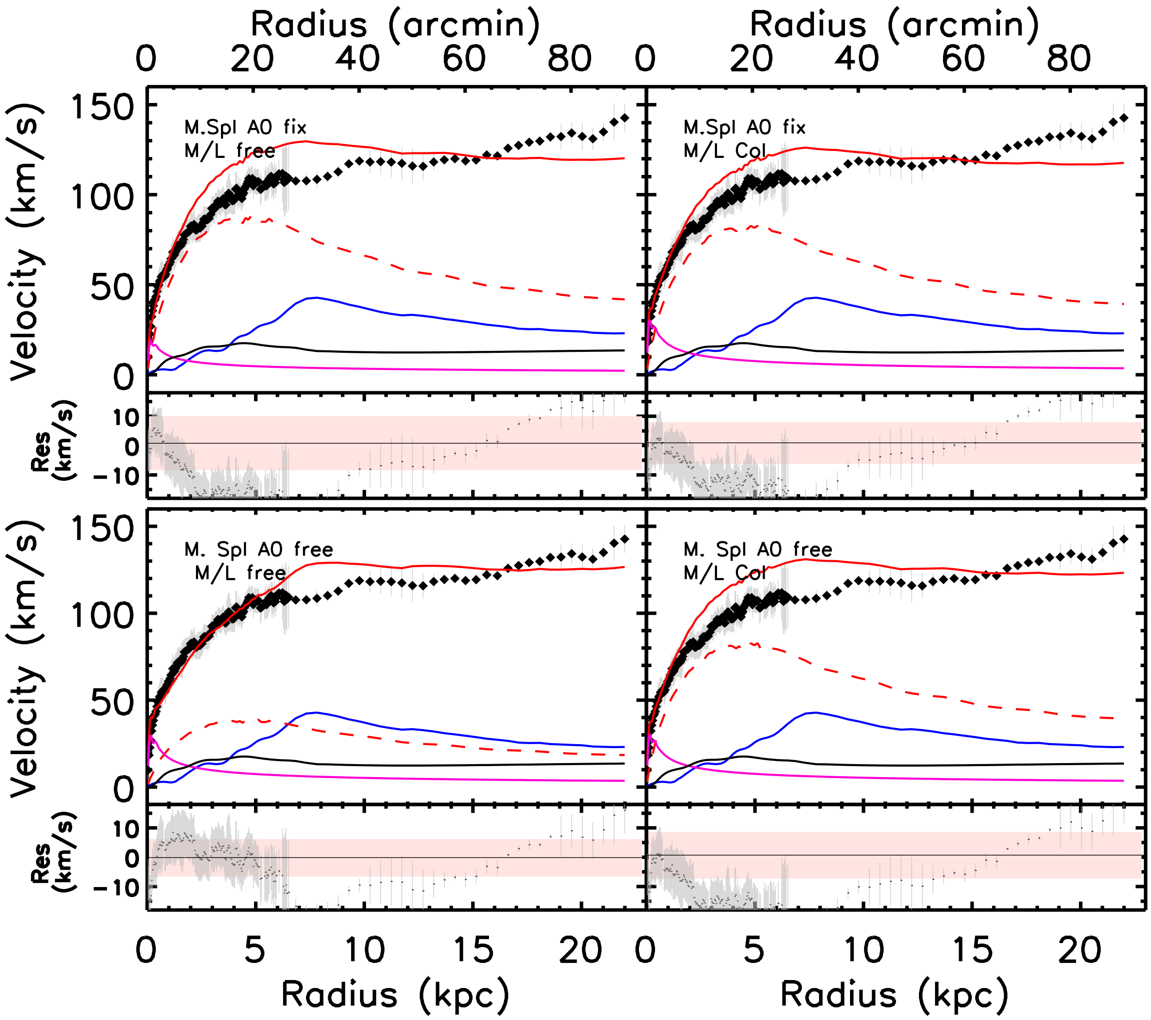

FIGURE 3.21: Same as in Figure 3.19 with the contribution of the bulge presented in magenta.

the warp. The comparison with the rotation curve of Corbelli et al. (2014) is shown in Fig. 3.22. The most notable differences occur for $2 < R < 5$ kpc, where our velocities are smaller by $5 - 10$ km.s^{-1}, and at $R > 20$ kpc where our curve increases while that of Corbelli et al. (2014) decreases. With the exception of the $R > 22$ kpc points, the two curves are consistent with each other within the quoted uncertainties. For the mass models analysis, the Hα RC of Kam15 is used out to 6.5 kpc and than the HI RC of this study out to the last measured point around 22 kpc.

3.4.5.2 Mass models

For the mass distribution analysis, we used the Spitzer/IRAC 3.6μm profile, which gives a good representation of the old disk population, which contributes most of the stellar mass. Our combined DRAO and Arecibo data give us a good representation of the HI disk. It was

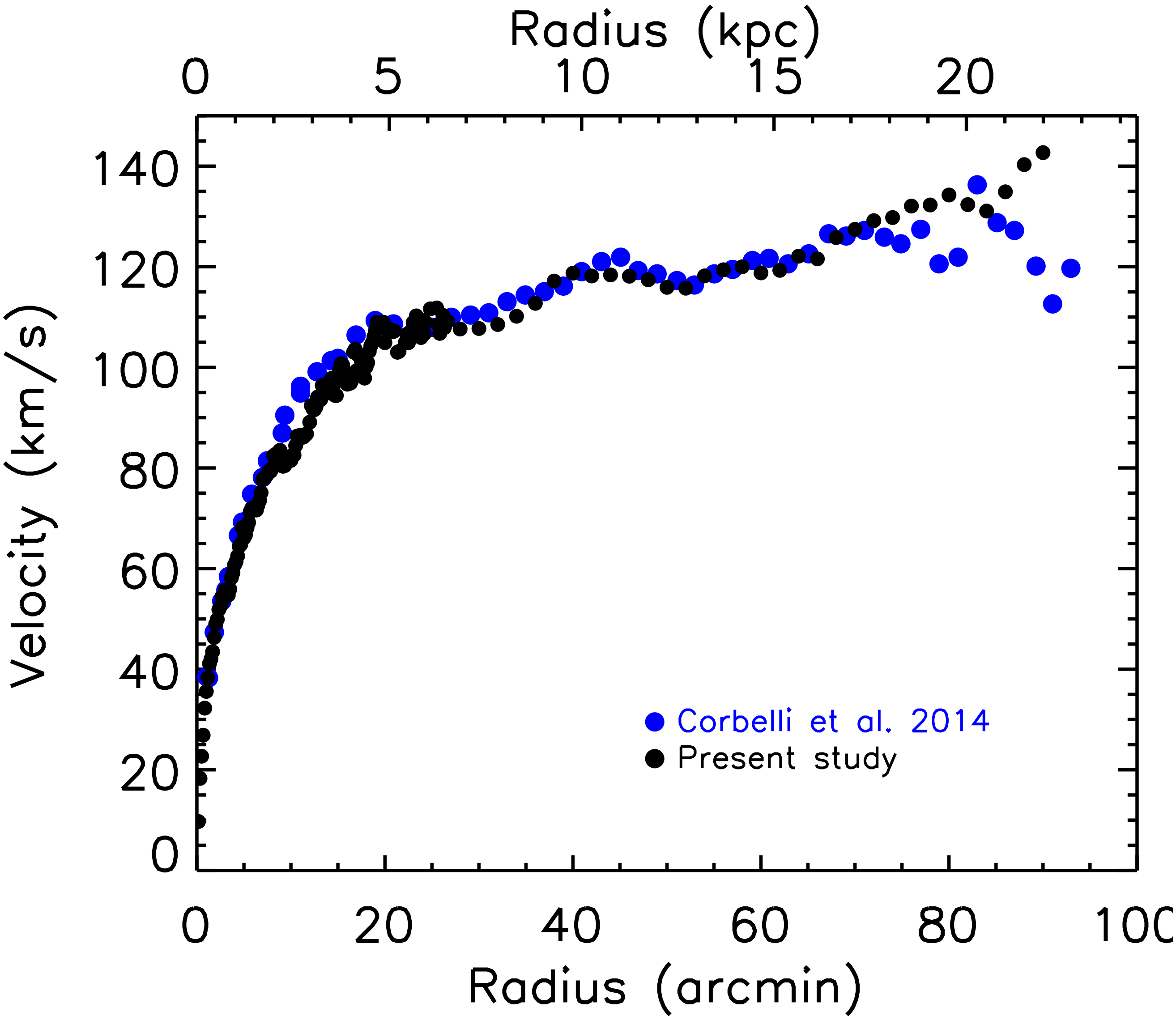

FIGURE 3.22: Comparison of our hybrid Hα-HI rotation curve (black symbols) with the HI curve from Corbelli et al. (2014) (blue symbols).

multiplied by 4/3 to take into account primordial helium. For the second in importance gas component, we used the H_2 data from Druard et al. (2014), who used a CO to H_2 conversion factor two times larger than the value found for the Milky Way, arguing that M33 has half the solar metallicity. Three types of DM models were constructed : the pseudo-isothermal (ISO) model, the Navarro-Frenk-White (NFW) model and the Einasto (EIN) model. We performed best-fit models and models where the M/L has been constrained by IR colors and stellar population models. In terms of the stellar mass distribution, we explored disk-only models and bulge+disk models, after doing a decomposition of our IR profile. However, with a bulge-to-disk ratio of only 0.04, we were not expecting a big difference.

3.4.5.2.1 DM Models

Results listed in Table 3.6 for the mass distribution models with a DM component first show that best-fit models are of similar quality ($\chi_r^2 \sim 0.3$), irrespective of the halo model, and of the assumption made on the stellar distribution with or without a bulge. The halo parameters for every models but the EIN one at free index are very comparable with or without the bulge. However, mass models with fixed color-based mass-to-light ratios for the pure disk case tend to be better than those with the bulge component. It seems thus preferable to omit the negligible bulge contribution when modelling the mass distribution of Messier 33 at fixed stellar mass. We thus focus on the disk-only results hereafter. Furthermore, the scale density and radius of the halo of the EIN model (free index) are significantly degenerated. Because of this degeneracy, and despite the apparent good quality of the fits, we reject this model for the remaining of the analysis.

At first order, it appears impossible to disentangle the halo shape from best-fit models, as the reduced χ^2 are very comparable (~ 0.3). However we notice that the halo parameters of the ISO and EIN $n = 1.4$ haloes are significantly better constrained, and more realistic than for the two other haloes. By estimating the slope of the EIN density profile at the first data point of the rotation curve ($R = 41$ pc) for the $n = 1.4$ model ($\alpha = -0.02 \pm 0.1$) and $n = 6$ model ($\alpha = -0.4 \pm 0.1$), one thus deduces that the degeneracy between parameters increases towards steeper density profiles. Curiously, the $n = 6$ EIN halo of M33 is not a cusp, while it was expected from Chemin et al. (2011) that haloes with $n = 6$ are as cuspy as those modelled in cosmological simulations (Navarro et al., 2004, 2010). This discrepancy is explained by the value of the scale radius R_{-2}, which appears considerably large, even larger than simulated galaxy cluster haloes. In other words, though starting from initial parameters of a pure galaxy-sized cusp, the modelling has produced a halo as shallow as possible with this index $n = 6$, but at the price of an unrealistically large halo. The possibly shallow nature of the density profile of M33 would also explain the unrealistic smaller concentration parameter, and larger V_{200}, than expectations from simulations for galaxy-sized haloes (Bullock et al., 2001; Neto et al., 2007). Note here that nearly half of the NFW models of de Blok et al. (2008b) from THINGS also have $c < 0.1$ and one third have $V_{200} > 500$ km.s^{-1} (but see Chemin et al. (2011) for a re-modelling of the de Blok's sample with uncorrelated data points). Finally, we note that the mass-to-light ratio of the disk has to be 15-20% larger than the color-based $\Upsilon_\star^{3.6}$ value for the preferred ISO and EIN $n = 1.4$ models.

Results for the fixed $\Upsilon_\star^{3.6}$ show that the EIN $n = 6$ and NFW haloes are better than the ISO and EIN $n = 1.4$ models, but again with unrealistic, and not well constrained parameters. This result is not surprising since a shallow halo combined with a heavier stellar mass is needed to best-fit the observational data, as explained above. Such effect is indeed better reproduced by a combination 'light' mass-steeper density profiles than by 'light' mass-shallow density profiles.

It is worth noting here that the apparent inhomogeneous distribution of the rotation velocity uncertainties is not responsible of the observed trend that M33 favours a core-dominated halo. Indeed, we have verified that all the results remain unchanged when using more homogeneous error bars, by propagating the mean error of the Hα velocities to the outer HI points, and the mean error of the HI velocities to the inner Hα points.

3.4.5.2.2 Comparison with the DM models in the literature

We first notice that the parameters of the ISO model are consistent with the relationship of Kormendy & Freeman (2004), whose 1σ parameter range is $R_c = 3-11$ kpc and $\rho_0 = 0.006-0.013$ M$_\odot$ pc^{-3} for galaxies of similar absolute magnitude as M33, and those of the NFW model with the range $R_c = 1 - 17$ kpc and $\rho_0 = 0.003 - 0.1$ M$_\odot$ pc^{-3} found by Randriamampandry & Carignan (2014). Our EIN $n = 1.4$ parameters are also in good agreement with those of the THINGS disks within the quoted uncertainties (Chemin et al., 2011).

The comparison of our results with recent mass distribution models of Messier 33 (Corbelli et al., 2014; Hague & Wilkinson, 2015) is not straightforward, as different datasets and stellar population synthesis models have been used in both studies. The modelling of Corbelli et al. (2014) shows that the NFW with a concentration parameter $c = 10$ is the most likely model, while Hague & Wilkinson (2015) favour a steep inner cusp and large $\Upsilon^{3.6}$, excluding the combination of $\Upsilon^{3.6} < 2$ with an inner slope < 0.9 measured at the first velocity point of their HI rotation curve

($R \sim 2'$). Our results are thus not in agreement with these studies. This is likely explained by the impact of a different rotation curve. At a similar inner radius as Hague & Wilkinson (2015), the maximum absolute slope inferred by our EIN models is 0.7 for $n = 6$, thus significantly not as cuspy as their result.

Using the best-fit case for the $n = 1.4$ EIN halo, the estimated gas, stellar, dark matter and total masses enclosed within $R = 22$ kpc (i.e. at the last radius of the rotation curve) are $\sim 3 \times 10^9$ M$_\odot$, $\sim 9 \times 10^9$ M$_\odot$, $\sim 8.6 \times 10^{10}$ M$_\odot$ and $\sim 9.8 \times 10^{10}$ M$_\odot$, respectively, implying a luminous-to-total mass fraction of $\sim 12\%$. We estimate a virial radius of $R_{200} = 178 \pm 10$ kpc for a virial mass of $M_{200} = (7 \pm 1) \times 10^{11}$ M$_\odot$ at this radius, with a total luminous baryon mass accounting for 2% of the virial mass. A concentration R_{200}/R_{-2} for the dark matter of 5.1 ± 0.7 is found. Our stellar mass is thus 1.8 times larger than the best-fit one of Corbelli et al. (2014), as very likely caused by the use of different stellar population synthesis models and rotation curve. Corbelli et al. (2014) give a total mass of $\sim 4.4 \times 10^{11}$ M$_\odot$, but not the virial radius. Our estimate would thus be about 60% larger than their value, provided that a similar virial radius has been used. Such a difference is due to different best-fit mass models of the different rotation curves. Notice finally that M33 is therefore about 1.4 times less massive than the Andromeda galaxy, if we assume that the M31 virial mass is $\sim 10^{12}$ M$_\odot$ (Chemin et al., 2009).

3.4.5.2.3 No-DM MOND models

Figs. 3.18, 3.19, 3.20 and 3.21 clearly show it is impossible to reproduce the rotation curve of Messier 33, irrespective of the assumptions made on a_0, on the disk mass-to-light ratio, or the interpolation function. Table 3.7 lists large χ^2_r, from 3 to 35. The failure of MOND is however not a surprise, since such a mass model produces flat outer rotation curves while our RC rises steadily out to the last point. The resulting models generally overestimate the rotation velocities inside $R = 10 - 15$ kpc, and underestimate them beyond. We notice that Corbelli et al. (2014) also rejected MOND for M33, even using a different RC than ours.

3.4.6 Summary and conclusions

New high sensitivity HI observations using data from the DRAO interferometer combined with single dish Arecibo data have been presented. They reach very low column densities $\sim 5 \times 10^{18}$ cm^{-2}.

The main results on the HI distribution and kinematics of M33 are as follows :

- While the bulk of the HI is found within the optical disk (≤ 8.4 kpc or R_{25} = 35.4′), the faint outer HI disk was traced out to $\geq 90'$ = 2.7 R_{25}.
- At the adopted distance of 840 kpc, the HI mass is $\sim 2 \times 10^9$ $M_\odot$ for a M_{HI}/L_V = 1.8.
- There is slightly more HI on the NW side (in the direction of M31 : see the discussion in p.e.Ibata et al. (2014)) than on the SE side and its radial distribution is nearly constant out to the edge of the optical disk, where it drops abruptly (Figure 3.6).
- The faint outer disk (see the last 2 contours of Figure 3.5) is found to be strongly warped with a variation of PA from 202° to 165° and a small increase of inclination, which is clearly seen in the twist of the isovelocity contours (Figure 3.9). Clear wider or even double-peaked profiles are seen (Figure 3.8, where our line-of-sight is expected to cross the disk more than once due to the warp.
- Following the faint outer disk, the RC is extended out to ∼22 kpc in this study and shows a good agreement between the approaching and receding sides (Fig. 3.10), except for $10 \leq R \leq 14$ kpc, the radius range corresponding to the sharp change in PA seen in Figure 3.10.
- Position-velocity diagrams (Fig. 3.11) at the more or less constant PA values in the inner parts (202°) and in the outer parts (165°) show a good agreement between our adopted RC and the kinematics observed on the major axis. Similarly, a model velocity field constructed using the adopted RC shows very small residuals ≤ 10 km.s^{-1} which gives us confidence in our derived kinematical parameters.
- Both the top PV-diagram of Figure 3.11 and the adopted RC of Figure 3.13 show a very good agreement between our HI data and the Hα data of Kam15.
- The new rotation curve, used for the mass modelling, is a combination of the Hα rotation curve at arcsec-resolution presented in the first article from this series (Kam15) out to 6.5 kpc, and the new arcmin-resolution HI rotation curve derived in this study out to 22 kpc.

The main results from the modelling of the mass distribution are as follows.

- Despite a very accurate rotation curve, it was not possible, based on the goodness of the fits, to establish that one of the three DM models (ISO, NFW and EIN) was representing better than the others the DM distribution in M33. The three functional forms used give more or less equally acceptable fits. This may not be surprising in view of the known existence of a small bar (Corbelli & Walterbos, 2007) in M33, which makes it difficult to constrain the shape of the M33's inner dark matter halo profile, where lies the main difference e.g. between ISO and NFW.
- DM models at fixed mass-to-light ratios constrained by stellar population synthesis using

a diet-Salpeter IMF tend to prefer haloes with steep inner density profiles. Best-fit mass models give equally acceptable fits, irrespective of the shallow or cuspy density shape. However, such cuspy models are highly unrealistic, showing characteristic parameters of velocity, concentration, scale radius and density that are rarely seen in other observational studies or in cosmological simulations. We thus reject cupsy models for Messier 33, which is in disagreement with recent mass models found in the literature.

- The inner density slope of the EIN model at fixed index $n = 1.4$ is -0.01 at 41 pc, the innermost point of the rotation curve, and the disk mass-to-light ratio in the Spitzer 3.6μm band is 0.83. These values are fully consistent with the pseudo-isothermal sphere model. The inferred stellar mass of Messier 33 is 9×10^9 $M_\odot$.
- The mass enclosed within 22 kpc, the last point of the rotation curve, is 9.8×10^{10} $M_\odot$, implying a luminous (gas+stars) to total mass fraction of 12%. The total mass estimated at the virial radius of 178 kpc is 7×10^{11} $M_\odot$. Messier 33 is thus about 1.4 times less massive than Messier 31.
- This study shows clearly that, even when letting the MOND constant a_0 and/or the disk M/L free to vary and allowing for different interpolation functions, there is no way a MOND model (no DM) can represent the mass distribution in M33. This result is consistent with Corbelli et al. (2014) and questions the universality of MOND as suggested by many studies (see e.g. Begeman et al., 1991; Sanders & Verheijen, 1998; de Blok & McGaugh, 1998; Gentile et al., 2010). This is similar to what was seen recently for the late-type spiral NGC 3109 (Carignan et al., 2013).
- M33, a galaxy with a well constrained distance and rotation curve, shows the importance of deriving the RCs out to large R because, with a RC derived only out to the edge of the optical disk ∼8 kpc, previous studies (see e.g. Sanders, 1996; Sanders & McGaugh, 2002) were showing a good agreement between the M33's RC and MOND. This can be seen also in Figure 3.23, where we derived MOND models using only the optical Hα data of Kam15 out to ∼8 kpc. It can be seen that especially the bulge+disk models give very good fits for both interpolation functions. However, this is not the case when the RC is extended out to 22 kpc.

Acknowledgements

The Dominion Radio Astrophysical Observatory is operated as a national facility by the National Research Council of Canada. ZKS's work was supported by CC's Discovery grant of

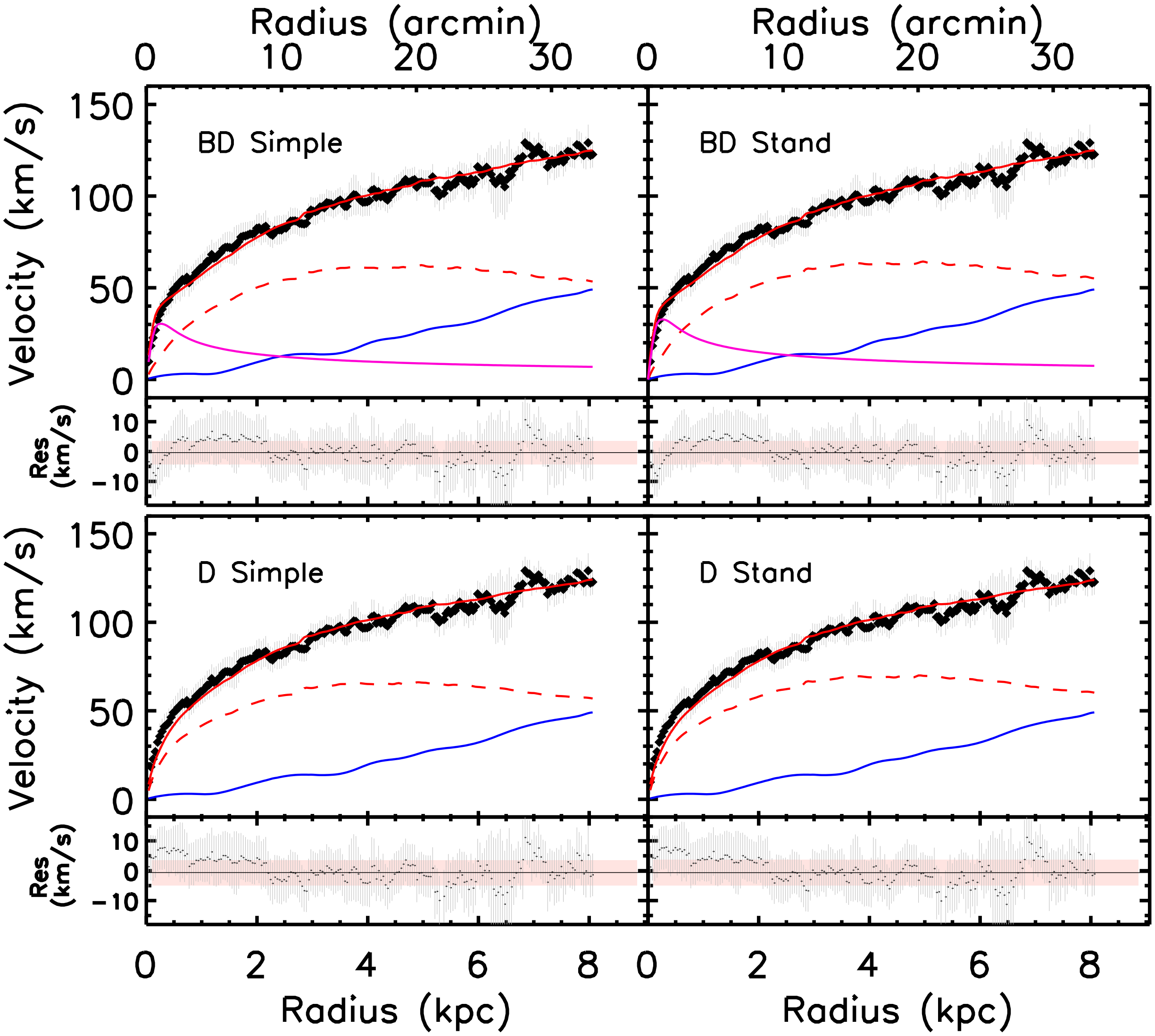

FIGURE 3.23: MOND models with the Hα RC : the models at the top are for bulge+disk and at the bottom for disk-only. The left side is for the simple interpolation and the right side for the standard interpolation. In each case, the residuals are given in the small bottom panels.

the Natural Sciences and Engineering Research Council of Canada. CC's work is based upon research supported by the South African Research Chairs Initiative (SARChI) of the Department of Science and Technology (DST), the Square Kilometer Array South Africa (SKA SA) and the National Research Foundation (NRF). L.C. acknowledges a financial support from CNES. TF's work has partially been supported by a grant from the Brandon University Research Committee (BURC). We are very grateful to Kevin Douglas and Mary Putman for providing us the Arecibo TOGS data.

Conclusion

Chapitre 4

Conclusion

La cinématique d'une galaxie est un moyen efficace pour mieux sonder et comprendre les phénomènes qui régulent le fonctionnement de cette dernière. M33 est une galaxie proche et bien que spéciale, est assez représentative des galaxies spirales. L'étude de sa cinématique et de sa dynamique donne une meilleure compréhension des galaxies extérieures et nous renseignent également sur la nôtre, la Voie Lactée, qui est une spirale.
Plusieurs études de la cinématique des galaxies voisines M33 et de M31 ont été réalisées en HI (par exemple Huchtmeier, 1973; **?**; Corbelli, 2003; Corbelli et al., 2008; Braun et al., 2009; Chemin et al., 2009; Corbelli et al., 2014). Cependant, peu d'études en Hα existaient sur la cinématique de ces galaxies voisines ; Rubin & Ford (1970), Boulesteix & Monnet (1970); **?**); Huchtmeier (1973); Boulesteix et al. (1974) et Braun (1991) ont présenté des études sur la cinématique de M33 à petite échelle.

Nous avons dans ce document, présenté la cinématique de M33 en utilisant le gaz ionisé (Hα) et le gaz neutre HI. Les chapitres 2 et 3 décrivent de manière détaillée la méthodologie de l'étude : la cartographie Hα dans le chapitre 2 et l'étude à grande échelle et haute résolution avec l'apport du HI et la contribution du Hα dans les régions intérieures dans le chapitre 3..

4.1 Les observations Hα de M33

La cartographie Fabry-Perot (FP) Hα de M33 a été réalisée au télescope de 1.6m de l'Observatoire du mont Mégantic (OMM) utilisant un étalon FP de haute résolution (ordre = 765) et une caméra EMCCD très sensible (efficacité quantique $\leq$ 90%), utilisée en mode comptage de photons. Les 10 champs observés ont été combinés pour former une mosaïque de $42' \times 56'$($\sim 10 \times 13.5$

kpc), avec une résolution spatiale de 3 secondes d'arc. Les régions HII sont très bien définies, ayant une haute résolution spatiale et spectrale. Bien que le but premier de notre étude était de dériver la cinématique de M33 à haute résolution, la présente base de données pourra être utilisée ultérieurement pour l'étude détaillée de ces régions HII. Les données ont été calibrées en flux utilisant les résultats de Relaño et al. (2013).

L'étude de la dispersion des vitesses en fonction du rayon montre que σ est essentiellement constant autour de 16 ± 2 km.s^{-1} jusqu'à ~ 7.5 kpc et atteint 20 - 25 km.s^{-1} dans les régions externes où le gauchissement de la galaxie commence dans les données HI (entre 7.5 et 8.0 kpc). Une comparaison entre M33 et un échantillon de galaxies ayant une activité de formation stellaire (l'échantillon GHASP) montre que la dispersion moyenne des vitesses de M33 est dans la limite inférieure tandis que l'ensemble de l'échantillon a un σ entre 15 et 35 km.s^{-1}. L'étude de la dispersion montre également une forte corrélation entre le flux Hα et la dispersion des vitesses (σ vs I$_{\mathrm{H}\alpha}$).

La haute résolution des données Hα a permis de faire une étude de la cinématique d'ensemble de la galaxie. La CR extraite à haute résolution (5 arcsec) est utilisée pour tester les modèles de masse. La CR montre une croissance continue jusqu'à $\sim$ 8 kpc. Elle est en accord avec plusieurs études en HI à l'intérieur de 6.5 kpc, et présente une différence ("une surestimation en Hα") par rapport au HI aux rayons de 6.5 - 8 kpc. Aux extrémités du disque optique, la CR Hα est plus élevé que celle obtenue en HI. Pour la détermination de la CR, le centre cinématique utilisé est légèrement décalé du centre optique. Les principaux paramètres utilisés sont $V_{sys} = -178 \pm 2.7$, $PA = 202° \pm 4.3°$ et $i = 52.0° \pm 1.6°$. Nous avons trouvé que la CR déduite est en accord avec des études en HI et en CO. La composante stellaire de M33 utilisée dans cette thèse dérive des données Spitzer à $3.6\mu m$. Le profil de brillance de surface montre que la composante du bulbe est assez faible. Le disque stellaire est défini avec le rayon R$_d = 1.8 \pm 0.02$ kpc et une brillance de surface centrale de $\mu_0 = 18.01 \pm 0.03$ mag/arcsec^2.

Les modèles ISO et NFW ont été présentés dans l'article sur la cinématique Hα (cf. chapitre 2). Dans les régions intérieures, ces deux modèles représentent bien la courbe de rotation même en ne tenant pas compte du gaz neutre. Pour les modèles de masse, il a été décidé d'adopter les modèles avec seulement un disque, puisque qu'avec un rapport Bulbe/Disque de 0.04, le fait d'ajouter un bulbe ne fait qu'augmenter les incertitudes. Dans ce cas, les modèles ISO donne un meilleur résultat que les modèles plus piqués au centre NFW. Les modèles ISO donnent pour les 2 paramètres libres du halo sombre, ρ_0 et R_c, des valeurs près de celles retrouvées dans la littérature pour ce type de galaxies.

4.2 La combinaison de deux traceurs HI et Hα

Les études HI ne donnent pas autant de précision que le Hα à cause des problèmes de résolution imposés par la grandeur du faisceau. Bien que limité par son faible flux à grands rayons, le Hα permet de donner une bonne détermination des paramètres cinématiques des galaxies. Les observations HI combinées de DRAO et de Arecibo couvrant un champ de plus de $2^\circ \times 2^\circ$ permettent d' étendre l'étude de la cinématique de M33 dans les régions externes avec une sensibilité de $\sim 5 \times 10^{18}$ cm^{-2}. L'analyse de ces données montre une masse HI M$_{HI} = 2 \times 10^9$ M$_\odot$. La majeure partie du HI se trouve concentré dans un rayon de 35 $'$, correspondant au disque optique. La détection du HI va à des rayons plus grands que 90$'$ avec plus de HI détectable du coté Nord-Ouest (dans la direction de M31). Le caractère gauchi de M33 a été confirmé par la variation des paramètres (PA et inclinaison) suivant le rayon. L'ange PA subit une forte variation (de 200° à 170°) entre 35$'$ et 70$'$.

Suivant le faible flux HI dans les régions extérieures, la courbe de rotation (RC) a été étendue jusqu'à 22 kpc et montre un bon accord entre les 2 côtés. Des diagrammes position-vitesse montrent un très bon accord entre la RC adoptée et la cinématique sur l'axe majeur, de même qu'avec la cinématique Hα dans les régions intérieures. Pour l'analyse de la distribution de masse, nous avons donc combiné les données Hα du centre jusqu'à 6.5 kpc aux données HI jusqu'à 22 kpc. Dans cette analyse la contribution stellaire a été obtenue des données Spitzer et celle du gaz moléculaire des observations de Gratier et al. (2010). Nous avons utilisé trois modèles de halos avec matière sombre ; le modèle pseudo-isothermal (ISO), le modèle de Navarro-Frenk-White (NFW) et celui de Einasto (EIN). Le formalisme de MOND (sans matière sombre) a également été testé. Les trois modèles avec un halo sombre donnent des résultats satisfaisants avec des $\chi_r^2 \sim 0.3$. Le résultat principal est que d'aucune façon on modèle MOND, sans matière sombre, ne peut reproduire la RC observée, peu importe la constante utilisée ou la fonction d'interpolation. L'échec de MOND ne devrait pas être une surprise puisque MOND produit des courbes plates et que la RC de M33 continue de croitre dans les régions extérieures. Il en résulte une sur estimation dans le régions intérieures et une sous estimation dans les régions extérieures.

4.3 Perspectives

Les observations Hα réalisées à l'OMM ont une très grande résolution spatiale et spectrale. Ces données permettront d'étudier individuellement les régions HII de M33. Nous avons présenté dans ce document une étude globale sur la dispersion des vitesses en fonction de l'intensité. Cela permettra d'approfondir l'étude les régions HII individuellement que nous avons commencé dans l'article sur les observations Hα.

Nous avons en cours un projet d'étude du comportement de la dispersion radiale dans les régions HII de M33 suivant leurs positions (distances galactocentriques). Nous prévoyons étudier les vitesses d'expansion dans les régions sous forme de bulles qui sont bien résolues dans nos observations. Dans nos observations, nous sommes en mesure de distinguer pour une même région des gradients de vitesses, qui pourraient être utiles dans l'identification de l'expansion des bulles.

Dans l'étude de la cinématique des galaxies, le HI est connu pour être optiquement mince. Cette propriété permet d'expliquer les raies multiples lors de l'observation du gaz neutre. L'impact des composantes secondaires sur la cinématique n'est pas bien connu. Des travaux à venir permettront de revenir sur l'impact des composantes secondaires du HI dans la détermination des paramètres cinématiques. De même nous nous intéresserons au comportement du Hα où la composante secondaire est non négligeable.

L' expérience et les techniques examinées dans cette étude seront mises à profit pour l'étude de la galaxie M31, dont les observations ont débuté. Dans ce cas nous tenterons d'observer les faibles émissions Hα dans les régions centrales et autour du trou noir central. Ces observations permettront de contraindre les modèles de masse de M31 avec un apport de points de données dans le centre.

Vue la particularité de M33, nous avons mis en place un échantillon de galaxies floculantes pour lesquelles nous voulons étudier et comparer leurs cinématiques à celle de M33 qui pourrait à certaines longueurs d'ondes être considérée comme une galaxie floculente. L'étude des dispersions dans les bras spiraux de M33 pourrait être un indicateur pour voir si dans une floculente on pourrait tracer ou justifier efficacement la présence de bras spiraux.

Les données haute résolution des radio télescopes MeerKat[a] et du Square Kilometre Array (SKA)[b] nous permettront de reprendre ce type d'analyse sur d'autres galaxies. Avec le projet MHONGOOSE (MeerKAT HI Observations of Nearby Galactic Objects : Observing Southern Emitters), nous aurons une gamme variée de galaxies. Ce type de données permettra de mieux comprendre la formation stellaire et l'évolution des galaxies proches.

---

[a] http ://www.ska.ac.za/meerkat/

[b] http ://www.ska.ac.za/

Références bibliographiques

Références

Abraham, R. G. & van den Bergh, S. 2001, Science, 293, 1273

Allen, R. J., Ekers, R. D., & Terlouw, J. P. 1985, in Data Analysis in Astronomy, ed. V. di Gesu, L. Scarsi, P. Crane, J. H. Friedman, & S. Levialdi, 271

Amram, P. 1991, PhD thesis, Université de Provence - Aix-Marseille I

Amram, P., Balkowski, C., Boulesteix, J., Cayatte, V., Marcelin, M., & Sullivan, III, W. T. 1996, A&A, 310, 737

Amram, P. & Georgelin, Y. 2000, Physica Scripta Volume T, 86, 76

Amram, P., Marcelin, M., Balkowski, C., Cayatte, V., Sullivan, III, W. T., & Le Coarer, E. 1994, A&AS, 103, 5

Amram, P., Marcelin, M., Boulesteix, J., & Le Coarer, E. 1992, A&A, 266, 106

An, D., Terndrup, D. M., & Pinsonneault, M. H. 2007, ApJ, 671, 1640

Baugh, C. M., Cole, S., & Frenk, C. S. 1996, MNRAS, 283, 1361

Begeman, K. G. 1987, PhD thesis, Kapteyn Astronomical Institute, Rijksuniversiteit Groningen

—. 1989, A&A, 223, 47

Begeman, K. G., Broeils, A. H., & Sanders, R. H. 1991, MNRAS, 249, 523

Bell, E. F. & de Jong, R. S. 2001, ApJ, 550, 212

Blais-Ouellette, S. 2000, PhD thesis, Université de Montréal (Canada)

Blais-Ouellette, S., Carignan, C., Amram, P., & Côté, S. 1999, AJ, 118, 2123

Bordalo, V. & Telles, E. 2010, in COSPAR Meeting, Vol. 38, 38th COSPAR Scientific Assembly, 3658

Bosma, A. 1978, PhD thesis, PhD Thesis, Groningen Univ., (1978)

Boulesteix, J., Courtes, G., Laval, A., Monnet, G., & Petit, H. 1974, A&A, 37, 33

Boulesteix, J. & Monnet, G. 1970, A&A, 9, 350

Braine, J., Gratier, P., Kramer, C., Schuster, K. F., Tabatabaei, F., & Gardan, E. 2010, A&A, 520, A107

Braun, R. 1991, ApJ, 372, 54

Braun, R. & Thilker, D. 2004, in Astronomical Society of the Pacific Conference Series, Vol. 327, Satellites and Tidal Streams, ed. F. Prada, D. Martinez Delgado, &amp ; T. J. Mahoney, 139

Braun, R., Thilker, D. A., Walterbos, R. A. M., & Corbelli, E. 2009, ApJ, 695, 937

Bullock, J. S., Kolatt, T. S., Sigad, Y., Somerville, R. S., Kravtsov, A. V., Klypin, A. A., Primack, J. R., & Dekel, A. 2001, MNRAS, 321, 559

Burkert, A. 1995, ApJL, 447, L25

Capaccioli, M. 1989, in World of Galaxies (Le Monde des Galaxies), ed. H. G. Corwin, Jr. & L. Bottinelli, 208–227

Cardone, V. F., Piedipalumbo, E., & Tortora, C. 2005, MNRAS, 358, 1325

Carignan, C., Frank, B. S., Hess, K. M., Lucero, D. M., Randriamampandry, T. H., Goedhart, S., & Passmoor, S. S. 2013, AJ, 146, 48

Carignan, C. & Freeman, K. C. 1985, ApJ, 294, 494

Carignan, C., Hernandez, O., Beckman, J. E., & Fathi, K. 2008, in Astronomical Society of the Pacific Conference Series, Vol. 390, Pathways Through an Eclectic Universe, ed. J. H. Knapen, T. J. Mahoney, & A. Vazdekis, 168

Carranza, G., Courtes, G., Georgelin, Y., Monnet, G., & Pourcelot, A. 1968, Annales d'Astrophysique, 31, 63

Carroll, B. W. & Ostlie, D. A. 1996, An Introduction to Modern Astrophysics, 2nd edn. (Institute for Mathematics and Its Applications)

Chemin, L., Balkowski, C., Cayatte, V., Carignan, C., Amram, P., Garrido, O., Hernandez, O., Marcelin, M., Adami, C., Boselli, A., & Boulesteix, J. 2006, MNRAS, 366, 812

Chemin, L., Carignan, C., Foster, T., & Kam, Z. S. 2012, in SF2A-2012 : Proceedings of the Annual meeting of the French Society of Astronomy and Astrophysics, ed. S. Boissier, P. de Laverny, N. Nardetto, R. Samadi, D. Valls-Gabaud, & H. Wozniak, 519–522

Chemin, L., Carignan, C., & Tyler, F. 2009, ApJ, 705, 1395

Chemin, L., de Blok, W. J. G., & Mamon, G. A. 2011, AJ, 142, 109

Cockcroft, R., McConnachie, A. W., Harris, W. E., Ibata, R., Irwin, M. J., Ferguson, A. M. N., Fardal, M. A., Babul, A., Chapman, S. C., Lewis, G. F., Martin, N. F., & Puzia, T. H. 2013, MNRAS, 428, 1248

Cole, S. & Lacey, C. 1996, MNRAS, 281, 716

Collins, M. L. M., Chapman, S. C., Irwin, M. J., Martin, N. F., Ibata, R. A., Zucker, D. B., Blain, A., Ferguson, A. M. N., Lewis, G. F., McConnachie, A. W., & Peñarrubia, J. 2010, MNRAS, 407, 2411

Corbelli, E. 2003, MNRAS, 342, 199

Corbelli, E., Magrini, L., & Verley, S. 2008, in Astronomical Society of the Pacific Conference Series, Vol. 396, Formation and Evolution of Galaxy Disks, ed. J. G. Funes & E. M. Corsini, 19–24

Corbelli, E. & Salucci, P. 2000, MNRAS, 311, 441

—. 2007, MNRAS, 374, 1051

Corbelli, E. & Schneider, S. E. 1997, ApJ, 479, 244

Corbelli, E., Thilker, D., Zibetti, S., Giovanardi, C., & Salucci, P. 2014, A&A, 572, A23

Corbelli, E. & Walterbos, R. A. M. 2007, ApJ, 669, 315

Courtes, G., Petit, H., Petit, M., Sivan, J., & Dodonov, S. 1987, A&A, 174, 28

Daigle, O. 2005, Master's thesis, Université de Montréal (Canada)

Daigle, O., Carignan, C., Gach, J., Guillaume, C., Lessard, S., Fortin, C., & Blais-Ouellette, S. 2009a, PASP, 121, 866

Daigle, O., Carignan, C., Gach, J.-L., Guillaume, C., Lessard, S., Fortin, C.-A., & Blais-Ouellette, S. 2009b, PASP, 121, 866

Daigle, O., Carignan, C., Hernandez, O., Chemin, L., & Amram, P. 2006, MNRAS, 368, 1016

Daigle, O., Gach, J., Guillaume, C., Lessard, S., Carignan, C., & Blais-Ouellette, S. 2008, in SPIE Conference Series, Vol. 7014, 70146L

de Blok, W. J. G. 2010, Advances in Astronomy, 2010

de Blok, W. J. G. & Bosma, A. 2002, A&A, 385, 816

de Blok, W. J. G. & McGaugh, S. S. 1998, ApJ, 508, 132

de Blok, W. J. G., Walter, F., Brinks, E., Trachternach, C., Oh, S.-H., & Kennicutt, Jr., R. C. 2008a, AJ, 136, 2648

—. 2008b, AJ, 136, 2648

de Vaucouleurs, G. 1959, Handbuch der Physik, 53, 275

de Vaucouleurs, G., de Vaucouleurs, A., Corwin, Jr., H. G., Buta, R. J., Paturel, G., & Fouque, P. 1991, S&T, 82, 621

Dicaire, I., Carignan, C., Amram, P., Marcelin, M., Hlavacek-Larrondo, J., de Denus-Baillargeon, M.-M., Daigle, O., & Hernandez, O. 2008, AJ, 135, 2038

Dressler, A. 1980, ApJ, 236, 351

Druard, C., Braine, J., Schuster, K. F., Schneider, N., Gratier, P., Bontemps, S., Boquien, M., Combes, F., Corbelli, E., Henkel, C., Herpin, F., Kramer, C., van der Tak, F., & van der Werf, P. 2014, ArXiv e-prints

Einasto, J. 1969, Astronomische Nachrichten, 291, 97

Ellis, R. S. 1997, ARAA, 35, 389

Ellis, R. S., Abraham, R. G., Brinchmann, J., & Menanteau, F. 2000, Astronomy and Geophysics, 41, 020000

Epinat, B. 2008, Theses, Université de Provence - Aix-Marseille I

Epinat, B., Amram, P., Balkowski, C., & Marcelin, M. 2010, Monthly Notices of the Royal Astronomical Society, 401, 2113

Epinat, B., Amram, P., & Marcelin, M. 2008a, MNRAS, 390, 466

Epinat, B., Amram, P., Marcelin, M., Balkowski, C., Daigle, O., Hernandez, O., Chemin, L., Carignan, C., Gach, J.-L., & Balard, P. 2008b, MNRAS, 388, 500

Famaey, B. & Binney, J. 2005, MNRAS, 363, 603

Famaey, B. & McGaugh, S. S. 2012, Living Reviews in Relativity, 15, 10

Ferguson, A., Irwin, M., Chapman, S., Ibata, R., Lewis, G., & Tanvir, N. Resolving the Stellar Outskirts of M31 and M33, xxiv edn., ed. R. S. de Jong, Astrophysics and Space Science Proceedings (Springer Netherlands), 239–244

Fraternali, F., Oosterloo, T., Sancisi, R., & van Moorsel, G. 2001, ApJL, 562, L47

Freedman, W. L., Madore, B. F., Gibson, B. K., Ferrarese, L., Kelson, D. D., Sakai, S., Mould, J. R., Kennicutt, Jr., R. C., Ford, H. C., Graham, J. A., Huchra, J. P., Hughes, S. M. G., Illingworth, G. D., Macri, L. M., & Stetson, P. B. 2001, ApJ, 553, 47

Freeman, K. C. 1970, ApJ, 160, 811

Frenk, C. S., White, S. D. M., Efstathiou, G., & Davis, M. 1985, Nature, 317, 595

Fukushige, T. & Makino, J. 1997, ApJL, 477, L9

Galleti, S., Bellazzini, M., & Ferraro, F. R. 2004, A&A, 423, 925

Gardan, E., Braine, J., Schuster, K. F., Brouillet, N., & Sievers, A. 2007, A&A, 473, 91

Gebhardt, K., Lauer, T. R., Kormendy, J., Pinkney, J., Bower, G. A., Green, R., Gull, T., Hutchings, J. B., Kaiser, M. E., Nelson, C. H., Richstone, D., & Weistrop, D. 2001, AJ, 122, 2469

Gehrz, R. & Willner, S. 2004, M33 Mapping and Spectroscopy, spitzer Proposal

Gentile, G., Baes, M., Famaey, B., & van Acoleyen, K. 2010, MNRAS, 406, 2493

Gieren, W., Górski, M., Pietrzyński, G., Konorski, P., Suchomska, K., Graczyk, D., Pilecki, B., Bresolin, F., Kudritzki, R.-P., Storm, J., Karczmarek, P., Gallenne, A., Calderón, P., & Geisler, D. 2013, ApJ, 773, 69

Goerdt, T., Moore, B., Read, J. I., & Stadel, J. 2010, ApJ, 725, 1707

Gooch, R. 1996, in Astronomical Society of the Pacific Conference Series, Vol. 101, Astronomical Data Analysis Software and Systems V, ed. G. H. Jacoby & J. Barnes, 80

Gordon, K. D., Hanson, M. M., Clayton, G. C., Rieke, G. H., & Misselt, K. A. 1999, ApJ, 519, 165

Graham, A. W. & Worley, C. C. 2008, MNRAS, 388, 1708

Gratier, P., Braine, J., Rodriguez-Fernandez, N. J., Schuster, K. F., Kramer, C., Corbelli, E., Combes, F., Brouillet, N., van der Werf, P. P., & Röllig, M. 2012, A&A, 542, A108

Gratier, P., Braine, J., Rodriguez-Fernandez, N. J., Schuster, K. F., Kramer, C., Xilouris, E. M., Tabatabaei, F. S., Henkel, C., Corbelli, E., Israel, F., van der Werf, P. P., Calzetti, D., Garcia-Burillo, S., Sievers, A., Combes, F., Wiklind, T., Brouillet, N., Herpin, F., Bontemps, S., Aalto, S., Koribalski, B., van der Tak, F., Wiedner, M. C., Röllig, M., & Mookerjea, B. 2010, A&A, 522, A3

Grossi, M., Giovanardi, C., Corbelli, E., Giovanelli, R., Haynes, M. P., Martin, A. M., Saintonge, A., & Dowell, J. D. 2008, A&A, 487, 161

Guidoni, U., Messi, R., & Natali, G. 1981, A&A, 96, 215

Hague, P. R. & Wilkinson, M. I. 2015, ApJ, 800, 15

Haynes, M. P. & Giovanelli, R. 1984, AJ, 89, 758

Hernandez, O., Carignan, C., Amram, P., Chemin, L., & Daigle, O. 2005, MNRAS, 360, 1201

Hernandez, O., Gach, J., Carignan, C., & Boulesteix, J. 2003, in Presented at the Society of Photo-Optical Instrumentation Engineers (SPIE) Conference, Vol. 4841, Society of Photo-Optical Instrumentation Engineers (SPIE) Conference Series, ed. M. Iye ; A. F. M. Moorwood, 1472–1479

Hernquist, L. 1990, ApJ, 356, 359

Hinshaw, G., Weiland, J. L., Hill, R. S., Odegard, N., Larson, D., Bennett, C. L., Dunkley, J., Gold, B., Greason, M. R., Jarosik, N., Komatsu, E., Nolta, M. R., Page, L., Spergel, D. N., Wollack, E., Halpern, M., Kogut, A., Limon, M., Meyer, S. S., Tucker, G. S., & Wright, E. L. 2009, ApJS, 180, 225

Hlavacek-Larrondo, J. 2009, Master's thesis, Université de Montréal (Canada)

Hoopes, C. G., Walterbos, R. A. M., & Bothun, G. D. 2001, ApJ, 559, 878

Hubble, E. P. 1926, ApJ, 64, 321

—. 1929, ApJ, 69, 103

Huchtmeier, W. 1973, A&A, 22, 91

Ibata, R. A., Lewis, G. F., McConnachie, A. W., Martin, N. F., Irwin, M. J., Ferguson, A. M. N., Babul, A., Bernard, E. J., Chapman, S. C., Collins, M., Fardal, M., Mackey, A. D., Navarro, J., Peñarrubia, J., Rich, R. M., Tanvir, N., & Widrow, L. 2014, ApJ, 780, 128

Inoue, S. & Saitoh, T. R. 2011, MNRAS, 418, 2527

Ishiyama, T., Rieder, S., Makino, J., Portegies Zwart, S., Groen, D., Nitadori, K., de Laat, C., McMillan, S., Hiraki, K., & Harfst, S. 2013, ApJ, 767, 146

Ivanov, G. R. & Kunchev, P. Z. 1985, Astrophysics and Space Science, 116, 341

Jaffe, W. 1983, MNRAS, 202, 995

Jarrett, T. H., Chester, T., Cutri, R., Schneider, S. E., & Huchra, J. P. 2003, AJ, 125, 525

Kam, Z. S., Carignan, C., Chemin, L., Amram, P., & Epinat, B. 2015, Monthly Notices of the Royal Astronomical Society, 449, 4048

Kennicutt, Jr., R. C. 1984, ApJ, 287, 116

—. 1998, ARAA, 36, 189

Kennicutt, Jr., R. C., Bothun, G. D., & Schommer, R. A. 1984, AJ, 89, 1279

Kent, S. M. 1987, AJ, 94, 306

Kormendy, J. & Bender, R. 2012, ApJS, 198, 2

Kormendy, J. & Freeman, K. C. 2004, in IAU Symposium, Vol. 220, Dark Matter in Galaxies, ed. S. Ryder, D. Pisano, M. Walker, & K. Freeman, 377

Kothes, R., Landecker, T. L., & Gray, A. D. 2010, in Astronomical Society of the Pacific Conference Series, Vol. 438, Astronomical Society of the Pacific Conference Series, ed. R. Kothes, T. L. Landecker, & A. G. Willis, 415

Kramer, C., Abreu-Vicente, J., García-Burillo, S., Relaño, M., Aalto, S., Boquien, M., Braine, J., Buchbender, C., Gratier, P., Israel, F. P., Nikola, T., Röllig, M., Verley, S., van der Werf, P., & Xilouris, E. M. 2013, A&A, 553, A114

Kramer, C., Boquien, M., Braine, J., Buchbender, C., Calzetti, D., Gratier, P., Mookerjea, B., Relaño, M., & Verley, S. 2011, in EAS Publications Series, Vol. 52, EAS Publications Series, ed. M. Röllig, R. Simon, V. Ossenkopf, & J. Stutzki, 107–112

Kravtsov, A. V., Klypin, A. A., Bullock, J. S., & Primack, J. R. 1998, ApJ, 502, 48

Landecker, T. L., Dewdney, P. E., Burgess, T. A., Gray, A. D., Higgs, L. A., Hoffmann, A. P., Hovey, G. J., Karpa, D. R., Lacey, J. D., Prowse, N., Purton, C. R., Roger, R. S., Willis, A. G., Wyslouzil, W., Routledge, D., & Vaneldik, J. F. 2000, A&AS, 145, 509

Lauer, T. R., Faber, S. M., Ajhar, E. A., Grillmair, C. J., & Scowen, P. A. 1998, AJ, 116, 2263

Li, H.-B. & Henning, T. 2011, Nature, 479, 499

Lockman, F. J., Free, N. L., & Shields, J. C. 2012, AJ, 144, 52

Łokas, E. L. & Mamon, G. A. 2001, MNRAS, 321, 155

Lynden-Bell, D., Faber, S. M., Burstein, D., Davies, R. L., Dressler, A., Terlevich, R. J., & Wegner, G. 1988, ApJ, 326, 19

Magrini, L., Corradi, R. L. M., Mampaso, A., & Perinotto, M. 2000, A&A, 355, 713

Marcelin, M., Amram, P., Balard, P., Balkowski, C., Boissin, O., Boulesteix, J., Carignan, C., Daigle, O., de Denus Baillargeon, M.-M., Epinat, B., Gach, J.-L., Hernandez, O., Rigaud, F., & Vallée, P. 2008, in Society of Photo-Optical Instrumentation Engineers (SPIE) Conference Series, Vol. 7014, Society of Photo-Optical Instrumentation Engineers (SPIE) Conference Series

Martínez-Delgado, D., Peñarrubia, J., Jurić, M., Alfaro, E. J., & Ivezić, Z. 2007, ApJ, 660, 1264

Mateo, M. 1998, Annual review of Astronomy and Astrophysics, 36, 435

Mazurek, T. J. 1982, in Astrophysics and Space Science Library, Vol. 93, Regions of Recent Star Formation, ed. R. S. Roger & P. E. Dewdney, 61–66

McConnachie, A. W., Ferguson, A. M. N., Irwin, M. J., Dubinski, J., Widrow, L. M., Dotter, A., Ibata, R., & Lewis, G. F. 2010, ApJ, 723, 1038

McConnachie, A. W., Irwin, M. J., Ferguson, A. M. N., Ibata, R. A., Lewis, G. F., & Tanvir, N. 2004, MNRAS, 350, 243

—. 2005, MNRAS, 356, 979

McConnachie, A. W., Irwin, M. J., Ibata, R. A., Dubinski, J., Widrow, L. M., & al. 2009, Nature, 461, 66

McLean, I. S. 2008, Electronic Imaging in Astronomy : Detectors and Instrumentation (Second Edition) (Praxis Publishing)

McLean, I. S. & Liu, T. 1996, ApJ, 456, 499

McMullin, J. P., Waters, B., Schiebel, D., Young, W., & Golap, K. 2007, in Astronomical Society of the Pacific Conference Series, Vol. 376, Astronomical Data Analysis Software and Systems XVI, ed. R. A. Shaw, F. Hill, & D. J. Bell, 127

Merritt, D., Graham, A. W., Moore, B., Diemand, J., & Terzić, B. 2006, AJ, 132, 2685

Milgrom, M. 1983a, ApJ, 270, 371

—. 1983b, ApJ, 270, 365

Minniti, D., Olszewski, E., & Rieke, M. 1994, in European Southern Observatory Conference and Workshop Proceedings, Vol. 51, European Southern Observatory Conference and Workshop Proceedings, ed. A. Layden, R. C. Smith, & J. Storm, 159

Moiseev, A. V. & Lozinskaya, T. A. 2012, MNRAS, 423, 1831

Moore, B., Governato, F., Quinn, T., Stadel, J., & Lake, G. 1998, ApJL, 499, L5

Moore, B., Quinn, T., Governato, F., Stadel, J., & Lake, G. 1999, MNRAS, 310, 1147

Munoz-Tunon, C., Tenorio-Tagle, G., Castaneda, H. O., & Terlevich, R. 1996, AJ, 112, 1636

Navarro, J. F., Frenk, C. S., & White, S. D. M. 1996a, ApJ, 462, 563

—. 1996b, ApJ, 462, 563

—. 1997, ApJ, 490, 493

Navarro, J. F., Hayashi, E., Power, C., Jenkins, A. R., Frenk, C. S., White, S. D. M., Springel, V., Stadel, J., & Quinn, T. R. 2004, MNRAS, 349, 1039

Navarro, J. F., Ludlow, A., Springel, V., Wang, J., Vogelsberger, M., White, S. D. M., Jenkins, A., Frenk, C. S., & Helmi, A. 2010, MNRAS, 402, 21

Neto, A. F., Gao, L., Bett, P., Cole, S., Navarro, J. F., Frenk, C. S., White, S. D. M., Springel, V., & Jenkins, A. 2007, MNRAS, 381, 1450

Newton, K. 1980, MNRAS, 190, 689

Ogiya, G. & Mori, M. 2011, ApJL, 736, L2

Oh, S.-H., de Blok, W. J. G., Brinks, E., Walter, F., & Kennicutt, Jr., R. C. 2011, AJ, 141, 193

Oh, S.-H., de Blok, W. J. G., Walter, F., Brinks, E., & Kennicutt, Jr., R. C. 2008, AJ, 136, 2761

Oosterloo, T., Fraternali, F., & Sancisi, R. 2007, AJ, 134, 1019

Ostriker, J. P. & Peebles, P. J. E. 1973, ApJ, 186, 467

Paturel, G., Andernach, H., Bottinelli, L., di Nella, H., Durand, N., Garnier, R., Gouguenheim, L., Lanoix, P., Marthinet, M. C., Petit, C., Rousseau, J., Theureau, G., & Vauglin, I. 1997, A&AS, 124, 109

Paturel, G., Teerikorpi, P., Theureau, G., Fouqué, P., Musella, I., & Terry, J. N. 2002, A&A, 389, 19

Plummer, H. C. 1911, MNRAS, 71, 460

Pontzen, A. & Governato, F. 2012, MNRAS, 421, 3464

Putman, M. E., Peek, J. E. G., Muratov, A., Gnedin, O. Y., Hsu, W., Douglas, K. A., Heiles, C., Stanimirovic, S., Korpela, E. J., & Gibson, S. J. 2009, ApJ, 703, 1486

Randriamampandry, T. H. & Carignan, C. 2014, MNRAS, 439, 2132

Regan, M. W. & Vogel, S. N. 1994, ApJ, 434, 536

Relaño, M., Verley, S., Pérez, I., Kramer, C., Calzetti, D., Xilouris, E. M., Boquien, M., Abreu-Vicente, J., Combes, F., Israel, F., Tabatabaei, F. S., Braine, J., Buchbender, C., González, M., Gratier, P., Lord, S., Mookerjea, B., Quintana-Lacaci, G., & van der Werf, P. 2013, A&A, 552, A140

Roberts, M. S. & Whitehurst, R. N. 1975, ApJ, 201, 327

Rubin, V. 2006, Physics Today, 59, 8

Rubin, V. C. & Ford, Jr., W. K. 1970, ApJ, 159, 379

Saha, A., Thim, F., Tammann, G. A., Reindl, B., & Sandage, A. 2006, ApJS, 165, 108

Salucci, P. & Burkert, A. 2000, ApJL, 537, L9

Sandage, A. & Humphreys, R. M. 1980, ApJL, 236, L1

Sanders, R. H. 1996, ApJ, 473, 117

Sanders, R. H. & McGaugh, S. S. 2002, ARAA, 40, 263

Sanders, R. H. & Verheijen, M. A. W. 1998, ApJ, 503, 97

Sault, R. J., Teuben, P. J., & Wright, M. C. H. 1995, in Astronomical Society of the Pacific Conference Series, Vol. 77, Astronomical Data Analysis Software and Systems IV, ed. R. A. Shaw, H. E. Payne, & J. J. E. Hayes, 433

Seigar, M. S. 2011, ISRN Astronomy and Astrophysics, 2011, 1

Smith, M. G. & Weedman, D. W. 1970, ApJ, 160, 65

—. 1971, ApJ, 169, 271

Smith, S. 1936, ApJ, 83, 23

Spitzer, Jr., L. & Tomasko, M. G. 1968, ApJ, 152, 971

Springel, V., White, S. D. M., Jenkins, A., Frenk, C. S., Yoshida, N., Gao, L., Navarro, J., Thacker, R., Croton, D., Helly, J., Peacock, J. A., Cole, S., Thomas, P., Couchman, H., Evrard, A., Colberg, J., & Pearce, F. 2005, Nature, 435, 629

Stonkutė, R., Vansevičius, V., Arimoto, N., Hasegawa, T., Narbutis, D., Tamura, N., Jablonka, P., Ohta, K., & Yamada, Y. 2008, AJ, 135, 1482

Swaters, R. A., Madore, B. F., & Trewhella, M. 2000, ApJL, 531, L107

Swaters, R. A., Sanders, R. H., & McGaugh, S. S. 2010, ApJ, 718, 380

Swaters, R. A., Schoenmakers, R. H. M., Sancisi, R., & van Albada, T. S. 1999, MNRAS, 304, 330

Tenorio-Tagle, G. 1979, A&A, 71, 59

Tenorio-Tagle, G., Munoz-Tunon, C., & Cox, D. P. 1993, ApJ, 418, 767

Teyssier, R., Pontzen, A., Dubois, Y., & Read, J. I. 2013, MNRAS, 429, 3068

Tosaki, T., Kuno, N., Onodera, Rie, S. M., Sawada, T., Muraoka, K., Nakanishi, K., Komugi, S., Nakanishi, H., Kaneko, H., Hirota, A., Kohno, K., & Kawabe, R. 2011, PASJ, 63, 1171

van Albada, T. S., Bahcall, J. N., Begeman, K., & Sancisi, R. 1985, ApJ, 295, 305

van der Hulst, J. M., Terlouw, J. P., Begeman, K. G., Zwitser, W., & Roelfsema, P. R. 1992, in Astronomical Society of the Pacific Conference Series, Vol. 25, Astronomical Data Analysis Software and Systems I, ed. D. M. Worrall, C. Biemesderfer, & J. Barnes, 131

van der Kruit, P. C. & Searle, L. 1981, A&A, 95, 105

Vogelaar, M. G. R. & Terlouw, J. P. 2001, in Astronomical Society of the Pacific Conference Series, Vol. 238, Astronomical Data Analysis Software and Systems X, ed. F. R. Harnden, Jr., F. A. Primini, & H. E. Payne, 358

Warner, P. J., Wright, M. C. H., & Baldwin, J. E. 1973, MNRAS, 163, 163

White, S. D. M. & Rees, M. J. 1978, MNRAS, 183, 341

Wilson, C. D. & Scoville, N. 1989, ApJ, 347, 743

Wolfe, S. A., Pisano, D. J., Lockman, F. J., McGaugh, S. S., & Shaya, E. J. 2013, Nature, 497, 224

Wu, X., Zhao, H., Famaey, B., Gentile, G., Tiret, O., Combes, F., Angus, G. W., & Robin, A. C. 2007, ApJL, 665, L101

Yang, H., Chu, Y.-H., Skillman, E. D., & Terlevich, R. 1996, AJ, 112, 146

Zaritsky, D., Elston, R., & Hill, J. M. 1989, AJ, 97, 97

Zhao, H. 1996, MNRAS, 278, 488

Zhao, H. S. & Famaey, B. 2006, ApJL, 638, L9

Zwicky, F. 1933, Helvetica Physica Acta, 6, 110

—. 1937, ApJ, 86, 217

Annexes

Annexe A

Observation Fabry Perot à l'OMM

A.1 Matériel

Pour une bonne mission il faut toujours s'assurer d'avoir ;

- La camera
  À l'OMM il y a deux cameras Andor (1024x1024 et 512x512) et la caméra prototype des caméras de la compagnie nüvü Cameras.
- Le câble Andor et ceux du contrôleur CCCP.
- L'ordinateur d'acquisition (Macbook) et l'ensemble de ses accessoires.
- Le CS100 (qui est rangé généralement dans la salle 'Carignan').
- Le bon FP .
- Des écrans supplémentaires
- Un bon câble réseau. Le câble réseau permet de transférer les données de l'ordinateur du télescope à l'ordinateur d'acquisition.
- Tous les connecteurs du FP.
- Un des ordinateurs Rackable. Deux ordinateurs permettent de faire la connection avec les différents types de camera. Se rassurer que celui qui sera mis au télescope contient la carte PCI qu'il faut.
- Les bons filtres. Pour les cibles à observer faire un calcul des longueurs d'onde avec la variation de température. Un ensemble d'une vingtaine de filtres interférentiels est disponible à l'OMM.

A.2 Applications pour l'acquisition : Guide des observations Fabry Perot à l'OMM

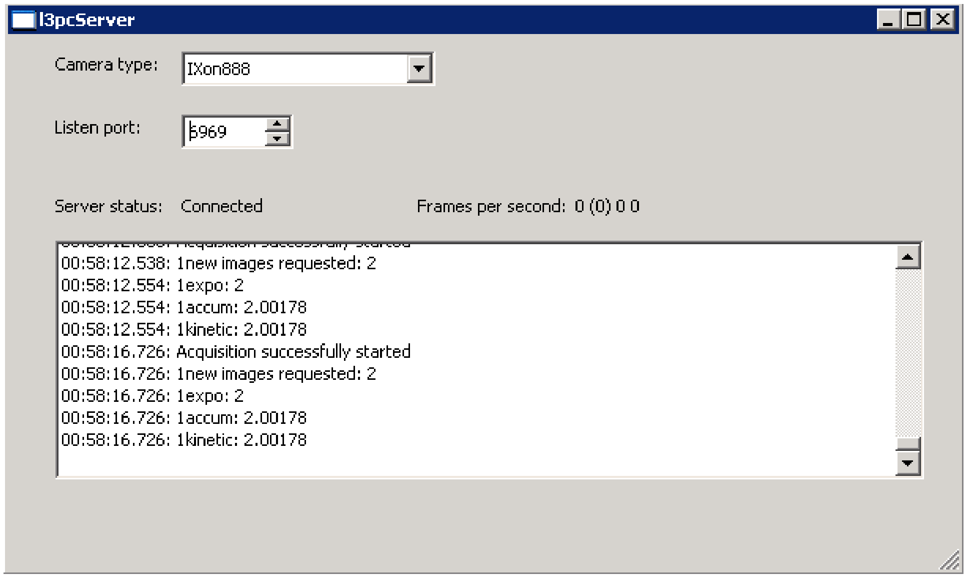

Camera type: IXon888

Listen port: 6969

Server status: Connected

Frames per second: 0 (0) 0 0

```
00:58:12.538: 1new images requested: 2
00:58:12.554: 1expo: 2
00:58:12.554: 1accum: 2.00178
00:58:12.554: 1kinetic: 2.00178
00:58:16.726: Acquisition successfully started
00:58:16.726: 1new images requested: 2
00:58:16.726: 1expo: 2
00:58:16.726: 1accum: 2.00178
00:58:16.726: 1kinetic: 2.00178
```

FIGURE A.24: L'image montre le statu de connexion de la camera. l3fpserver est installé sur l'ordinateur lié à la camera. Cet outil permet à l'utilisateur de passer les commandes à la camera en passant par un ordinateur du télescope.

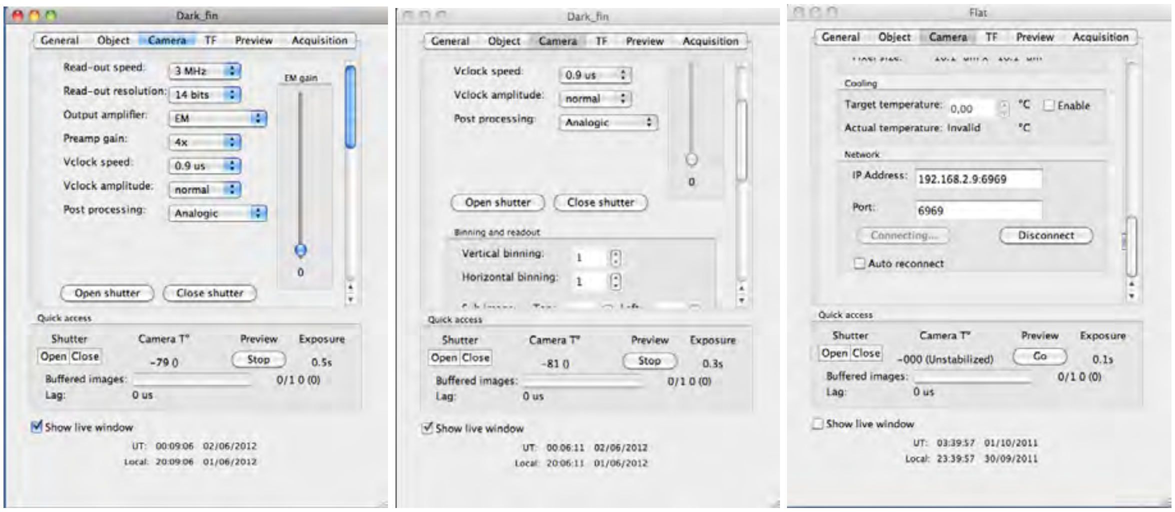

Read-out speed: 3 MHz
Read-out resolution: 14 bits
Output amplifier: EM
Preamp gain: 4x
Vclock speed: 0.9 us
Vclock amplitude: normal
Post processing: Analogic
Camera T°: -79 0
Exposure: 0.5s
Buffered images: 0/1 0 (0)
Lag: 0 us
☑ Show live window
UT: 00:09:06 02/06/2012
Local: 20:09:06 01/06/2012

Vclock speed: 0.9 us
Vclock amplitude: normal
Post processing: Analogic
Vertical binning: 1
Horizontal binning: 1
Camera T°: -81 0
Exposure: 0.3s
Buffered images: 0/1 0 (0)
Lag: 0 us
☑ Show live window
UT: 00:06:11 02/06/2012
Local: 20:06:11 01/06/2012

Target temperature: 0,00 °C ☐ Enable
Actual temperature: Invalid °C
IP Address: 192.168.2.9:6969
Port: 6969
☐ Auto reconnect
Camera T°: -000 (Unstabilized)
Exposure: 0.1s
Buffered images: 0/1 0 (0)
Lag: 0 us
☐ Show live window
UT: 03:39:57 01/10/2011
Local: 23:39:57 30/09/2011

FIGURE A.25: Les trois images montrent les options de réglage de la camera.

Cette figure comporte les options de réglages disponibles pour la mise en route de la caméra. Nous avons mis par défaut les paramètres d'observation. Ces paramètres peuvent être changés, mais les plus sensibles sont fixés afin de garder la stabilité de la caméra.

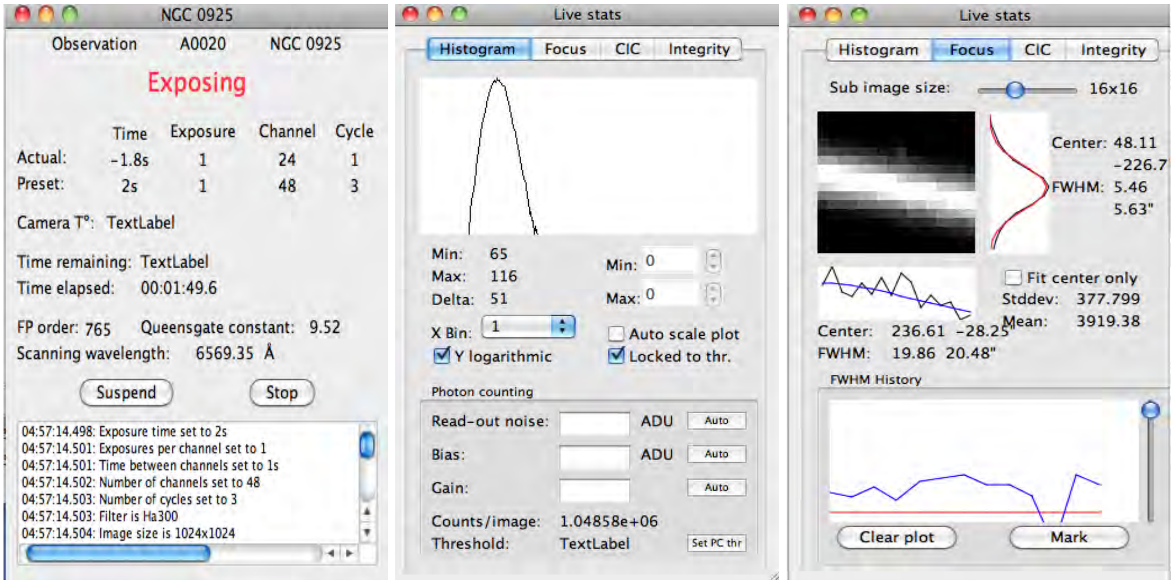

Observation A0020 NGC 0925

	Time	Exposure	Channel	Cycle
Actual:	-1.8s	1	24	1
Preset:	2s	1	48	3

Camera T°: TextLabel
Time remaining: TextLabel
Time elapsed: 00:01:49.6
FP order: 765 Queensgate constant: 9.52
Scanning wavelength: 6569.35 Å

```
04:57:14.498: Exposure time set to 2s
04:57:14.501: Exposures per channel set to 1
04:57:14.501: Time between channels set to 1s
04:57:14.502: Number of channels set to 48
04:57:14.503: Number of cycles set to 3
04:57:14.503: Filter is Ha300
04:57:14.504: Image size is 1024x1024
```

Min: 65
Max: 116
Delta: 51
Min: 0
Max: 0
X Bin: 1
☐ Auto scale plot
☑ Y logarithmic
☑ Locked to thr.
Read-out noise: ADU
Bias: ADU
Gain:
Counts/image: 1.04858e+06
Threshold: TextLabel

Sub image size: 16x16
Center: 48.11 -226.7
FWHM: 5.46 5.63"
☐ Fit center only
Stddev: 377.799
Mean: 3919.38
Center: 236.61 -28.25
FWHM: 19.86 20.48"

FIGURE A.26: Acquisition de données : panneaux de contrôle du fonctionnement et de la progression des acquisitions. L'image de gauche donne l'évolution des acquisitions, celle du milieu donne en temps réel les statistiques des images enregistrées. L'image de droite donne le seing et sa variation en temps réel.

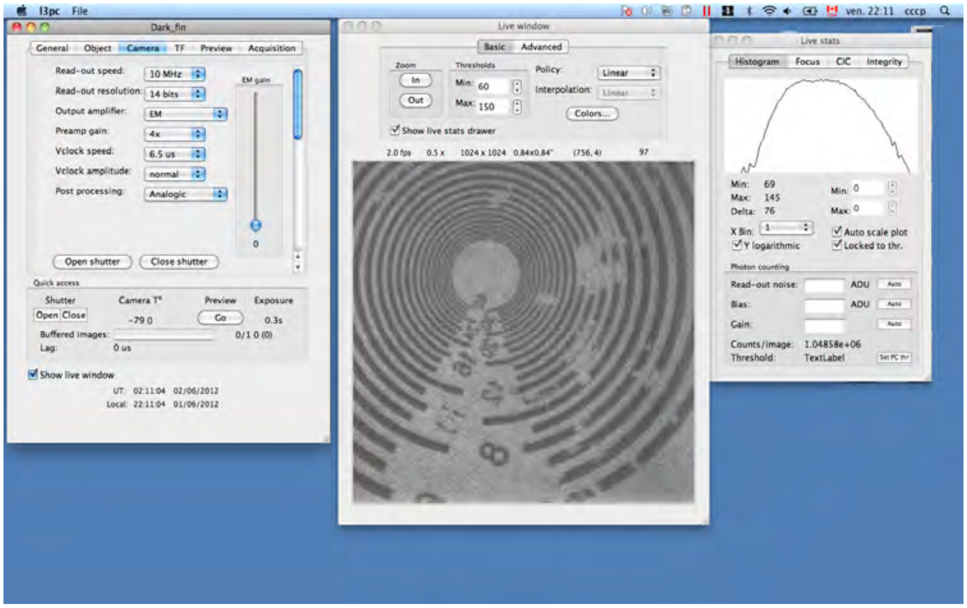

Read-out speed: 10 MHz
Read-out resolution: 14 bits
Output amplifier: EM
Preamp gain: 4x
Vclock speed: 6.5 us
Vclock amplitude: normal
Post processing: Analogic
Shutter: Open Close
Camera T°: -79 0
Preview
Exposure: 0.3s
Buffered images: 0/1 0 (0)
Lag: 0 us
☑ Show live window
UT: 02:11:04 02/06/2012
Local: 22:11:04 01/06/2012

Min: 60
Max: 150
Policy: Linear
Interpolation: Linear
☑ Show live stats drawer
2.0 fps 0.5 x 1024 x 1024 0.84x0.84" (756, 4) 97

Min: 69
Max: 145
Delta: 76
Min: 0
Max: 0
X Bin: 1
☑ Auto scale plot
☑ Y logarithmic
☑ Locked to thr.
Read-out noise: ADU
Bias: ADU
Gain:
Counts/image: 1.04858e+06
Threshold: TextLabel

FIGURE A.27: Réglage du foyer en début de mission ou après changement de température.

Pour régler la position des lentilles, un objet (e.g. feuille millimétrique) est posé dans le chemin optique du réducteur focal et de fins réglages sont faits sur la position des lentilles pour avoir la netteté dans la camera. Pour la finition de mise au foyer et pour avoir un foyer net une étoile est observée dans le ciel et le foyer du télescope est réglé avec précision.

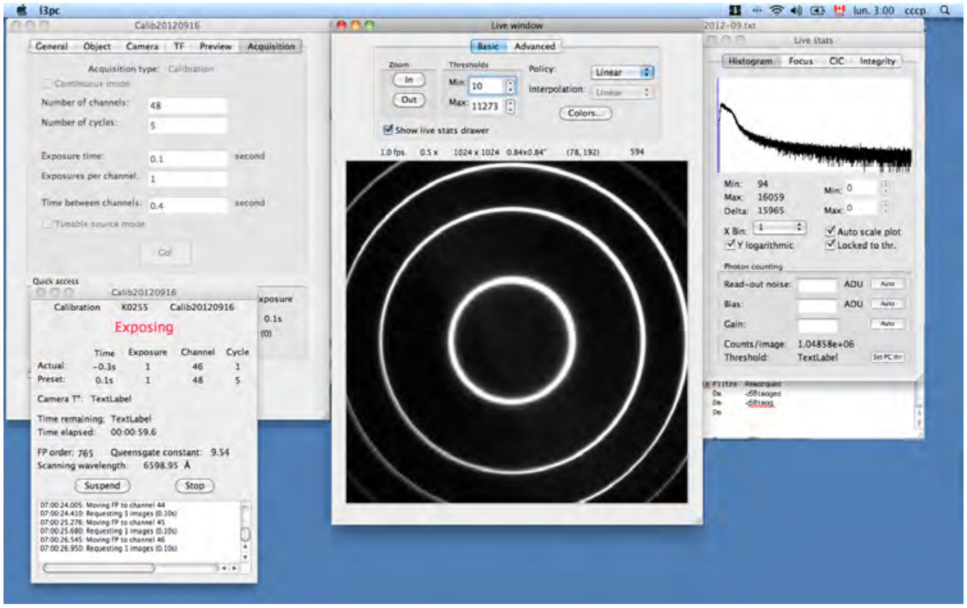

Acquisition type: Calibration
Number of channels: 48
Number of cycles: 5
Exposure time: 0.1 second
Exposures per channel: 1
Time between channels: 0.4 second

Calibration K0255 Calib20120916
Exposing

	Time	Exposure	Channel	Cycle
Actual:	-0.3s	1	46	1
Preset:	0.1s	1	48	5

Camera T°: TextLabel
Time remaining: TextLabel
Time elapsed: 00:00:59.6
FP order: 765 Queensgate constant: 9.54
Scanning wavelength: 6598.95 Å

```
07:00:24.005: Moving FP to channel 44
07:00:24.410: Requesting 1 images (0.10s)
07:00:25.276: Moving FP to channel 45
07:00:25.680: Requesting 1 images (0.10s)
07:00:26.545: Moving FP to channel 46
07:00:26.950: Requesting 1 images (0.10s)
```

Min: 10
Max: 11273
Policy: Linear
Interpolation: Linear
☑ Show live stats drawer
1.0 fps 0.5 x 1024 x 1024 0.84x0.84" (78, 192) 594

Min: 94
Max: 16059
Delta: 15965
Min: 0
Max: 0
X Bin: 1
☑ Y logarithmic
☑ Auto scale plot
☑ Locked to thr.
Read-out noise: ADU
Bias: ADU
Gain:
Counts/image: 1.04858e+06
Threshold: TextLabel

FIGURE A.28: Acquisition de données : image des anneaux du FP. Exposition en mode calibration

Cette image montre la visualisation des anneaux donnés par la lampe de Néon pendant la calibration. La forme des anneaux indique du parallélisme du FP dans un plan du faisceau collimé.

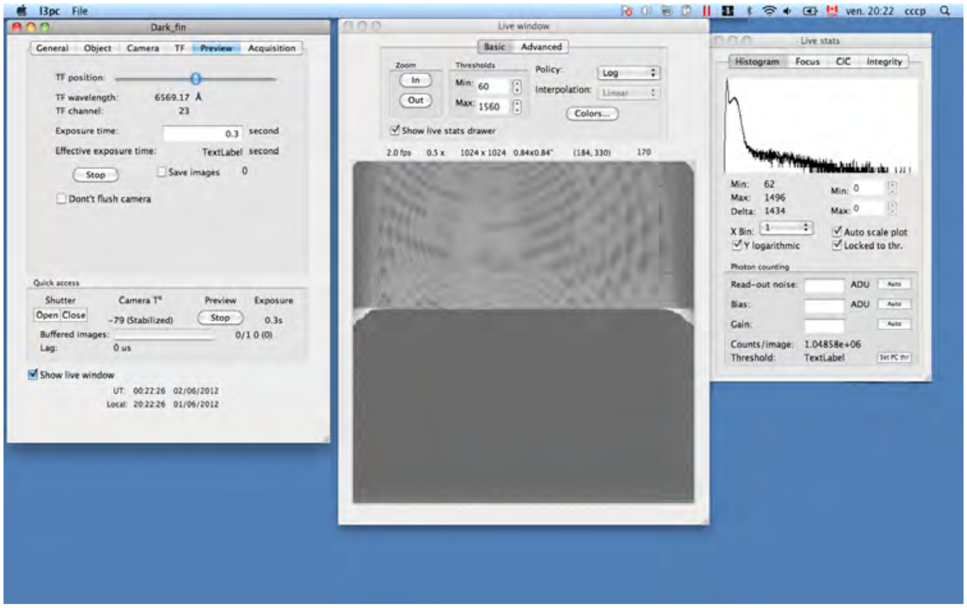

TF position:
TF wavelength: 6569.17 Å
TF channel: 23
Exposure time: 0.3 second
Effective exposure time: TextLabel second
☐ Save images 0
☐ Don't flush camera

Shutter	Camera T°	Preview	Exposure
Open Close	-79 (Stabilized)	Stop	0.3s

Buffered images: 0/1 0 (0)
Lag: 0 us
☑ Show live window
UT: 00:22:26 02/06/2012
Local: 20:22:26 01/06/2012

Min: 60
Max: 1560
Policy: Log
Interpolation: Linear
☑ Show live stats drawer
2.0 fps 0.5 x 1024 x 1024 0.84x0.84" (184, 330) 170

Min: 62
Max: 1496
Delta: 1434
Min: 0
Max: 0
X Bin: 1
☑ Y logarithmic
☑ Auto scale plot
☑ Locked to thr.
Read-out noise: ADU
Bias: ADU
Gain:
Counts/image: 1.04858e+06
Threshold: TextLabel

FIGURE A.29: Problème de mise en marche de la camera

L'image ci dessus montre un cas de mal fonctionnement de la camera. Cette image révèle un problème de transfert sur le panneau d'affichage central. La forme de l'histogramme seulement ne permettrait pas de le savoir.

Annexe B

Reducl3fp

Reducl3fp est un routine mis au point pour construire les cubes 3D calibrés en longueur d'onde. Reducl3fp permet de prendre en charge les images de type CCD. En effet les programmes de réduction de données FD ne prennent pas des format .fits ou fits.gz comme données brutes, alors cette routine est mise en place afin d'intégrer ces types de données. Elle permet de corriger les bruits provenant de la camera, prend en compte le gain, le dark, le biais et corrige et calibre les données brutes.

pro reducl3fp, baseDir, gainDir, obsDir, outToFits=f, darkDir=darkDir, calibDir=calibDir, flatDir=flatDir, guidingCorrection=guidingCorrection, sequential=sequential, keepAll=keepAll, photonCounting=photonCounting, ignoreCycle=ignoreCycle, nocosmic=nocosmic, cosmicsWithinChannel=cosmicsWithinChannel, film=film

B.1 Mots clés

- *baseDir* : indique le répertoire de travail.
- *gainDir* donne le répertoire qui contient les observations pour la correction du gain.
- *obsDir* donne le répertoire des observations.
- *outToFits* si cette option est à 1, les cartes produites sont en format .FITS sinon les fichiers seront en formats compatibles avec ADHOCs.
- *darkDir* indique le répertoire dans lequel se trouve les fichiers destinés à la correction du courant sombre.
- *calibDir* pointe les dossier qui contient les calibrations.
- *guidingCorrection* si cette option est à 1 alors une correction du guidage du télescope est

réalisée ; cela nécessite une interaction avec le programme pour le choix des étoiles de guidage.

– *photonCounting* doit être à 1 pour que la réduction soit faite en comptage de photons.
– *ignoreCycle* permet d'écarter les cycles compromis, douteux, perturbés ou pollués pendant l'observation.
– *nocosmic* mettre à 1 pour enlever les rayons cosmiques enregistrés (différents du continuum).

B.2 Produit

A la fin de la réduction, les principaux produits sont les fichiers lambda.fits et lambda.ad3. Ces fichiers sont les fichiers qui donnent les cubes calibrés en longueur d'onde, corrigés des défaut de guidage et des rayons cosmiques (si désiré). Les flats sont pris en compte si l'utilisateur le demande. D'autres fichiers sont produits entre autres les fichiers de calibration, de correction de phase, de finesse etc...

Appel de reducl3fp

reducl3fp, '/Users/observations/megantic', 'Z0888', 'Z0889', outtofits=1, calibDir='Z0887', photonCounting=1, cosmicsWithinChannel=1, guidingCorrection=0, nocosmic=1

Dans ce cet exemple de lancement, reducl3fp cherchera l'ensemble des fichiers et dossiers d'observation pour les opérations dans le dossier "/Users/observations/megantic". Pour intégrer les fichiers d'observation, la routine cherchera dans le sous dossier 'Z0888'. Pour le calcul des gains, les fichiers dans le dossier 'Z0889' seront utilisés. La calibration en longueur d'onde se fera en utilisant le dossier 'Z0887'. Le paramètre photonCounting est mis à 1 pour signaler l'utilisation de l'option de comptage de photons dans la construction des canaux. Pour corriger les effets de rayons cosmiques, le paramètre cosmicsWithinChannel est à 1. guidingCorrection=1 indique que des étoiles du champ seront utilisées pour évaluer et corriger la stabilité du guidage lors des observations.

Annexe C

Computeeverything

Les descriptions de Computeeverything sont celles tirées de la thèses de Benoît Epinat et de la thèse de maitrise d'Olivier Daigle. Dans mes analyses, ces routines ont été mises à jour pour mes données. Computeeverything est écrit en IDL et est en cours de migration vers Python. Les étapes utilisées dans Computeeverything sont les suivantes :

- L'intégration des fichiers d'observation ;
- La construction du fichier de phase à partir du ou des fichiers de calibration ;
- L'application de la phase parabolique aux données brutes d'observation ;
- Le lissage spectral du cube de données ;
- La correction spectrale du cube de données en utilisant le spectre du ciel nocturne contenu dans le cube de données ;
- La soustraction du spectre du ciel nocturne du cube de données ;
- Le lissage adaptatif du cube de données ;
- L'extraction des cartes de vitesses radiales, flux monochromatique, continu et des largeurs des raies d'émission ;
- La recherche automatique des raies d'émission dans les régions à très faible flux monochromatique, corrélées aux plus fortes raies d'émission environnantes ;
- L'ajustement automatique d'un cube de données en fonction des vitesses radiales.

Deux syntaxes existent dans l'utilisation de Computeeverything. La première manière consiste à appeler la routine en lui passant des mots clés et la seconde manière consiste à générer un fichier de configuration qui se chargera de ré attribuer les mots clés pendant l'appel de la fonction. L'application reducwizard est utilisée pour créer les fichiers de configuration.

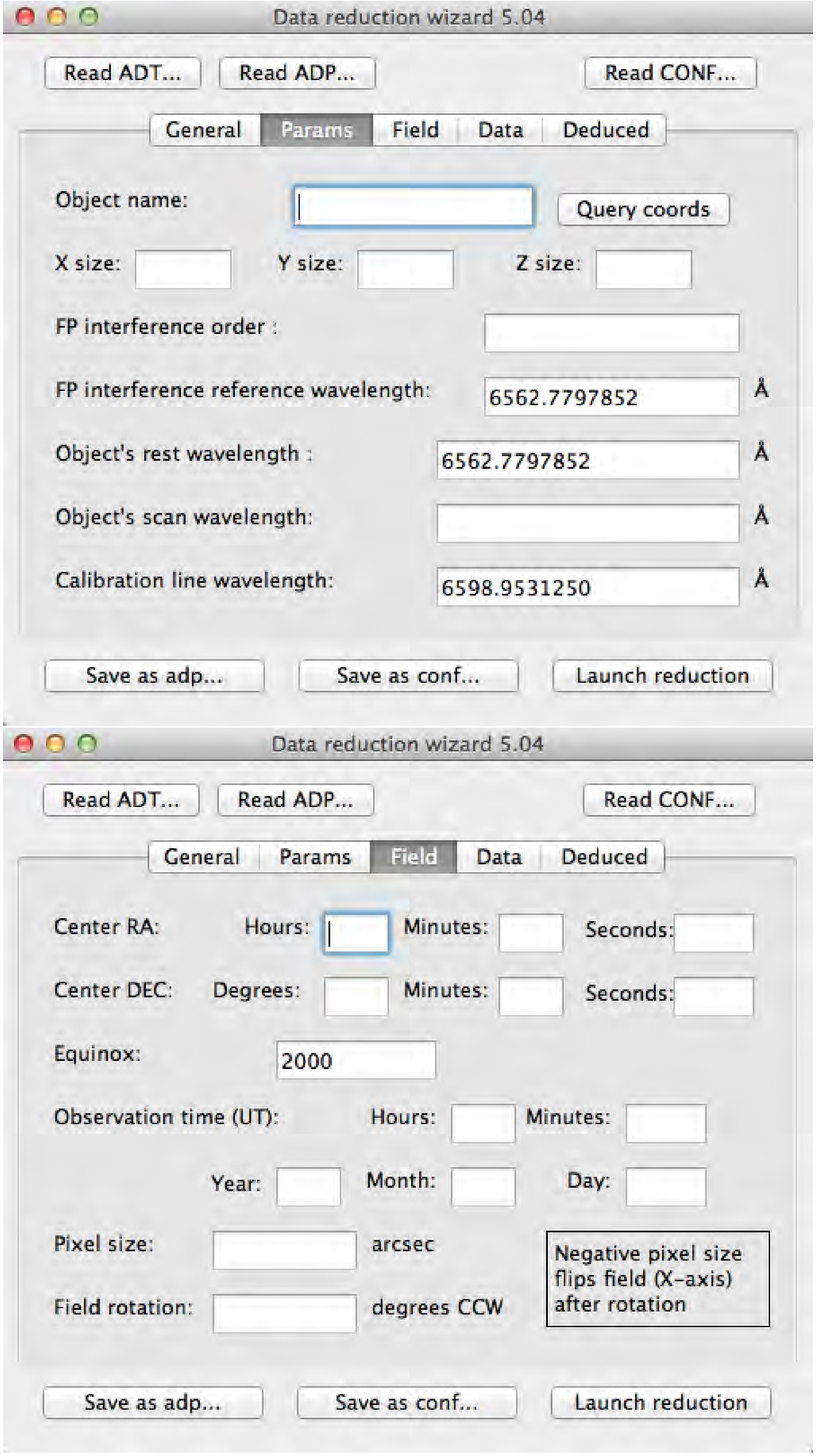

Object name:
X size: Y size: Z size:
FP interference order :
FP interference reference wavelength: 6562.7797852 Å
Object's rest wavelength : 6562.7797852 Å
Object's scan wavelength: Å
Calibration line wavelength: 6598.9531250 Å

Center RA: Hours: Minutes: Seconds:
Center DEC: Degrees: Minutes: Seconds:
Equinox: 2000
Observation time (UT): Hours: Minutes:
Year: Month: Day:
Pixel size: arcsec
Field rotation: degrees CCW

Negative pixel size flips field (X-axis) after rotation

FIGURE C.1: Deux fenêtres de l'application reducwizard pour la conception du fichier de configuration ou la rédaction du fichier adp pour la réduction en IDL.

Entête de computeeverything

pro computeeverything, dir, cieldir, calibdir, adadir, conffile = conffile, name = name, astron = astron, plot = plot, fits = fits, correctguiding = correctguiding, guidingnobreak = guidingnobreak, igno- recycle = ignorecycle, spectral_smooth = spectral_smooth, snr = snr, targetsn = targetsn, fwhm = fwhm, remove_sky = remove_sky, ohmap_remove_sky = ohmap_remove_sky, ohmap_degree = ohmap_degree, maps = maps, clean = clean, manual_clean = manual_clean, fsr=fsr, align = align, thresholdalign = thresholdalign, maxalign = maxalign, passalign = passalign, coadd = coadd, conti- numflat = continumflat, noflat = noflat, autorvmonolevel = autorvmonolevel, expand = expand, adjustrv_nosmooth = adjustrv_nosmooth, tryhard_voro = tryhard_voro, calibadhoc = calibadhoc, startfrom- neb = startfromneb, adacieldir = adacieldir, scalefactorciel = scalefactorciel, exit_at_end = exit_at_end

L'utilisation de cette routine et de bien d'autres comme coaddlambdafiles, addcubesastrometry, ghost2d, ghost3d, readad3, writead3, fitsToAd3, fitsToAd2, readad2 ou ad2ToFits sont nécessaires dans la réduction de données FP, elles se trouvent dans l'Annexe B de la thèse de Benoit Epinat (Epinat, 2008).

Annexe D

Mosaic3Dcube

Mosaic3dcube est une routine IDL mise au point pour gérer les cubes 3D des observations Fabry-Perot. Mosaic3dcube permet de créer des mosaïques de données FP en utilisant des sous cubes pour des fins de dépouillement et d'analyse cinématiques. Cette routine peut être utilisée en association avec computeeverything.

Ce programme permet de créer automatiquement les entêtes nécessaires, les dossiers et les clés qu'il faut à la réduction. Mosaic3dcube fait appel à des parties du package *Montage* pour faire les projections sur le plan du ciel. L'interactivité du programme est de base mais les étapes importantes pour une bonne réduction sont traitées de manière rigoureuse avec plusieurs options et mots clés.

Entête de MosaicCube3D

pro MosaicCube3D, dir=dir, Obj=obj, mk_framesfromlambdas=mk_framesfromlambdas, CommonSubcubeNames=CommonSubcubeNames, pond_ncy=pond_ncy, Mtotal_size=Mtotal_size, overlapfile=overlapfile, MframeMode=MframeMode, Bgcorr=Bgcorr, flatfile=flatfile, clean=clean, END_EXIT=End_exit, mozhelp=mozhelp, Sigclip=Sigclip, lambda_clip=lambda_clip

Les mots clés de MosaicCube3D

- dir : désigne le répertoire de travail.
- obj : donne le nom de la cible. Important de donner un nom valide pour l'entête (header), qui n'existe pas, ou n'est pas incomplet.
- mk_framesfromlambdas : est la clé qui permet de commencer avec les cubes set 1,
- CommonSubcubeNames : désigne mot clé à rechercher dans les cubes 3D si le mk_framesfromlambdas est activé.
- pond_ncy : permet de faire la pondération en temps ou du nombre de cycles d'observation.

La pondération peut se faire vers le Cycle pondération le minimum ou vers le maximum.

- Mtotal_size : donne la taille de la mosaïque.
- overlapfile : autorise les corrections dans les zones de superposition.
- MframeMode : permet de spécifier à quel cube de la mosaïque il faut commencer.
- Bgcorr : à 1, cette clé permet la correction du background entre les cubes.
- flatfile : est la clé autorisant l'application des flats.
- Sigclip :
- exit_at_end : permet de sortir d'idl à la fin.

Plusieurs de ces mots clés peuvent être ignorés.

Le produit de MosaicCube3D

Le programme donnera un cube 3D qui est la mosaïque des sous cubes dans les dossiers de départ (dossier datadir), une carte de la couverture, une carte des superpositions et portions de zones superposées. Si l'option de correction du fond est activée, alors des cartes supplémentaires sur l'ajustement du fond sont produites.

Appel de MosaicCube3D

MosaicCube3D, dir=dir, obj=obj, mk_framesfromlambdas=mk_framesfromlambdas, CommonSubcubeNames=CommonSubcubeNames, pond_ncy=pond_ncy, Mtotal_size=Mtotal_size, overlapfile=overlapfile, MframeMode=MframeMode, Bgcorr=Bgcorr, flatfile=flatfile, clean=clean, END_EXIT=End_exit, mozhelp=mozhelp, Sigclip=Sigclip, lambda_clip=lambda_clip

Annexe E

Contributions sur HI et Hα de M33

Tracing the Ancestry of Galaxies (on the land of our ancestors)
Proceedings IAU Symposium No. 277, 2010
C. Carignan, F. Combes & K.C. Freeman, eds.
© International Astronomical Union 2011
doi:10.1017/S1743921311022599

HI and Hα Mapping of M31 & M33

Z. S. Kam[1] , **C. Carignan**[1,3,4], **L. Chemin**[2], **O. Hernandez**[1],
M. de Denus-Baillargeon[1] and **Y. Djabo**[1]

[1] Laboratoire d'Astrophysique Expérimentale (LAE), Département de physique,
Université de Montréal, C.P. 6128, Succ. Centre-ville, Montréal, Qc, Canada H3C 3J7

[2] Laboratoire d'Astrophysique de Bordeaux 2, rue de l'Observatoire,
BP 89, 33271 Floirac Cedex France.

[3] Observatoire d'Astrophysique de l'Université de Ouagadougou (ODAUO),
UFR/SEA, B.P. 7021, Ouagadougou 03, Burkina Faso

[4] Department of Astronomy, University of Cape Town,
Private Bag X3, Rondebosh 7701, South Africa

Résumé. We performed a deep HI and Hα mapping of M31 and M33 in order to get accurate kinematical data of those two galaxies and also to make a comparison between the HI and Hα kinematics. The HI data were obtained with the DRAO interferometer and the Hα data with the Fabry-Perot system of the Observatoire du mont Mégantic using an EMCCD as a detector. These data will give us the best possible datasets to derive accurate rotation curves and mass models for those two Local Group spirals and provide some new data for the HII regions studies of these galaxies. While the HI observations are of low resolution ($\sim$1 arcmin), the high resolution of the Hα data ($\sim$1 arcsec) should allow us to get much more details in the central regions, allowing at the same time a much better determination of the kinematical parameters. Hence, the inner part of the rotation curve, so inportant to constraint properly the mass models, will be determined more accurately.

Keywords. Galaxy : individual : M31, M33, Galaxy : kinematics, ISM : lines : HI, Hα

1. Introduction and background

Messier 33 and Messier 31 are very interesting Local Group galaxies. There are, with the Milky Way, the three massive galaxies of the group. These galaxies give us the oportunity to study in great detail the interstellar medium, star formation, galaxy evolution and kinematic and dynamic of galaxies similar to the Milky Way (Klypin *et al.* 2002). We have thus two real laboratories for testing our models and theories on spiral structure and galaxy formation.

Andromeda was the subject of a large number of studies since 1612 (Brandt 1965; Braun 1991; Braun *et al.* 2009; Thilker *et al.* 2005; Carignan *et al.* 2006; Chemin *et al.* 2009; Corbelli *et al.* 2010). The neutral gas in this galaxy is observed with a great interest (Corbelli *et al.* 2010) and with technics more and more powerful. Interestingly, observations of the Large Magellanic Cloud, despite being a satellite of our Galaxy, may give some clues on the past history of M31 (Kallivayalil *et al.* 2009; Yang & Hammer 2010). Hammer *et al.* (2010) and Yang & Hammer (2010) have proposed a dynamic model with the MW, M31 and the LMC, which reproduces M31's parameters with the LMC being a tidal dwarf ejected by M31 past merger process. Moreover, a large number of studies (mainly in HI) helped to have more information about its spiral arms, the interaction

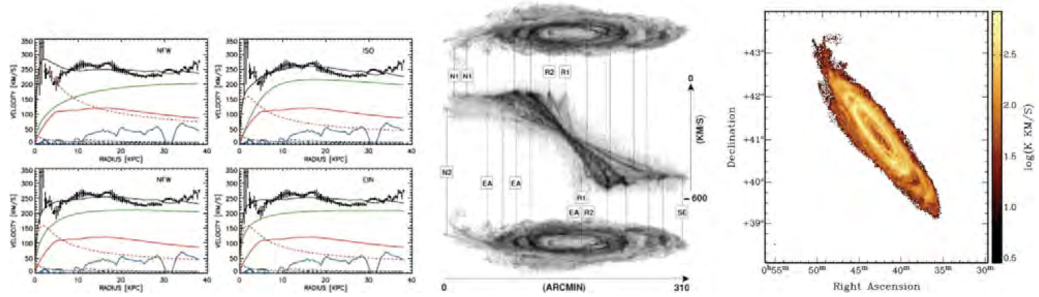

Fig. 1. HI kinematical results of M31 (Chemin *et al.* 2009) : (left) mass distribution models, (middle) 3D data cube showing its structures, (right) HI distribution.

with M32, its warped disk or its ring-like structures. Despite the low HI resolution in the inner part of M31, it is still possible to get some information about its the dark matter content (Chemin *et al.* 2009).

The Triangulum Galaxy (M33) is the third most massive galaxy of the Local Group. With a mass ∼ 10 times lower than M31 and the MW, M33 is not as well studied as its two neighbours. The major studies on M33 related to the molecular gas (CO), neutral and ionised gas, in some well known HII regions (Boulesteix *et al.* 1974; Lagrois & Joncas 2009). As is the case for M31, there is a lack of Hα kinematical studies at high resolution in the inner part of M33.

In this paper, we first discussed the HI kinematical studies of our Galaxy neighbours (Carignan *et al.* 2006; Chemin *et al.* 2009) and, in the next two sections, the HI and Hα observations are presented in more detail. The HI observations were taken with the DRAO radio interferometer and the Hα with the 1.6m telescope of the Observatoire du Mont Mégantic, using an optical Fabry-Perot system.

2. HI Kinematics of M31 and M33

The HI observations allow to get the kinematics on large scales. We already have those sensitive HI observations from DRAO observations : Chemin *et al.* (2009) for M31 ; Chemin (in preparation) for M33.

2.1. *M31*

The HI observations of M31 were the motor of this study. In fact, the HI velocities in M31 show peculiarities both at small and large radii (Chemin *et al.* 2009). Using those DRAO observations, Chemin *et al.* (2009) showed some new structures and also an increasing rotation curve at large radius. Part of his work is represented in figure 1. This figure shows on the left some velocities curves, with increasing velocities at large radii, and decreasing velocities at the center as well as at ∼ 30 kpc. These curves present also some difficulties to represent the inner part of the galaxy even using different mass models. Moreover, the HI profiles cannot explain the high velocities or components revealed by the CO observations. So another question is : what will we find for the Hα velocities at small radius ? Will they agree with the CO observations and CO velocities or with the HI ?

2.2. *M33*

Messier 33 has been observed in 2008 and 2009 with DRAO at 1 arcmin resolution and with a spectral sampling of 1 km.s^{-1} . Six DRAO fields were used to map the whole galaxy, with about 200 hours of integration per field. Single dish Arecibo HI observations from Putman *et al.* (2009) have also been used to recover shorter spacings. The first image of Figure 2 shows the preliminary integrated HI emission of M33. The bright inner disk of M33 is clearly identified as well as diffuse HI streams located in the north-western and south-eastern outer regions of the disk. Those streams correspond to the HI warp of the galaxy. HI column densities down to about 5 $\times 10^{19}$ atoms.cm^{-2} are observed in the warped structure (Chemin *et al.* in preparation).

3. Hα mapping and kinematics of M31 and M33

Hα observations have most of the time better resolution in the inner part of the galaxies. The observations in the Hα band were obtained at the OMM in the summer 2010 and more observations are to come in the 2011 summer. The OMM has a 1.6 m Ritchey-Chrétien telescope, located at the summit of mont Mégantic at an altitude of 1111m. We started observing M33 with an EMCCD, using the CCD Controller for Counting Photons (CCCP) (Daigle *et al.* 2008, 2009). With CCCP, it is possible to reduce the Clock Induced Charge (CIC - the major source of noise when the EMCCD is operated at high gain). This capability allows for greater efficiency in photon counting mode. Its low CIC rate renders possible the detection of faint fluxes down to $\sim$ 0.001 photon/pixel/image (Daigle *et al.* 2009). The camera has a field of $\sim 9.1'$ (the pixel scale $\sim$ 1.0 arcsec/pix). Each field was exposed for one hour. Frames were taken with 0.5 seconde/image, 10 images/channel and 48 chanels/cycle. The interference filter had a central wavelength of λ_c=6565.0 Å, and a FWHM of 15 Å. Maximum transmission was $\sim$ 80%. The FP interference order was p = 765 at Hα , with a Free Spectral Range (FSR) of 8.58 Å(391.77 km s^{1}). The mean Finesse during the observations was $\sim$ 16.5, with an etalon spectral resolution of $\sim$ 0.53 Å($\Delta\lambda$ = FSR(Å)/Finesse).

We expose also 20 to 30 minutes on the sky in order to subtract efficiently sky lines during the reduction. Between the observations of each field, a calibration cube was obtained. For the M33 mapping with this camera, we have defined more than thirty fields to allow overlap for mosaicing. The reduction system consists of the creation of a wavelength-sorted data cube corrected for airmass dependance, guiding shift, cosmic rays, dark, noise and gain. It takes also into account, ghosts correction (see Epinat 2008), heliocentric velocity correction, hanning spectral smoothing and sky subtraction (Daigle *et al.* 2006). Options as spatial binning procedure, single gaussian fitting procedure, deconvolution of the profile for the filter dependance, extraction of the velocity, dispersion and Hα integrated maps are possible (Hlavacek-Larrondo *et al.* 2010; Daigle *et al.* 2006). The right image of figure 2 shows, the radial velocity image of the field identified in the middle frame (no smoothing was applied). We use Adhocw to compute the RV maps. We present here one field of the first mosaic of this survey taken with the EMCCD and Fabry-Perot at OMM. These preliminary pictures are not accurate analyses of our survey but they give velocities higher than 120 $\pm$10 km.s^{-1} in an external field of the galaxy. More accurate values are coming soon (Kam *et al.*in preparation).

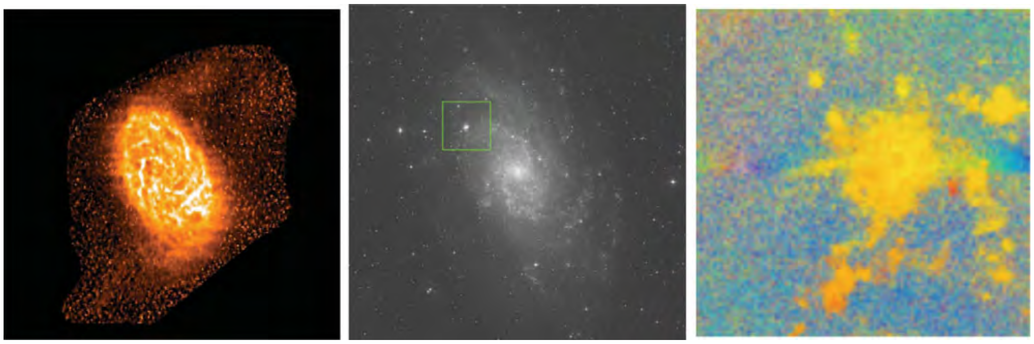

Fig. 2. (left) : preliminary integrated HI emission of M33 (Chemin *et al.*in preparation). (central) : DSS bleu image of M33 & the field of view of the camera is shown by a green square. (right) : preliminary results about the Hα mapping of M33 (Kam *et al.* in preparation).

4. Conclusion

M31 and M33 are two galaxies near the MW,. These galaxies are fairly typical of spiral galaxies. Their kinematics and dynamics give a good indication of other external galaxies, but also a good idea on our own Galaxy. Several studies of the kinematics of M33 and M31 were carried out in HI and Hα . Chemin *et al.* (2009) and Corbelli *et al.* (2010), present the most accurate kinematical parameters on large scale using the HI for M31. The results of these studies show the presence of new structures and increasing velocities in the outer parts of the galaxy.

Kinematics from HI for M33 on is presented by Warner *et al.* (1973); Huchtmeier (1973), and Westmeier *et al.* (2005). The HI does not give us as precise details as Hα because of the low spatial resolution and of beam smearing. Only a few studies at Hα exist on those galaxies : (Rubin & Ford 1970; Boulesteix & Monnet 1970; Boulesteix *et al.* 1974) presented some studies on those galaxies on small scales. This new mapping at Hα will allow us to calculate more precisely the kinematical parameters for those galaxies and to make a comparison of these results with those at HI already well-known. In fact, the capacities of our instrument allow to get more details and resolution in galaxies observations (Daigle *et al.* 2008, 2009).

References

Boulesteix, J., Courtes, G., Laval, A., Monnet, G., & Petit, H. 1974, *A&A*, 37, 33

Boulesteix, J. & Monnet, G. 1970, *A&A*, 9, 350

Brandt, F. 1965, *MNRAS*, 129, 309

Braun, R. 1991, *ApJ*, 372, 54

Braun, R., Thilker, D. A., Walterbos, R. A. M., & Corbelli, E. 2009, *ApJ*, 695, 937

Carignan, C., Chemin, L., Huchtmeier, W. K., & Lockman, F. J. 2006, *ApJL*, 641, L109

Chemin, L., Carignan, C., & Tyler, F. 2009, *ApJ*, 705, 1395

Corbelli, E., Lorenzoni, S., Walterbos, R., Braun, R., & Thilker, D. 2010, *A&A*, 511, A89

Daigle, O., Carignan, C., Gach, J., Guillaume, C., Lessard, S., Fortin, C., & Blais-Ouellette, S. 2009, *PASP*, 121, 866

Daigle, O., Carignan, C., Hernandez, O., Chemin, L., & Amram, P. 2006, *MNRAS*, 368, 1016

Daigle, O., Gach, J., Guillaume, C., Lessard, S., Carignan, C., & Blais-Ouellette, S. 2008, in SPIE Conference Series, Vol. 7014, 70146L

Epinat, B. e. a. 2008, *MNRAS*, 388, 500

Hammer, F., Yang, Y. B., Wang, J., Puech, M., Flores, H., & Fouquet, S. 2010, *ApJ*, 725, 542

Hlavacek-Larrondo, J., Carignan, C., Daigle, O., de Denus-Baillargeon, M., Marcelin, M., Epinat, B., & Hernandez, O. 2010, *MNRAS*, 1649

Huchtmeier, W. 1973, *A&A*, 22, 91

Kallivayalil, N., Besla, G., Sanderson, R., & Alcock, C. 2009, *ApJ*, 700, 924

Klypin, A., Zhao, H., & Somerville, R. S. 2002, *ApJ*, 573, 597

Lagrois, D. & Joncas, G. 2009, *ApJ*, 700, 1847

Putman, M. E., Peek, J. E. G., Muratov, A., Gnedin, O. Y., Hsu, W., Douglas, K. A., Heiles, C., Stanimirovic, S., Korpela, E. J., & Gibson, S. J. 2009, *ApJ*, 703, 1486

Rubin, V. C. & Ford, Jr., W. K. 1970, *ApJ*, 159, 379

Thilker, D. A., Braun, R., & Westmeier, T. 2005, in ASP Conference Series, Vol. 331, Extra-Planar Gas, ed. R. Braun, 113

Warner, P. J., Wright, M. C. H., & Baldwin, J. E. 1973, *MNRAS*, 163, 163

Westmeier, T., Braun, R., & Thilker, D. 2005, Astronomy and Astrophysics, 436, 15

Yang, Y. & Hammer, F. 2010, *ApJL*, 725, L24

SF2A 2012
S. Boissier, P. de Laverny, N. Nardetto, R. Samadi, D. Valls-Gabaud and H. Wozniak (eds)

KNOW (BETTER) YOUR NEIGHBOUR: NEW HI STRUCTURES IN MESSIER 33 UNVEILED BY A MULTIPLE PEAK ANALYSIS OF HIGH-RESOLUTION 21-CM DATA

Laurent Chemin[1], Claude Carignan[2], Tyler Foster[3] and Zacharie Sie Kam[4]

Abstract. In our quest to constrain the dynamical and structural properties of Local Group spirals from high-quality interferometric data, we have performed a neutral hydrogen survey in the direction of Messier 33. Here we present a few preliminary results from the survey and show the benefits of fitting the HI spectra by multiple peaks on constraining the structure of the Messier 33 disk. In particular we report on the discovery of new inner spiral-like and outer annular structures overlaying with the well-known main HI disk of Messier 33. Possible origins of the additional outer annular structure are presented.

Keywords: galaxies: individual (M33, NGC 598) – galaxies: ISM – galaxies: kinematics and dynamics – galaxies: structure – Local Group – Techniques: imaging spectroscopy

1 Context

The dynamical and structural properties of HI disks of nearby spirals mainly result from the analysis of the 0th and 1st moments of HI spectra obtained from single-dish and interferometric observations. Curiously more thorough analyses of HI spectra making profit from current high spectroscopic precision and sensitive cm-data remain rare.

In 2006 we have started a HI survey of the most massive spiral disks from the Local Group (except the Milky Way) to revisit their structure, kinematics and dynamics. Aperture synthesis at DRAO combined with short spacing data have been used to perform 21-cm observations of the Andromeda galaxy (Messier 31) at spectral resolution $\lesssim 5$ km s^{-1}, angular resolution ~ 300 pc ($D \sim 800$ kpc) and sensitivity down to $\sim 2 \times 10^{19}$ cm^{-2} (Chemin et al. 2009).

Since many spectra are far from being dominated by one single HI component we have shown that the moment analysis of datacubes was not appropriate (see Fig. 1 and §3.2 of Chemin et al. 2009, and left panel of Fig. 1 below). This is the reason why we developed a 'search and fit' algorithm of multiple (gaussian) components. Applied to new Messier 31 data this algorithm has allowed the detection of sometimes up to five HI significant components per profile, which had never been reported beforehand for nearby HI spirals. So many multiple peaks likely result from the combination of extreme projection effects of the warped Messier 31 disk with internal and external dynamical perturbations (spiral density wave, lagging halo, expanding gas shells, accretion of gas from the intergalactic medium or from nearby minor companions, etc). The discovery of outer HI spurs and spiral arm was also reported, as well as the characterization of the disk warp in terms of twist and tilt angles and the measurement of the most extended rotation curve for Messier 31.

We note that this kind of hyperspectral decomposition within multiple gaussian peaks is not new and has been used several times (e.g. Sicotte & Carignan 1997; Oh et al. 2008). It is nonetheless not generalized in HI studies. From a dynamical point-of-view, the multiple peak analysis has led to (marginally) different rotation velocities and inclinations than those derived with another recent and high-quality HI datacube of Messier 31 from the 0th- and 1st-moment analysis (Braun et al. 2009; Corbelli et al. 2010). Again, such differences have already been reported (see e.g. Figs. 11 and 13 of Oh et al. 2008).

---

[1] LAB, CNRS UMR 5804, Université de Bordeaux, F-33270, Floirac, France,
[2] Dept. of Astronomy, University of Cape Town, Rondebosch 7700, South Africa
[3] Dept. of Physics and Astronomy, Brandon University, Brandon, MB R7A 6A9, Canada
[4] Dépt. de physique, Université de Montréal, Montréal, QC H3C 3J7, Canada

2 Yet another new HI survey of Messier 33

In pursuit of our project we present here very preliminary results for Messier 33, a late-type spiral whose HI disk is known to be warped (Corbelli & Schneider 1997). The 21-cm interferometric data were still obtained at DRAO (combined with the Arecibo data of Putman et al. 2009) but at a larger spectral resolution (3.3 km s^{-1}) than for Messier 31 observations. Of course it is very likely to detect multiple components with highly resolved spectra. However this does not guarantee the success of detecting *realistic* ones because noise becomes important at high resolution. Furthermore the number of components that can be fitted per spectra depends on the resolution. With more and more peaks found in an individual spectrum (as for Messier 31), it becomes less and less straightforward to interpret the data and identify for instance the component that is the most representative of the disk circular rotation to those that are caused by all abovementioned perturbing effects. The HI datacube of Messier 33 has thus been filtered to lower resolution to simplify the hyperspectral decomposition.

3 Preliminary results: evidence for new HI structures in Messier 33

Other recent HI surveys of Messier 33 have been performed at VLA and Arecibo (Thilker et al. 2002; Putman et al. 2009). The VLA data of Thilker et al. (2002) have allowed to determine for the first time the inner structure of the HI disk with unprecedented details (resolution of 20 pc). The Arecibo data of Putman et al. (2009) were more appropriate to study the nearby environment of Messier 33 at a resolution of about 1 kpc. In particular they have shown the HI disk of Messier 33 is surrounded by arc-like structures and clumps. A hint of such perturbations had been presented in another (earlier) Arecibo view of Messier 33 (Corbelli, Schneider, & Salpeter 1989). Our DRAO survey has thus an intermediate angular resolution to them.

Working with a datacube of effective spectral resolution of 10 km s^{-1} our 'search and fit' algorithm of multiple peaks identifies sometimes up to 3 significant HI components in the datacube. An example of two distinct components is shown in Fig 1 (left-hand panel). Here the components are separated by $\sim$ 45 km s^{-1}. The total integrated HI emission of Messier 33 is shown in Fig 1 (central panel). The external arc-lile structure and the SW clump are clearly detected, even within our $\sim$ 300-pc resolution data, as well as the 'main' inner disk. Multiple components are not observed over the whole field-of-view, as seen in Figure 1 (right panel), but are preferentially distributed along a 'secondary' spiral-like structure in the inner disk and an annular structure in the outer regions ($r \sim 80'$ or 19 kpc). It is obvious that none of these new structures would have been identified with a moment analysis of the datacube.

A preliminary tilted-ring model has been fitted to the velocity field of the 'main' HI component shown in the left-hand panel of Fig. 2. A significant twist of the orientation of the major kinematical axis is evidenced, as well as a tilt of the HI disk (Fig. 3). This result thus confirms the warped nature of the HI disk of Messier 33. The kinematics of the external arc-like structure does not differ so much from that of the inner disk, implying that this perturbation is bound to the disk. We have not yet fitted the warp parameters for it, as shown by constant inclination and position angles at those locations ($r > 100'$, Fig. 3).

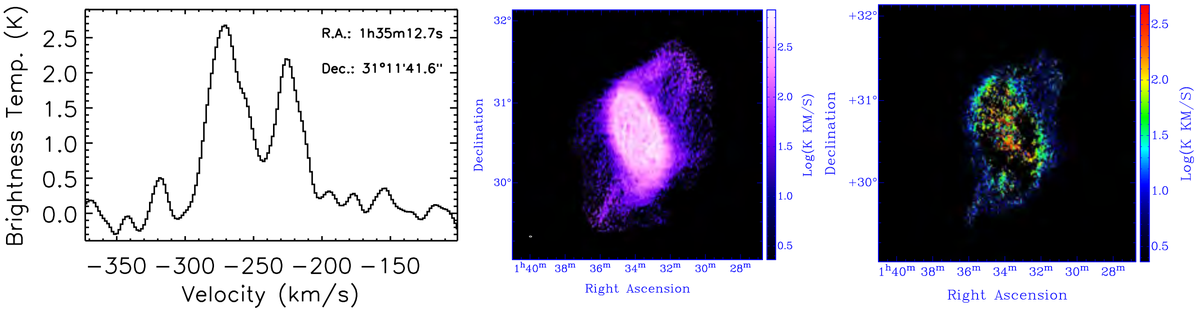

Fig. 1. Illustration of a HI profile with two distinct components (left). Total integrated HI emission map of Messier 33 (middle). HI integrated emission map of the 'secondary' fitted HI component in Messier 33 (right). A logarithmic stretch is used for them. The ellipse in the bottom-left corner of the midle panel represents the size of the synthesized beam.

The kinematics of the outer annular structure is shown in the middle panel of Fig. 2 and its residual field

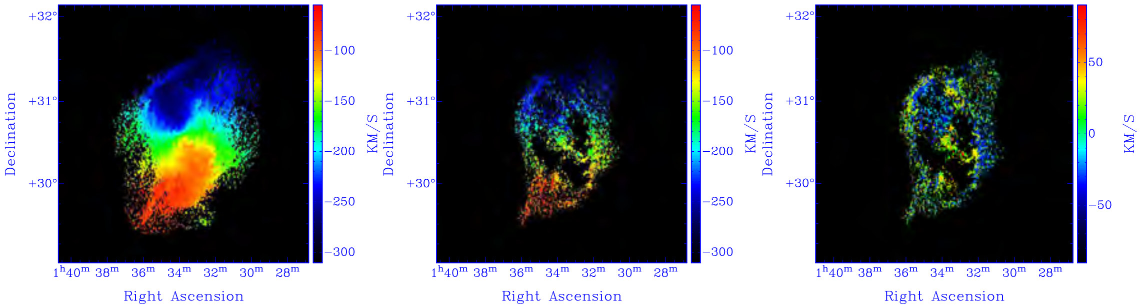

Fig. 2. Velocity fields of the 'main' HI component of Messier 33 (left) and of the secondary component (middle). The residual field from their mutual subtraction is shown in the right-hand panel.

when subtracted from the velocity field of the 'main' HI component in the right-hand panel of Fig. 2. Differences of radial velocities sometimes reach 40-50 km s^{-1} in absolute values. At this stage of our analysis it is too early to firmly identify which of the multiple components is the real tracer of the 'main' disk kinematics to that of the inner 'secondary' spiral-like structure on one hand, and to that of the outer HI annulus on another hand. Indeed the disk kinematics is strongly perturbed in those regions (warp, connection with the external arc-like structure, etc). It is also too early to constrain the exact origins of the inner 'secondary' spiral-like pattern and the outer annular structure. Origins for this later could be:

- The annular structure has external origins to Messier 33. Gas accretion on the outer disk parts from e.g. the external arc-like strucure or the intergalactic medium could be ongoing. Messier 33 has an obvious perturbed environment, and past tidal interactions with other galaxies may not be excluded. Numerical simulations would be needed to test those assumptions.
- The annular structure is a genuine ring, with internal origins. For instance it could have been developed by gas accumulation at the outer Lindblad resonance. In this case an obvious perturbing density wave could be grand-design spiral structure of Messier 33. This hypothesis could be tested by measuring the pattern speed of the spiral density wave with a modified version of the Tremaine-Weinberg method, and by determining the locations of various Lindblad resonances.
- The annular structure is not a real ring but is only caused by a fortuitous projection effect of a peculiar warping of Messier 33 (and maybe also a disk flaring) at the periphery of the HI disk. One would need here gas orbits that have orientation angles significantly different from the constant one displayed in Fig. 3 from $r \sim 85'$ to generate a distinct structure in superimposition to the outer disk.

Noteworthy is the fact that insights for asymmetric HI profiles along a ring-like structure as caused by the warped gas orbits has been reported in Corbelli & Schneider (1997). The location of that ring-like structure found by Corbelli & Schneider (1997) corresponds with that of the external arc-like structure, but not to that of the outer HI annulus we evidence here. Furthermore the HI annulus does not share the same orientation parameters than the external arc-like structure (Fig. 1). Two different ring-like structures thus seem to coexist in the outer regions of Messier 33.

4 Conclusions

Provisional results from a new HI survey in the direction of Messier 33 performed with aperture synthesis observations at the Dominion Radio Astrophysical Observatory have been presented. Evidence for new HI structures in Messier 33 have been found from a multiple HI peak analysis of the datacube. Among them is the detection of an annular-like structure in the outer regions of the HI disk. That annulus does not correspond to the already known arc-like structure around Messier 33. Complete details of the observing campaign, the data reduction and the hyperspectral decomposition will be presented soonly (Chemin et al. 2013). Our main objectives are to revisit the structure and dynamics of Messier 33, derive an accurate and extended rotation curve for it, and model its mass distribution. With the results already obtained for the Andromeda galaxy, this new dataset should help to better constrain the evolution of massive spirals in the Local Group.

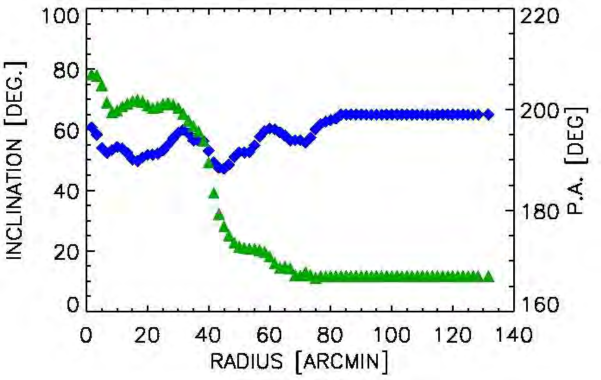

Fig. 3. Preliminary results of the tilted-ring model fitted to the 'main' HI velocity field of Messier 33 from central panel of Fig. 2. Blue squares are for the disk inclination and green triangles for the position angle of the major kinematial axis.

We are very grateful to Mary Putman and Nigel Douglas for having provided us with their single dish data.

References

Braun R., Thilker D. A., Walterbos R. A. M., & Corbelli E, ApJ, 695, 937
Chemin L., Carignan C., & Foster T., 2009, ApJ, 705, 1395
Chemin L., Carignan C., et al., 2013, ApJ, in preparation
Corbelli E., Schneider S. E., & Salpeter E. E., 1989, AJ, 97, 390
Corbelli E., & Schneider S. E., 1997, ApJ, 479, 244
Corbelli E., Lorenzoni S., Walterbos R., Braun R., & Thilker D., 2010, A&A, 511, 89
Oh S.-H., de Blok W. J. G., Walter F., Brinks E., & Kennicutt R. C. Jr., 2008, AJ, 136, 2761
Putman M. E., et al., 2009, 703, 1486
Sicotte V., & Carignan C., 1997, AJ, 113, 609
Thilker D. A., Braun R., & Walterbos R. A. M., 2002, ASPC, 276, 370

Monthly Notices
of the
ROYAL ASTRONOMICAL SOCIETY

MNRAS **449,** 4048–4070 (2015) doi:10.1093/mnras/stv517

Kinematics and mass modelling of M33: Hα observations

Z. S. Kam,[1,2,3]⋆ C. Carignan,[1,2,3]⋆ L. Chemin,[4] P. Amram[5] and B. Epinat[5]

[1] *Laboratoire d'Astrophysique Expérimentale, Département de physique, Université de Montréal, C.P. 6128, Succ. centre-ville, Montréal, Québec H3C 3J7, Canada*
[2] *Observatoire d'Astrophysique de l'Université de Ouagadougou, BP 7021, Ouagadougou 03, Burkina Faso*
[3] *Department of Astronomy, University of Cape Town, Private Bag X3, Rondebosch 7701, South Africa*
[4] *Université de Bordeaux and CNRS, LAB, UMR 5804, F-33270 Floirac, France*
[5] *Université Aix Marseille, CNRS, LAM (Laboratoire d'Astrophysique de Marseille), F-13388 Marseille, France*

Accepted 2015 March 3. Received 2015 February 28; in original form 2014 November 12

ABSTRACT

As part of a long-term project to revisit the kinematics and dynamics of the large disc galaxies of the Local Group, we present the first deep, wide-field (∼42 arcmin × 56 arcmin) 3D-spectroscopic survey of the ionized gas disc of Messier 33. Fabry–Perot interferometry has been used to map its Hα distribution and kinematics at unprecedented angular resolution ($\lesssim$3 arcsec) and resolving power (∼12 600), with the 1.6 m telescope at the Observatoire du Mont Mégantic. The ionized gas distribution follows a complex, large-scale spiral structure, unsurprisingly coincident with the already-known spiral structures of the neutral and molecular gas discs. The kinematical analysis of the velocity field shows that the rotation centre of the Hα disc is distant from the photometric centre by ∼168 pc (sky-projected distance) and that the kinematical major-axis position angle and disc inclination are in excellent agreement with photometric values. The Hα rotation curve agrees very well with the H I rotation curves for $0 < R < 6.5$ kpc, but the Hα velocities are 10–20 km s^{-1} higher for $R > 6.5$ kpc. The reason for this discrepancy is not well understood. The velocity dispersion profile is relatively flat around 16 km s^{-1}, which is at the low end of velocity dispersions of nearby star-forming galactic discs. A strong relation is also found between the Hα velocity dispersion and the Hα intensity. Mass models were obtained using the Hα rotation curve but, as expected, the dark matter halo's parameters are not very well constrained since the optical rotation curve only extends out to 8 kpc.

Key words: techniques: interferometric – ISM: bubbles – H II regions – galaxies: individual: M33 – galaxies: ISM – galaxies: kinematics and dynamics – dark matter.

1 INTRODUCTION

Late-type spiral and dwarf irregular (dIrr) galaxies present an extended H I emission. The H I emission usually extends to larger radii than the optical emission. This makes H I a powerful tool for probing the dark matter (DM)-dominated regions and for characterizing the parameters of the flat part of the rotation curves (RCs). However, it is the rising inner part of the RCs that constrains the parameters of the mass models (see e.g. Blais-Ouellette et al. 1999). Two-dimensional Hα observations are ideally suited to give more accurate velocities in the inner parts of galaxies having a better spatial resolution than the H I (Amram et al. 1992, 1994; Swaters, Madore & Trewhella 2000). The ideal approach is then to combine high spatial resolution Hα observations in the inner parts and sensitive lower spatial resolution H I observations in the outer parts to derive the most accurate mass models for the luminous disc and the dark halo. The objective of this project is to perform a new mass distribution model of Messier 33 (M33), combining high-sensitivity Hα and H I interferometric data. In particular, this article presents the first Hα survey devoted to the large-scale distribution and kinematics of the M33 ionized gas disc.

M33 is the second most luminous spiral (SA(s)cd) galaxy in our neighbourhood after M31. With an absolute magnitude of $M_V \sim -19.3$, it presents several arms (Sandage & Humphreys 1980). Although two main arms are well known, M33 has not a clearly defined grand-design pattern. A system of seven spiral arms is pointed out by Ivanov & Kunchev (1985). In the optical bands, it could be considered as a flocculent spiral galaxy, but UV and IR observations show more prominent arms. The M33 profile presents a small bulge-like component in the IR bands. Its bulge and nucleus are the subject of numerous studies (e.g. McLean & Liu 1996;

⋆

Published by Oxford University Press on behalf of the Royal Astronomical Society

Table 1. Optical parameters of M33.

Parameter	Value	Source
Morphological type	SA(s)cd	RC3
R.A. (2000)	$01^{h}\ 33^{m}\ 33^{s}.1$	RC3
Dec. (2000)	$+30^{\circ}39'18''$	RC3
Optical inclination, i	$52^{\circ} \pm 3^{\circ}$	WW
Optical major axis, PA	$22^{\circ}.5 \pm 1^{\circ}$	WW
Apparent magnitude, m_V	5.28	RC3
Absolute magnitude, M_V	−19.34	
(J–K)	0.89	JTH
Optical radius, R_{25} (arcmin)	35.4 ± 1.0	RC3
Systemic velocity, V_{sys}	-179 ± 3 km s^{-1}	RC3

References: WW: Warner, Wright & Baldwin (1973), RC3: de Vaucouleurs et al. (1991), JTH: Jarrett et al. (2003).

Table 2. Distances for M33.

Method (indicator)	Distance Modulus $m-M$ (mag)	Distance (Mpc)	Source
TRGB	24.54 ± 0.06	0.81	(1)
TRGB	24.75 ± 0.10	0.89	(2)
TRGB	24.64 ± 0.15	0.85	(3)
PNLF	24.62 ± 0.25	0.84	(4)
Cepheids	24.64 ± 0.06	0.85	(5)
Cepheids	24.70 ± 0.13	0.87	(6)
Cepheids	24.52 ± 0.14	0.80	(7)
Cepheids	24.55 ± 0.28	0.81	(8)
Cepheids	24.58 ± 0.10	0.84	(9)
Cepheids	24.62 ± 0.01	0.84	(10)
Mean adopted distance	0.84 ± 0.04		
		1 arcsec ≡ 4 pc	

References: (1) McConnachie et al. (2005), (2) Stonkutė et al. (2008), (3) Galleti, Bellazzini & Ferraro (2004), (4) Magrini et al. (2000), (5) Saha et al. (2006), (6) Paturel et al. (2002), (7) McConnachie et al. (2004), (8) An, Terndrup & Pinsonneault (2007), (9) Freedman et al. (2001), (10) Gieren et al. (2013).

Lauer et al. 1998; Gordon et al. 1999; Corbelli & Walterbos 2007). The optical parameters of M33 are given in Table 1.

In the literature, one can find distances to M33 varying from 700 to 940 kpc. Table 2 gives recent distance measurements for M33. The adopted distance for this study is $D = 0.84$ Mpc (scale 1 arcmin = 244 pc). It is the mean distance estimated by using resolved sources techniques such as Cepheids, Planetary Nebulae Luminosity Function (PNLF) and Tip of the Red Giant Branch (TRGB). The optical disc of M33 has a scalelength of ∼9.2 arcmin (2.25 kpc) in the V band (Kent 1987; Guidoni, Messi & Natali 1981) and its optical radius is $R_{25} = 35.4$ arcmin (RC3). A cut-off in the radial surface brightness profile appears at ∼ 36 arcmin (∼9 kpc) in the I band (Ferguson et al. 2007).

Mapping the environment of the Local Group galaxies, as is done by the Pan-Andromeda Archaeological Survey (PAndAS; McConnachie et al. 2009), confirms that there were many mergers and interactions between them. The discovery of dwarf galaxies around the Milky Way and M31 and the tidal streams between M31 and M33 (PAnDAS) confirm our ideas about galaxy formation. The particular structure (star streams) seen in M33 could be associated with this history of mergers and interactions. In fact, many of the structures presented in McConnachie et al. (2009, 2010), Cockcroft et al. (2013) and Wolfe et al. (2013) around M31 and M33 can only be explained by these interactions. Deep Hα observations of M33 reveal the presence of low-density H II regions outside the optical disc (Hoopes, Walterbos & Bothun 2001). This suggests recent star formation activity, possibly due to recent interactions.

Studying the kinematics of such a galaxy will provide a better understanding of the contribution of DM and of the best functional form describing its distribution. Still today, the cusp–core problem remains as one compares observations to predictions, especially for dwarf systems and this, despite the numerous studies on the DM distribution in galaxies in the last 30 years. While, on large scales, N-body cosmological simulations reproduce well the observations, it is more problematic at galaxy scales. The NFW profile, derived from those simulations, predicts a cuspy distribution in the central parts of the DM haloes (e.g. Fukushige & Makino 1997; Navarro, Frenk & White 1997; Moore et al. 1999; Navarro et al. 2010; Ishiyama et al. 2013), while observations especially of dwarf systems show more a core distribution (Oh et al. 2011). Those results can be explained by the gravitational potential related to the gas in those simulations, since the gas, which is important in the inner parts, is not accurately introduced in those simulations. Phenomena such as stellar feedbacks, galactic winds or massive clumps are not often well handled and reproduced (Goerdt et al. 2010; Inoue & Saitoh 2011; Ogiya & Mori 2011; Pontzen & Governato 2012; Teyssier et al. 2013).

Several studies of the kinematics of M33 exist (e.g. Corbelli & Salucci 2000; Corbelli 2003; Putman et al. 2009; Corbelli et al. 2014), mainly based on H I. It appears from those studies that M33 is DM dominated (the DM mass is >10 times larger than the mass of the stellar disc) and that its H I disc is strongly warped. The gas in the disc of M33 is estimated ∼1.4–3 × 10^9 $\mathrm{M}_{\odot}$ (Corbelli 2003; Putman et al. 2009). In the mass model derived by Corbelli (2003), the stellar mass is estimated at ∼3–6 × 10^9 $\mathrm{M}_{\odot}$ and the dark halo mass at ∼5 × 10^{10} $\mathrm{M}_{\odot}$. Most of the M33 kinematical studies use H I or CO (H_2), with a probable beam smearing impact on the innermost parts of the RC due to the lower spatial resolution of the H I data. Among the few Hα (optical) studies, the results presented by Carranza et al. (1968) show small velocity dispersions from 5 to 9 km s^{-1} in the disc. However, they argue that these values could even be lower if taking into account the instrumental corrections. The mass-to-light ratio (M/L) is an important parameter in the determination of the DM halo shape. In M33, Boulesteix & Monnet (1970) show very low values of M/L in the central (<50 arcmin) part of the galaxy and increasing in the outer parts of the disc. The kinematics of the inner regions was studied using the warm gas (Hα; Boulesteix & Monnet 1970; Boulesteix et al. 1974; Zaritsky, Elston & Hill 1989) and the cold molecular gas (H_2 via CO; Wilson & Scoville 1989; Gratier et al. 2010, 2012; Kramer et al. 2013; Druard et al. 2014).

The precise determination of the rising parts of RCs with high-resolution data and a better estimate of the M/L ratio for the stellar disc could define more accurately the shape of its DM halo. High-resolution optical observations of a nearby galaxy such as M33 is complex in view of the large size of the galaxy compared to the small field of view (FOV) of high-resolution integral field spectroscopic instruments. For M33, there is a lack of high-resolution optical data available for the kinematical study. An exception is the study by Corbelli & Walterbos (2007) on the central 5 arcmin using the gas and stellar kinematics obtained by long-slit spectroscopy.

Mass models are sensitive to the rising part of the RCs (see e.g. Amram et al. 1996; Blais-Ouellette et al. 1999; Swaters et al. 1999). High-resolution Hα RCs give a more accurate determination of the kinematical parameters for the derivation of the RCs and subsequently a more accurate determination of the mass model parameters. The high-resolution Fabry–Perot (FP) integral field observations at Hα with a resolution ≳10 000 give optimal kinematical data for the optical disc. The Hα RC can be used to test the shape of the DM halo allowing us to compare the derived DM distribution with cold dark matter (CDM) predictions.

To address these problems, this study presents FP mapping of M33 obtained at the Observatoire du mont Megantic (OMM). Relaño et al. (2013) have studied the spectral energy distribution of the H II regions of M33 and the star formation rate and star formation efficiency have been investigated by Gardan et al. (2007) and Kramer et al. (2011). More than 1000 H II regions can be resolved by the Hα observations; Courtes et al. (1987) gave a catalogue of 748 H II regions. Observing those regions allows us to derive the ionized gas (optical) kinematics of M33. Determination of the M33 kinematics with a spatial resolution $\lesssim$3 arcsec (∼12 pc) using the Hα velocity field and the derivation of an accurate RC in the inner parts are the main goals of this paper. The 3D data will be used to derive mass models with a dark halo component (ISO and NFW).

Section 2 describes the data acquisition and the instrumentation used while Section 3 discusses the data reduction techniques. Section 4 details the kinematical analysis and Section 5 gives the details of the mass models analysis. A discussion of the M33 velocity dispersion, a comparison with other studies and the results from the mass modelling can be found in Section 6. Finally, a summary and the general conclusions are given in Section 7.

2 FP OBSERVATIONS

2.1 Telescope and instrument configuration

The observations took place at the 1.6-m telescope of the OMM, Quebec, in 2012 September. A scanning FP etalon interferometer has been used during the observations with the device IXON888, a commercial Andor EM-CCD camera of 1024 pixels× 1024 pixels. The details of this camera, based on e2v chip, are given in Table 3.

The IXON888 camera provides a large FOV and was set to Electron Multiplying (EM) mode, 14 bits read-out resolution and its detector was cooled to −85 K during the observations. The camera clocks, gains and read-out speeds were adjusted in order to reduce the noise.

The order-sorter filter is a narrow-band interference filter, centred at $\lambda_c = 6557$Å (nearly at the systemic velocity ∼−180 km s^{-1}) with a FWHM of 30Å. Its maximum transmission is ∼80 per cent. The interference order of the FP interferometer is $p = 765$ at Hα. The FP has a free spectral range (FSR) of 8.16Å (∼373 km s^{-1}), which has been scanned through 48 channels, corresponding to a spectral sampling of ∼0.17Å (7.8 km s^{-1}). The finesse f of the FP etalon provides the spectral resolution $\Delta\lambda$ = FSR/f. Our observations were done with a mean finesse of $f = 16.5$, as determined from data cubes of a Neon calibration lamp. The FWHM spectral resolution is thus $\Delta\lambda_{\max}$ ∼0.53Å (resolving power of ∼12 620 at Hα). This corresponds to an FWHM instrumental broadening of 23 km s^{-1} (dispersion of ∼10 km s^{-1}) at the scanning wavelength of the observation of 6558.8 Å.

Table 3. Photon counting cameras at OMM.

Parameters	IXON888 ^{a}
Pixels size	0.84 arcsec × 0.84 arcsec
Active pixels	1024 × 1024
Quantum efficiency (QE)	$\gtrsim$90 per cent
Cooling	−85°C
Max. readout speed	10 MHz
RON	$<1e^-$ with EM gain
Detector	CCD201-20^b
CIC^c level	5–8 × 10^{-3d}

Notes. 1 arcsec ≡ 4 pc, 0.8 arcsec ≡ 3.3 pc at a distance of 0.84 Mpc

[a] http://www.andor.com

[b] http://www.e2v.com/resources/account/download-datasheet/1491

[c] Clock-induced charges per pixel per frame

[d] Daigle et al. (2009)

RON : Read-out noise given per pixel per frame

2.2 Data acquisition

The wide FOV of ∼14 arcmin × 14 arcmin allows us to map the bright inner disc regions of M33 with only 10 pointings. The different pointings overlap by a few arcseconds to allow the derivation of one final large mosaic with no gaps (Section 3.3). Fig. 1 shows those pointings, whose centre coordinates are listed in Table 4. Note that the central field has been observed more than once to yield very deep Hα data for the innermost regions of M33. A region of the sky, free from apparent H II regions from M33, has been observed before and after each galaxy pointing whose duration was larger than 30 min. Those acquisitions were done with the same interference filter as the one used for the galaxy, in order to perform the subtraction of the night-sky emission lines.

The data were obtained by operating the camera at two seconds exposure per frame. A gap of 0.4 s between two consecutive channels was necessary to move the reflective plates of the FP etalon and in order to avoid overlapping frames during the fast transfer.

Dark current, gain, flat-field and noise calibration observations have been acquired at the beginning and the end of each night. The 'Dark' observations consisted in a series of at least 50 images during which the detector is exposed for 2 s without light, and the gain is set to its largest amplitude, like during the observations of every sky/galaxy FOV. The 'Gain' observations consisted of about 200 frames, again acquired with the largest gain value. The 'Noise' observations consisted in an integration of zero second, with the lowest gain value. A minimum of 50 frames were collected in order to calculate the read out noise of the CCDs. The noise, gain and dark were observed in off-light mode in the dome.

The total exposure time performed for each field is listed in Table 4. In total, the time spent to integrate on the M33 fields was >30 h. The seeing of the observations was $\lesssim$3 arcsec. To perform the wavelength calibration, the system (filter+lenses+FP+camera) has been illuminated by a Neon (Ne) lamp. A narrow-band filter centred on 6598Å and of FWHM = 16.3Å was used to isolate the Ne line at $\lambda = 6598.95$Å.

3 DATA REDUCTION

3.1 Wavelength calibration, spectral smoothing

The raw frames of the observations contain interferograms giving the information on the number of photons per frame per channel and per cycle. We used Interactive Data Language (IDL) routines to integrate raw 2D files into a 3D data cube. A phase correction consisting in shifting every pixels such that they are at the same wavelength across the field has been applied to the raw data cubes to yield wavelength-calibrated data cubes. For that purpose, a phase map has been derived from a Ne line calibration observation. Data cubes are then wavelength-sorted and corrected for guiding shifts and cosmic rays. The 'Noise','Dark' and 'Gain' observations (Section 2.2) were then used to correct and calibrate the detector response.

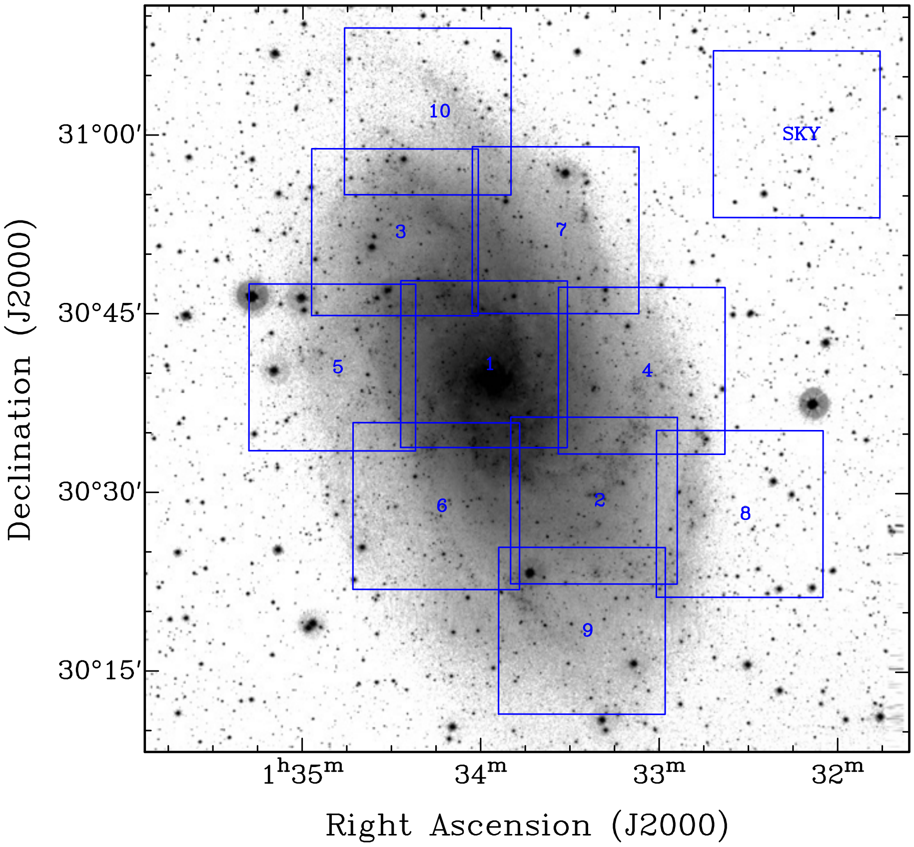

Figure 1. Mosaic of the 10 FP pointings in the direction of M33, shown with the sky field to the NW. The FOV of each field is ∼14 arcmin × 14 arcmin, with an overlap of ∼5 arcsec. The background image is an *R*-band archive image from KPNO (Hoopes et al. 2001).

Table 4. Characteristics of the observations.

Fields ID (1)	RA (2)	DEC. (3)	T (4)	S (5)	am (6)	V_h (7)
M33_01a	1:33:59	+30:40:48.54	2.0	2.7	1.1	19.6
M33_01b	1:33:59	+30:40:48.54	1.4	2.2	1.3	17.5
M33_01c	1:33:59	+30:40:48.54	2.0	2.2	1.1	17.5
M33_02a	1:33:22	+30:29:22.27	1.4	2.8	1.1	17.0
M33_02b	1:33:22	+30:29:22.27	2.7	2.5	1.3	17.0
M33_03	1:34:29	+30:51:52.41	2.4	2.4	1.3	19.3
M33_04	1:33:06	+30:40:16.96	2.5	2.4	1.1	19.2
M33_05	1:34:50	+30:40:30.72	2.5	2.3	1.4	18.9
M33_06	1:34:15	+30:28:52.98	3.0	2.3	1.1	19.0
M33_07	1:33:35	+30:52:04.25	2.6	2.1	1.3	18.5
M33_08	1:32:33	+30:28:16.19	2.7	2.1	1.1	18.5
M33_09	1:33:26	+30:18:26.23	2.4	2.2	1.1	17.4
M33_10	1:34:18	+31:02:01.11	2.6	2.5	1.1	17.2
Sky	1:32:14	+31:00:09.48	0.2			17.5
Dark			0.1			
Noise			0.1			
Gain			0.1			
Flat	Dome	Dome	0.1			

Columns notes: (1) Identification of the field. (2) and (3) Coordinates of the field centre (J2000). Each FOV is 14 arcmin × 14 arcmin. Observations presented in this paper have been taken in 2012 September. (4) Exposure time in hours, (5) Seeing FWHM during observations. (6) Airmass correction factor. (7) V_h is the heliocentric velocity correction (km s^{-1}).

A Hanning filter with a width of three channels has then been applied to the spectra to increase the sensitivity. This reduction step is the same as the one applied to the Virgo Cluster, GHASP or SINGS samples (Chemin et al. 2006; Epinat, Amram & Marcelin 2008b; Epinat et al. 2008a; Daigle et al. 2006; Dicaire et al. 2008). The same process is used for the sky observations, whose data cubes have been subtracted of all the other fields to produce the M33-only Hα emission line data cubes. For pointings having more than one observation, all night-sky-corrected and wavelength-calibrated data cubes have been combined into a single data cube, to increase the sensitivity.

3.2 Airmass and ghosts corrections

Because the centre of the interference rings of the observations is near the centre of the detector, there are some reflections about the optical axis, called ghosts. The size and the intensity of the ghost depend on the shape of the region which produces the effect. We have used the method described in Epinat (2009) to reduce the number of pixels dominated by those ghosts. The typical residuals after ghost removal are about 10 per cent of the initial ghosts flux.

Then, an airmass correction has to be applied. Indeed, differences in airmass during the multiple sessions of observations can affect the number of counts received by the detector, which implies field-to-field sensitivity variations. In Table 4, we give the airmass correction factor (AM) which has to be applied to each field in order to get the counts equivalent to an airmass of 1.0. Starting from the observed counts $C_{\rm obs}$ at a given airmass, the true value of the counts $C_{\rm true}$ is given by

$$C_{\rm true} = 10^{-0.4AX} \times C_{\rm obs}. \quad (1)$$

The parameter A represents the Hα extinction coefficient. Our FP system has already been used by Hlavacek-Larrondo (2009) to determine the value of that coefficient. We used their value of 1.03. The X quantity is given by $X = {\rm AM} - 1.0$, with the airmass correction factors AM listed in Table 4.

3.3 Mosaicking and binning the data cubes

Due to the large angular size of M33, there are two possibilities to generate the final set of moment maps (Hα-integrated emission, line-of-sight velocity and velocity dispersion maps, continuum map). A first one is to compute for each of the 10 pointings its own moment maps, and combine all the maps to produce a single FOV moment map. The second approach is first to combine all data cubes into a mosaic data cube, and then generate moment maps. The first approach is easier to do, but it introduces more errors in radial velocities in regions of overlap. Instead, we think it is better to combine and correct the Hα spectra directly, than radial velocities or velocity dispersions. We thus chose the second approach, which is a more powerful process, though less straightforward to implement. Combining the data cubes increases the signal to noise per pixel, which results in increasing the numbers of pixels for which we can measure a line. To minimize the errors in the overlap regions, astrometry information has been added in each single cube headers. The different steps in the process are as follows.

(i) White light image (sum of all channels).
(ii) Accurate astrometry on the white light image.
(iii) Field positioning from astrometry.
(iv) Generation of an exposure map with the sum of exposures.
(v) Accurate spectral calibration, taking into account the heliocentric correction.
(vi) Generation for each channel of a mosaic.
(vii) Weighting of each channel by the exposure map.
(viii) Combination of all channels to generate the mosaic cube.

In order to process projections and make an accurate mosaic, some parts of the MONTAGE packages from IPAC (Infrared Processing and Analysis Center) have been used to develop our tools.

Once the mosaic data cube has been obtained, an adaptive spatial binning has been performed. That adaptive spatial binning is based on Voronoi 3D binning (e.g. Chemin et al. 2006; Daigle et al. 2006; Dicaire et al. 2008). The Voronoi technique consists in combining pixels to larger bins up to a given value of S/N (signal-to-noise ratio) or more. The pixels/bins with an S/N lower than the threshold S/N are combined with the neighbouring pixels until the threshold S/N value is reached. An S/N of 7 has been targeted for this study. This particularly allows us to preserve the angular resolution where the S/N is high.

Fig. 2 gives the channel maps of the data cube used to determine the kinematical parameters of M33. The detections plotted in Fig. 2 are those above 3σ. It represents the wavelength variation from 6556.5 to 6560.6Å (from channel 11 to channel 35 in our data) where the channels width is 0.18 Å. The H II regions appear progressively from the north-east side to the south-west side.

3.4 Moment maps derivation

The integrated emission field is the zeroth-moment map derived from the spectra and the velocity field the first moment map. Radial velocities are given in the heliocentric rest frame. Making the assumption that the point spread function (PSF) has a Gaussian profile, the velocity dispersion field is the second moment map:

$$\sigma_{\rm corr} = \sqrt{\frac{\sum_i \lambda_i^2 F(\lambda_i)}{\sum_i F(\lambda_i)} - \Lambda^2 - \sigma^2_{\rm PSF}}, \quad (2)$$

where $F(\lambda_i)$ is the flux corrected for the continuum level at wavelength λ_i, Λ is the barycentre of the emission line, and $\sigma_{\rm PSF}$ is the instrumental dispersion. Velocity dispersions have not been corrected for thermal broadening of the medium, nor for the natural width of the Hα line. While the natural width of the Hα line remains negligible ($\sim$3 km s^{-1}), the reason for not correcting for the thermal dispersion of the gas was that the temperature of the ionized interstellar medium of M33 is not known accurately. A typical broadening of $\sim$10 km s^{-1} is often given in the literature, for a temperature of $\sim$10^4 K for the ionized gas. However, we have observed many bins of dispersion (after instrumental broadening correction) lower than this usual value of $\sim$10 km s^{-1}, implying that a typical temperature of $\sim$10^4 K cannot be valid everywhere.

Finally, the moment maps have been cleaned to get rid of all possible unrealistic patterns, like those from reflection, noise and background emission residuals. For that purpose, we have masked all pixels with data values lower than twenty counts. We are left with maps having 546 941 independent bins.

3.5 Flux calibration

The flux calibration that turns FP data counts into surface brightness (in erg s^{-1} cm^{-2} arcsec^{-2}) is given by

$$\mathrm{SB} = \mathrm{Cst} \times \mathrm{SB}_{\rm fp}. \quad (3)$$

Here, Cst is a calibration constant, SB is the corresponding surface brightness value and SB$_{\rm fp}$ is the calibrated value of FP count pixel^{-1} s^{-1}. The FP fluxes calibration using an Hα map is a linear relation. We have used the catalogue of H II regions of Relaño et al. (2013) as reference fluxes to calibrate our interferometric data. Fig. 3 shows the selected regions and their associated aperture size used to integrate the Hα counts. For each region, the total integrated flux is computed using the counts and the mean exposure time.

The calibration constant for the M33 Hα FP image is given by 1 count pixel^{-1} s^{-1} = $2.45 \pm 0.03 \times 10^{-17}$ erg s^{-1} cm^{-2} arcsec^{-2}. The typical error that can be noticed on the flux determination at an aperture used, is $\sim 2.4 \times 10^{-16}$ erg s^{-1} cm^{-2} arcsec^{-2}. It takes into account the errors on the Hα flux provided in Relaño et al. (2013) and the dispersion of the fit. Fig. 4 shows the comparison between our FP-calibrated data, and the Relaño et al. (2013) data in units of flux, erg s^{-1} cm^{-2}.

4 Hα DISTRIBUTION AND KINEMATICS

4.1 Hα maps

The observations obtained at the OMM give 13 cubes on 10 fields. Those cubes were used to build a mosaic cube as described in Section 3.3. Fig. 5 shows the Hα emission of M33 in the $\sim$42 arcmin × 56 arcmin field. The contours are from H I and CO

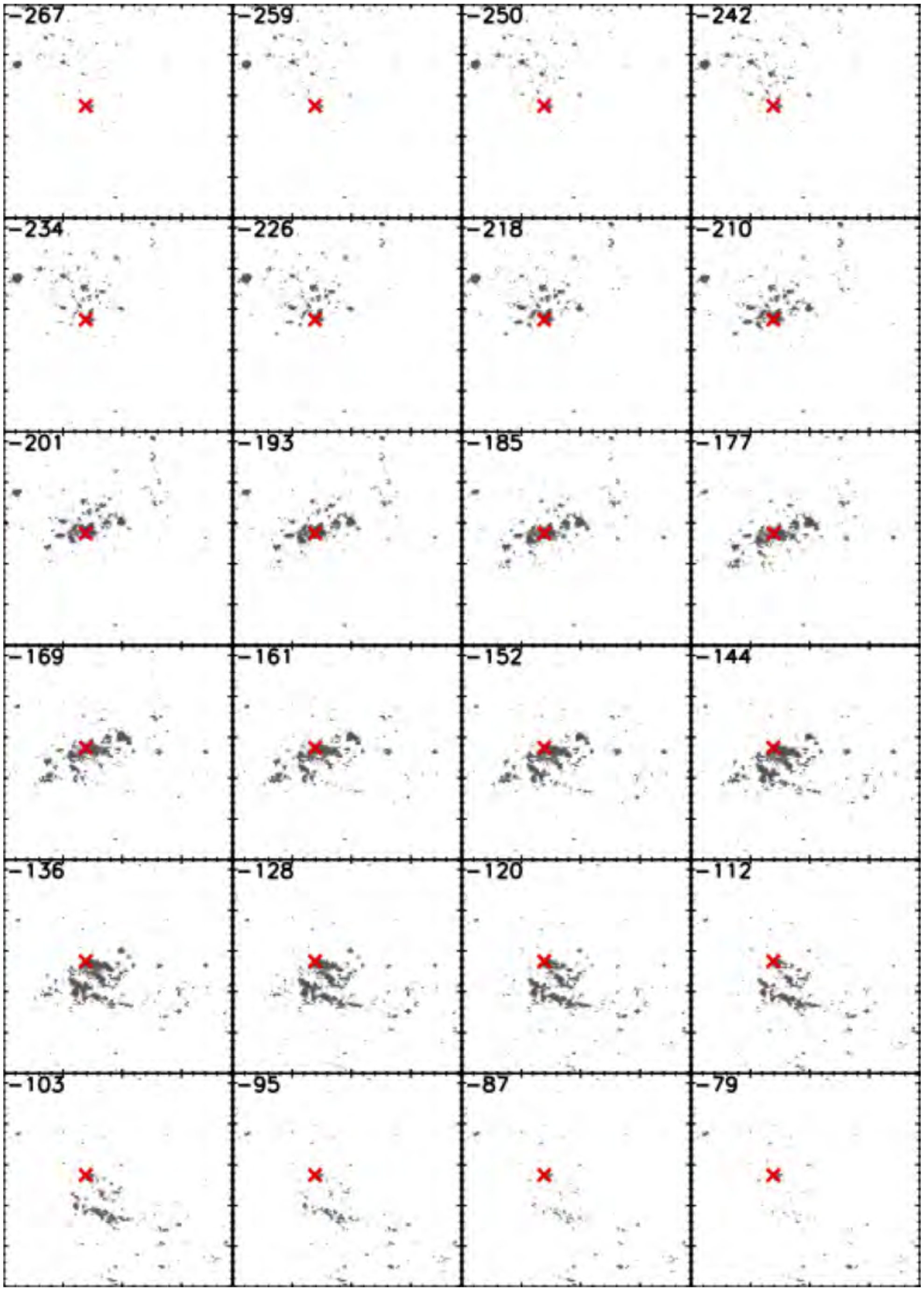

Figure 2. Hα channel maps. The radial velocity (km s^{-1}) is indicated in the upper-left corner of each channel and the cross indicate the kinematical centre.

emission. We can see that while the Hα emission follows roughly the H I emission, it is even more so for the CO emission. The H I and CO structures seem to follow the arms described by the H II regions. The final cube was produced with the same FSR and same spectral resolution as the small cubes observed. The Hα monochromatic image (moment zero map) is presented at the top right of Fig. 6 and can be compared to the *WISE* I NIR image on the left. The discrete H II regions have different sizes and shapes, filled and clear shell regions as described by Relaño et al. (2013). Two main strong arms are clearly defined along with the multi-arms structure as presented by Boulesteix et al. (1974).

The velocity field (first moment map) at the bottom left of Fig. 6 was obtained by using the zeroth-moment map as a mask. The bins of the Voronoi binning with data values greater than 20 counts are shown. This criterion was chosen in order to avoid all probable unreal pattern introduced by ghosts of strong Hα regions, noise and/or background. The velocity dispersion map (second moment) is shown in the bottom right of Fig. 6.

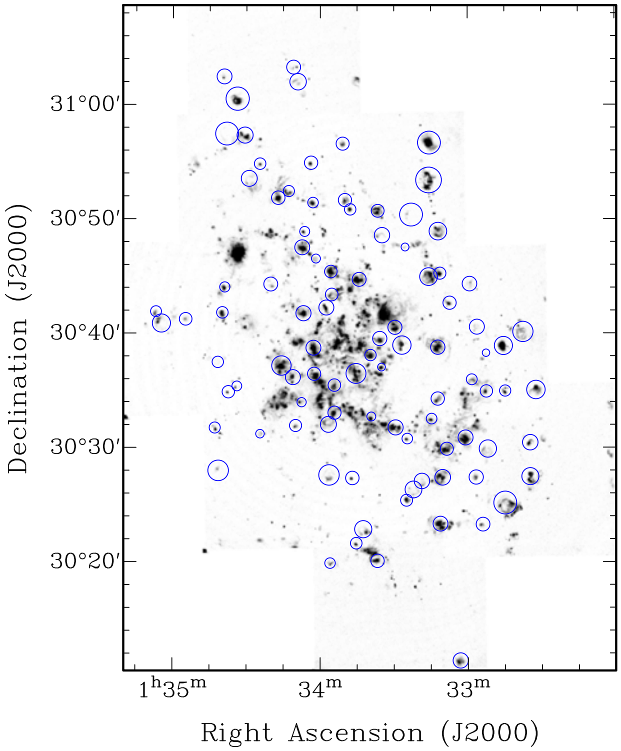

Figure 3. Selected H II regions for the Hα flux calibration overplotted on the Hα line flux map obtained from our set of observations. The aperture size around each region is the same as in Relaño et al. (2013).

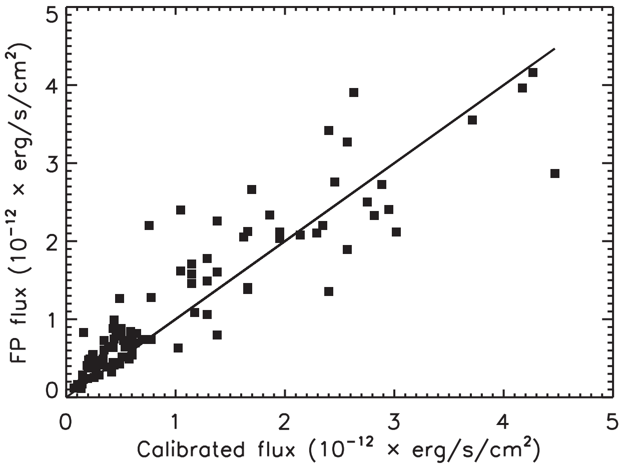

Figure 4. Comparison between the derived FP Hα fluxes and the reference Hα fluxes of Relaño et al. (2013) used for the FP flux calibration. Square symbols represent data from individual H II regions (Fig. 3) and the solid line is the linear fit to the data.

For this study, the data will be used mainly to derive the overall kinematics and derive the optical RC. Fig. 7 shows that the resolution of this data set (~3 arcsec) could be used to study the detailed kinematics of H II regions, shells, cavities, bubbles, filaments, loops, outflows and ring-like structures. This will be done in another publication. Except within such local features, the large-scale Hα velocity field of M33 seems regular, typical of nearby disc galaxies, without significant apparent twist of the major axis, and with mild streamings inherent to spiral arms (see Section 4.2.4).

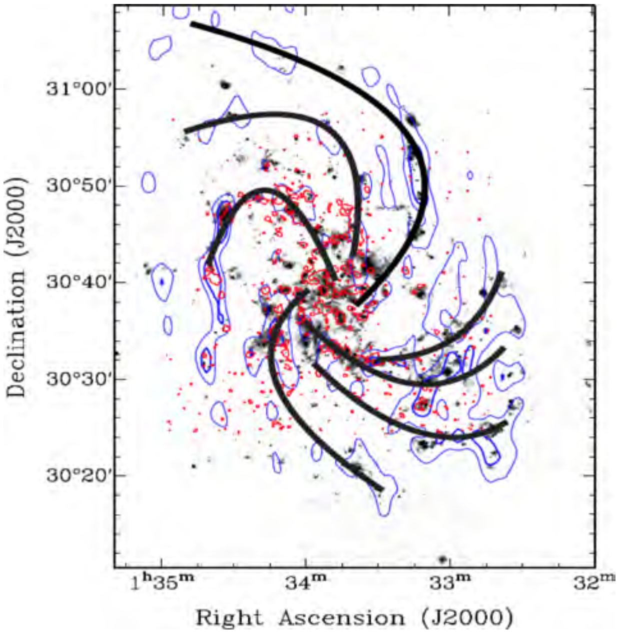

Figure 5. Hα map of M33 derived from our FP data. The CO peak contours are in red (120 K km s^{-1}) from Tosaki et al. (2011) and the H I peak contours are in blue (9500 and 1200 K km s^{-1}) from Chemin et al. (2012). The black sketches are drawn to follow the H II regions and trace the multi-arms profile of M33. These arms are close to those shown in Li & Henning (2011) or Boulesteix et al. (1974).

Fig. 8 provides a zoom of the ~8 arcmin × 8 arcmin central regions of M33. When compared to the *WISE* I NIR image to the lop left, it can be seen clearly that emission is detected all the way to the very centre of the galaxy. The velocity dispersion map shows that brighter H II regions exhibit larger dispersion (20–30 km s^{-1}), though the largest dispersions (up to 60 km s^{-1}) are only seen in bins with the faintest Hα emission. The map also shows that the inner regions exhibit smaller dispersion (see Section 6 for more details). Finally, Fig. 9 provides a zoom of the giant H II region NGC 604.

4.2 Kinematics

We performed a kinematical analysis in order to recover the set of kinematical parameters and the best possible RC with meaningful uncertainties.

4.2.1 *Initial parameters*

The ROTCUR algorithm implemented in the reduction package GIPSY (Groningen Image Processing System; Vogelaar & Terlouw 2001) has first been used to find the mean initial values of the kinematical parameters, and to verify that no significant warp of the ionized gas disc exists. ROTCUR is based on the tilted-ring model described in Begeman (1987). Starting from initial values of $i = 51°$ and PA $= 200°$, $V_{\rm sys}$ and the rotation centre (x_0, y_0) are first determined. A second run allowed us to derive the inclination and PA profiles. From those profiles, we measured an inclination $i = 52° \pm 2°$, and a PA $= 202° \pm 2°$, both values being very close to the optical morphological values (see Table 1). In both cases, the errors are determined using the deviation around the mean values. No trend has been detected in the inclination and position angle profiles, and the small standard deviations are clear indications that

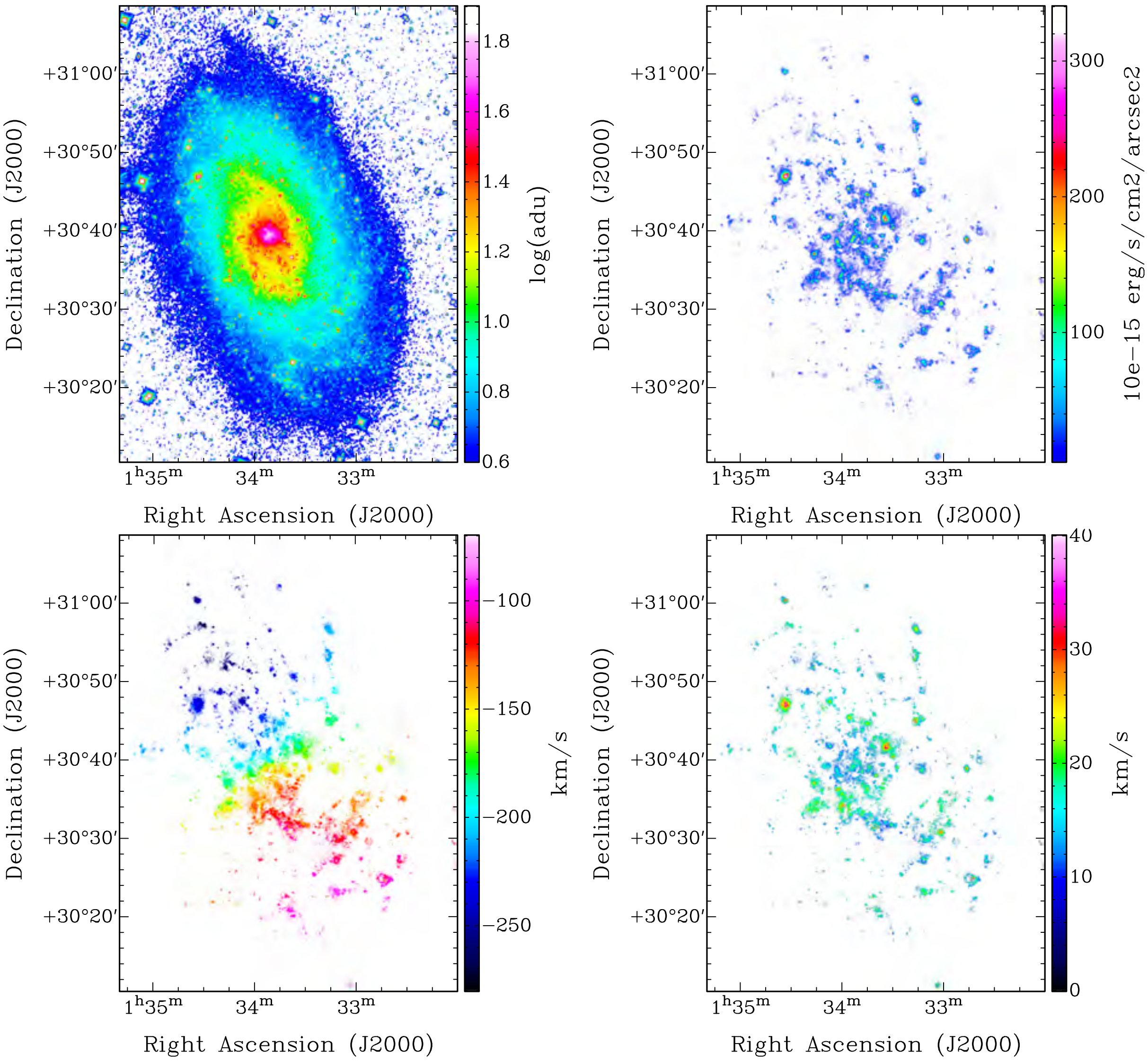

Figure 6. 3.4 μm and narrow-band Hα maps of M33. The NIR image from *WISE* I (top-left) is shown with a logarithmic stretch. The FP interferometry images are the Hα-integrated emission map, velocity field and velocity dispersion field (top-right, bottom-left and bottom-right, respectively).

no significant warp of the Hα disc exists (at least in the regions covered by our observations), as is usually the case for the optical discs (warps are mainly seen in the extended H I discs).

4.2.2 *Rotating disc model*

Since no warp is detected in the Hα disc using ROTCUR (tilted ring model), we used a model in which the gas is supposed to lie in a unique plane in order to derive the kinematical parameters and the RC. Thus, we use the whole 2D information to derive the projection parameters and their uncertainties. The model is explained in Epinat et al. (2008a) and was used for the GHASP sample data analysis. When the vertical motion velocities are not considered, the observed line-of-sight velocities are expressed as

$$V_{\mathrm{obs}} = V_{\mathrm{sys}} + (V_{\mathrm{rot}}(R)\cos(\theta) + V_{\mathrm{exp}}(R)\sin(\theta))\sin(i), \qquad (4)$$

where R and θ are the polar coordinates in the plane of the galaxy, i is the disc inclination, $V_{\mathrm{rot}}(R)$ is the azimuthal velocity (i.e. the RC) and $V_{\mathrm{exp}}(R)$ is the radial velocity in the galaxy plane (often referred to as the expansion velocity). Defining the kinematical position angle PA as the anticlockwise angle between the north and the direction of the receding side, the azimuthal angle θ can be deduced at each position (more details in the annexes of Epinat et al. 2008a).

With the hypothesis that the radial velocities of the ionized gas are negligible with respect to the azimuthal rotation, the observed velocities become $V_{\mathrm{obs}} = V_{\mathrm{sys}} + V_{\mathrm{rot}}(R)\cos(\theta)\sin(i)$. We therefore build a 2D model with a set of projection parameters (centre, position angle and inclination) and a set of kinematics parameters describing the RC and the motion of the galaxy with respect to the Earth (systemic velocity). All these parameters have no dependence with radius, contrary to what is done in tilted ring models (e.g. Begeman 1987).

The RC we used in our model is described by the Zhao function (Kravtsov et al. 1998) with reduced parameters:

$$V_{\mathrm{rot}} = V_{\mathrm{t}}\frac{(R/r_{\mathrm{t}})^{g}}{1+(R/r_{\mathrm{t}})^{a}}, \qquad (5)$$

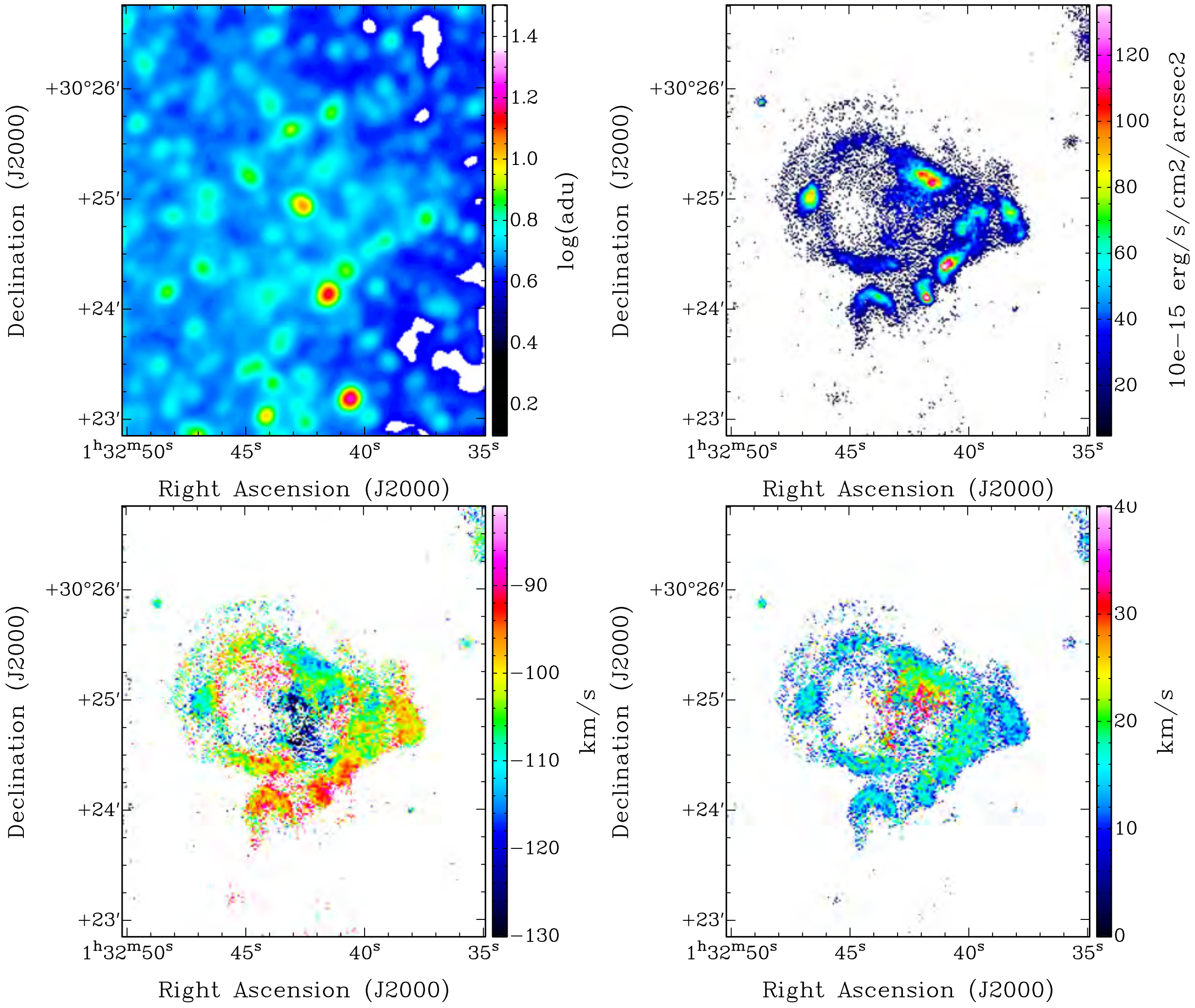

Figure 7. Same as in Fig. 6, zoomed on the star forming region located at $\alpha = 01^{\rm h}32^{\rm m}43^{\rm s}$, $\delta = 30°24'57''$.

where $r_{\rm t}$ and $V_{\rm t}$ define the transition ('turnover') radius and velocity, a and g describe the sharpness of this transition and the shape before and after the transition. Therefore, the 2D model is described by a set of nine parameters (i, PA, $X_{\rm cen}$, $Y_{\rm cen}$, $V_{\rm sys}$, $V_{\rm t}$, $r_{\rm t}$, g, a). The optimization starts with the initial parameters i, PA, $V_{\rm sys}$ and the rotation centre previously found using ROTCUR, which are compatible with morphological parameters. The method uses a χ^2 minimization calling the IDL LMFIT routine based on the Levenberg–Marquardt method in order to find the best-fitting model. The uncertainties on the parameters are derived using a Monte Carlo method based on the power spectrum of the residual velocity map (see Epinat et al. 2008a for details).

4.2.3 *Derived kinematical parameters*

With thousands of degrees of freedom, the optimized model converges rapidly towards a stable solution. The optimized centre is found at R.A. = $01^{\rm h}33^{\rm m}54\overset{\rm s}{.}1$, DEC. = $30°39'42''$. That location is ∼42 arcsec (168 pc) from the photometric centre (sky-projected distance), towards the NE direction, with an angle of 60° with respect to the semimajor axis of the approaching side. This offset corresponds to a deprojected distance of 63 arcsec (252 pc) in the galaxy plane of M33. As a comparison, sky-projected offsets between photometric and kinematical centres of bright spirals in the Virgo cluster of galaxies have been found between 70 and 800 pc (Chemin et al. 2006). The offset we find for M33 is thus comparable with other spirals, at the low end of the distribution for other galaxies.

The derived systemic velocity is $V_{\rm sys} = -178 \pm 3$ km s^{-1}, the position angle PA = $202° \pm 4°$ and the disc inclination $i = 52° \pm 2°$. These parameters are in excellent agreement with those found with ROTCUR, and with literature values. The values for the other parameters are $g = 1.2 \pm 0.7$ and $a = 1.01 \pm 0.6$; those parameters being in good agreement with best fits parameters range of rotating discs described by Kravtsov et al. (1998). Rotation can be approximated to a linear function of radius in the inner parts where $R < r_{\rm t} = 1.1$ arcmin and velocities $V < V_{\rm t} = 50$ km s^{-1}.

4.2.4 *Rotation curve*

RCs for the entire disc, and for the separate approaching and receding sides of the disc have been extracted using the projection parameters obtained from the model fitting described above. As detailed

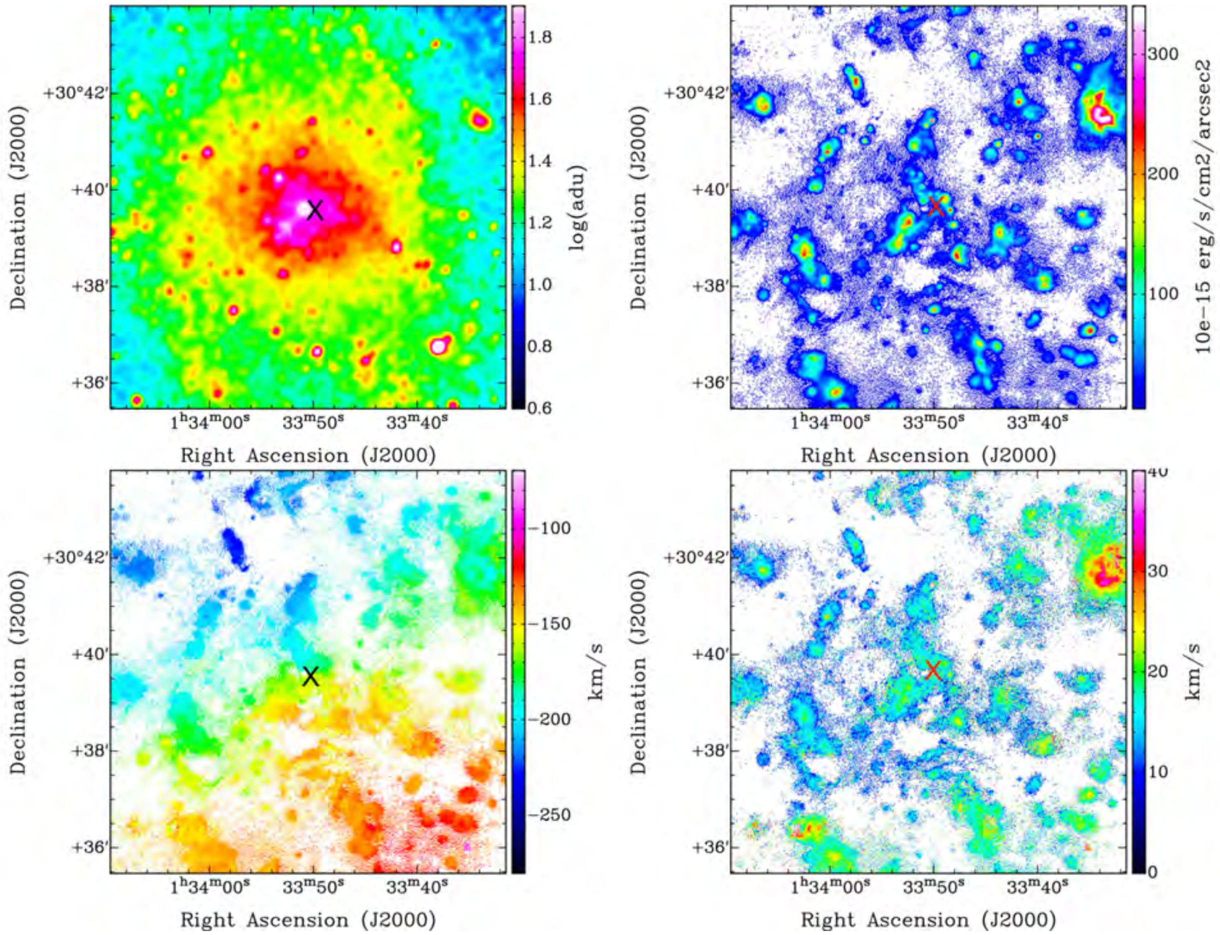

Figure 8. M33 central ~8 arcmin field – same caption as in Fig. 6. The data points presented are the barycentre after an adaptive binning with S/N = 7. The cross indicate the kinematical centre.

in Epinat et al. (2008a), the RC is extracted in rings whose width is optimized by gathering a minimum of 15 velocity measurements in the velocity field within each ring. Because the velocity field contains more than 500 000 independent pixels, it was very easy to define rings with such a number of pixels. As a result, the RCs were incredibly resolved, with thousands of rings for $0 < R < 35$ arcmin. Therefore, for practical reasons we decided to rebin the resulting curves at radii regularly spaced by 5 arcsec, and of 5 arcsec width. The top panel of Fig. 10 shows the Hα RCs for the approaching and receding sides, while the bottom panel shows the global RC, as fitted using both sides of the disc simultaneously. The adopted RC is given in Table 5 with the associated velocity errors ΔV. The adopted rotation velocity uncertainty is given by $\Delta V = \sqrt{\epsilon^2 + |V_{\rm a} - V_{\rm r}|^2/4}$. The term ϵ is the dispersion around the mean value within each ring (statistical error for the both sides velocity calculation). The second part $|V_{\rm a} - V_{\rm r}|/2$ is the systematic uncertainty that expresses the asymmetry between rotation velocities for the approaching ($V_{\rm a}$) and receding ($V_{\rm r}$) disc halves. The formal statistical error is usually smaller than the systematic error. The RC used for the mass models is the adopted RC of Fig. 10 (bottom panel). Only the points where data are present on both sides are used. As shown in Fig. 10 (top panel), the RC on the receding side goes out to ≥8.5 kpc and only out to ~8.1 kpc on the approaching side. So, the adopted RC stops at ~8.1 kpc. The RC was smoothed at a binning of 5 arcsec to get constant step in the mass modelling. The Hα RC exhibits a regular rising gradient within the inner $R = 8$ kpc, reaching a maximum velocity of ~125km $\rm s^{-1}$ at the last data points. Many wiggles are obviously seen, as probable consequences of the crossing of the spiral arms of M33 or due to co-rotation effects. The axisymmetry of the rotation is very good. Indeed, the most significant differences (~35 km $\rm s^{-1}$) between $V_{\rm a}$ and $\rm V_r$ are only observed in a narrow range around $R = 6.5$ kpc. The axisymmetric velocity field model, as deduced from the adopted RC with all kinematical parameters kept constant with radius, and its subtraction to the observed velocity field are shown in Fig. 11. The distribution of residuals is centred on 0 km $\rm s^{-1}$, with a standard deviation of 8 km $\rm s^{-1}$, implying a very accurate kinematical model for most of the disc. We note that locally, bright Hα emission in spiral arms can exhibit larger velocity differences. For instance, the star-forming region at R.A. = $01^{\rm h}33^{\rm m}15\overset{\rm s}{.}4$, DEC. = 30°56′48″ has an average residual of ~10 km $\rm s^{-1}$. This likely shows the limit of the axisymmetric rotation model at those angular resolution (5 arcsec, i.e. 20 pc). Our observations are indeed sensitive to very local, non-axisymmetric motions inherent to such star-forming regions (expanding shell, etc.), which cannot be modelled correctly by the large-scale rotation of the galaxy. Note also that larger residuals in spiral arms indicate the presence of asymmetric or streaming motions. Such motions are often observed in disc galaxies, but cannot be modelled by the axisymmetric rotation. Finally, larger residuals at the outskirts of the Hα disc could indicate that some H II regions may not necessarily lie in the main equatorial

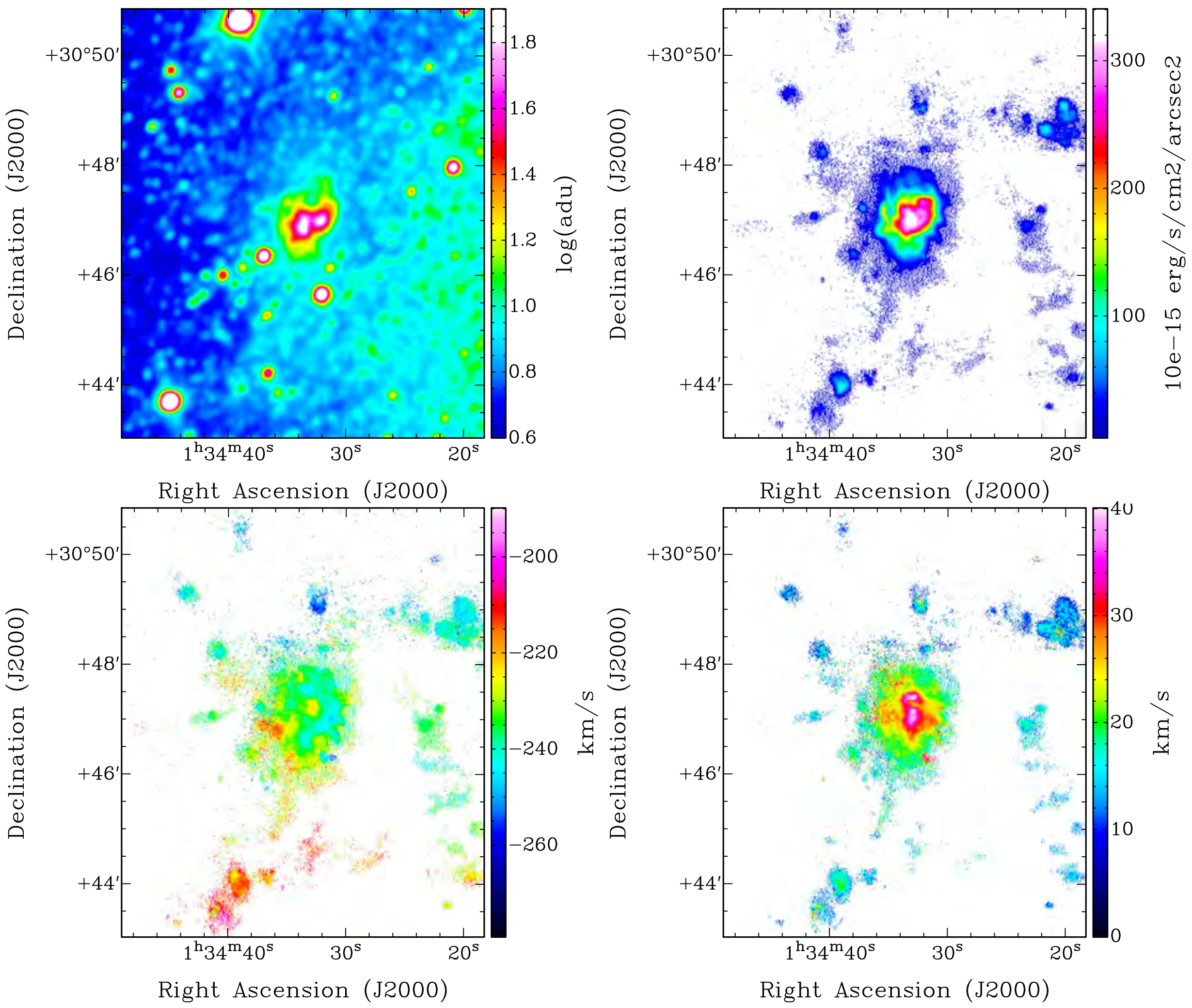

Figure 9. Same as in Fig. 7, zoomed on the star-forming region NGC 604.

plane of inclination $i = 52°$, so that deprojection of their velocities has not been performed correctly.

4.2.5 Velocity dispersions

The velocity dispersion profile has been derived by azimuthally averaging the velocity dispersions σ in annuli of 5 arcsec width, in 5 arcsec steps (Fig. 12). Annuli have been computed using the projection parameters determined from the kinematical model (Section 4.2.3) The σ profile is almost consistent with a flat profile. The mean dispersion is 16 km s^{-1}. Like for the RC, wiggles are detected. They are likely caused by increased dispersion when crossing the spiral arms. They are none the less not significant to make a noticeable increase of the scatter. We measure a standard deviation of the dispersion profile of 2 km s^{-1}. The profile marginally decreases from $R = 1.5$ kpc towards the centre. From $R \sim 7.5$ kpc, the velocity dispersions increase to ∼20–25 km s^{-1}. This radius is the location of the beginning of the warp of the H I disc where the twist of the position angle starts (Corbelli & Salucci 2000). However, it would be interesting to have Hα data with good S/N beyond these radius to better understand the Hα dispersions behaviour in regions where the H I disc warp is more pronounced.

5 MASS MODELLING

The Hα RC describes accurately the velocity gradient in the centre of galaxies, usually better than any other kinematical tracer. Such optical high resolution is crucial to test different inner shapes of DM haloes, like cuspy or shallow models. This section only focuses on the modelling of the mass distribution of M33 within the inner 8 kpc from our newly derived Hα RC. However, with a RC only derived out to 8 kpc, we do not expect strong constraints on the halo's parameters. We postpone to a forthcoming article a more complete modelling of the mass distribution from a more extended RC that will merge our inner Hα RC with a new H I RC for the outer regions of M33 (Kam et al., in preparation).

5.1 Luminous mass components

5.1.1 The neutral gaseous disc

Provisional data on the H I gas component have been presented in Chemin et al. (2012). Those observations will be fully described in a future Kam et al.'s paper. Fig. 13 presents (left-hand panel) the H I mass density profile overlaid on the ionized gas brightness profile

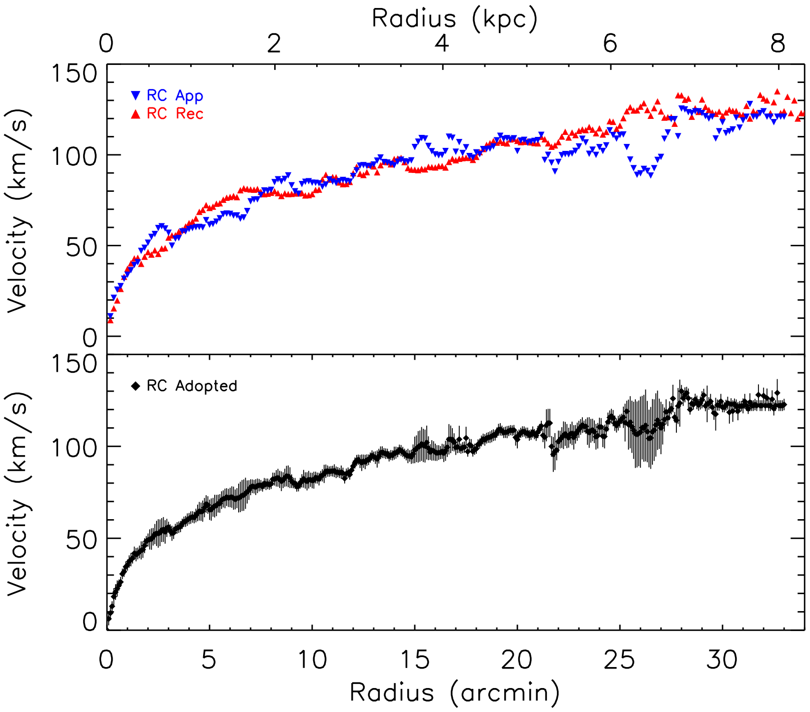

Figure 10. Hα RC of M33. The top panel shows the curves for the approaching and receding disc sides (blue downward triangles and red upward triangles, respectively). The adopted RC of M33 is shown in the bottom panel.

Table 5. Sample of the Hα RC of M33. Full table available online.

Rad (1)	V (2)	ΔV (3)	σ (4)	$\Delta\sigma$ (5)	Rad (6)	V (7)	ΔV (8)	σ (9)	$\Delta\sigma$ (10)	Rad (11)	V (12)	ΔV (13)	σ (14)	$\Delta\sigma$ (15)
0.08	6	4	14	10	11.08	87	4	16	5	22.08	104	5	17	7
0.17	9	4	12	6	11.17	86	3	16	5	22.17	105	6	17	7
0.25	13	3	12	4	11.25	86	3	16	6	22.25	106	8	18	7
0.33	18	5	14	5	11.33	86	3	16	6	22.33	107	7	19	8
0.42	21	4	15	4	11.42	86	4	15	6	22.42	106	7	18	8
0.50	23	4	16	4	11.50	85	3	15	6	22.50	105	5	17	7
0.58	25	3	15	4	11.58	83	3	15	6	22.58	107	5	16	7
0.67	26	3	16	5	11.67	85	3	16	6	22.67	107	6	17	8
0.75	31	3	16	5	11.75	86	3	16	6	22.75	105	7	16	7
0.83	32	3	15	5	11.83	85	3	16	6	22.83	107	5	15	7
0.92	35	3	15	4	11.92	87	3	16	6	22.92	108	5	16	7
1.00	35	3	15	4	12.00	89	3	17	7	23.00	109	5	15	6
2.00	49	4	14	4	13.00	94	3	18	8	24.00	110	5	17	8
3.00	56	3	14	5	14.00	96	4	16	6	25.00	114	4	16	7
4.00	61	3	15	5	15.00	98	7	15	7	26.00	108	19	17	7
5.00	65	6	16	5	16.00	97	5	16	6	27.00	110	14	14	8
6.00	72	5	17	5	17.00	99	4	17	6	28.00	130	3	19	12
7.00	78	4	17	6	18.00	99	3	17	7	29.00	125	5	19	9
8.00	80	3	17	6	19.00	107	3	17	7	30.00	121	3	14	10
9.00	81	4	17	6	20.00	104	5	16	6	31.00	122	4	15	11
10.0	81	4	15	6	21.00	108	3	15	8	32.00	128	4	22	21

Notes: Column (1): radius in arcmin, (2) the rotation velocities in km s^{-1}, (3) errors on V (4): σ (velocity dispersion) profile and (5) errors on the velocity dispersion. The following columns (up to 15) have the same definitions as the previous columns.

(in arbitrary units). Both profiles have been derived with the task ELLINT in GIPSY. The H I disc mass is $\sim 2 \times 10^9$ $M_\odot$. The surface density only slightly varies around 8 $M_\odot$ pc^{-2} within $R = 7$ kpc, then decreases at larger radii.

5.1.2 *The bulge–disc decomposition*

For the stellar contribution, the surface brightness profile is derived from the *Spitzer*/IRAC 3.6 µm data. The archive mosaic file from guaranteed time observations of Robert Gehrz, Observer

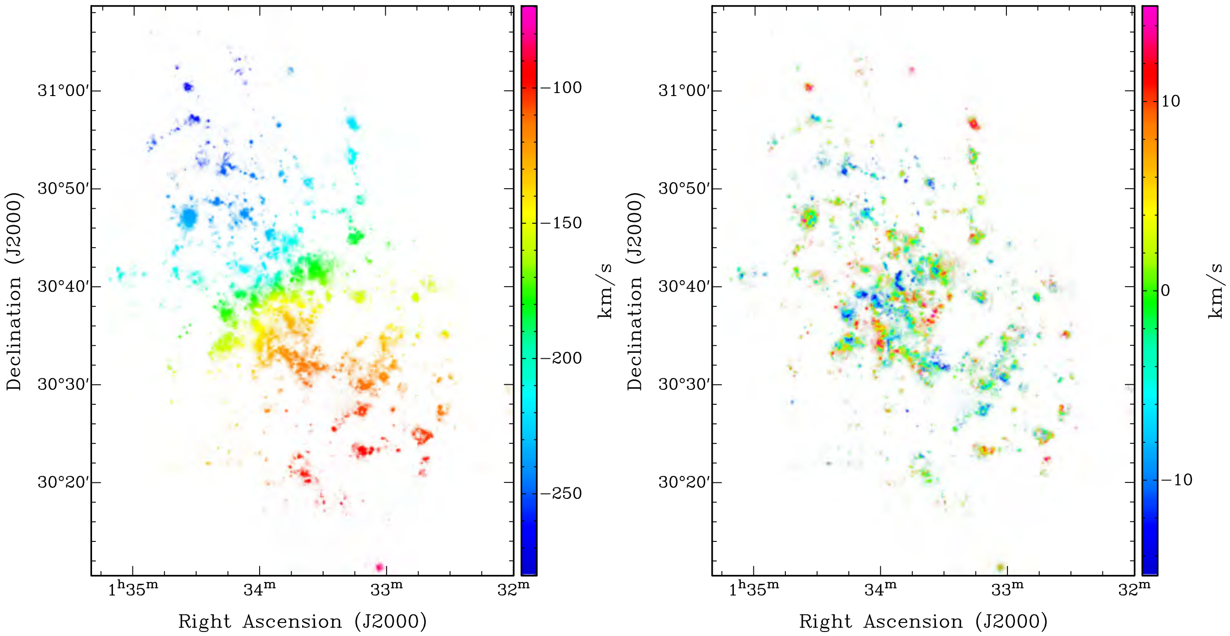

Figure 11. The left-hand image gives the axisymmetric model obtained with the kinematical parameters obtained with the Zhao model (See Section 4.2.2). The map was masked with the Hα monochromatic map (top right map in Fig. 6). The right-hand image gives the residual map (observed model).

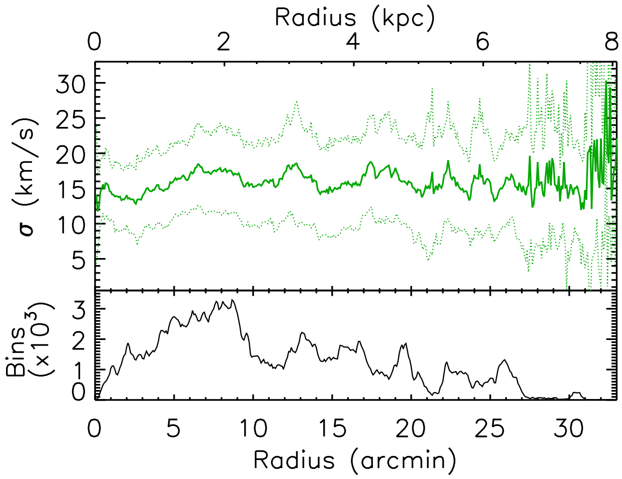

Figure 12. Hα velocity dispersion profile of M33. Dotted lines display values at +/− one standard deviation derived in each radial bin. The bottom panel shows the number of independent bins used to calculate the dispersion.

Programme ID 5 was used (Gehrz & Willner 2004). After removing the stars and the background, the *Chandra*'s CIAO[1] tools have been used to derive the profile of Fig. 13. The *Spitzer*/IRAC 3.6 μm profile is compared to the *WISE* I (3.4 μm) data. The profile presented in the right-hand panel of Fig. 13 (red), reaches a surface brightness of $\mu_{3.6} \sim 21.0$ mag arcsec^{-2} at a radius of 21 arcmin (∼5 kpc), which is similar to the *WISE* I profile (blue). The surface brightness $\mu_{\rm cor}$, corrected for the inclination and dust, is obtained by

$$\mu_{\rm cor} = \mu_{\rm obs} + A_\lambda + 2.5 \times b_\lambda \log(\cos(i)), \tag{6}$$

where the correction parameters A_λ and b_λ are tabulated in Graham & Worley (2008). The mean inclination of 52° is used for the density correction. In this correction, the influence of polycyclic aromatic hydrocarbon at 3.3 μm is considered as very weak and the maximum dust correction used in the IR comes from the *J* band (Graham & Worley 2008). In the right-hand panel of Fig. 13, the central 3 arcmin shows a small spheroidal component in the 3.6 μm band. This small central bulge has been discussed by many authors (Minniti, Olszewski & Rieke 1994; Regan & Vogel 1994; Gebhardt et al. 2001; Seigar 2011). Kent (1987) found that the nucleus in M33 is similar to a point source and the rising inner 3 arcmin part of the surface brightness profile suggests the presence of a small bulge. Corbelli & Salucci (2007) found for M33 a bulge component extending up to 1.7 kpc and Seigar (2011) only to 0.39 kpc. In view of those different results, it is clear that a disc–bulge decomposition has to be done using the IR profile from this study.

The best fit of the bulge–disc decomposition, shown in Fig. 13, is obtained using an exponential disc with a Sérsic model for the bulge. The black solid line gives the best fit of the sum of the decomposition. The disc is described by

$$\mu(r) = \mu_0 + 1.108\,57 \frac{R}{R_{\rm d}}, \tag{7}$$

where μ_0 is the central surface brightness and $R_{\rm d}$ the scalelength of the disc. The disc parameters found are $R_{\rm d} = 1.82 \pm 0.02$ kpc (slightly smaller than the scalelength in the optical) and $\mu_0 = 18.01 \pm 0.03$ mag arcsec^{-2}. As seen in Fig. 13, the *WISE* I profile has a slightly shorter scalelength. The disc parameters found for the *WISE* I profile are $R_{\rm d} = 1.70$ kpc and $\mu_0 = 17.60$ mag arcsec^{-2}.

The bulge is described by

$$\mu(r) = \mu_{\rm e} + 2.5 b_n \left[\left(\frac{R}{R_{\rm e}} \right)^{1/n} + 1 \right], \tag{8}$$

where, $\mu_{\rm e}$ is the effective surface brightness at $R_{\rm e}$, the effective radius. $R_{\rm e}$ defines the radius that contains half of the total light. The

---

[1] http://cxc.harvard.edu/ciao/

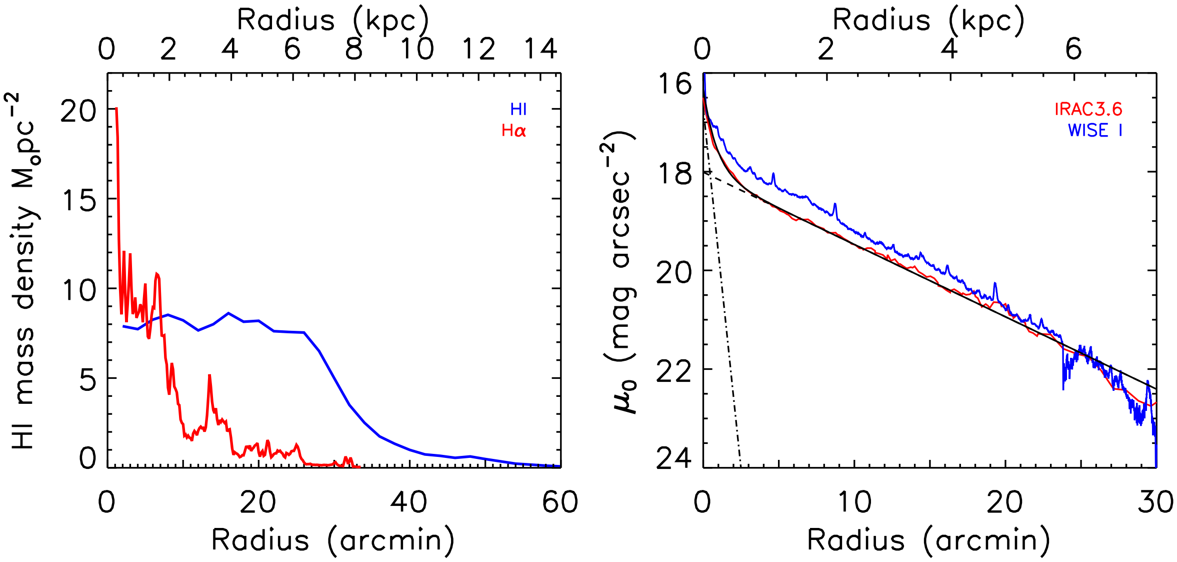

Figure 13. Left-hand panel: H I surface density profile (blue line) and Hα brightness profile (red line, in arbitrary units). Right-hand panel: in red the M33 surface brightness profile using the *Spitzer*/IRAC 3.6 μm and in blue using the *WISE* I (Jarrett, private communication) data. The dash–dotted line is the bulge component, the dashed line is the disc component, the other line is the contribution of both components.

parameter n determines the curvature of the luminosity profile. b_n is defined as $b_n = 1.9992n - 0.3271$ for $0.5 < n < 10$ (Capaccioli 1989). The best fit in Fig. 13 gives $\mu_e = 20.8 \pm 0.3$ mag arcsec^{-2}, $n = 1.12 \pm 0.1$ and an effective radius $R_e = 0.35 \pm 0.05$ kpc for the IRAC profile and $\mu_e = 21.5 \pm 0.4$ mag arcsec^{-2}, $n = 1.20 \pm 0.05$ and an effective radius $R_e = 0.40 \pm 0.05$ kpc for the *WISE* profile. With these values, our study leads to a bulge-to-disc ratio of $B/D = 0.04 \pm 0.012$ that is in agreement with $B/D = 0.03$ obtained by Seigar (2011) with IRAC data at 3.6 μm. The bulge component is subtracted from the total profile in order to get the disc contribution.

Stars in a disc have a vertical thickness. For the vertical distribution of the stellar component, we adopted a $\mathrm{sech}^2(z/z_0)$ law (van der Kruit & Searle 1981). We used a vertical scaleheight of ∼ 365 pc, which is ∼20 per cent of the stellar disc scalelength.

5.1.3 *The mass-to-light ratio*

With such a small bulge-to-disk ratio (and consequently R_e), M33 can be considered as nearly a pure disc galaxy. In this paper, both cases are considered; the pure disc case and the disc + small bulge case. However, with such a small bulge, they should be fairly similar. The colour M/L are defined separately for the bulge and the disk and are used to obtain the actual total stellar mass contribution using the method described in Oh et al. (2008):

$$\Upsilon_*^{3.6} = B^{3.6} \times \Upsilon_*^K + A^{3.6}, \tag{9}$$

where $\Upsilon_*^{3.6}$ is the M/L at 3.6 μm, Υ_*^K, the M/L in the K band and $B^{3.6}$ and $A^{3.6}$ the correction coefficients. For the K-band M/L, we used the relation $\log(\Upsilon_*^K) = 1.46(J - K) - 1.38$ taken from de Blok et al. (2008), obtained by using an extrapolation of Bell & de Jong (2001), where the stellar mass synthesis uses a Salpeter initial mass function. The $\Upsilon_*^{3.6}$ for nearby galaxies is obtained using Υ_*^K (de Blok et al. 2008):

$$\Upsilon_*^{3.6} = 0.92 \times \Upsilon_*^K - 0.05. \tag{10}$$

The K-band M/L is obtained using the 2MASS $(J-K)$ colour computed by Jarrett et al. (2003). The $(J-K)$ colour has been computed separately for the bulge in the inner part and for the disc in the outer parts. The first data points $(J-K)$ are used for the bulge. For the pure disc case, the mean colour from 65 to 570 arcsec has been used. The $(J-K)$ decomposition gives for the bulge and disc 0.94 ±0.03 and 0.86 ±0.03, respectively. However, it is quite likely that the bulge colour is underestimated, being contaminated by disc light. Those values give the mean M/L in the 3.6 μm band : $\Upsilon_d^{3.6} = 0.72 \pm 0.1$ for the disc and $\Upsilon_b^{3.6} = 0.80 \pm 0.1$ for the bulge. The effective mass density profile is obtained by (Oh et al. 2008):

$$\Sigma[\mathrm{M}_\odot\,\mathrm{pc}^{-2}] = \Upsilon_*^{3.6} \times 10^{-0.4\times(\mu_{3.6}-24.8)}, \tag{11}$$

where $\Upsilon_*^{3.6}$ is the M/L in the *Spitzer*/IRAC 3.6 μm band. The density profile is used in GIPSY to compute the contribution of the stellar component.

5.2 DM halo density profile

The total rotation velocity is given by

$$V_{\mathrm{rot}}^2 = V_\star^2 + V_{\mathrm{gas}}^2 + V_{\mathrm{DM}}^2, \tag{12}$$

where $V_\star^2$ is the contribution of the stars, V_{gas}^2 the contribution of the gas component and V_{DM}^2 the contribution of the DM halo. The DM contribution is required to explain the outermost flat part of the RCs in galaxies (Bosma 1978; Carignan & Freeman 1985). The DM distribution can be defined by different types of density profile. We will limit this study to the most commonly used halo density profiles, the pseudo-isothermal (ISO) and the Navarro, Frenk and White (NFW) halo distributions, which show the largest differences in the inner parts, where the RC is well defined by the Hα data.

5.2.1 *ISO density profile*

The pseudo-isothermal (ISO) DM halo is a core-dominated type of halo. The ISO density profile is given by

$$\rho_{\mathrm{ISO}}(R) = \frac{\rho_0}{1 + (\frac{R}{R_c})^2}, \tag{13}$$

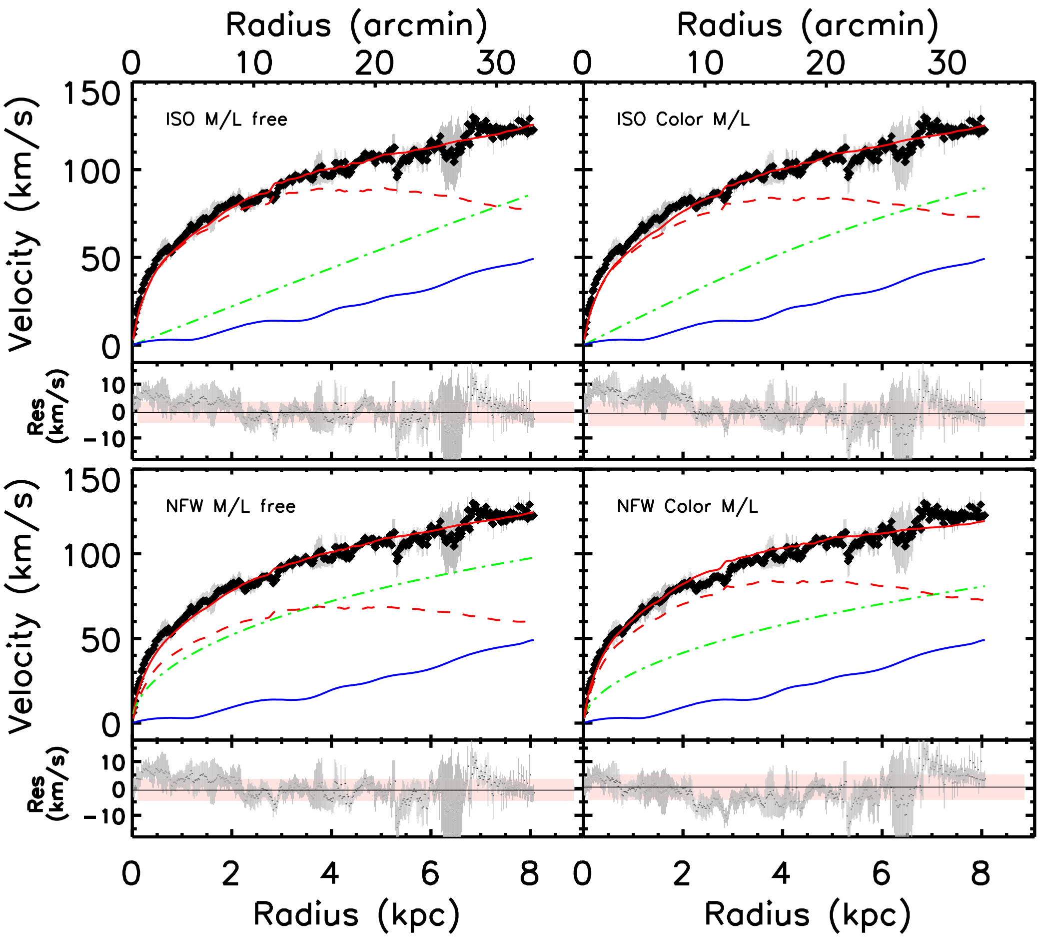

Figure 14. M33 mass models with a DM halo for the pure disc case. Models on the left are best fits while models on the right have a fixed M/L determined by the IR colour (see Section 5.1). The top panels represent the models with the ISO and the bottom panels those with the NFW density distributions. The stellar disc contribution is in broken red, the H I contribution in blue, the halo contribution in broken green and the sum of the three components is shown as a continuous red line. At the bottom of each model, the mean residuals (observation model) are presented.

where ρ_0 is the central density and R_c the core radius of the halo. The velocity contribution of a ISO halo is given by

$$V_{\rm ISO}(R) = \sqrt{4\pi G\rho_0 R_c^2\left(1-\frac{R_c}{R}\,{\rm atan}\left(\frac{R}{R_c}\right)\right)}. \tag{14}$$

5.2.2 *NFW density profile*

The NFW model is derived from ΛCDM simulations (Navarro, Frenk & White 1996; Navarro et al. 1997). This density profile (so-called universal halo) is known as the cuspy type and follows an R^{-1} law (de Blok 2010) in the innermost regions. The NFW halo density profile is described by

$$\rho_{\rm NFW}(R) = \frac{\rho_i}{\frac{R}{R_S}\left(1+\frac{R}{R_S}\right)^2}, \tag{15}$$

where $\rho_i \approx 3H_0^2/(8\pi G)$ is the critical density for closure of the universe and R_S is a scale radius. The velocity contribution corresponding to this halo is given by

$$V_{\rm NFW}(R) = V_{200}\sqrt{\frac{\ln(1+cx) - cx/(1+cx)}{x(\ln(1+c) - c/(1+c))]}}, \tag{16}$$

where V_{200} is the velocity at the virial radius R_{200}, $c = R_{200}/R_S$ gives the concentration parameter of the halo and x is defined as R/R_S. The relation between V_{200} and R_{200} is given by

$$V_{200} = \frac{R_{200}\times H_0}{100}, \tag{17}$$

where H_0 is the Hubble constant taken as $H_0 = 72$ km s^{-1} Mpc^{-1} (Hinshaw et al. 2009).

5.2.3 *Results*

The Hα RC of Fig. 10 (bottom panel) will be used for the mass modelling. Fig. 14 shows the models using the ISO (top) and the NFW (bottom) DM distributions for the pure disc case and Fig. 15 for the bulge–disc decomposition. The left-hand panels of the figures give the best-fitting models and the right-hand panels, the models with the M/L constrained by the IR colour and population synthesis models (Oh et al. 2008). Both fits use Levenberg–Marquardt least-squares fitting techniques. At the bottom of each model, the mean residuals (observation model) are represented by a black line with the same error bars as the velocity errors of the top panels. The part coloured in pink gives the dispersion of the residuals around the black regression line.

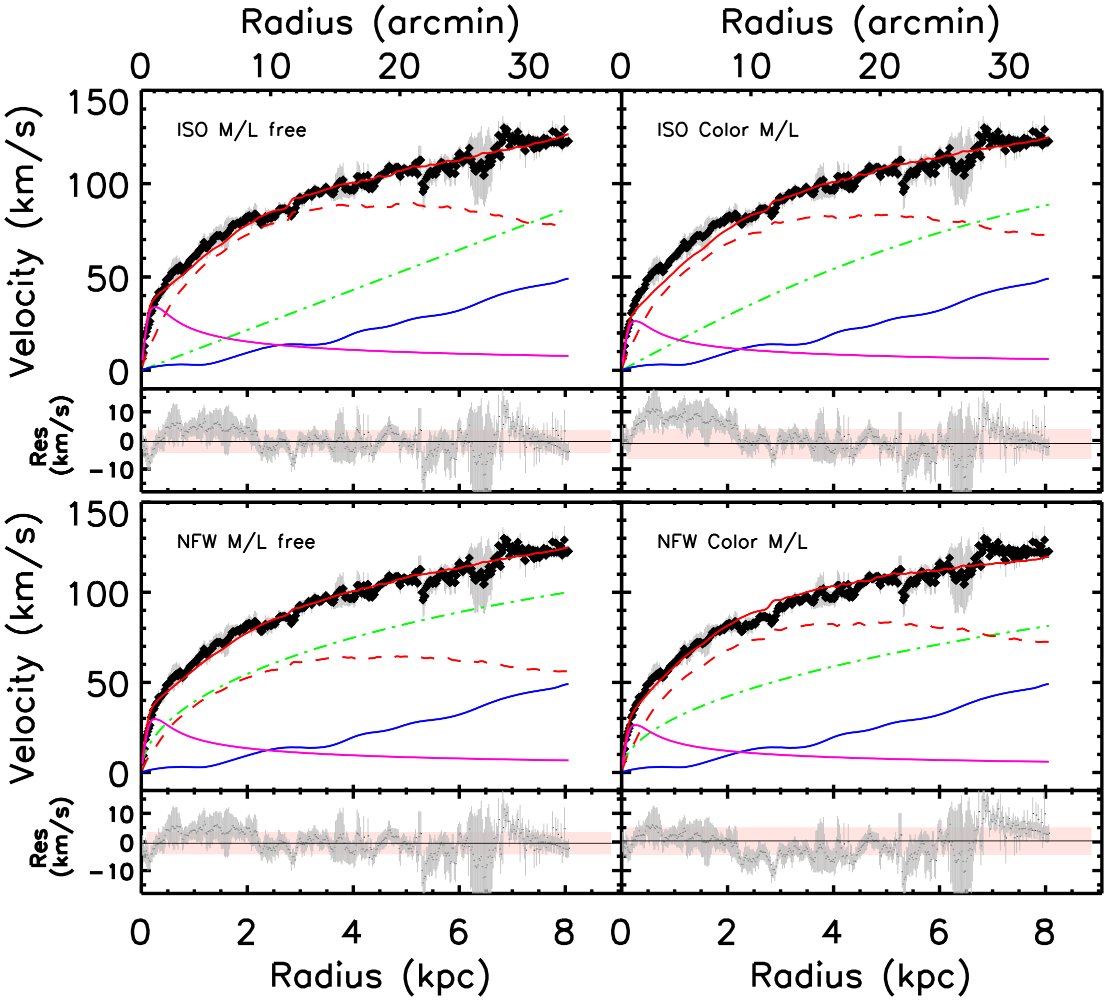

Figure 15. Same as in Fig. 14 but with the bulge contribution (in cyan).

Table 6. Hα mass model results with DM haloes for the pure disc case.

Halo model (1)	Params (2)	Best fit (3)	Colour M/L* (4)
ISO	ρ_0	6.75 ± 0.57	7.46 ± 0.43
	R_c	24.23 ± 17.02	11.13 ± 0.40
	Υ	0.81 ± 0.01	0.72
	χ_r^2	0.88	1.16
NFW	R_{200}	240.00 ± 188.34	300.26 ± 106.55
	c	4.41 ± 4.15	2.37 ± 0.91
	Υ	0.48 ± 0.11	0.72
	χ_r^2	0.87	1.56

Notes. *M/L fixed by the colour of the disc;
ρ_0, the central DM density, is given in units of 10^{-3} M$_\odot$ pc^{-3};
R_c and R_{200} are in kpc.

Table 7. Hα mass model results with DM haloes, using the bulge–disc decomposition.

Halo model (1)	Params (2)	Best fit (3)	Colour M/L* (4)
ISO	ρ_0	6.41 ± 0.60	12.52 ± 0.53
	R_c	119.50 ± $\gtrsim$200	6.32 ± 0.40
	Υ_d	0.82 ± 0.01	0.72
	Υ_b	1.32 ± 0.06	0.80
	χ_r^2	0.85	1.34
NFW	R_{200}	211.55 ± 0.72	2.78 ± 0.78
	c	8.67 ± 0.12	0.76 ± 0.45
	Υ_d	0.43 ± 0.01	0.72
	Υ_b	1.01 ± 0.11	0.80
	χ_r^2	0.75	1.43

Notes. *M/L fixed by the colour of the disc and of the bulge;
ρ_0, the central DM density is given in units of 10^{-3} M$_\odot$ pc^{-3};
R_c and R_{200} are in kpc.

Tables 6 and 7 give the results of the mass models: column (1) gives the type of halo density profile used; column (2) gives the parameters of the halo. In the tables, Υ gives the M/L obtained from the fits and χ_r^2 the goodness of the fit. Column (3) shows the results using the best fits and column(4) the results when the M/L are kept fixed at the value obtained using the ($J-K$) colour and population synthesis models. In Table 7, the parameter for the bulge M/L is given by Υ_b. The results of the mass models will be discussed in the next section.

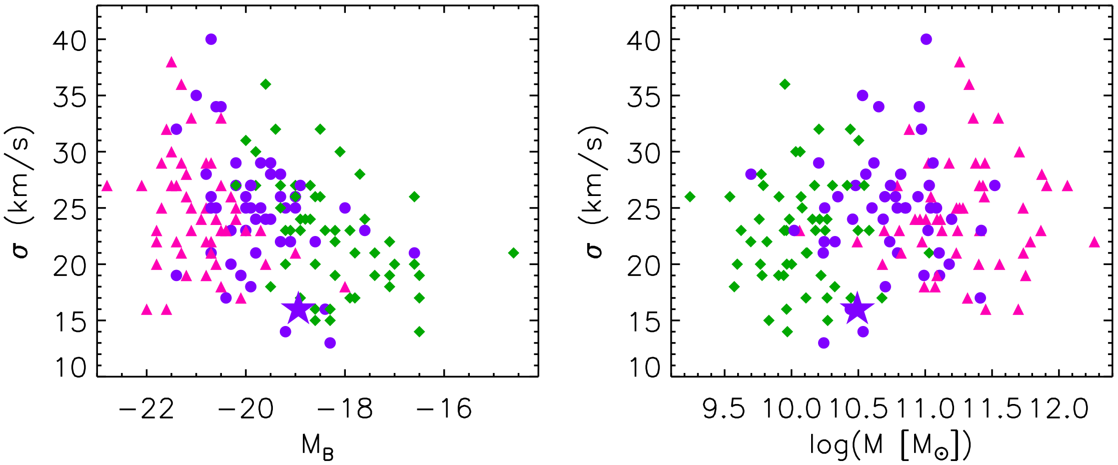

Figure 16. Mean velocity dispersion of M33 (star) and of other nearby star-forming disc galaxies from Epinat et al. (2010). On the right, the mass is given by $M = V_{\max}^2 R_{25}/G$, where $V_{\max}$ is the maximum velocity of each Hα RC.

6 DISCUSSION

6.1 M33 velocity dispersion

Our new data set is ideal to study the internal velocity dispersion of H II regions in M33, and the mean velocity dispersion of the galaxy. In Fig. 16, we compare the mean velocity dispersion of M33 to a subsample of 151 nearby star-forming galactic discs from the GHASP survey (Epinat et al. 2008a) studied in Epinat et al. (2010). It is obvious how the ionized interstellar medium of M33 appears dynamically colder (lower velocity dispersion) than in other galaxies. We have divided the sample into three classes of size: small galaxies with $R_{25} < 7.5$ kpc, intermediate size galaxies with $7.5 < R_{25} < 11.5$ kpc and large galaxies with $R_{25} > 11.5$ kpc. Though being within the class of intermediate galaxy size, M33 curiously behaves like smaller galaxies that have lower mass and absolute magnitude.

Giant extragalactic H II regions seen in gas-rich spiral and dIrr galaxies are regions of strong star formation with a size ranging between 0.1 and 1 kpc, a Hα luminosity of 10^{39}–10^{40} erg s^{-1}, a mean density of 1–10 cm^{-3} and an ionized mass of 10^4–10^5 M$_\odot$, which embeds a population of 100–200 ionizing stars (Kennicutt, Bothun & Schommer 1984; Kennicutt 1984). In addition, the velocity dispersion of the gas presents distinct kinematics with subsonic and supersonic emission-line widths (Smith & Weedman 1970, 1971). Uniform expansion of H II regions into a medium of constant density results in subsonic expansion velocities (Spitzer & Tomasko 1968). Supersonic motions are inferred for velocity dispersion typically larger than $(kT/m)^{0.5} \sim 10$–13 km s^{-1}, where k is the Boltzmann constant, m the typical hydrogen mass weighted by the molecular content and $T = 10^4$ K, the characteristic temperature of the H II region. Supersonic velocity dispersions ranging from 15 to 40 km s^{-1} are observed and give rise to different interpretations (see discussion in Bordalo & Telles (2010). In the 'champagne' model (Tenorio-Tagle 1979), the expanding H II bubble bursts thought the surface of the surrounding molecular cloud where the sharp gas density discontinuity generates a shock wave that accelerates the gas to supersonic speeds. Density gradient within the H II regions may generate supersonic motions prior to their acceleration through the surface of the cloud (Mazurek 1982).

Our data confirm that the region NGC 604 (Fig. 9), like many other giant H II regions, displays both single Gaussian and complex line profiles (Munoz-Tunon et al. 1996; Yang et al. 1996). Single Gaussian profiles essentially come from the bright regions and show the broadening mechanics due to self-gravitation. More complex lines come from faint regions and emanate from the wind-driven mechanical energy injection due to massive stars that produce expanding shells, cavities and bubbles, filaments and outflows, loops and ring-like regions.

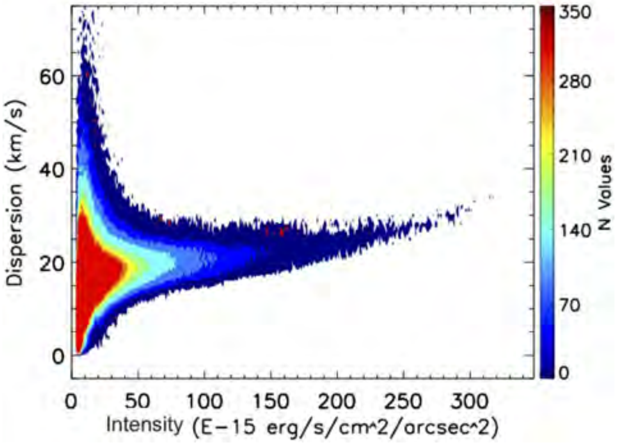

Figure 17. Corrected velocity dispersion ($\sigma_{\mathrm{cor}}^2 = \sigma_{\mathrm{obs}}^2 - \sigma_{\mathrm{PSF}}^2$), computed using a single Gaussian, versus integrated line intensity for the whole FOV of M33. The number of pixels having a given intensity and dispersion is given by the colour scale.

A velocity dispersion versus intensity (σ–I) diagram provides diagnostics used to separate the main broadening mechanisms detected in the emission lines of giant H II regions, such as differentiating the broadening produced by virial motions resulting from the total gravitational potential and that resulting from the superposition of shells and loops generated by massive stars, which ends up dispersing the parent clouds (Munoz-Tunon et al. 1996; Yang et al. 1996; Martínez-Delgado et al. 2007; Moiseev & Lozinskaya 2012). Such a diagram is given for the whole disc of the galaxy in Fig. 17. We used the total intensity in the line rather than the intensity peak because the total intensity is independent from the spectral resolution (which is not the case of the intensity peak). In the following, we use intensity to refer to the total line intensity. Fig. 17 shows the strong relation between the Hα velocity dispersion and the Hα intensity. Only low-intensity regions show a broad range of velocity dispersions. In other words, the range of velocity dispersions decreases when intensity increases. Regions showing larger velocity dispersions arise from diffuse emitting areas rather than from intense H II regions. Subsonic dispersions are only observed in low-intensity regions, whereas supersonic motions are both observed in the low surface brightness medium and the brightest star-forming regions. These latter have a roughly constant velocity dispersion (20–30 km s^{-1}), while the largest supersonic dispersions (40–60 km s^{-1}) are only seen among the lowest intensities.

As described in Munoz-Tunon et al. (1996), in the frame of the CSM for stellar cluster formation (Tenorio-Tagle, Munoz-Tunon & Cox 1993), the gravitational collapse fragments the gas clouds and first forms the low-mass stars. The bow shocks and wakes caused by their stellar winds suspend the collapse of the cloud and communicate the stellar velocity dispersion to the surrounding gas. The core of the cloud is thus virialized and the supersonic gas velocity dispersion traces its gravitational potential, despite dissipation. Massive stars form later in a cloud at equilibrium in which the velocity dispersion of the gas is constant and does not depend on the intensity of the newly formed giant H II regions. In the σ–I diagram, this corresponds to the horizontal area (with the almost constant velocity dispersion of 20 ± 3 km s^{-1}) displaying a broad range of intensities.

As massive stars evolve, strong mechanical energy sweeps the ISM into shells displaying supersonic velocities higher than the ambient stellar velocity dispersion. The velocity dispersion of these shells decreases with age while their luminosity increases: young and faint shells produce a large range of velocity dispersions and low intensities while older and bright shells display a narrower velocity dispersion amplitude and higher intensities. If the shells are embedded in the virialized core, their velocities cannot be lower than the stellar velocity dispersion but, if the shells are outside the core, their velocities can decrease to lower values, down to subsonic velocities. In the σ–I diagram, these shell phases, ages and locations are found within the broad range of velocity dispersions at low intensities. To fully understand how this last area of the σ–I diagram is filled by expanding shells, this zone should be understood as the result of different projection effects.

On the one hand, emission from a line-of-sight passing across the centre of an expanding spherical shell of gas will present the largest velocity difference across the shell due to the large distance separating its two edges and an intermediate intensity. On the other hand, a line-of-sight going through the inner edge of the shell will present a lower velocity difference but a very high intensity due to the large quantity of gas integrated along the line of sight. Finally, a line of sight running through the outer edge of the shell will display even a much lower velocity difference and a very low intensity due to the small quantity of gas integrated along the line of sight. In addition to these shells that cannot be distinguished individually on this plot, this area of the σ–I diagram mainly corresponds to diffuse Hα emission.

6.2 Comparison of the Hα kinematics with H I results

In this section, a comparison of our Hα kinematical results is done with previous H I studies. Normally, our 5 arcsec binning Hα RC should give the optimal representation of the kinematics in the inner parts of M33, without suffering from e.g. the beam smearing that may affect earlier H I data. Fig. 18 compares the H I RC derived by Corbelli et al. (2014), as well as older H I studies by Corbelli & Schneider (1997) and Newton (1980) and recent VLA data at 12 arcsec resolution (Gratier et al. 2010) with the Hα RC obtained in this study. It is not surprising that the Arecibo data of Corbelli & Schneider (1997) suffer from beam smearing in the inner kpc and underestimate the rotational velocities while the 1.5 arcmin × 3.0 arcmin resolution Newton (1980) data are quite consistent with the 12 arcsec resolution (∼48 pc) H I data and our 5 arcsec step (∼20 pc) Hα data, at least out to 6.5 kpc. Comparing our Hα data to the H I for $R > 6.5$ kpc seems to suggest that we may overestimate the RC in the outer parts. Since the difference occurs at radii with the lowest number of independent bins (see bottom panel of Fig. 12), it could simply reflect the difficulty to derive accurate Hα rotation velocities by our fitting procedure within these regions. However, it should be noted that the 2010 VLA data of Gratier et al. (2010) have lower velocities than Corbelli et al. (2014) in those same outer parts.

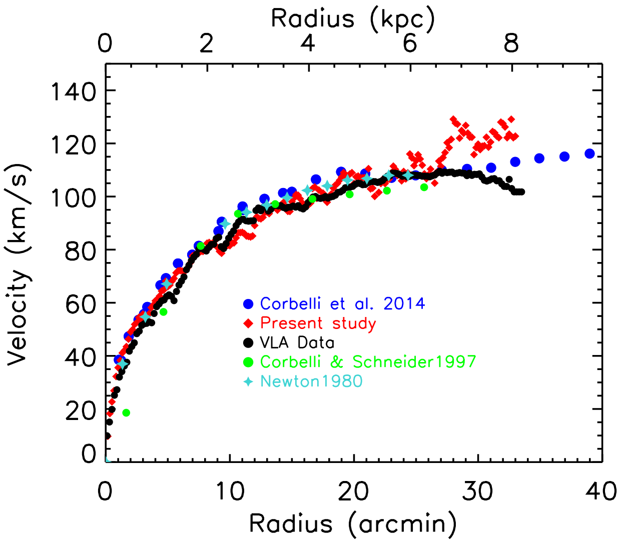

Figure 18. Comparison of Hα and H I RCs. Blue represents the H I (squares) RC from Corbelli et al. (2014); black is for Gratier et al. (2010) VLA data; green circles are for Corbelli & Schneider (1997) data; green crosses for Newton (1980) data and red symbols are for our Hα RC.

6.3 Mass modelling results

The extent of the spheroidal component shown in the surface brightness profile is very small $r \leq 1.5$ arcmin (≤350 pc); with a bulge-to-disc ratio of only ∼0.04, large differences between the mass models with and without a bulge component are not expected. In each case, a best-fitting model and a fixed M/L model are explored. The reduced chi-square χ_r^2 is used to determine the goodness of the fit.

In the pure disc case (Fig. 14), the two DM best-fitting models (ISO and NFW) give very similar good fits as shown by the values of the χ_r^2 in Table 6. The residuals (bottom panels) shows that the only discrepancy is in the very inner parts. When using the fixed M/L value of the disc, it can be seen that ISO gives a better fit ($\chi_r^2 = 1.16$ versus 1.56), despite the fact that it still slightly underestimates the velocities for $R < 2$ kpc. This may point out that the method used to derive the M/L may underestimates it slightly (0.72 versus 0.83). This could also point out that an additional mass component (a small bar or nuclear disc) is missing in our models in the innermost parts of the disc.

As expected, in the bulge–disc case, it is clear that the addition of a bulge component does not bring anything more than the disc only model due to its very small R_e and the extra uncertainty coming from the M/L of the bulge. Looking at Fig. 15 and Table 7, the conclusions are that both functional forms (ISO and NFW) yields very similar results. Because in the bulge+disc case, we add one free parameter (Υ_b of the bulge) and because the uncertainty on that parameter is large since the IR colour used to derive it is polluted by disc light with the result of underestimating the IR colour and thus the Υ_b of the bulge, we favour the results of the disc-only models.

We conclude, that the pure-disc ISO models (best-fitting and/or fixed M/L) give a slightly better representation of the mass distribution using the Hα RC that is derived out to ~8 kpc with a M/L for the luminous disc ~0.72–0.82, a core radius ~12–24 kpc and a central density $\rho_0 \sim 0.007$–$0.008\ \mathrm{M_\odot\ pc^{-3}}$ for the dark isothermal halo. It is clear that when we will combine those Hα data to more extended H I kinematics, we should be able to constrain much better the parameters of the mass distribution.

7 SUMMARY AND CONCLUSIONS

New Hα FP mapping of the nearby galaxy M33 has been presented. The data were obtained on the 1.6 m telescope of the OMM using a high-resolution FP etalon ($p = 765$) and a very sensitive photon counting EMCCD camera (QE ~ 90 per cent). The 10 fields observed cover a field of ~42 arcmin × 56 arcmin (10 kpc × 13.5 kpc) with a spatial resolution ~3 arcsec. The H II regions inside this area are well defined spatially and spectrally. This study provides for the whole field, as well as for each H II regions and nebulae (e.g. NGC 604, NGC 595, NGC 588, IC 137, IC 136) velocity and dispersion maps. The data were flux calibrated using Relaño et al. (2013) data.

Looking at the velocity dispersion σ profile as a function of radius, we found that it is essentially flat at an average value of $16 \pm 2\ \mathrm{km\ s^{-1}}$. From $R \sim 7.5$ kpc, the velocity dispersions increase to ~20–25 $\mathrm{km\ s^{-1}}$. This radius is the location of the beginning of the warp of the H I disc where the twist of the position angle starts. The mean velocity dispersion of M33 was found to be small when compared to a sample of nearby star-forming galactic discs (GHASP sample) which have σ varying from 15 to 35 $\mathrm{km\ s^{-1}}$. Finally, a velocity dispersion versus intensity (σ–I) diagram shows clearly a strong relation between the Hα velocity dispersion and the Hα intensity.

The main aim of this study was to derive a high spatial resolution Hα RC for M33 in order to try to constrain the best functional form representing the DM distribution between the cored ISO models and the cosmologically motivated cuspy NFW models. The rotation centre found is very close to the optical centre. The other kinematical parameters found are $V_{\mathrm{sys}} = -178 \pm 3\ \mathrm{km\ s^{-1}}$, PA = 202° ±4° and $i = 52° \pm 2°$. The RC was derived separately for the approaching, receding and for both sides. The RC was computed using a constant 5 arcsec step to perform the mass modelling. Besides the intrinsic error in each ring, we added an error to represent the asymmetry of both sides since this RC will be compared to axisymmetric mass models. After a steep rise in the inner 1 kpc, the RC rises slowly to its maximum value of ~123±3 $\mathrm{km\ s^{-1}}$ at the last point (33 arcmin).

Comparing our adopted RC to H I RCs in the literature, we found that our Hα data agree very well with the H I from the centre out to ~ 6.5 kpc. The only exception is the first inner point of Corbelli & Schneider (1997), which may a bit suffer from beam smearing due to the large Arecibo beam. With our high-resolution data, we bring more data points in the inner part of the RC, which is very useful for the mass modelling. On the other hand, for $R > 6.5$ kpc, this comparison suggests that our Hα data may overestimate the velocities in the outer parts.

For the mass model analysis, the *Spitzer*/IRAC 3.6 μm profile was used to represent the stellar disc mass contribution. The disc parameters found are a scalelength $R_d = 1.82 \pm 0.02$ kpc and an extrapolated surface brightness $\mu_0 = 18.01 \pm 0.03\ \mathrm{mag\ arcsec^{-2}}$. A bulge–disc decomposition was also done even if it will not alter significantly the results of the mass models with a bulge to disc ratio of only 0.04. Besides best-fitting models, models with fixed M/L based on IR colours and population synthesis models, following the method used by Oh et al. (2008) and de Blok et al. (2008) are also explored.

For the mass models, we decided to favour the disc-only models because of the extra uncertainties introduced by adding a bulge which contributes very little (B/D = 0.04) to the luminous mass. In this case, the ISO models give a better fit despite the fact that they seem to underestimate the velocities in the inner 2 kpc (see the residual curves at the bottom of Fig. 14). This may point out to the fact that the determination of the M/L values using the IR colours and population synthesis models slightly underestimates the M/L ratio of the disc or that an inner mass component has been omitted in the modelling.

An ideal RC using our high spatial resolution Hα RC in the inner 6.5 kpc and a high sensitivity but low spatial resolution H I RC in the outer parts should allow us to constrain much better the parameters of the mass models. This should be done in a subsequent study presenting new deep H I observations.

ACKNOWLEDGEMENTS

ZSK's work was supported by a grant of the CIOSPB of Burkina Faso, CC's Discovery grant of the Natural Sciences and Engineering Research Council of Canada and CC's South African Research Chairs Initiative (SARChI) grant of the Department of Science and Technology (DST), the SKA SA and the National Research Foundation (NRF). LC acknowledges a financial support from CNES. We would like to thank Tom Jarrett for providing the *WISE* I data, the staff of the OMM for their support and Yacouba Djabo for observing with us at OMM. A part of the MONTAGE package of IPAC have been used in the process of our reduction. The optical image in blue band comes from the Digitized Sky Surveys (DSS images). The IR archives images are from the *Spitzer* and *WISE* Space Telescopes.

REFERENCES

Amram P., Marcelin M., Boulesteix J., Le Coarer E., 1992, A&A, 266, 106
Amram P., Marcelin M., Balkowski C., Cayatte V., Sullivan W. T., III, Le Coarer E., 1994, A&AS, 103, 5
Amram P., Balkowski C., Boulesteix J., Cayatte V., Marcelin M., Sullivan W. T., III, 1996, A&A, 310, 737
An D., Terndrup D. M., Pinsonneault M. H., 2007, ApJ, 671, 1640
Begeman K. G., 1987, PhD thesis, Kapteyn Institute
Bell E. F., de Jong R. S., 2001, ApJ, 550, 212
Blais-Ouellette S., Carignan C., Amram P., Côté S., 1999, AJ, 118, 2123
Bordalo V., Telles E., 2010, 38th COSPAR Scientific Assembly, Vol. 38, HII Galaxies As Alternative Cosmic Tracers To Measure The Dark Energy And The Matter Content Of The Universe. p. 3658
Bosma A., 1978, PhD thesis, Univ. Groningen
Boulesteix J., Monnet G., 1970, A&A, 9, 350

Boulesteix J., Courtes G., Laval A., Monnet G., Petit H., 1974, A&A, 37, 33

Capaccioli M., 1989, in Corwin H. G., Jr Bottinelli L., eds, World of Galaxies (Le Monde des Galaxies) Photometry of Early-Type Galaxies and the R exp 1/4 Law. p. 208

Carignan C., Freeman K. C., 1985, ApJ, 294, 494

Carranza G., Courtes G., Georgelin Y., Monnet G., Pourcelot A., 1968, Ann. d'Astrophys., 31, 63

Chemin L. et al., 2006, MNRAS, 366, 812

Chemin L., Carignan C., Foster T., Kam Z. S., 2012, in Boissier S., de Laverny P., Nardetto N., Samadi R., Valls-Gabaud D., Wozniak H., eds, SF2A-2012: Proc. Annu. Meeting French Soc. Astron. Astrophys., Know (better) your neighbour: New H I Structures in Messier 33 Unveiled by a Multiple Peak Analysis of High-Resolution 21-cm Data. p. 519

Cockcroft R. et al., 2013, MNRAS, 428, 1248

Corbelli E., 2003, MNRAS, 342, 199

Corbelli E., Salucci P., 2000, MNRAS, 311, 441

Corbelli E., Salucci P., 2007, MNRAS, 374, 1051

Corbelli E., Schneider S. E., 1997, ApJ, 479, 244

Corbelli E., Walterbos R. A. M., 2007, ApJ, 669, 315

Corbelli E., Thilker D., Zibetti S., Giovanardi C., Salucci P., 2014, A&A, 572, A23

Courtes G., Petit H., Petit M., Sivan J., Dodonov S., 1987, A&A, 174, 28

Daigle O., Carignan C., Hernandez O., Chemin L., Amram P., 2006, MNRAS, 368, 1016

Daigle O., Carignan C., Gach J.-L., Guillaume C., Lessard S., Fortin C.-A., Blais-Ouellette S., 2009, PASP, 121, 866

de Blok W. J. G., 2010, Adv. Astron., 2010

de Blok W. J. G., Walter F., Brinks E., Trachternach C., Oh S.-H., Kennicutt R. C., Jr, 2008, AJ, 136, 2648

de Vaucouleurs G., de Vaucouleurs A., Corwin H. G., Jr, Buta R. J., Paturel G., Fouque P., 1991, Sky Telesc., 82, 621

Dicaire I., Carignan C., Amram P., Marcelin M., Hlavacek-Larrondo J., de Denus-Baillargeon M.-M., Daigle O., Hernandez O., 2008, AJ, 135, 2038

Druard C. et al., 2014, A&A, 567, 118

Epinat B., 2009, PhD thesis, Université Aix-Marseille

Epinat B. et al., 2008a, MNRAS, 388, 500

Epinat B., Amram P., Marcelin M., 2008b, MNRAS, 390, 466

Epinat B., Amram P., Balkowski C., Marcelin M., 2010, MNRAS, 401, 2113

Ferguson A., Irwin M., Chapman S., Ibata R., Lewis G., Tanvir N., 2007, Resolving the Stellar Outskirts of M31 and M33, 24th edn. Springer, Netherlands, p. 239

Freedman W. L. et al., 2001, ApJ, 553, 47

Fukushige T., Makino J., 1997, ApJ, 477, L9

Galleti S., Bellazzini M., Ferraro F. R., 2004, A&A, 423, 925

Gardan E., Braine J., Schuster K. F., Brouillet N., Sievers A., 2007, A&A, 473, 91

Gebhardt K. et al., 2001, AJ, 122, 2469

Gehrz R., Willner S., 2004, M33 Mapping and Spectroscopy., spitzer Proposal ID #5

Gieren W. et al., 2013, ApJ, 773, 69

Goerdt T., Moore B., Read J. I., Stadel J., 2010, ApJ, 725, 1707

Gordon K. D., Hanson M. M., Clayton G. C., Rieke G. H., Misselt K. A., 1999, ApJ, 519, 165

Graham A. W., Worley C. C., 2008, MNRAS, 388, 1708

Gratier P. et al., 2010, A&A, 522, A3

Gratier P. et al., 2012, A&A, 542, A108

Guidoni U., Messi R., Natali G., 1981, A&A, 96, 215

Hinshaw G. et al., 2009, ApJS, 180, 225

Hlavacek-Larrondo J., 2009, Master's thesis, Univ. Montréal

Hoopes C. G., Walterbos R. A. M., Bothun G. D., 2001, ApJ, 559, 878

Inoue S., Saitoh T. R., 2011, MNRAS, 418, 2527

Ishiyama T. et al., 2013, ApJ, 767, 146

Ivanov G. R., Kunchev P. Z., 1985, Ap&SS, 116, 341

Jarrett T. H., Chester T., Cutri R., Schneider S. E., Huchra J. P., 2003, AJ, 125, 525

Kennicutt R. C., Jr, 1984, ApJ, 287, 116

Kennicutt R. C., Jr, Bothun G. D., Schommer R. A., 1984, AJ, 89, 1279

Kent S. M., 1987, AJ, 94, 306

Kramer C. et al., 2011, in Röllig M., Simon R., Ossenkopf V., Stutzki J., eds, EAS Publ. Ser. Vol. 52, Star Formation in M 33 (HerM33es). p. 107

Kramer C. et al., 2013, A&A, 553, A114

Kravtsov A. V., Klypin A. A., Bullock J. S., Primack J. R., 1998, ApJ, 502, 48

Lauer T. R., Faber S. M., Ajhar E. A., Grillmair C. J., Scowen P. A., 1998, AJ, 116, 2263

Li H.-B., Henning T., 2011, Nature, 479, 499

McConnachie A. W., Irwin M. J., Ferguson A. M. N., Ibata R. A., Lewis G. F., Tanvir N., 2004, MNRAS, 350, 243

McConnachie A. W., Irwin M. J., Ferguson A. M. N., Ibata R. A., Lewis G. F., Tanvir N., 2005, MNRAS, 356, 979

McConnachie A. W. et al., 2009, Nature, 461, 66

McConnachie A. W., Ferguson A. M. N., Irwin M. J., Dubinski J., Widrow L. M., Dotter A., Ibata R., Lewis G. F., 2010, ApJ, 723, 1038

McLean I. S., Liu T., 1996, ApJ, 456, 499

Magrini L., Corradi R. L. M., Mampaso A., Perinotto M., 2000, A&A, 355, 713

Martínez-Delgado D., Peñarrubia J., Jurić M., Alfaro E. J., Ivezić Z., 2007, ApJ, 660, 1264

Mazurek T. J., 1982, in Roger R. S., Dewdney P. E., eds, Astrophysics and Space Science Library, Vol. 93, Regions of Recent Star Formation. Reidel, Dordrecht, p. 61

Minniti D., Olszewski E., Rieke M., 1994, in Layden A., Smith R. C., Storm J., eds, European Southern Observatory Conference and Workshop Proceedings, Vol. 51, IR Photometry of M33. ESO, Garching, p. 159

Moiseev A. V., Lozinskaya T. A., 2012, MNRAS, 423, 1831

Moore B., Quinn T., Governato F., Stadel J., Lake G., 1999, MNRAS, 310, 1147

Munoz-Tunon C., Tenorio-Tagle G., Castaneda H. O., Terlevich R., 1996, AJ, 112, 1636

Navarro J. F., Frenk C. S., White S. D. M., 1996, ApJ, 462, 563

Navarro J. F., Frenk C. S., White S. D. M., 1997, ApJ, 490, 493

Navarro J. F. et al., 2010, MNRAS, 402, 21

Newton K., 1980, MNRAS, 190, 689

Ogiya G., Mori M., 2011, ApJ, 736, L2

Oh S.-H., de Blok W. J. G., Walter F., Brinks E., Kennicutt R. C., Jr, 2008, AJ, 136, 2761

Oh S.-H., de Blok W. J. G., Brinks E., Walter F., Kennicutt R. C., Jr, 2011, AJ, 141, 193

Paturel G., Teerikorpi P., Theureau G., Fouqué P., Musella I., Terry J. N., 2002, A&A, 389, 19

Pontzen A., Governato F., 2012, MNRAS, 421, 3464

Putman M. E. et al., 2009, ApJ, 703, 1486

Regan M. W., Vogel S. N., 1994, ApJ, 434, 536

Relaño M. et al., 2013, A&A, 552, A140

Saha A., Thim F., Tammann G. A., Reindl B., Sandage A., 2006, ApJS, 165, 108

Sandage A., Humphreys R. M., 1980, ApJ, 236, L1

Seigar M. S., 2011, Int. Scholarly Res. Not.: Astron. Astrophys., 2011, 1

Smith M. G., Weedman D. W., 1970, ApJ, 160, 65

Smith M. G., Weedman D. W., 1971, ApJ, 169, 271

Spitzer L., Jr, Tomasko M. G., 1968, ApJ, 152, 971

Stonkutė R. et al., 2008, AJ, 135, 1482

Swaters R. A., Schoenmakers R. H. M., Sancisi R., van Albada T. S., 1999, MNRAS, 304, 330

Swaters R. A., Madore B. F., Trewhella M., 2000, ApJ, 531, L107

Tenorio-Tagle G., 1979, A&A, 71, 59

Tenorio-Tagle G., Munoz-Tunon C., Cox D. P., 1993, ApJ, 418, 767

Teyssier R., Pontzen A., Dubois Y., Read J. I., 2013, MNRAS, 429, 3068

Tosaki T. et al., 2011, PASJ, 63, 1171

van der Kruit P. C., Searle L., 1981, A&A, 95, 105

Vogelaar M. G. R., Terlouw J. P., 2001, in Harnden F. R., Jr Primini F. A., Payne H. E., eds, Proc. ASP Conf. Ser. Vol. 238, Astronomical Data Analysis Software and Systems X. Astron. Soc. Pac., San Francisco, p. 358
Warner P. J., Wright M. C. H., Baldwin J. E., 1973, MNRAS, 163, 163
Wilson C. D., Scoville N., 1989, ApJ, 347, 743
Wolfe S. A., Pisano D. J., Lockman F. J., McGaugh S. S., Shaya E. J., 2013, Nature, 497, 224
Yang H., Chu Y.-H., Skillman E. D., Terlevich R., 1996, AJ, 112, 146
Zaritsky D., Elston R., Hill J. M., 1989, AJ, 97, 97

APPENDIX A: DATA FOR THE RC AND THE Hα DISPERSION PROFILE: ONLINE

Table A1. The Hα RC of M33.

Rad (1)	V (2)	ΔV (3)	σ (4)	$\Delta\sigma$ (5)	Rad (6)	V (7)	ΔV (8)	σ (9)	$\Delta\sigma$ (10)	Rad (11)	V (12)	ΔV (13)	σ (14)	$\Delta\sigma$ (15)
0.08	6	4	14	10	11.08	87	4	16	5	22.08	104	5	17	7
0.17	9	4	12	6	11.17	86	3	16	5	22.17	105	6	17	7
0.25	13	3	12	4	11.25	86	3	16	6	22.25	106	8	18	7
0.33	18	5	14	5	11.33	86	3	16	6	22.33	107	7	19	8
0.42	21	4	15	4	11.42	86	4	15	6	22.42	106	7	18	8
0.50	23	4	16	4	11.50	85	3	15	6	22.50	105	5	17	7
0.58	25	3	15	4	11.58	83	3	15	6	22.58	107	5	16	7
0.67	26	3	16	5	11.67	85	3	16	6	22.67	107	6	17	8
0.75	31	3	16	5	11.75	86	3	16	6	22.75	105	7	16	7
0.83	32	3	15	5	11.83	85	3	16	6	22.83	107	5	15	7
0.92	35	3	15	4	11.92	87	3	16	6	22.92	108	5	16	7
1.00	35	3	15	4	12.00	89	3	17	7	23.00	109	5	15	6
1.08	37	3	14	4	12.08	91	3	17	7	23.08	111	4	15	6
1.17	38	4	14	4	12.17	92	3	17	7	23.17	112	4	15	6
1.25	39	3	14	5	12.25	93	3	18	7	23.25	111	3	15	6
1.33	42	4	14	5	12.33	92	4	18	7	23.33	111	4	15	5
1.42	41	4	14	5	12.42	91	4	18	6	23.42	108	7	15	5
1.50	42	3	14	5	12.50	92	4	18	7	23.50	108	8	15	6
1.58	43	3	14	5	12.58	91	4	18	7	23.58	108	6	14	5
1.67	43	5	13	4	12.67	92	3	18	8	23.67	109	6	13	5
1.75	44	5	13	4	12.75	93	3	18	9	23.75	108	6	14	7
1.83	46	4	13	4	12.83	94	3	19	9	23.83	105	7	15	7
1.92	48	3	14	5	12.92	95	3	18	8	23.92	106	7	16	8
2.00	49	4	14	4	13.00	94	3	18	8	24.00	110	5	17	8
2.08	49	5	14	4	13.08	94	3	18	8	24.08	111	5	16	7
2.17	50	6	14	5	13.17	93	5	17	7	24.17	105	6	16	7
2.25	51	5	13	5	13.25	95	4	17	7	24.25	105	6	16	8
2.33	52	5	13	5	13.33	96	3	17	7	24.33	109	3	18	9
2.42	53	7	13	5	13.42	97	3	17	7	24.42	113	5	17	8
2.50	53	8	13	5	13.50	96	3	17	7	24.50	116	4	17	9
2.58	53	7	13	5	13.58	96	3	17	7	24.58	116	4	16	7
2.67	54	7	13	6	13.67	96	3	17	7	24.67	115	4	16	7
2.75	55	7	13	6	13.75	95	3	17	8	24.75	113	4	16	7
2.83	53	6	13	5	13.83	95	3	16	6	24.83	111	4	16	7
2.92	56	5	13	5	13.92	95	3	16	6	24.92	113	4	16	6
3.00	56	3	14	5	14.00	96	4	16	6	25.00	114	4	16	7
3.08	54	3	14	5	14.08	97	3	16	7	25.08	115	3	14	6
3.17	53	4	15	5	14.17	97	3	15	6	25.17	116	6	14	6
3.25	53	3	15	5	14.25	98	3	14	7	25.25	113	10	13	6
3.33	55	3	15	6	14.33	98	3	14	6	25.33	119	6	14	6
3.42	56	3	15	5	14.42	97	3	15	6	25.42	112	14	14	6
3.50	56	3	15	5	14.50	96	3	15	6	25.50	113	14	14	6
3.58	56	3	15	5	14.58	95	3	15	6	25.58	111	14	15	6
3.67	58	3	15	6	14.67	95	4	14	6	25.67	109	16	15	6
3.75	59	3	15	6	14.75	95	3	15	6	25.75	107	19	15	5
3.83	59	3	15	5	14.83	94	4	14	6	25.83	106	18	15	6
3.92	60	3	15	6	14.92	96	5	15	7	25.92	107	18	16	6
4.00	61	3	15	5	15.00	98	7	15	7	26.00	108	19	17	7
4.08	61	3	15	5	15.08	99	7	15	6	26.08	110	17	17	6
4.17	62	3	15	5	15.17	100	9	15	6	26.17	110	18	16	6

Table A1 – *continued*

Rad (1)	V (2)	ΔV (3)	σ (4)	$\Delta\sigma$ (5)	Rad (6)	V (7)	ΔV (8)	σ (9)	$\Delta\sigma$ (10)	Rad (11)	V (12)	ΔV (13)	σ (14)	$\Delta\sigma$ (15)
4.25	61	3	15	5	15.25	100	9	15	7	26.25	111	20	16	6
4.33	62	4	15	5	15.33	101	9	15	7	26.33	108	17	17	6
4.42	64	5	15	5	15.42	100	9	15	7	26.42	104	16	17	6
4.50	65	5	15	5	15.50	100	9	15	7	26.50	105	17	16	6
4.58	64	5	15	5	15.58	102	9	15	7	26.58	108	18	15	6
4.67	65	6	15	5	15.67	99	6	16	7	26.67	109	17	15	7
4.75	67	5	16	6	15.75	97	4	16	6	26.75	112	17	15	7
4.83	69	5	16	5	15.83	98	6	16	6	26.83	114	16	16	8
4.92	68	5	16	5	15.92	98	5	16	6	26.92	112	14	15	8
5.00	65	6	16	5	16.00	97	5	16	6	27.00	110	14	14	8
5.08	66	6	16	5	16.08	96	4	16	7	27.08	112	11	15	8
5.17	67	5	16	5	16.17	97	4	16	6	27.17	115	7	15	9
5.25	67	6	16	5	16.25	97	4	16	6	27.25	119	7	14	9
5.33	68	6	16	5	16.33	97	4	15	6	27.33	116	4	15	9
5.42	69	5	16	5	16.42	96	5	16	7	27.42	119	5	15	12
5.50	69	5	17	5	16.50	98	5	16	6	27.50	121	3	20	14
5.58	71	5	17	5	16.58	100	5	16	7	27.58	126	8	15	7
5.67	71	5	17	5	16.67	104	8	15	6	27.67	116	3	12	8
5.75	72	5	16	5	16.75	104	8	16	7	27.75	114	7	13	7
5.83	72	5	16	5	16.83	104	6	15	6	27.83	122	10	15	8
5.92	72	5	16	5	16.92	102	5	16	5	27.92	124	13	15	8
6.00	72	5	17	5	17.00	99	4	17	6	28.00	130	3	19	12
6.08	72	6	17	5	17.08	100	3	17	6	28.08	126	4	15	9
6.17	72	6	17	5	17.17	104	7	17	6	28.17	128	4	16	9
6.25	71	5	17	5	17.25	99	3	17	6	28.25	129	3	16	11
6.33	72	5	18	6	17.33	99	3	18	7	28.33	126	5	14	6
6.42	72	8	18	6	17.42	100	3	19	7	28.42	120	3	14	7
6.50	72	8	18	6	17.50	105	6	19	7	28.50	123	3	17	10
6.58	73	8	18	6	17.58	97	3	19	6	28.58	123	3	19	13
6.67	73	9	18	6	17.67	101	3	18	7	28.67	126	3	16	9
6.75	74	8	18	6	17.75	100	4	18	7	28.75	124	4	19	9
6.83	75	6	17	6	17.83	97	3	16	6	28.83	123	3	15	9
6.92	76	5	17	6	17.92	98	3	17	6	28.92	124	4	19	10
7.00	78	4	17	6	18.00	99	3	17	7	29.00	125	5	19	9
7.08	78	4	17	6	18.08	101	3	17	7	29.08	128	3	16	7
7.17	78	4	17	6	18.17	102	3	17	7	29.17	122	3	15	8
7.25	78	4	17	6	18.25	103	3	18	7	29.25	123	10	15	8
7.33	79	4	17	5	18.33	104	3	18	7	29.33	123	3	17	10
7.42	79	3	17	6	18.42	104	3	18	8	29.42	124	4	13	5
7.50	79	3	18	6	18.50	104	3	18	7	29.50	121	3	15	8
7.58	78	3	18	6	18.58	105	3	18	7	29.58	118	4	15	5
7.67	80	3	17	6	18.67	105	3	18	8	29.67	118	9	19	10
7.75	79	3	18	6	18.75	105	3	17	7	29.75	122	3	15	8
7.83	80	3	18	6	18.83	106	3	17	6	29.83	122	3	15	15
7.92	79	3	18	6	18.92	106	3	17	7	29.92	124	4	14	7
8.00	80	3	17	6	19.00	107	3	17	7	30.00	121	3	14	10
8.08	82	4	17	6	19.08	109	3	18	7	30.08	121	3	16	10
8.17	82	3	18	6	19.17	109	3	17	6	30.17	122	3	15	7
8.25	83	4	18	6	19.25	108	3	17	6	30.25	124	3	14	7
8.33	83	5	17	6	19.33	107	3	16	6	30.33	119	6	15	6
8.42	82	5	17	6	19.42	108	3	16	6	30.42	123	3	15	7
8.50	81	5	18	6	19.50	108	3	16	6	30.50	119	6	15	7
8.58	82	4	18	6	19.58	108	3	16	6	30.58	123	3	15	7
8.67	83	5	17	6	19.67	109	3	16	6	30.67	122	4	14	6
8.75	84	6	17	5	19.75	109	3	16	6	30.75	119	5	12	8
8.83	84	6	17	5	19.83	109	3	16	6	30.83	122	3	13	6
8.92	83	6	17	5	19.92	105	4	16	7	30.92	122	3	12	7
9.00	81	4	17	6	20.00	104	5	16	6	31.00	122	4	15	11
9.08	80	3	17	6	20.08	106	3	16	7	31.08	124	4	13	8
9.17	80	3	17	6	20.17	107	3	15	6	31.17	122	3	20	14

Table A1 – *continued*

Rad (1)	V (2)	ΔV (3)	σ (4)	$\Delta\sigma$ (5)	Rad (6)	V (7)	ΔV (8)	σ (9)	$\Delta\sigma$ (10)	Rad (11)	V (12)	ΔV (13)	σ (14)	$\Delta\sigma$ (15)
9.25	78	3	16	6	20.25	108	3	15	8	31.25	120	3	20	19
9.33	78	3	16	6	20.33	108	3	15	8	31.33	124	5	21	23
9.42	80	3	15	6	20.42	107	3	14	7	31.42	122	3	12	7
9.50	81	4	15	6	20.50	107	3	15	7	31.50	122	3	19	14
9.58	82	5	16	6	20.58	106	3	15	6	31.58	123	3	22	16
9.67	81	4	16	6	20.67	106	3	15	7	31.67	122	3	17	11
9.75	81	5	15	6	20.75	108	3	14	7	31.75	128	6	22	11
9.83	82	5	16	6	20.83	107	3	14	8	31.83	122	3	17	12
9.92	82	4	16	6	20.92	106	3	15	8	31.92	122	3	15	13
10.00	81	4	15	6	21.00	108	3	15	8	32.00	128	4	22	21
10.08	82	5	15	5	21.08	109	3	15	10	32.08	122	3	16	7
10.17	83	3	15	6	21.17	111	3	15	11	32.17	126	5	16	9
10.25	83	3	15	6	21.25	106	4	15	9	32.25	122	3	25	17
10.33	82	3	16	6	21.33	105	6	16	10	32.33	122	3	30	3
10.42	84	3	16	6	21.42	111	9	17	12	32.42	126	5	20	19
10.50	84	3	15	6	21.50	113	8	14	7	32.50	121	4	19	7
10.58	85	5	16	5	21.58	113	8	15	8	32.58	122	3	29	20
10.67	86	4	16	6	21.67	100	6	15	7	32.67	129	8	13	9
10.75	87	3	16	6	21.75	96	10	15	8	32.75	122	3	15	4
10.83	86	3	16	6	21.83	97	10	16	8	32.83	122	3	18	8
10.92	87	3	16	6	21.92	98	6	15	8	32.92	122	3	18	13
11.00	87	3	16	5	22.00	103	6	15	7	33.00	123	3	22	3

SUPPORTING INFORMATION

Additional Supporting Information may be found in the online version of this article:

M33RCadoptedV2.tex (http://mnras.oxfordjournals.org/lookup/suppl/doi:10.1093/mnras/stv517/-/DC1).

This paper has been typeset from a TeX/LaTeX file prepared by the author.

Mon. Not. R. Astron. Soc. **000**, 1–22 (2014) Printed 22 June 2015 (MN LaTeX style file v2.2)

Kinematics and mass modelling of M33: HI Observations

Kam, Z. S.[1,2,3], Chemin, L.[4], Carignan, C.[1,2,3], Foster, T.[5,6]
[1] *Laboratoire d'Astrophysique Expérimentale, Département de physique,*
Université de Montréal, C.P. 6128, Succ. centre-ville, Montréal, Québec, H3C 3J7, Canada
[2] *Observatoire d'Astrophysique de l'Université de Ouagadougou, BP 7021, Ouagadougou 03, Burkina Faso*
[3] *Department of Astronomy, University of Cape Town, Private Bag X3, Rondebosch 7701, South Africa*
[4] *Univ. Bordeaux and CNRS, LAB, UMR 5804, F-33270, Floirac, France*
[5] *Department of Physics and Astronomy, Brandon University, 270-18th Street, Brandon, MB, R7A 6A9, Canada*
[6] *National Research Council Canada, Dominion Radio Astrophysical Observatory, P.O. Box 248, Penticton, British Columbia, V2A 6J9, Canada*

22 June 2015

ABSTRACT

A new large scale study of the HI kinematics and mass distribution of Messier 33 is presented, based on observations obtained with the Dominion Radio Astrophysical Observatory interferometer, combined with data from the Arecibo 305 m single dish telescope. An area larger than $2° \times 2°$ is surveyed, with a final spatial resolution of $2'$. Mass models using Modified Newtonian Dynamics (MOND) and three different functional forms of dark matter (DM) halo (the pseudo-isothermal sphere, the Navarro-Frenk-White and the Einasto models) are fitted to a hybrid Hα-HI rotation curve of M33. There is no way to get a satisfying MOND model, even when allowing the constant a_0 and/or the mass-to-light ratio of the disk to vary, or using different interpolation functions. The DM models show that while both cuspy and shallow inner density profiles give comparable good fits to the rotation curve, haloes with steep inner density profiles are highly unrealistic. The density slope derived at a radius of 41 pc, the radius of the innermost velocity point of the rotation curve, is consistent with a core-dominated halo, in disagreement with other recent mass models favouring a cosmological cusp. The inferred stellar and total masses inside 22 kpc are $\sim 9 \times 10^9$ M$_\odot$ and $\sim 10^{11}$ M$_\odot$, respectively. At the virial radius of 180 kpc, a total mass of $\sim 7 \times 10^{11}$ M$_\odot$ is found for M33, about 1.4 times less massive than its companion M31.

Key words: techniques: interferometric – galaxies: individual: M 33 – galaxies: kinematics and dynamics – galaxies: haloes – cosmology: dark matter

1 INTRODUCTION

With the Milky Way and Andromeda, the Triangulum galaxy (Messier 33, the third most massive disk of the Local Group) has long been among the most studied nearby galaxies to scrutinize the chemical, dynamical and structural properties of the stellar populations and the interstellar medium. In particular, as it is a prototype of gas-rich spiral of moderate inclination (Tab. 1) it is very appropriate to study the relationships of the atomic and molecular gas content with the star formation inside the disk. Since it is now well admitted that M33 has undergone a tidal encounter with a massive galaxy as its close environment is perturbed (very likely Andromeda, Braun & Thilker 2004; McConnachie et al. 2010), it is expected that gas expelled during that interaction is currently returning into the M33 disk, fueling the active star formation (Putman et al. 2009).

The implied important population of HII regions (e.g. Boulesteix et al. 1974; Zaritsky et al. 1989; Relaño et al. 2013) has thus been a motivation for us to present the first large-scale, arcsec-resolution, 3D spectroscopic survey of the disk of Messier 33 in the Hα emission line (Kam et al. 2015, hereafter Kam15). On one hand, the objectives of this survey was to study the internal kinematics of the HII regions. For instance, Kam15 pointed out the complex relation between the velocity dispersion and the integrated intensity of the Hα line, underlying the physical processes occurring in the brightest regions and in the diffuse interstellar medium. The catalog of HII regions that will follow from this survey will be essential to study the relationships with other tracers of star formation in M33 at an unprecedented level of details. On the other hand, the Hα mapping has been a unique opportunity to determine for the first time the most extended Hα velocity field of M33. The modelling of the velocity field led Kam15 to conclude that the kinematical parameters of the ionized gas disk are very consistent with those of the stellar disk, and that the positional difference of the dynamical centre from the photometric centre is typical of what is observed in many nearby galaxies (about one hundred parsecs in projection). Maybe the most important result of Kam15 is the determination of the Hα rotation curve out to 8 kpc. That curve perfectly traces the velocity gradient in the inner disk, and presents many wiggles characteristic of spiral arms perturbations, but that have been barely showed in previous HI and CO observations. These irregularities however do not prevent the Hα, HI or CO rotation velocities to remain in good agreement.

The derivation of the Hα rotation curve actually constitutes the first pillar of a broader project devoted to revisit the modelling of the mass distribution of M33. The other pillar inherent to such modelling is to get the HI rotation curve to cover as far as possible the outer disk, ensuring as much degrees of freedom as possible to perform accurate fits of dark matter parameters, or of alternate dynamics like MOND.

Existing HI studies of M33 attest to which extent the tidal interaction with Andromeda has not been without consequences on the gas distribution in the disk outskirts, revealing perturbed features like a warp, arc-like structures or diffuse and discrete gas around the disk (Corbelli & Schneider 1997; Putman et al. 2009; Lockman et al. 2012). Recently, Corbelli et al. (2014) used VLA+GBT observations to model the HI warp and rotation curve. They have presented a new, flat rotation curve that extends about 5 kpc further than previously known. They have also shown that the distribution of dark matter in Messier 33 is consistent with a model for which the mass density steeply decreases in the centre of the halo (the cosmological cusp à la Navarro-Frenk-White, see Navarro et al. 1997). Comparable results have been obtained by Hague & Wilkinson (2015), but from a lower resolution HI curve derived earlier by Corbelli & Salucci (2000). They concluded that models with density slopes < 0.9 at $R \sim 0.5$ kpc (the first velocity point of their rotation curve) with 3.6-μm mass-to-light ratios < 2 are ruled out in M33.

In this context, we have performed an HI survey of Messier 33 at the Dominion Radio Astrophysical Observatory (DRAO). This arcminute-resolution survey is a good intermediate between VLA and Arecibo or GBT measurements. The objectives of this article are first to present the survey, the gas content and distribution of M33, a new tilted-ring model of the HI velocity field and the HI rotation curve. We also want to examine the shape and amplitude of the outer rotation curve, at radii beyond $R = 17$ kpc where Corbelli et al. (2014) presented new velocities. The second objective of the article is to benefit from the high-resolution survey of Kam15 and perform accurate mass distribution models from an hybrid Hα-HI rotation curve. In particular we want to test the Modified Newtonian Dynamics model, determine the best-fit slope of the density profile of the dark matter halo at the first point of the rotation curve ($R = 41$ pc) and infer the total mass of M33.

Throughout the article, we have adopted a Hubble constant of 72 km $\mathrm{s}^{-1}\mathrm{Mpc}^{-1}$ (Hinshaw et al. 2009) and a distance to Messier 33 of 0.84 Mpc (see Kam15 and references therein). The basic optical parameters of M33 are summarized in Table 1. The observations and the reduction of the HI data are presented in section 2. Section 3 presents the HI kinematics, the tilted-ring model, the HI rotation curve and the adopted combined Hα-HI rotation curve. The modelling of the mass distribution is done in Section 4. Section 5 presents a discussion of the results, and conclusions are given in Section 6.

Table 1. Optical parameters of M 33.

Parameters	Value	Source
Morphological type	SA(s)cd	RC3
R.A. (2000)	$01^{\mathrm{h}}\ 33^{\mathrm{m}}\ 33.1^{\mathrm{s}}$	RC3
Dec. (2000)	$+30^\circ\ 39'\ 18''$	RC3
Optical inclination, i	$52^\circ \pm 3^\circ$	W73
Optical major axis, PA	$22.5^\circ \pm 1^\circ$	W73
Apparent magnitude, m_V	5.28	RC3
Absolute magnitude, M_V	-19.34	
(J-K)	0.89	TJ03
Optical radius, $\mathrm{D}_{25}/2$	$35'.4 \pm 1'.0$	RC3
Systemic Velocity	-179 ± 3 km s^{-1}	RC3

RC3: de Vaucouleurs et al. (1991), W73: Warner et al. (1973), TJ03= Jarrett et al. (2003)

2 HI LINE STUDY

2.1 Observations and data reduction

The primary observations for this study were made in the 21 cm line of neutral hydrogen HI with the synthesis telescope of the DRAO. This telescope is an East-West interferometer consisting of seven ($\sim$9 m diameter) dishes spaced along a maximum baseline of 617.2 m. This longest baseline achieves a synthesized half-power beamwidth of $49''$(EW) by $49''/\sin\,\delta$(NS) with uniform weighting although, in the HI line, we chose natural weighting (a Gaussian taper in the u, v plane) to increase the sensitivity at the slight expense of resolution ($58''\times 58''/\sin\delta$) Further specifications and capabilities of the DRAO telescope can be found in Landecker et al. (2000) and Kothes et al. (2010). Other frequencies were also observed with a 30 MHz continuum band centred at 1420 MHz (λ21 cm), and a 2 MHz band at 408 MHz (λ74 cm), although these data are not presented here.

For the HI line observations of M33, the spectrometer was set to a 2 MHz-wide band with 256 channels, each spaced by $\Delta V = 1.65$ km s^{-1} . The band was centred on a heliocentric velocity of $V_{\mathrm{HEL}} = -180$ km s^{-1}. The typical RMS noise in each (empty) channel is $1.2 - 1.4$ K. To increase the sensitivity to the faint outermost HI disk of M33, a total of 6 full-synthesis pointings on and around the galaxy were observed and mosaiced together, each having a field-of-view equal to the half-power width of the primary beam of the individual antenna ($107'.2$). Table 2 lists the field centres for the six individual fields (in J2000.0 coordinates). Two fields are centred precisely on M33, and four others are positioned along the galaxy's major axis (position angle $\sim$100° CCW from E) with two inner ones spaced $31'$ from the central ones, and two outer fields $46'.5$ from the two inner ones. The integration time for each field was 288 hours for a total integration time of $6 \times 288 = 1728$ hours, equivalent to 144 half days of observation (24/field). Data processing and mosaic-making steps are identical to those described in Chemin et al. (2009) for the M31 observations using the DRAO telescope. However, for M33, we merge single-dish data obtained from the Turn-On GALFA Survey (TOGS) portion of the GALFA-HI survey done at Arecibo.

Table 2. Summary of the six 21 cm HI line synthesis fields centred on and surrounding M33, observed with the DRAO synthesis telescope in 2008.

Date	Field Centre (RA, DEC)(J2000.0)	Beam Parameters beam, angle(CCW E)
Sep. 29	$1^h33^m50.9^s$, $+30°39'36''$	$1'.90\times0'.97$, $-89.69°$
Sep. 29	$1^h36^m10.2^s$, $+31°50'34''$	$1'.85\times0'.97$, $-89.82°$
Nov. 05	$1^h31^m38.2^s$, $+29°28'12''$	$1'.98\times0'.97$, $-89.91°$
Nov. 05	$1^h34^m45.8^s$, $+31°08'13''$	$1'.86\times0'.97$, $-90.11°$
Dec. 04	$1^h32^m56.4^s$, $+30°11'01''$	$1'.94\times0'.97$, $-90.30°$
Dec. 04	$1^h33^m50.9^s$, $+30°39'36''$	$1'.91\times0'.97$, $-90.49°$

The beam is given as $\theta_{maj} \times \theta_{min}$

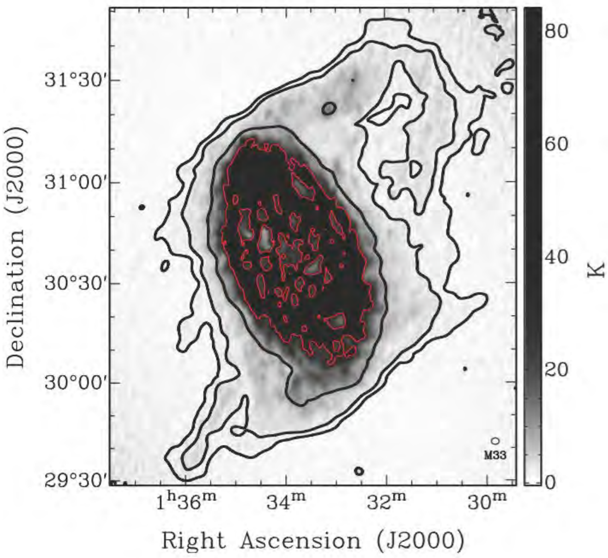

Figure 1. HI-peak final HI mosaic of M33. T_B contours (red) are at 1.2, 2 and 10 Kelvin. The outermost extent of the warped HI disk of M33 (black), is also visible in the individual channels of the high-resolution cube. The beam, showed at the bottom right corner, is $2'$, corresponding to $\sim$ 500 pc using the adopted distance of M33.

These data have been previously published by Putman et al. (2009) and have an angular resolution of $3'\!.4$, providing exceptional spatial-frequency overlap with the DRAO synthesis data (which are missing spatial structures larger than about one degree). TOGS HI data were added to the calibrated interferometer-only mosaic in the same manner as in Chemin et al. (2009) after converting them to the same spatial and velocity resolutions and grid. To gain further sensitivity, the final datacube was smoothed to a velocity resolution of 10.5 km s^{-1} (from 2.64 km s^{-1}). The measured 1σ noise at the pointing centre of the final short-spacings-added and velocity-smoothed mosaic is $\simeq$180 mK per (empty) channel for the full resolution of $115''\times58''$. A velocity-collapsed map of the resulting final mosaic (sum of channels with $-46 \leqslant v_{\mathrm{HEL}} \leqslant -320$ km s^{-1}) is shown in Figure 1. It shows an extended HI disk beyond the optical disk and the warp in the outer parts.

2.2 HI global profile and HI mass

The HI global profile derived from the datacube is shown in Figure 2. The profile can be corrected for various effects such as e.g. auto absorption (Haynes & Giovanelli 1984). If we were to correct for auto absorption according to the model proposed by Haynes & Giovanelli (1984), the fluxes would increase by $\gtrsim$8%.

A spatial smoothing on the $115''\times58''$ data cube is done in order to get a circular beam at $120''\times120''$. The RMS noise at 1σ in the new data is $\sim$ 2 mJy/beam using the empty channels. One can notice that the spatial smoothing of the data cube increases the noise but the HI fluxes are conserved. Using the smoothed cube, the Galactic emission appears strong in channels around -25 to -50 km s^{-1}. Figure 2 shows clearly that, channels with velocities $\geqslant -50$ km s^{-1} are affected by galactic HI.

There is slightly more flux on the SW side than on the NE side. The maximum flux is considered as the mean of the two maxima. The intensity weighted systemic velocity is -180.3 ± 2.3 km s^{-1} using the fluxes $\geqslant$ 10% of the maximum to avoid the Galactic HI emission. The width of the HI profile at 50% of the mean maximum, is $\Delta V_{50} = -182.8$ km s^{-1}. At this height, the mid point velocity is -180.4 ± 3.5 km s^{-1}, similar to the intensity weighted value. The arrow at the bottom axis of Figure 2 (left) indicates this mid point velocity. At the 20% level, the mid point velocity is -179.7 ± 3.5 km s^{-1} and the width $\Delta V_{20} = 200$ km s^{-1}. The total HI mass is $1.95 \pm 0.36 \times 10^9$ $\mathrm{M}_\odot$. While the HI is detected up to $\gtrsim 90'$, the mass density profile shows that most of the HI mass of M33 is within $40'$, so roughly within the optical radius ($\sim35'$).

Figure 3 presents the channel maps. The variation of the contours in this figure shows the variation of the PA of the galaxy (warp), especially in the channels between -136 to -208 km s^{-1}. Details on the variations of the disk inclination and position angle (PA) of the major axis are presented in Section 3.1.

2.3 Warp of the HI disk of M33

Figure 4 shows a model of the warp of the HI disk that takes into account the variations of PA and inclination presented in section 3. Rings are separated by $240''$ from each other. Within the region of the inner (optical) disk, the line-of-sight should, according to the model, cross the disk only once. Then the region of the warp should be crossed twice, and finally, once in the outermost regions of the HI disk.

This tilted-ring geometry is totally confirmed by the analysis of the HI profiles. Single peak profiles are seen within the inner disk (positions A and B). Multiple peaks or larger profiles are observed where the tilted rings overlap (positions C and D). Finally, single peak profiles (positions E and F) are observed in the outermost regions. A more detailed analysis of those multiple component profiles, and their spectral decomposition, as in Chemin et al. (2012), will be presented in a following paper.

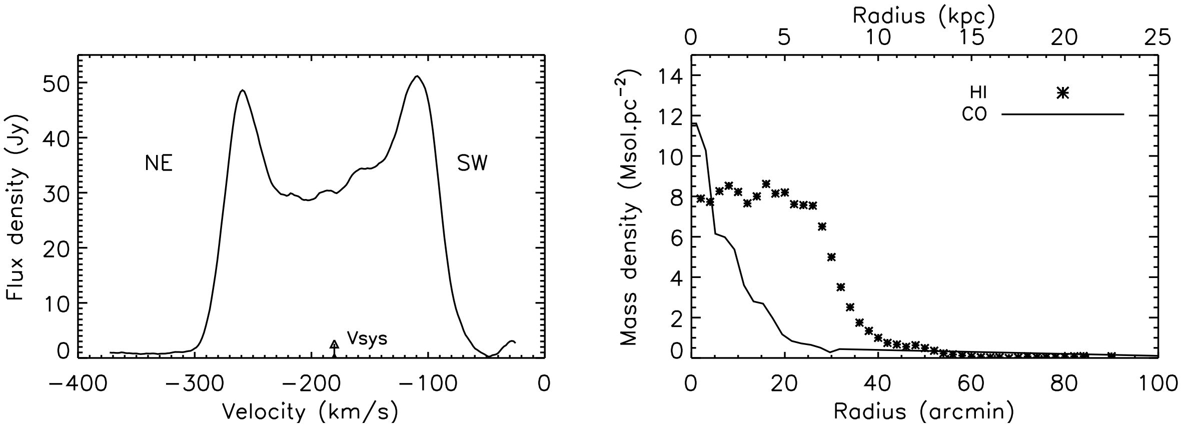

Figure 2. HI integrated emission profile of M33 (left panel). HI mass surface density profile (right panel). The molecular gas density profile of Druard et al. (2014) is overlaid (solid line).

3 HI ROTATION CURVE

3.1 Velocity field and kinematical parameters

The task MOMENTS in GIPSY has been used to compute the moment maps using the data cube smoothed at $120'' \times 120''$. Figure 5 show the 0th, 1st and 2nd moment maps.

The twist of the iso velocity contours, due to the warp, are clearly visible. The velocity dispersion are small and nearly constant in the central regions of the galaxy and increase when crossing holes or spiral arms in the inner parts. The mean dispersion in the disk is ∼11 km s^{-1}. The dispersion is getting higher in the outer parts of the disk where the PA starts changing due to the warp. This is due to crossing the disk more than once with the result of generating double peaks or wider profiles.

The outermost feature, the South-Western Cloud, well described by Putman et al. (2009) (see also Grossi et al. 2008), have been removed from the velocity map before deriving the RC. This cloud can be seen in green-yellow at the bottom right corner of the velocity field image of Figure 5. Only the features having a good agreement with the global velocity pattern have been considered. Several smoothing have been tried to see how far the HI disk can be extended. The map at $120'' \times 120''$ resolution was adopted in order to keep a good spatial resolution for the RC. The velocity map was clipped for observed velocities outside the range −290 km s^{-1} to −60 km s^{-1}. The bottom cut-off keep us away from galactic emission (see Figure 2).

The task ROTCUR in GIPSY has been used to derive the kinematical parameters and the rotation curve. Assuming negligible radial (expansion) velocity, the tilted-ring model fits the expression :

$$V_{obs} = V_{sys} + V_{rot}(R)cos(\theta)sin(i); \qquad (1)$$

to the HI velocity field, where R and θ are the polar coordinates in the plane of the galaxy and i the inclination. The position angle of the major axis (PA) is defined as the counterclockwise angle in the plane of the sky from the North to the receding side semi-major axis. In a first run, the position of the rotation centre, and of the systemic velocity V_{sys} were free to vary, using fixed inclination and PA at the optical values (52° and 202°, respectively). We find a systemic velocity of $V_{sys} \sim -183$ km s^{-1}, and a centre at $(\alpha, \delta)_{J2000} = (01h33m50.9s, +30°40'19.8'')$. Since the positional difference with respect to the photometric centre is much less than the beam size, we decided to fix the kinematical centre at the position of the photometric centre. Also, because the inferred systemic velocity is in agreement with the mean value determined from the global profile (section 2.1), we adopted $V_{sys} = -180$ km s^{-1}. A second run allows us to fit the inclination and PA using fixed centre and systemic velocity given by the adopted values. The results for the approaching and receding disk halves are shown in Figure 6.

3.2 Adopted Rotation Curve

3.2.1 *HI rotation curve*

The final HI rotation curve is then derived adopting fixed values of the centre, systemic velocity, inclination and PA. The adopted radial profiles of PA and inclination are modelled from the *both sides* solution and are shown by solid lines in Fig 6). Figure 6 also shows the obtained HI RC curve for the receding, approaching and both sides. The total velocity errors ΔV_{rot} are defined by:

$$\Delta V_{rot} = \sqrt{\epsilon^2 + \frac{|V_a - V_r|^2}{4}} \qquad (2)$$

where, V_a and V_r are the approaching and the receding sides velocities, and ϵ is the formal RMS error of the fits for both sides. The dominant error of the total uncertainty is the systematic difference between the two sides. The approaching and receding sides are in good agreement below ∼ 10 kpc and between 14 to 19 kpc. The errors are larger where the warp starts (between 10 and 14 kpc), and increase again beyond R=19 kpc, where the S/N and the number of points in the tilted-rings get lower.

Table 3 gives the adopted kinematical parameters and the RC. Column (1) gives the radii. Those radii were chosen to avoid oversampling the data. The smoothed circular beam used is $120'' \times 120''$, then the width used for the sampling is the beam size. Column (2) gives the HI velocities obtained

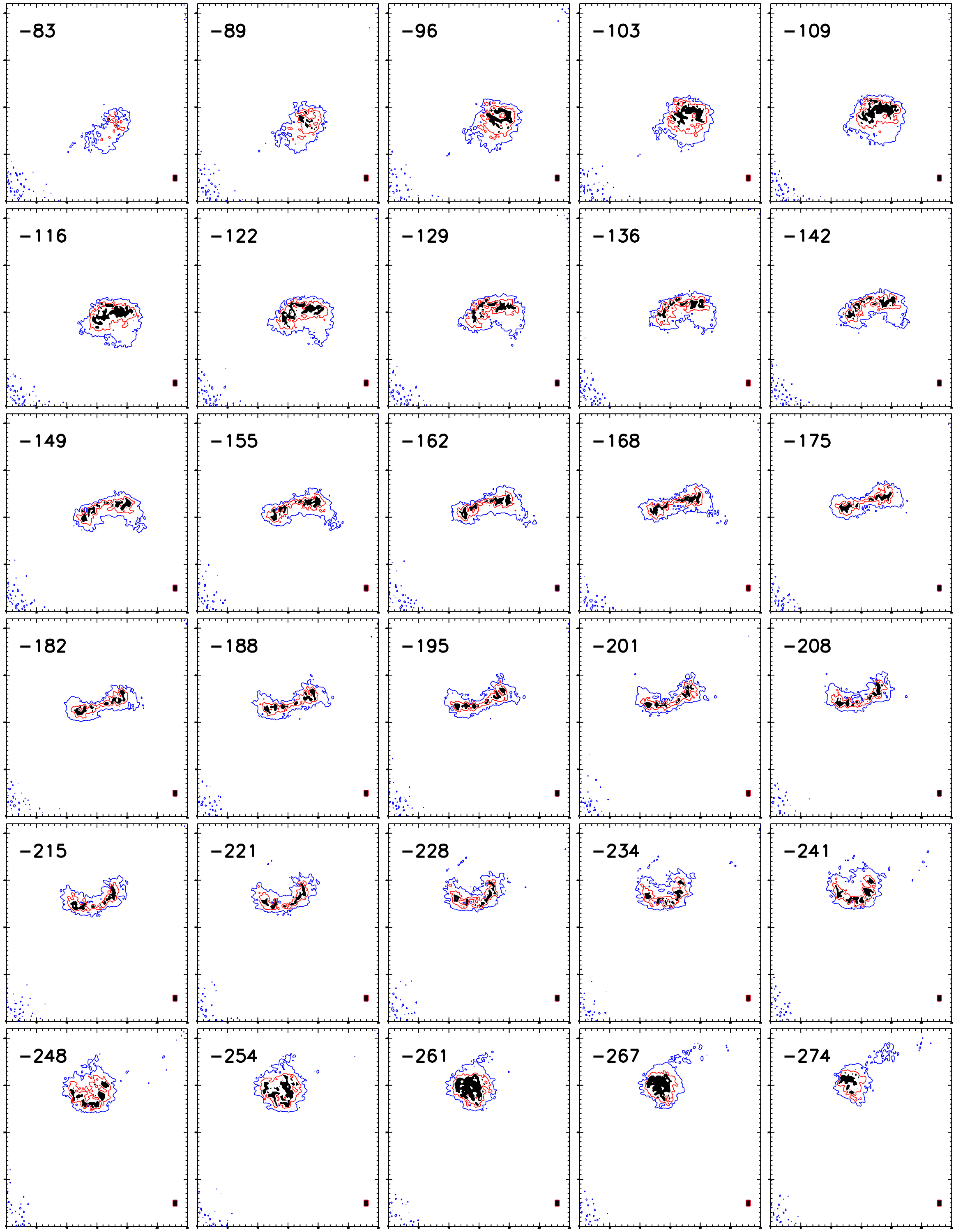

Figure 3. HI channels maps of M33 for the combined DRAO and Arecibo data. The contour levels are at 2.5 in blue, 8 in red and the filled grey regions represent the levels higher than 15 K. The velocity is noted at the upper left corner of each map. The beam is shown in the bottom right corner.

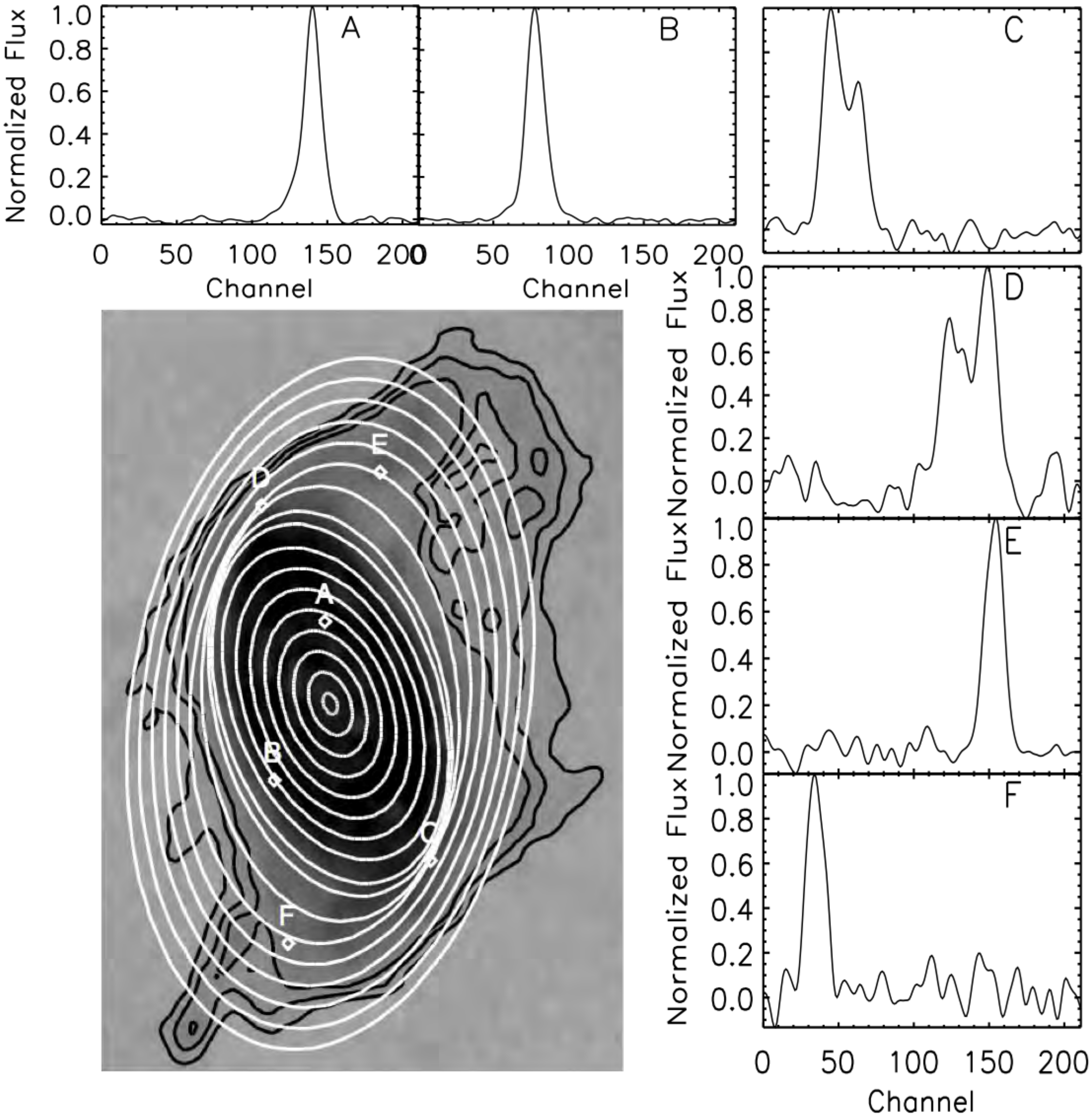

Figure 4. HI profiles given at several locations in the galaxy. The positions are indicated by the letters A, B, C , D, E, F. The ellipses show the results of the tilted-ring model of M33.

for both sides using the tilted ring model. Column (3) gives the errors on the velocities using equation 2. Column (4) presents the position angle defined from the North to the receding side and column (5) presents the inclination at each radius, Columns 6 to 10 are similar to columns 1 to 5.

3.2.2 Comparison of the adopted RC with the major axis kinematics

Figure 7 gives two Position-Velocity (PV) diagrams at PA=202° and at PA = 165°. Since the PA varies by nearly 40° from the optical disk to the outermost warped disk, the positions used are the extreme values of PA used for the RC determination. Figures 7 (top) shows the good agreement between the HI (red and blue) and Hα (green) kinematics along the major axis in the inner parts. On the top PV diagram notice the beard-like fainter contours, which suggests the presence of lagging HI in the M33's halo (Fraternali et al. 2001; Oosterloo et al. 2007).

The modelled velocity field and the residual velocity map (defined as the model minus the observation) are presented in Figure 8. No systematic velocity asymmetry is found, implying the goodness of the model. The higher residuals are noticed at the boundaries of the optical disc ($\sim \pm15 - \pm22$ km s^{-1}), where the PA changes by ~20 ° between 10−15 kpc. Notice that the velocity dispersions (Fig. 5) are larger in regions of large residuals.

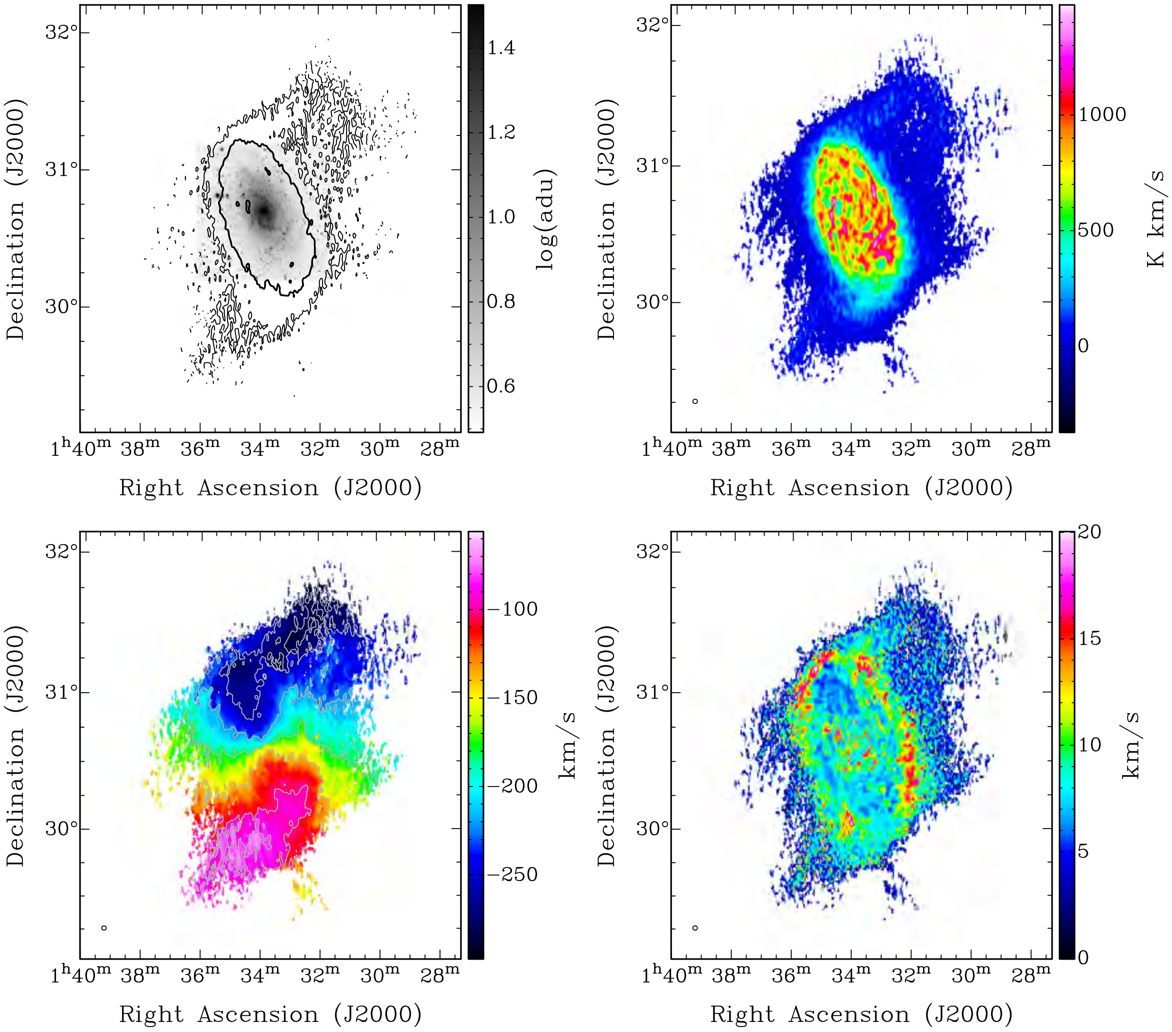

Figure 5. (top left) Wise w1-band image of M33 with overlaid HI integrated emission contours at 1.2, 3 and 10 K km s^{-1}. (top-right) Integrated emission map (0-th moment) (bottom-left) HI velocity field (1-st moment). The grey contours are for -280, -260, -220, -180, -140, -100, -80 km s^{-1}. (bottom-right) HI velocity dispersion map (2nd moment). The 2′ size of the synthesized beam is shown at the bottom left of the moment maps.

3.2.3 Hα kinematics and adopted RC

HI has a poorer spatial resolution in the central regions, where the gradient of the RC is the greatest. Because of this, Hα is a better tracer of the internal kinematics. High resolution Hα Fabry Perot data of M33, obtained at the Observatoire du Mont Mégantic, gives a good description of the kinematics of the central parts (Kam15). Figure 7 shows the good agreement of the Hα RC with the HI data. Taking advantage of the Hα high spatial resolution ($\lesssim 5''$), the outer parts of the HI RC is combined to the Hα RC within 6.5 kpc for the mass models. Figure 9 gives the final adopted RC of Messier 33 for the mass modelling. The Hα RC and associated errors have been derived following exactly the same process as for the HI RC. Notice that the average Hα uncertainty for R<6.5 kpc is about twice the average HI uncertainty for $R > 6.5$ kpc. This error inhomogeneity is often seen when combining arcsec resolution Hα data to lower resolution HI data. We have verified that it has no consequences on the mass model results described below.

4 MASS DISTRIBUTION MODELS OF MESSIER 33

To construct mass distribution models, one needs to take into account, as best as possible, all the mass components. For the stellar component, it is well known that IR data give the best representation of the old disk population, which contributes most of the stellar mass. We use 3.6μm data from *Spitzer*/IRAC. The only uncertainty left is the mass-to-light ratios $\Upsilon_\star$ of the disk and the bulge, which can be constrained using IR colours and population synthesis models. Mass distribution models with fixed and free mass-to-light ratios have thus been performed. Two types of models have been fitted to the hybrid Hα-HI rotation. We have first

Table 3. The HI rotation curve of M33.

Rad (’) (1)	V_{rot} (km/s) (2)	ΔV_{rot} (km/s) (3)	PA (^{o}) (4)	i (^{o}) (5)	Rad (’) (6)	V_{rot} (km/s) (7)	ΔV_{rot} (km/s) (8)	PA (^{o}) (9)	i (^{o}) (10)
2	42.6	2.1	201.3	52.2	48	117.4	9.0	174.2	54.5
4	59.5	1.4	201.3	52.3	50	115.9	9.9	173.8	54.6
6	69.9	0.5	201.3	52.4	52	115.7	7.3	173.4	54.7
08	79.8	4.2	201.3	52.5	54	118.2	4.9	172.9	54.8
10	87.8	2.0	201.3	52.6	56	119.4	2.7	172.5	54.9
12	92.3	2.7	201.3	52.7	58	120.0	1.0	172.1	55.0
14	94.9	5.1	201.3	52.8	60	118.8	2.7	171.6	55.1
16	97.6	5.6	201.3	52.9	62	119.3	2.5	171.2	55.2
18	100.6	3.7	201.3	53.0	64	122.1	2.5	170.8	55.3
20	102.9	1.5	201.3	53.1	66	121.6	2.5	170.3	55.4
22	104.7	0.3	201.3	53.2	68	125.8	0.5	169.9	55.5
24	106.8	0.9	201.3	53.3	70	127.4	1.0	169.5	55.6
26	106.6	2.0	201.3	53.4	72	129.2	1.8	169.0	55.7
28	107.6	2.6	201.3	53.5	74	129.8	0.8	168.6	55.8
30	107.7	3.6	201.3	53.6	76	132.1	0.8	168.2	55.9
32	108.5	4.5	198.8	53.7	78	132.3	7.1	167.7	56.0
34	110.2	3.5	195.4	53.8	80	134.3	5.9	167.3	56.1
36	112.7	3.4	192.0	53.9	82	132.4	7.3	166.8	56.2
38	117.2	1.7	188.7	54.0	84	131.1	6.2	166.4	56.3
40	118.7	2.3	185.3	54.1	86	134.9	5.0	166.0	56.5
42	118.2	6.4	181.9	54.2	88	140.3	10.1	165.5	56.6
44	118.4	7.3	178.5	54.3	90	142.7	7.9	165.1	56.7
46	118.1	8.3	174.2	54.4	92	146.3	19.0	164.7	56.8

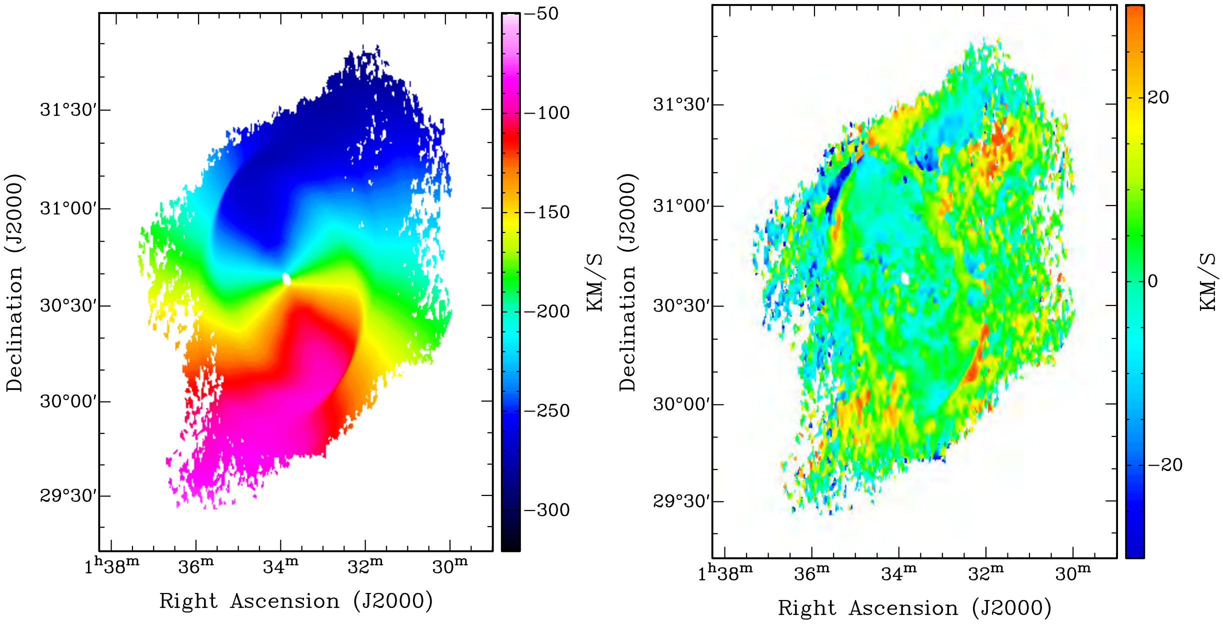

Figure 8. The left image give the model using the kinematical parameters presented in Figures 6, and Table 3. The right image is the residual map (model − observations) .

considered models with dark matter (DM) using three different functional forms for the DM halo: the pseudo-isothermal sphere (ISO), the Navarro-Frenk-White (NFW), and the Einasto (EIN) model. We have then performed models using the Modified Newtonian Dynamics (MOND) prescription. A description of those models is given hereafter.

4.1 Stellar component

Kam15 derived the surface brightness profile of M33 from the 3.6μm data of *Spitzer*/IRAC, where contaminating bright stars have been removed. More complete details on the derivation of the surface brightness profile are given in Kam15. The mass-to-light ratios $\Upsilon_{\rm bulge}$ and $\Upsilon_{\rm disk}$ of the

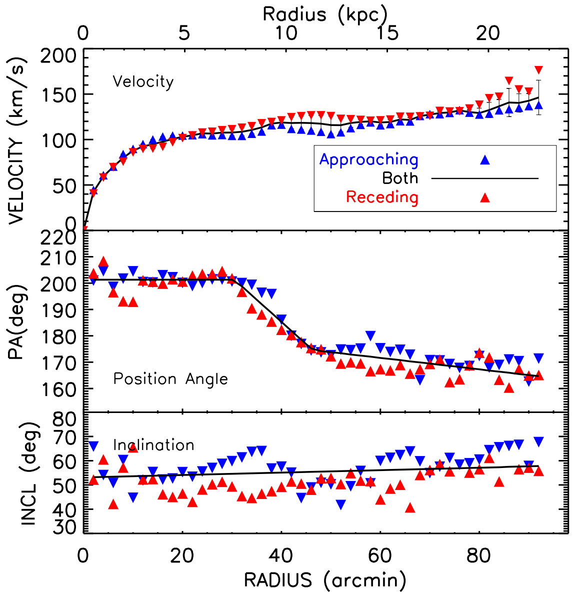

Figure 6. Determination of the rotation curve, PA and inclination for the HI disk of M33. The top panel gives the rotation velocities, the middle panel the variation of PA and the bottom panel the variation of inclination. The red upward triangles give the results for the receding side and the blue downward triangles for the approaching side. The solid lines give the adopted solutions for both sides.

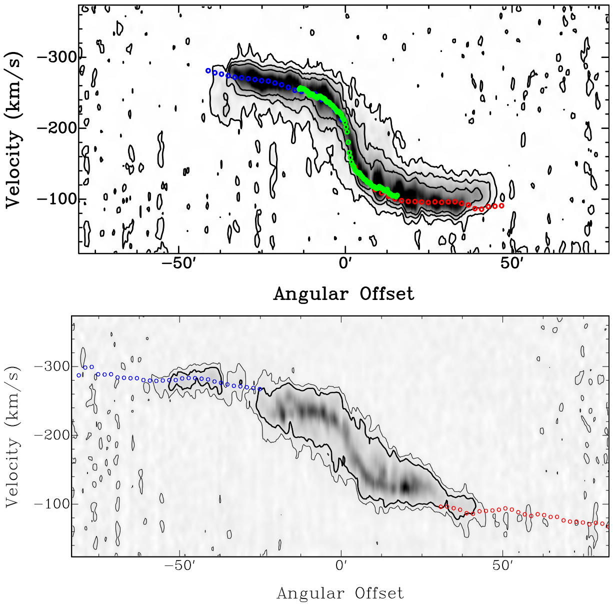

Figure 7. The top image represents the PV diagram along the major axis at PA=202°. The red and blue squares represent the solutions for the approaching and receding sides and the green ones show the Hα RC (Kam15) at 30″ resolution. The bottom image is at PA=165° without the Hα data and shows the outer warped region.

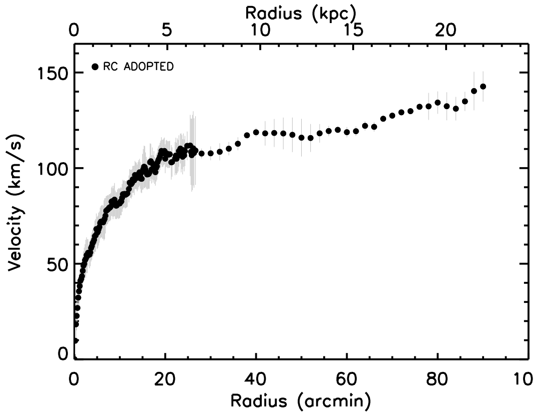

Figure 9. Final rotation curve of Messier 33 combining Hα velocities from Kam15 for $R < 6.5$ kpc, and our new derived HI rotation curve for the outer parts.

bulge and disk have been estimated from infrared colours and results of population synthesis models given by Oh et al. (2008) and de Blok et al. (2008):

$$\Sigma[\mathrm{M}_\odot\ \mathrm{pc}^{-2}] = \Upsilon_*^{3.6} \times 10^{-0.4\times(\mu_{3.6}-C^{3.6})} \qquad (3)$$

where $\Upsilon_*^{3.6}$ is given in the *Spitzer*/IRAC 3.6μm band, $\mu_{3.6}$ is the surface brightness and $C^{3.6} = 24.8$ is a correction value, as given in Oh et al. (2008). Using the $J - K$ colour index from Jarrett et al. (2003), Kam15 derived $\Upsilon_{\mathrm{bulge}} = 0.80$ and $\Upsilon_{\mathrm{disk}} = 0.72$.

An exponential profile has been fitted to the 3.6μm band surface density profile of the disk component using the equation:

$$\mu(R) = \mu_0 + 1.10857\ \frac{R}{h} \qquad (4)$$

where h defines the disk scale length and μ_0 the disk central surface brightness. The bulge component is described by a Sersic law:

$$\mu_(R) = \mu_e + 2.5\ b_n \left[\left(\frac{R}{R_e}\right)^{1/n} + 1\right] \qquad (5)$$

where b_n is defined as $b_n = 1.9992n - 0.3271$ for $0.5 < n < 10$ (Capaccioli 1989) and μ_e the equivalent surface brightness of the bulge. The parameters found by Kam15 for the stellar components are : $h = 1.8$ kpc, $\mu_0 = 18.0$ mag.arcsec^{-2} for the disk and $n = 1.2$, $R_e = 0.40$ kpc and $\mu_e = 20.8$ mag.arcsec^{-2} for the bulge. With a bulge-to-disk ratio of 0.04, large differences are not expected between pure disk and bulge+disk models, as found in Kam15 from a modelling of the Hα rotation curve in the inner $R = 8$ kpc. A sech^2(z/z$_0$) law has been adopted for the vertical density distribution of the stellar disk, with a scale-height of $\sim$ 400 pc ($\sim$20% of the disk scale length). The velocity contributions have been derived with the task ROTMOD from the GIPSY package (van der Hulst et al. 1992).

4.2 Atomic and molecular gas components

The contribution from the neutral gas comes from our deep DRAO+Arecibo dataset. The surface densities from Fig. 2, which were multiplied by a factor of ∼1.3 to take into account the contribution from Helium, have been used to infer the velocity contribution of the atomic gas disk. The molecular gas contribution, traced by the CO line, is mainly concentrated in the innermost kpcs. Molecular gas in M33 has been observed by Tosaki et al. (2011) with the Nobeyama Radio Observatory at 19″ resolution, and by Gratier et al. (2010) and Druard et al. (2014) with the IRAM 30-m dish at a resolution of ∼ 15″. Tosaki et al. (2011) report that the HI peaks and CO are not always correlated and that the density of the atomic gas is higher than that of the molecular gas in the inner parts, while Gratier et al. (2010) showed that the molecular gas density is higher than HI. Using a conversion factor of $N(H_2)/I_{CO(1\to0)} = 4\times10^{20}\mathrm{cm}^{-2}/(\mathrm{K\ km\ s}^{-1})$, twice the value found for the Milky Way (M33 as half the solar metallicity), they measured an average density of $\Sigma_{H_2} = 8.5 \pm 0.2\ \mathrm{M}_\odot\ \mathrm{pc}^{-2}$ for the central kpc, and a total molecular gas mass of $\sim 3.3\times10^8\ \mathrm{M}_\odot$ for the entire M33 disk. We used the H_2 density profile of Druard et al. (2014), scaled by a factor of ∼ 1.3 to infer the velocity contribution of the total molecular gas component.

4.3 Dark Matter mass models

The rotation velocities are defined as:

$$V_{rot}^2 = V_\star^2 + V_{\rm gas}^2 + V_{DM}^2 \qquad (6)$$

where $V_\star^2 = V_{\rm bulge}^2 + V_{\rm disk}^2$ is the velocity contribution from the total stellar component, $V_{\rm gas}^2 = V_{\rm atom}^2 + V_{\rm molec}^2$ is the one from the total gaseous component, and V_{DM} the contribution from the DM mass component.

The ISO and NFW models are the most commonly DM halo profiles used (e.g. de Blok & Bosma 2002), while it is only recently that the EIN model has been shown to be a good description of the DM mass (Chemin et al. 2011) in disk galaxies.

4.3.1 The pseudo-isothermal sphere model

The pseudo-isothermal dark matter halo is a core-dominated type of halo, as the density remains constant in the centre. The density profile is given by:

$$\rho_{\rm ISO}(\mathrm{R}) = \frac{\rho_0}{1+(\frac{\mathrm{R}}{\mathrm{R_c}})^2} \qquad (7)$$

where ρ_0 is the central density and R_c the core radius of the halo. The corresponding circular velocity is:

$$\mathrm{V_{ISO}(R)} = \sqrt{4\pi\ \mathrm{G}\ \rho_0\ \mathrm{R_c^2}(1-\frac{\mathrm{R}}{\mathrm{R_c}}\ \arctan(\frac{\mathrm{R}}{\mathrm{R_c}}))} \qquad (8)$$

4.3.2 The Navarro-Frenk-White model

The NFW model – the so-called 'universal halo' – is deduced from Cold Dark Matter simulations (Navarro et al. 1997). The density profile is cuspy, following a $\rho \propto R^{-1}$ law in the center, and is given by:

$$\rho_{NFW}(R) = \frac{\rho_i}{\frac{R}{R_s}(1+\frac{R}{R_s})^2} \qquad (9)$$

where $\rho_i \approx 3H_0^2/(8\pi G)$ is the critical density for closure of the Universe and R_S is a scale radius. The velocity contribution corresponding to this halo is given by:

$$\mathrm{V_{NFW}(R)} = \mathrm{V_{200}}\sqrt{\frac{\ln(1+\mathrm{cx})-\mathrm{cx}/(1+\mathrm{cx})}{\mathrm{x}(\ln(1+\mathrm{c})-\mathrm{c}/(1+\mathrm{c}))]}} \qquad (10)$$

where $\mathrm{V_{200}}$ is the velocity at the virial radius $\mathrm{R_{200}}$, $\mathrm{c} = \mathrm{R_{200}/R_s}$ gives the concentration parameter of the halo and x is $\mathrm{R/R_s}$. The relation between $\mathrm{V_{200}}$ and $\mathrm{R_{200}}$ is $V_{200} = 0.01.H_0.R_{200}$, where we used $\mathrm{H_0} = 72\ \mathrm{km\ s^{-1}Mpc^{-1}}$ for the Hubble constant (Hinshaw et al. 2009).

4.3.3 The Einasto model

Chemin et al. (2011) analyzed a large sample of nearby disk galaxies and found that the EIN model is a good candidate for being a standard DM halo. The EIN model also comes from cosmological simulations (e.g. Navarro et al. 2004), and its mass density is given by:

$$\rho_{\rm EIN}(\mathrm{R}) = \rho_{-2}\ \exp\left(\mathrm{f(n)}\left[\left(\frac{\mathrm{R}}{\mathrm{R_{-2}}}\right)^{\frac{1}{\mathrm{n}}}-1\right]\right), \qquad (11)$$

Here, n is the Einasto index that shapes the density profile, $f(n) = -2n\ (n > 0)$, R_{-2} is the radius where the density slope $\alpha = -2(R/R_{-2})^{1/n}$ is −2, and ρ_{-2} is the characteristic density at this radius. The differences with the ISO or NFW models are thus that the density decreases exponentially, and that α decreases continuously with radius, while the slopes of the two other models are constant at small and large radii. The velocity contribution of the EIN halo is then:

$$\mathrm{V_{EIN}(R)} = \mathrm{R}^{-1/2}\sqrt{4\pi\mathrm{GnR_{-2}^3}\rho_{-2}\ \mathrm{e^{2n}}\ (2\mathrm{n})^{-3\mathrm{n}}\gamma\,(3\mathrm{n},\mathrm{y})} \qquad (12)$$

where $\gamma(3\mathrm{n},\mathrm{y}) = \int_0^{\mathrm{y}} \mathrm{e^{-t}t^{3n-1}}\ \mathrm{dt}$ is the incomplete gamma function and $y = -\alpha$. The inner slope of the density profile depends on both the scale radius R_{-2} and the index. Disks with $R_{-2} \propto 10$ kpc have central cusps when $n \sim 5-7$, as seen in cosmological simulations (Navarro et al. 2004), and shallower density profiles when $n \sim 1$, as found by Chemin et al. (2011) from a modelling of rotation curves using the same stellar population synthesis model as the one we use here. We have thus fitted EIN models at free index, as well as constrained models at fixed index $n = 1.4$ (the average value from Chemin et al. (2011)) and $n = 6$.

4.4 Modified Newtonian Dynamics mass models

An alternative to dark matter to explain the missing mass problem is MOdified Newtonian Dynamics (Milgrom 1983a,b). MOND has been successful to reproduce correctly galaxy rotation curves (e.g. Sanders & Verheijen 1998; Gentile et al. 2010). It postulates that in regimes of acceleration much smaller than a universal, constant acceleration a_0, the

Table 4. Results of the DM models.

Disk-only case		Best-fit	Colour $\Upsilon_\star^{3.6}$	**Bulge+disk case**		Bestf-fit	Colour $\Upsilon_\star^{3.6}$
Halo model				Halo model			
ISO	ρ_0	5.0 ± 0.2	7.8 ± 0.3	ISO	ρ_0	5.0 ± 0.2	8.7 ± 0.4
	R_c	12.0 ± 0.5	8.3 ± 0.3		R_c	12.3 ± 0.6	8.1 ± 0.3
	Υ_d	0.86 ± 0.01	0.72		Υ_d	0.87 ± 0.02	0.72
	Υ_b	–	–		Υ_b	0.98 ± 0.10	0.80
	χ_r^2	0.30	0.55		χ_r^2	0.33	0.65
NFW	V_{200}	525 ± 300	598 ± 308	NFW	V_{200}	339 ± 88	556 ± 249
	c	0.63 ± 0.60	0.52 ± 0.50		c	1.40 ± 0.3	0.61 ± 0.5
	Υ_d	0.66 ± 0.02	0.72		Υ_d	0.65 ± 0.02	0.72
	Υ_b	–	–		Υ_b	0.88 ± 0.10	0.80
	χ_r^2	0.27	0.34		χ_r^2	0.31	0.34
EIN	ρ_{-2}	0.56 ± 0.03	0.83 ± 0.04	EIN	ρ_{-2}	0.54 ± 0.03	0.89 ± 0.04
$n = 1.4$	R_{-2}	35 ± 2	24 ± 1	$n = 1.4$	R_{-2}	37 ± 2.40	23 ± 1
	Υ_d	0.83 ± 0.01	0.72		Υ_d	0.86 ± 0.01	0.72
	Υ_b	–	–		Υ_b	1.04 ± 0.10	0.80
	χ_r^2	0.29	0.45		χ_r^2	0.33	0.60
EIN	ρ_{-2}	0.003 ± 0.001	0.006 ± 0.001	EIN	ρ_{-2}	0.003 ± 0.001	0.008 ± 0.001
$n = 6$	R_{-2}	1413 ± 345	758 ± 83	$n = 6$	R_{-2}	1409 ± 386	591 ± 66
	Υ_d	0.77 ± 0.02	0.72		Υ_d	0.79 ± 0.02	0.72
	Υ_b	–	–		Υ_b	1.05 ± 0.10	0.80
	χ_r^2	0.29	0.30		χ_r^2	0.32	0.36
EIN	ρ_{-2}	0.23 ± 0.37	0.002 ± 0.005	EIN	ρ_{-2}	0.02 ± 0.23	0.001 ± 0.005
free index	R_{-2}	66 ± 77	1756 ± 3657	free index	R_{-2}	341 ± 2330	1819 ± 4282
	n	2.2 ± 1.4	7.1 ± 2.7		n	4.2 ± 8.7	7.66 ± 3.03
	Υ_d	0.81 ± 0.03	0.72		Υ_d	0.80 ± 0.10	0.72
	Υ_b	–	–		Υ_b	1.06 ± 0.10	0.80
	χ_r^2	0.28	0.30		χ_r^2	0.32	0.35

Comments: Mass-to-light ratios $\Upsilon_\star^{3.6}$ are fixed by stellar population synthesis models, in $\mathrm{M}_\odot/L_\odot$; ρ_0 and ρ_{-2} are in 10^{-3} $\mathrm{M}_\odot$ pc^{-3}, R_c and R_{-2} in kpc and V_{200} in km s^{-1}.

classical Newtonian dynamics is no more valid, and the law of gravity is modified.

In the MOND framework, the gravitational acceleration of a test particle is given by :

$$\mu(x = g/a_0)g = g_N \tag{13}$$

where g is the gravitational acceleration, g_N the Newtonian acceleration and $\mu(x)$ is an interpolating function that must satisfy:

$$\mu(\mathrm{x}) = \begin{cases} 1 & \text{if } x \gg 1 \\ x & \text{if } x \ll 1 \end{cases}$$

The shape of the predicted MOND RCs depends on the shape of $\mu(x)$. The 'standard' μ-function proposed by Milgrom (1983a) is:

$$\mu(x) = \frac{x}{(1 + x^n)^{1/n}} \tag{14}$$

with $n = 2$. Using that form, the total velocity is written as:

$$V_{rot}^2 = \frac{V_{lum}^2}{\sqrt{2}} \sqrt{1 + \sqrt{(2\ R\ a_0/V_{lum}^2)^2}} \tag{15}$$

with $V_{lum}^2 = V_\star^2 + V_{\mathrm{gas}}^2$, $V_\star$ and V_{gas} being as in Eq. 6.

Famaey & Binney (2005) found that the 'simple' interpolation function with $n = 1$ yields a better fit to the rotation curve of the Milky Way than $n = 2$. That 'simple' form is also appropriate to other galaxy rotation curves (see Famaey & McGaugh 2012, and references therein). Here, the total velocity is obtained by:

$$V_{rot}^2 = V_{lum} \sqrt{a_0 R + V_{lum}^2} \tag{16}$$

4.5 Results of the mass models

Least-square fits to the rotation curve have been performed, using a normal weighting function set to the inverse of the squared velocity uncertainties. For each mass model, we have considered a pure disk case (without bulge) and a disk+bulge case for the stellar contribution. The mass-to-light ratio of the bulge and disk are either fixed at the value inferred by the color indices and stellar population models ('color $\Upsilon_\star^{3.6}$'), or left free ('best-fit'). The fits for the ISO, NFW and constrained EIN ($n = 1.4$ and $n = 6$) models have thus 2 to 4 free parameters, while the fits of the unconstrained EIN have the index n as additional free parameter. For MOND, fits have been performed with a_0 left fixed or free, yielding 1 to 3 free parameters. The 'simple' and 'standard' interpolation functions have been tested. Tables 4 and 5 give the fitted parameters for DM and MOND models, respectively, and Figures 10 to 17 show the resulting mass

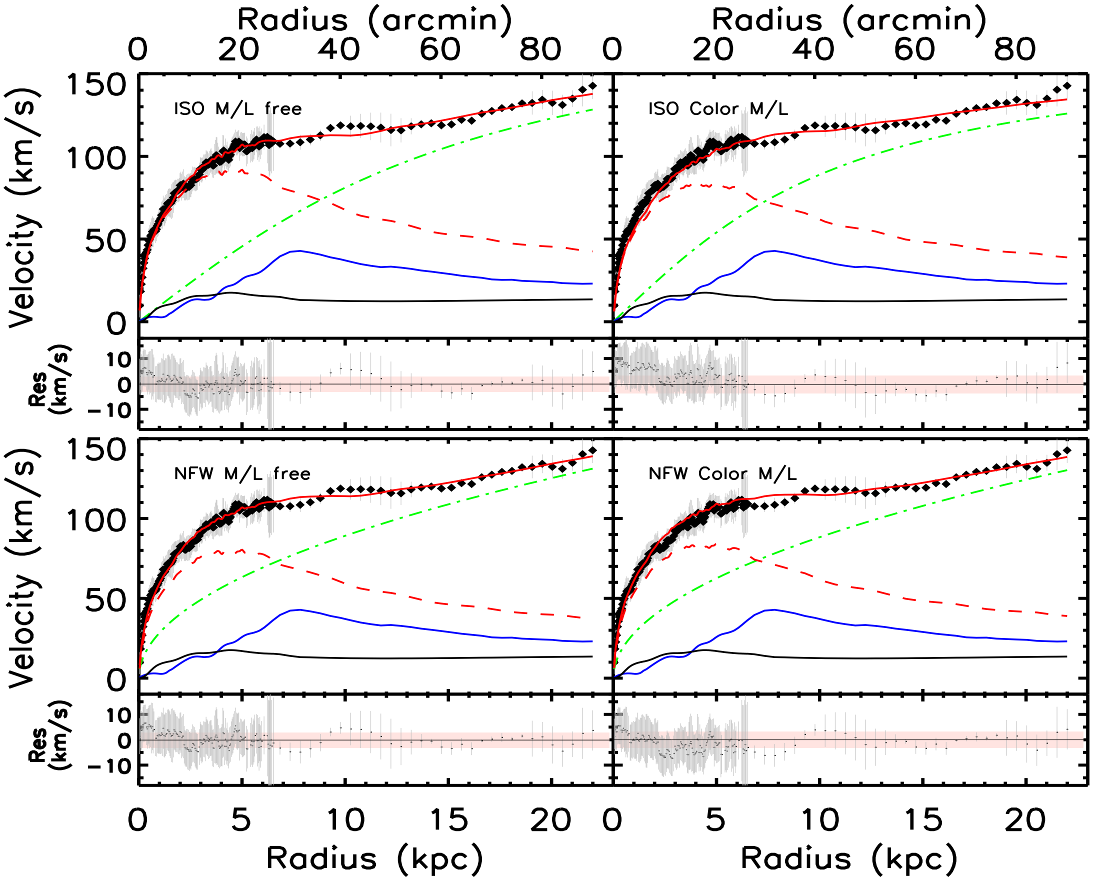

Figure 10. Pure disk ISO (top) and NFW (bottom) mass models. The panels on the left give the best-fit models and those on the right the models with a fixed mass-to-light ratio, derived from IR colours and population synthesis models. The filled diamonds with error bars represent the RC, The stellar disc contribution is in broken red, the HI contribution in blue, the H_2 contribution in black, the halo contribution in broken green and the sum of the three components is shown as a continuous red line. At the bottom of each model, the mean residuals (observations − model) are represented by a black line with the same error bars as the velocity errors of the top panels. The part coloured in pink gives the dispersion of the residuals around the black regression line.

models. The results for the EIN model at free index are not shown, but only reported in Tab. 4. The fits are excellent ($\chi_r^2 < 1$) for dark matter halo models, while they are of very poor quality for MOND ($\chi_r^2 >> 1$). The detailed analysis of the mass modelling results is done in Section 5.

5 DISCUSSION

5.1 Distribution and kinematics of the neutral hydrogen gas

Our combined DRAO and Arecibo HI distribution is in very good agreement with recent HI maps of Messier 33, such as the VLA-GBT mosaic of Corbelli et al. (2014). While HI is detected at $R > 90'$, most of the HI is within the optical radius of 35′, which is the region where the disk is more regular, showing many prominent spiral arms. A strong warp starts beyond 35′. The irregular gaseous tails observed to the North-East and South-West of the disk are part of that warp. A numerical modelling of these outer features shows that gas is likely being accreted in the disk (Putman et al. 2009). Our mosaic reaches sensitivities down to $\sim 5 \times 10^{18}$ cm^{-2} in the warped disk regions, which is much lower than in the inner disk.

At that level, a slice along the major axis seem to point out some lagging HI (see the example of NGC 2403 Fraternali et al. 2001), which suggests the presence of "anomalous" extraplanar gas that, due to the 52° inclination of the disk, can just be noticed kinematically since spatially it is superposed to the disk along our line-of-sight. This gas is apparent in the lowest contours of the cut shown in (Figure 7). Especially for the receding half of the galaxy, the PV diagram clearly highlights the presence of an anomalous HI component spanning a range of radial velocities that is offset from the high-intensity emission of the main disk, towards the systemic velocity of the system.

We find a total HI mass of $1.95 \pm 0.36 \times 10^9$ $M_\odot$, in agreement with Corbelli (2003), Putman et al. (2009) or Corbelli et al. (2014). Compared with the molecular gas mass of $\sim 3.3 \times 10^8$ $M_\odot$ (Gratier et al. 2010), the total neutral gas mass is thus about six times larger than the molecular content (would be larger if the MW conversion factor was

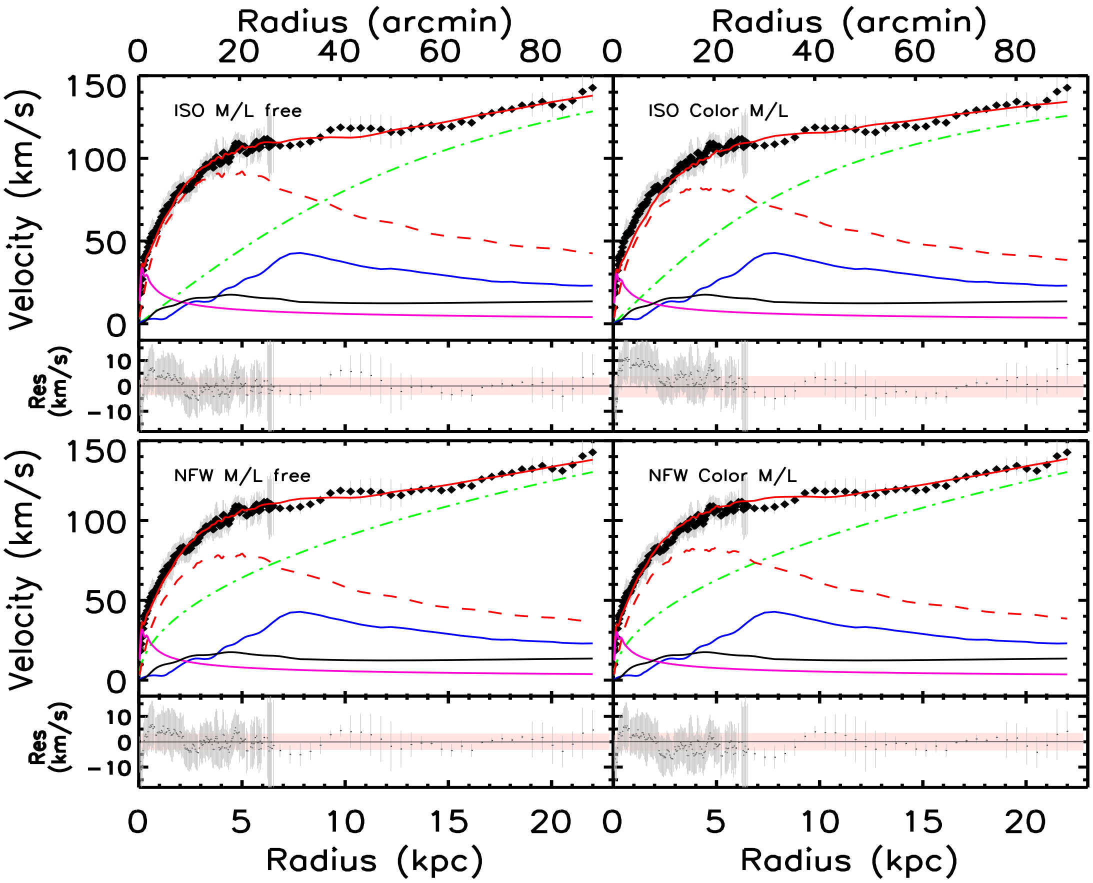

Figure 11. Same as Fig.10 but with the contribution of the bulge presented in magenta..

Table 5. Results of the MOND models

Disk-only case MOND model		Best-fit	Colour $\Upsilon_\star^{3.6}$	**Bulge+disk case** MOND model		Bestf-fit	Colour $\Upsilon_\star^{3.6}$
Stand’ard	a_0	1.21	1.21	Standard	a_0	1.21	1.21
fixed a_0	Υ_d	0.68 ± 0.03	0.72	fixed a_0	Υ_d	0.88 ± 0.02	0.72
	Υ_b	–	–		Υ_b	0.42 ± 0.37	0.80
	χ_r^2	24.41	25.00		χ_r^2	5.92	7.53
Standard	a_0	3.24 ± 0.21	1.27 ± 0.05	Standard	a_0	3.46 ± 0.21	1.50 ± 0.05
free a_0	Υ_d	0.19 ± 0.02	0.72	free a_0	Υ_d	0.16 ± 0.02	0.72
	Υ_b	–	–		Υ_b	0.87 ± 0.24	0.80
	χ_r^2	7.65	24.11		χ_r^2	2.68	4.71
Simple	a_0	1.21	1.21	Simple	a_0	1.21	1.21
fixed a_0	Υ_d	0.61 ± 0.02	0.72	fixed a_0	Υ_d	0.32 ± 0.30	0.72
	Υ_b	–	–		Υ_b	0.81 ± 0.02	0.80
	χ_r^2	30.40	35.40		χ_r^2	7.41	8.13
Simple	a_0	3.31 ± 0.20	1.17 ± 0.06	Simple	a_0	3.56 ± 0.20	1.46 ± 0.03
free a_0	Υ_d	0.18 ± 0.02	0.72	free a_0	Υ_d	0.15 ± 0.02	0.72
	Υ_b	–	–		Υ_b	0.78 ± 0.21	0.80
	χ_r^2	7.90	35.72		χ_r^2	2.77	6.07

Comment: a_0 is given in units of 10^{-8} cm.s^{-2}. Standard is the model with the standard interpolation function (Eq. 15), Simple is the model with the simple interpolation function (Eq. 16).

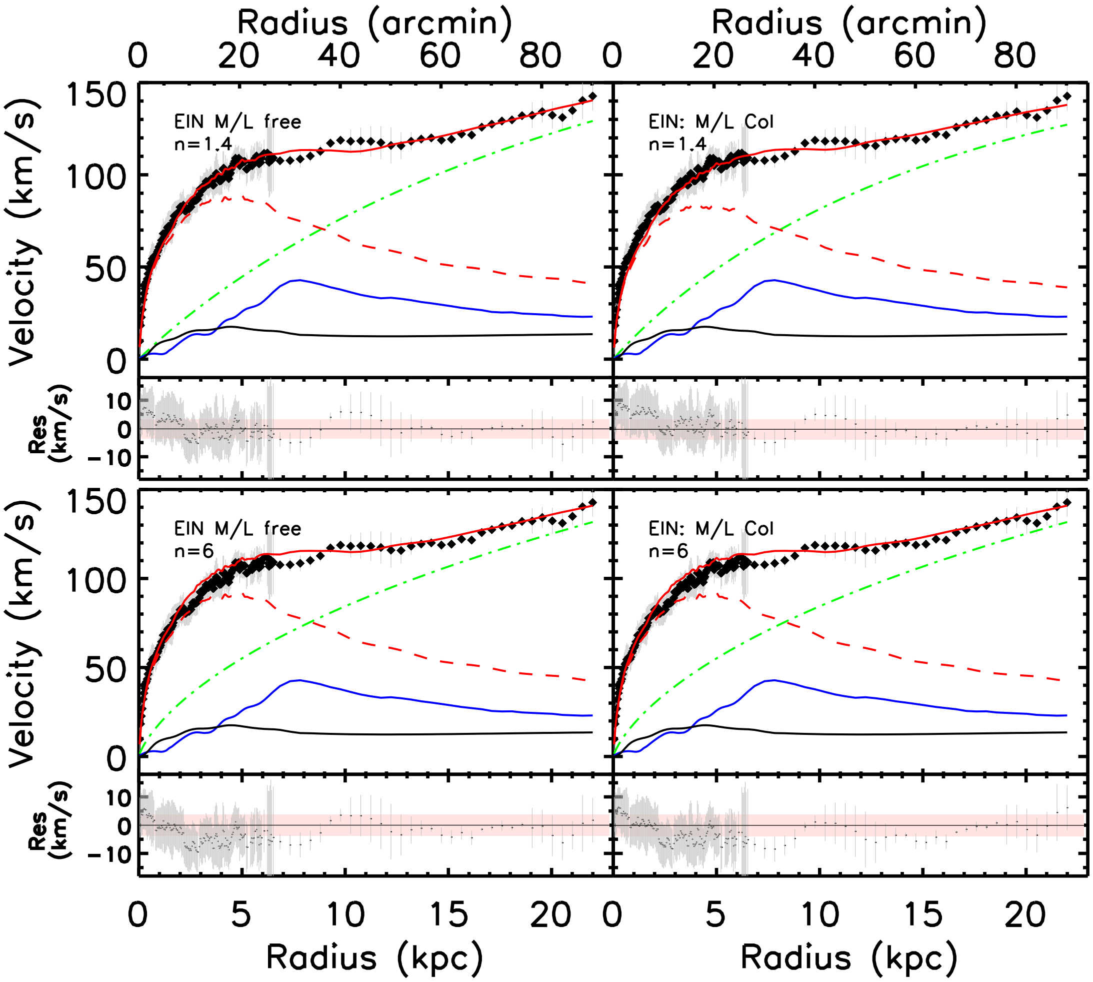

Figure 12. Pure disk EIN mass models with n=1.4 (top) and n=6 (bottom). The panels on the left give the best-fit models and those on the right the models with a fixed mass-to-light ratio, derived from IR colors and population synthesis models. The colour codes are the same as in Fig.10.

used). Naturally, H_2 is much more concentrated in the centre than the HI, both reaching central surface densities ∼10 $M_\odot$ pc^{-2}.

The warp of Messier 33 is clearly seen in the tilted-ring model of the HI velocity field, that shows a variation of the position angle from ∼ 202° to ∼ 165°. The variation of the inclination seems less spectacular, as it smoothly increases by about 5° from the centre to the disk outskirts. The physical geometry of the HI disk, implied by our model, is confirmed by the presence of double peaks in the HI datacube (see also Chemin et al. 2012). Here, we naturally expect the gas orbits crossing the line-of-sight twice, or more. The other effect is the observed increase of the velocity dispersion in the transition region. It is thought that the HI warp is likely due to an interaction with the nearby massive companion, the Andromeda galaxy (e.g. Putman et al. 2009). M33 is also surrounded by a prominent stellar structure that provides additional evidence of the encounter with M31 (McConnachie et al. 2009), or at least of recent gravitational interaction. This stellar structure extends ∼2° (30 kpc in projection) to the North-West towards M31, nearly three times farther out than the size of the optical disk of M33, and thus farther than the HI gas in the warp.

We find a perfect agreement of the systemic velocity, dynamical centre, position angle and inclination of the HI disk with the Hα parameters found in Kam15, within the optical disk. The tilted-ring model is also very consistent with previous HI studies (Corbelli & Schneider 1997; Corbelli et al. 2014), except the inclination profile that differs from the slightly declining one of Corbelli et al. (2014) for $R > 8$ kpc. The difference between the rotation curve of the approaching and receding sides are small (∼ 4 km s^{-1} on average). Only the transition region ∼35-55′ presents larger differences (∼ 20 km s^{-1}), as well as the outermost points, as likely due to lower quality fits at those radii and a genuine stronger asymmetry between opposite sides of the warp. The comparison with the rotation curve of Corbelli et al. (2014) is shown in Fig. 18. The most notable differences occur for $2 < R < 5$ kpc, where our velocities are smaller by $5 - 10$ km s^{-1}, and at $R > 20$ kpc where our curve increases while

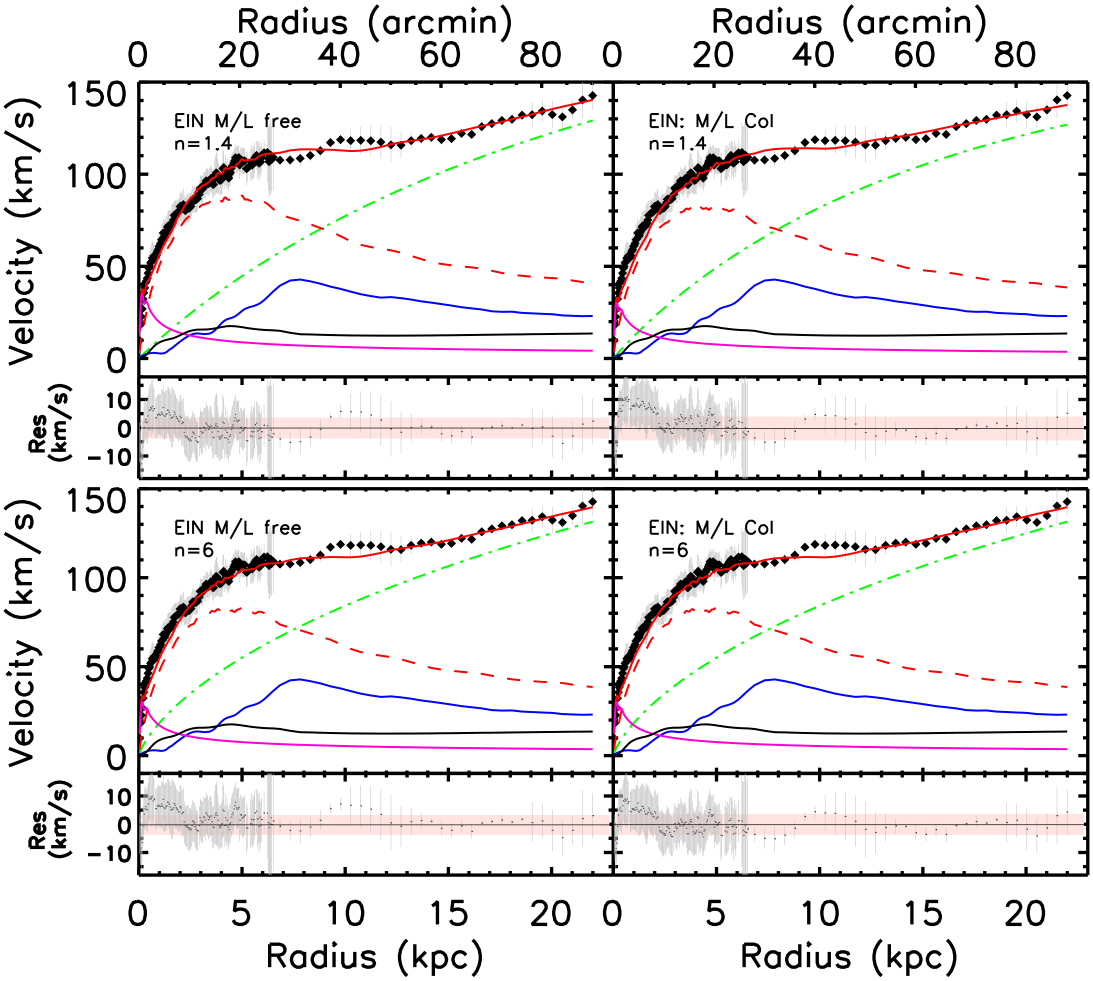

Figure 13. Same as Fig.12 but with the contribution of the bulge presented in magenta..

that of Corbelli et al. (2014) decreases. With the exception of the $R > 22$ kpc points, the two curves are consistent with each other within the quoted uncertainties. For the mass models analysis, the Hα RC of Kam15 is used out to 6.5 kpc and than the HI RC of this study out to the last measured point around 22 kpc.

5.2 Mass models

For the mass distribution analysis, we used the Spitzer/IRAC 3.6μm profile, which gives a good representation of the old disk population, which contributes most of the stellar mass. Our combined DRAO and Arecibo data give us a good representation of the HI disk. It was multiplied by 4/3 to take into account primordial helium. For the second in importance gas component, we used the H_2 data from Druard et al. (2014), who used a CO to H_2 conversion factor two times larger than the value found for the Milky Way, arguing that M33 has half the solar metallicity. Three types of DM models were constructed: the pseudo-isothermal (ISO) model, the Navarro-Frenk-White (NFW) model and the Einasto (EIN) model. We performed best-fit models and models where the M/L has been constrained by IR colors and stellar population models. In terms of the stellar mass distribution, we explored disk-only models and bulge+disk models, after doing a decomposition of our IR profile. However, with a bulge-to-disk ratio of only 0.04, we were not expecting a big difference.

5.2.1 DM Models

Results listed in Table 4 for the mass distribution models with a DM component first show that best-fit models are of similar quality ($\chi_r^2 \sim 0.3$), irrespective of the halo model, and of the assumption made on the stellar distribution with or without a bulge. The halo parameters for every models but the EIN one at free index are very comparable with or without the bulge. However, mass models with fixed color-based mass-to-light ratios for the pure disk case tend to be better than those with the bulge component. It seems thus preferable to omit the negligible bulge contribution when modelling the mass distribution of Messier 33 at fixed stellar

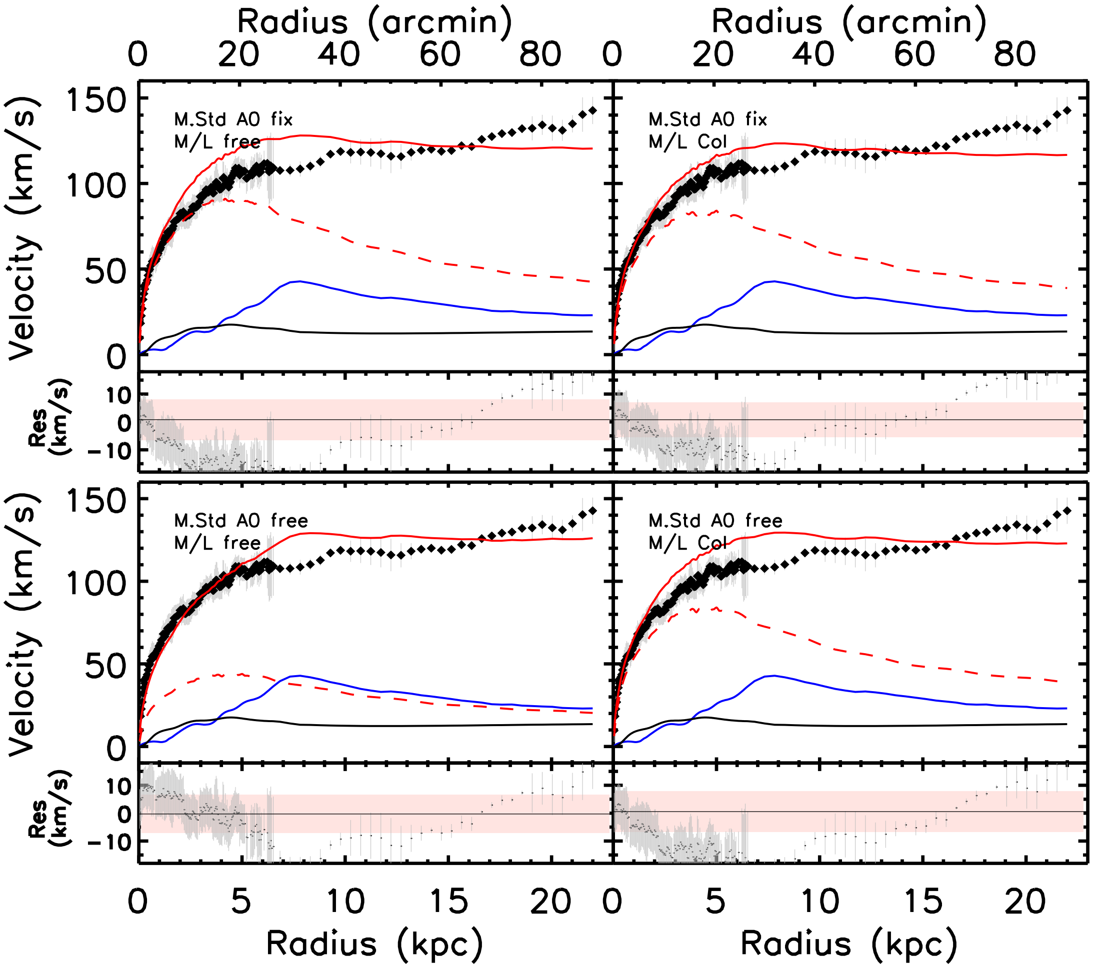

Figure 14. Pure disk MOND models with the standard interpolation function. The colour codes are the same as in Fig.10.

mass. We thus focus on the disk-only results hereafter. Furthermore, the scale density and radius of the halo of the EIN model (free index) are significantly degenerated. Because of this degeneracy, and despite the apparent good quality of the fits, we reject this model for the remaining of the analysis.

At first order, it appears impossible to disentangle the halo shape from best-fit models, as the reduced χ^2 are very comparable ($\sim$ 0.3). However we notice that the halo parameters of the ISO and EIN $n = 1.4$ haloes are significantly better constrained, and more realistic than for the two other haloes. By estimating the slope of the EIN density profile at the first data point of the rotation curve ($R = 41$ pc) for the $n = 1.4$ model ($\alpha = -0.02 \pm 0.1$) and $n = 6$ model ($\alpha = -0.4 \pm 0.1$), one thus deduces that the degeneracy between parameters increases towards steeper density profiles. Curiously, the $n = 6$ EIN halo of M33 is not a cusp, while it was expected from Chemin et al. (2011) that haloes with $n = 6$ are as cuspy as those modelled in cosmological simulations (Navarro et al. 2004, 2010). This discrepancy is explained by the value of the scale radius R_{-2}, which appears considerably large, even larger than simulated galaxy cluster haloes. In other words, though starting from initial parameters of a pure galaxy-sized cusp, the modelling has produced a halo as shallow as possible with this index $n = 6$, but at the price of an unrealistically large halo. The possibly shallow nature of the density profile of M33 would also explain the unrealistic smaller concentration parameter, and larger V_{200}, than expectations from simulations for galaxy-sized haloes (Bullock et al. 2001; Neto et al. 2007). Note here that nearly half of the NFW models of de Blok et al. (2008) from THINGS also have $c < 0.1$ and one third have $V_{200} > 500$ km s^{-1} (but see Chemin et al. (2011) for a remodelling of the de Blok's sample with uncorrelated data points). Finally, we note that the mass-to-light ratio of the disk has to be 15-20% larger than the color-based $\Upsilon_{\star}^{3.6}$ value for the preferred ISO and EIN $n = 1.4$ models.

Results for the fixed $\Upsilon_{\star}^{3.6}$ show that the EIN $n = 6$ and NFW haloes are better than the ISO and EIN $n = 1.4$ models, but again with unrealistic, and not well constrained parameters. This result is not surprising since a shallow halo combined with a heavier stellar mass is needed to best-fit the observational data, as explained above. Such effect is indeed better reproduced by a combination 'light' mass-steeper density profiles than by 'light' mass-shallow density profiles.

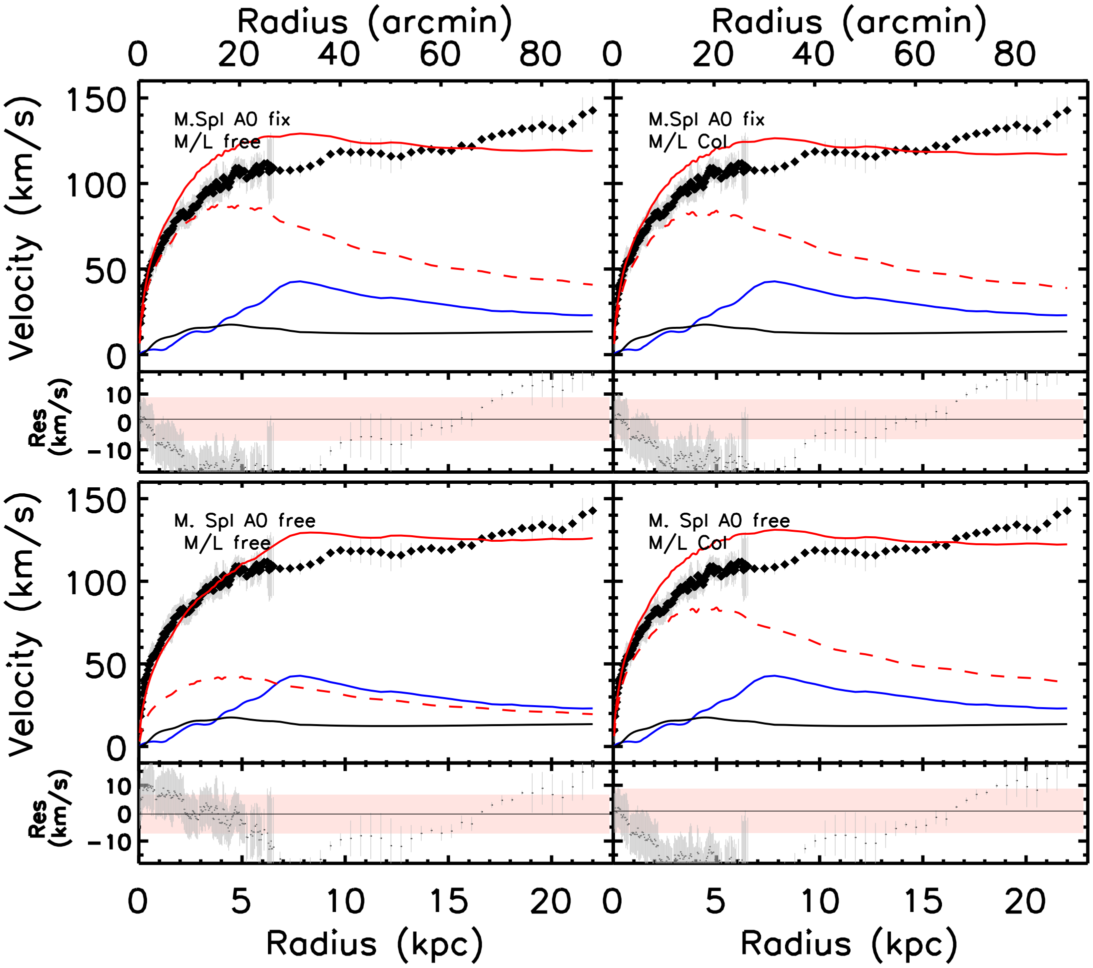

Figure 15. Pure disk MOND models with the simple interpolation function.

It is worth noting here that the apparent inhomogeneous distribution of the rotation velocity uncertainties is not responsible of the observed trend that M33 favours a core-dominated halo. Indeed, we have verified that all the results remain unchanged when using more homogeneous error bars, by propagating the mean error of the Hα velocities to the outer HI points, and the mean error of the HI velocities to the inner Hα points.

5.2.2 *Comparison with the DM models in the literature*

We first notice that the parameters of the ISO model are consistent with the relationship of Kormendy & Freeman (2004), whose 1σ parameter range is $R_c = 3 - 11$ kpc and $\rho_0 = 0.006 - 0.013$ M$_\odot$ pc^{-3} for galaxies of similar absolute magnitude as M33, and those of the NFW model with the range $R_c = 1 - 17$ kpc and $\rho_0 = 0.003 - 0.1$ M$_\odot$ pc^{-3} found by Randriamampandry & Carignan (2014). Our EIN $n = 1.4$ parameters are also in good agreement with those of the THINGS disks within the quoted uncertainties (Chemin et al. 2011).

The comparison of our results with recent mass distribution models of Messier 33 (Corbelli et al. 2014; Hague & Wilkinson 2015) is not straightforward, as different datasets and stellar population synthesis models have been used in both studies. The modelling of Corbelli et al. (2014) shows that the NFW with a concentration parameter $c = 10$ is the most likely model, while Hague & Wilkinson (2015) favour a steep inner cusp and large $\Upsilon^{3.6}$, excluding the combination of $\Upsilon^{3.6} < 2$ with an inner slope < 0.9 measured at the first velocity point of their HI rotation curve ($R \sim 2'$). Our results are thus not in agreement with these studies. This is likely explained by the impact of a different rotation curve. At a similar inner radius as Hague & Wilkinson (2015), the maximum absolute slope inferred by our EIN models is 0.7 for $n = 6$, thus significantly not as cuspy as their result.

Using the best-fit case for the $n = 1.4$ EIN halo, the estimated gas, stellar, dark matter and total masses enclosed within $R = 22$ kpc (i.e. at the last radius of the rotation curve) are $\sim 3 \times 10^9$ M$_\odot$, $\sim 9 \times 10^9$ M$_\odot$, $\sim 8.6 \times 10^{10}$ M$_\odot$ and $\sim 9.8 \times 10^{10}$ M$_\odot$, respectively, implying a luminous-to-total mass fraction of $\sim 12\%$. We estimate a virial radius of $R_{200} = 178 \pm 10$ kpc for a virial mass of $M_{200} = (7 \pm 1) \times 10^{11}$ M$_\odot$ at this radius, with a total

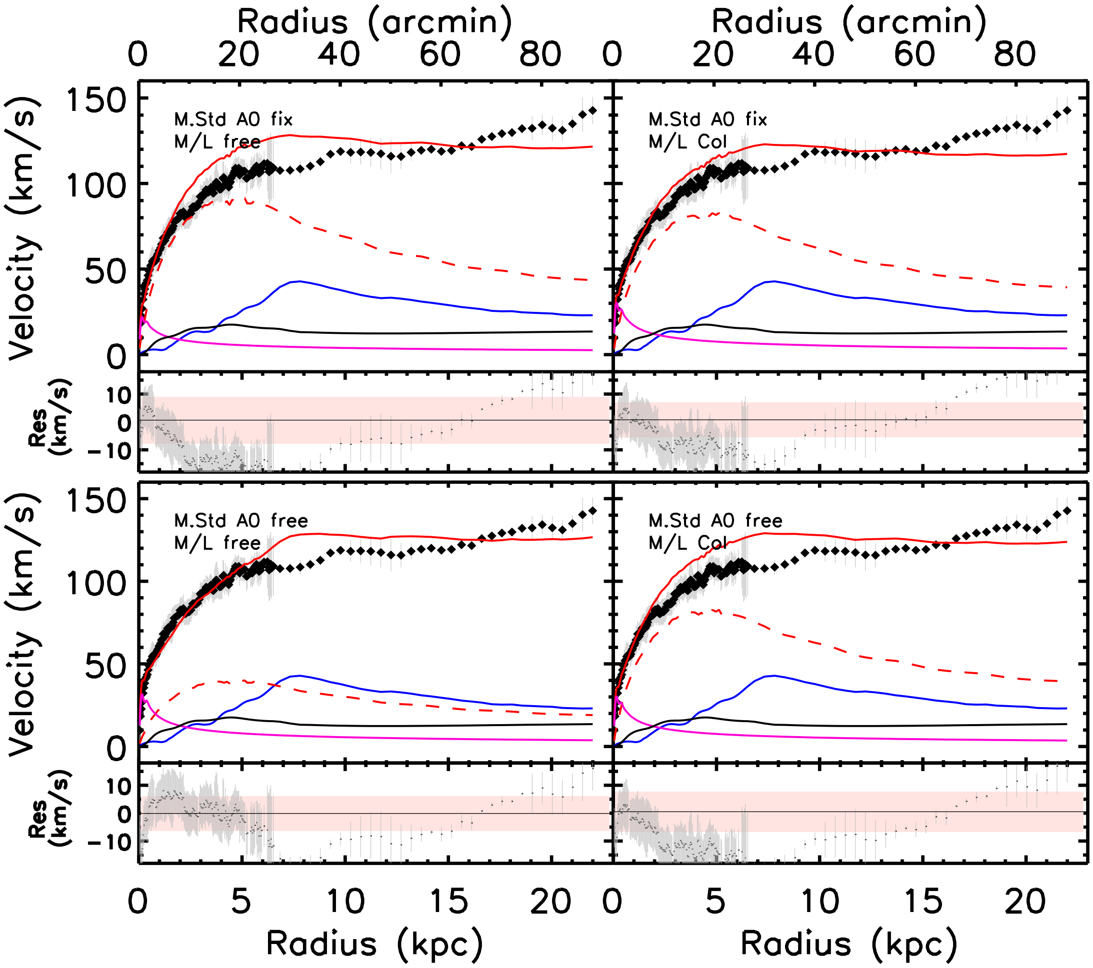

Figure 16. Same as in Figure 14 with the contribution of the bulge presented in magenta.

luminous baryon mass accounting for 2% of the virial mass. A concentration R_{200}/R_{-2} for the dark matter of 5.1 ± 0.7 is found. Our stellar mass is thus 1.8 times larger than the best-fit one of Corbelli et al. (2014), as very likely caused by the use of different stellar population synthesis models and rotation curve. Corbelli et al. (2014) give a total mass of $\sim 4.4 \times 10^{11}$ $M_{\odot}$, but not the virial radius. Our estimate would thus be about 60% larger than their value, provided that a similar virial radius has been used. Such a difference is due to different best-fit mass models of the different rotation curves. Notice finally that M33 is therefore about 1.4 times less massive than the Andromeda galaxy, if we assume that the M31 virial mass is $\sim 10^{12}$ $M_{\odot}$ (Chemin et al. 2009).

5.2.3 No-DM MOND models

Figs. 14, 15, 16 and 17 clearly show it is impossible to reproduce the rotation curve of Messier 33, irrespective of the assumptions made on a_0, on the disk mass-to-light ratio, or the interpolation function. Table 5 lists large χ^2_r, from 3 to 35. The failure of MOND is however not a surprise, since such a mass model produces flat outer rotation curves while our RC rises steadily out to the last point. The resulting models generally overestimate the rotation velocities inside $R = 10-15$ kpc, and underestimate them beyond. We notice that Corbelli et al. (2014) also rejected MOND for M33, even using a different RC than ours.

6 SUMMARY AND CONCLUSIONS

New high sensitivity HI observations using data from the DRAO interferometer combined with single dish Arecibo data have been presented. They reach very low column densities $\sim 5 \times 10^{18}$ cm^{-2}.

The main results on the HI distribution and kinematics of M33 are as follows:

- While the bulk of the HI is found within the optical disk ($\leqslant 8.4$ kpc or $R_{25} = 35.4'$), the faint outer HI disk was traced out to $\geqslant 90' = 2.7$ R_{25}.
- At the adopted distance of 840 kpc, the HI mass is $\sim 2 \times 10^9$ $M_{\odot}$ for a $M_{HI}/L_V = 1.8$.
- There is slightly more HI on the NW side (in the direction of M31: see the discussion in p.e.Ibata et al. (2014))

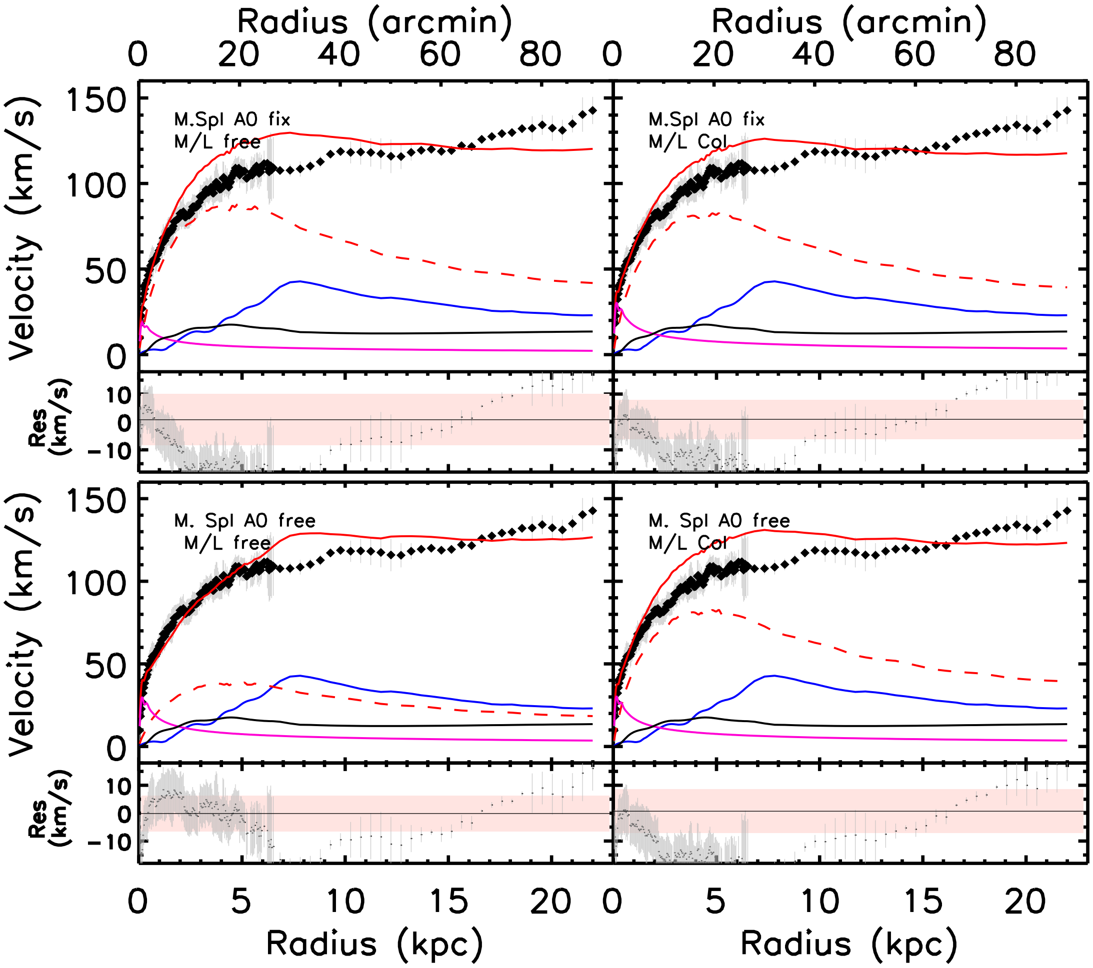

Figure 17. Same as in Figure 15 with the contribution of the bulge presented in magenta.

than on the SE side and its radial distribution is nearly constant out to the edge of the optical disk, where it drops abruptly (Figure 2).

- The faint outer disk (see the last 2 contours of Figure 1) is found to be strongly warped with a variation of PA from 202° to 165° and a small increase of inclination, which is clearly seen in the twist of the isovelocity contours (Figure 5). Clear wider or even double-peaked profiles are seen (Figure 4, where our line-of-sight is expected to cross the disk more than once due to the warp.
- Following the faint outer disk, the RC is extended out to ∼22 kpc in this study and shows a good agreement between the approaching and receding sides (Fig. 6), except for $10 \leqslant R \leqslant 14$ kpc, the radius range corresponding to the sharp change in PA seen in Figure 6.
- Position-velocity diagrams (Fig. 7) at the more or less constant PA values in the inner parts (202°) and in the outer parts (165°) show a good agreement between our adopted RC and the kinematics observed on the major axis. Similarly, a model velocity field constructed using the adopted RC shows very small residuals $\leqslant 10$ km s^{-1} which gives us confidence in our derived kinematical parameters.
- Both the top PV-diagram of Figure 7 and the adopted RC of Figure 9 show a very good agreement between our HI data and the Hα data of Kam15.
- The new rotation curve, used for the mass modelling, is a combination of the Hα rotation curve at arcsec-resolution presented in the first article from this series (Kam15) out to 6.5 kpc, and the new arcmin-resolution HI rotation curve derived in this study out to 22 kpc.

The main results from the modelling of the mass distribution are as follows.

- Despite a very accurate rotation curve, it was not possible, based on the goodness of the fits, to establish that one of the three DM models (ISO, NFW and EIN) was representing better than the others the DM distribution in M33. The three functional forms used give more or less equally acceptable fits. This may not be surprising in view of the known existence of a small bar (Corbelli & Walterbos 2007) in M33, which makes it difficult to constrain the shape of the M33's inner dark matter halo profile, where lies the main difference e.g. between ISO and NFW.
- DM models at fixed mass-to-light ratios constrained by

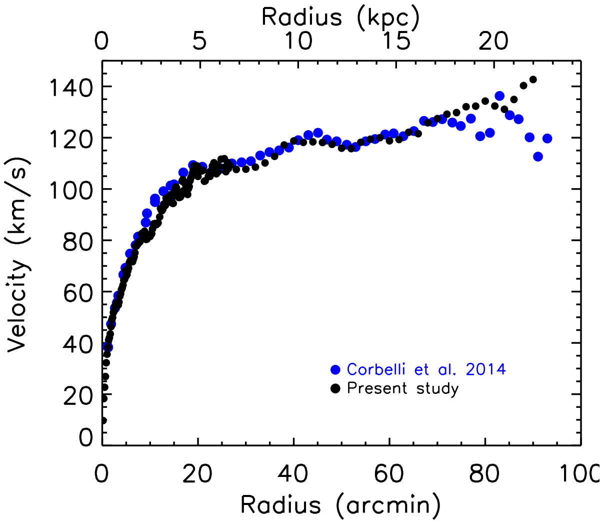

Figure 18. Comparison of our hybrid Hα-HI rotation curve (black symbols) with the HI curve from Corbelli et al. (2014) (blue symbols).

stellar population synthesis using a diet-Salpeter IMF tend to prefer haloes with steep inner density profiles. Best-fit mass models give equally acceptable fits, irrespective of the shallow or cuspy density shape. However, such cuspy models are highly unrealistic, showing characteristic parameters of velocity, concentration, scale radius and density that are rarely seen in other observational studies or in cosmological simulations. We thus reject cupsy models for Messier 33, which is in disagreement with recent mass models found in the literature.

- The inner density slope of the EIN model at fixed index $n = 1.4$ is -0.01 at 41 pc, the innermost point of the rotation curve, and the disk mass-to-light ratio in the Spitzer 3.6μm band is 0.83. These values are fully consistent with the pseudo-isothermal sphere model. The inferred stellar mass of Messier 33 is 9×10^9 M$_\odot$.

- The mass enclosed within 22 kpc, the last point of the rotation curve, is 9.8×10^{10} M$_\odot$, implying a luminous (gas+stars) to total mass fraction of 12%. The total mass estimated at the virial radius of 178 kpc is 7×10^{11} M$_\odot$. Messier 33 is thus about 1.4 times less massive than Messier 31.

- This study shows clearly that, even when letting the MOND constant a$_0$ and/or the disk M/L free to vary and allowing for different interpolation functions, there is no way a MOND model (no DM) can represent the mass distribution in M33. This result is consistent with Corbelli et al. (2014) and questions the universality of MOND as suggested by many studies (see e.g. Begeman et al. 1991; Sanders & Verheijen 1998; de Blok & McGaugh 1998; Gentile et al. 2010). This is similar to what was seen recently for the late-type spiral NGC 3109 (Carignan et al. 2013).

- M33, a galaxy with a well constrained distance and rotation curve, shows the importance of deriving the RCs out to large R because, with a RC derived only out to the edge of the optical disk ~8 kpc, previous studies (see e.g. Sanders 1996; Sanders & McGaugh 2002) were showing a good agreement between the M33's RC and MOND. This can be seen also in Figure 19, where we derived MOND models using only the optical Hα data of Kam15 out to ~8 kpc. It can be seen that especially the bulge+disk models give very good fits for both interpolation functions. However, this is not the case when the RC is extended out to 22 kpc.

ACKNOWLEDGEMENTS

The Dominion Radio Astrophysical Observatory is operated as a national facility by the National Research Council of Canada. ZKS's work was supported by CC's Discovery grant of the Natural Sciences and Engineering Research Council of Canada. CC's work is based upon research supported by the South African Research Chairs Initiative (SARChI) of the Department of Science and Technology (DST), the Square Kilometer Array South Africa (SKA SA) and the National Research Foundation (NRF). L.C. acknowledges a financial support from CNES. TF's work has partially been supported by a grant from the Brandon University Research Committee (BURC). We are very grateful to Kevin Douglas and Mary Putman for providing us the Arecibo TOGS data.

REFERENCES

Begeman, K. G., Broeils, A. H., & Sanders, R. H. 1991, MNRAS, 249, 523

Boulesteix, J., Courtes, G., Laval, A., Monnet, G., & Petit, H. 1974, A&A, 37, 33

Braun, R. & Thilker, D. 2004, in Astronomical Society of the Pacific Conference Series, Vol. 327, Satellites and Tidal Streams, ed. F. Prada, D. Martinez Delgado, & T. J. Mahoney, 139

Bullock, J. S., Kolatt, T. S., Sigad, Y., Somerville, R. S., Kravtsov, A. V., Klypin, A. A., Primack, J. R., & Dekel, A. 2001, MNRAS, 321, 559

Capaccioli, M. 1989, in World of Galaxies (Le Monde des Galaxies), ed. H. G. Corwin, Jr. & L. Bottinelli, 208–227

Carignan, C., Frank, B. S., Hess, K. M., Lucero, D. M., Randriamampandry, T. H., Goedhart, S., & Passmoor, S. S. 2013, AJ, 146, 48

Chemin, L., Carignan, C., Foster, T., & Kam, Z. S. 2012, in SF2A-2012: Proceedings of the Annual meeting of the French Society of Astronomy and Astrophysics, ed. S. Boissier, P. de Laverny, N. Nardetto, R. Samadi, D. Valls-Gabaud, & H. Wozniak, 519–522

Chemin, L., Carignan, C., & Tyler, F. 2009, ApJ, 705, 1395

Chemin, L., de Blok, W. J. G., & Mamon, G. A. 2011, AJ, 142, 109

Corbelli, E. 2003, MNRAS, 342, 199

Corbelli, E. & Salucci, P. 2000, MNRAS, 311, 441

Corbelli, E. & Schneider, S. E. 1997, ApJ, 479, 244

Corbelli, E., Thilker, D., Zibetti, S., Giovanardi, C., & Salucci, P. 2014, A&A, 572, A23

Corbelli, E. & Walterbos, R. A. M. 2007, ApJ, 669, 315

de Blok, W. J. G. & Bosma, A. 2002, A&A, 385, 816

de Blok, W. J. G. & McGaugh, S. S. 1998, ApJ, 508, 132

de Blok, W. J. G., Walter, F., Brinks, E., Trachternach, C., Oh, S.-H., & Kennicutt, Jr., R. C. 2008, AJ, 136, 2648

de Vaucouleurs, G., de Vaucouleurs, A., Corwin, Jr., H. G., Buta, R. J., Paturel, G., & Fouque, P. 1991, S&T, 82, 621

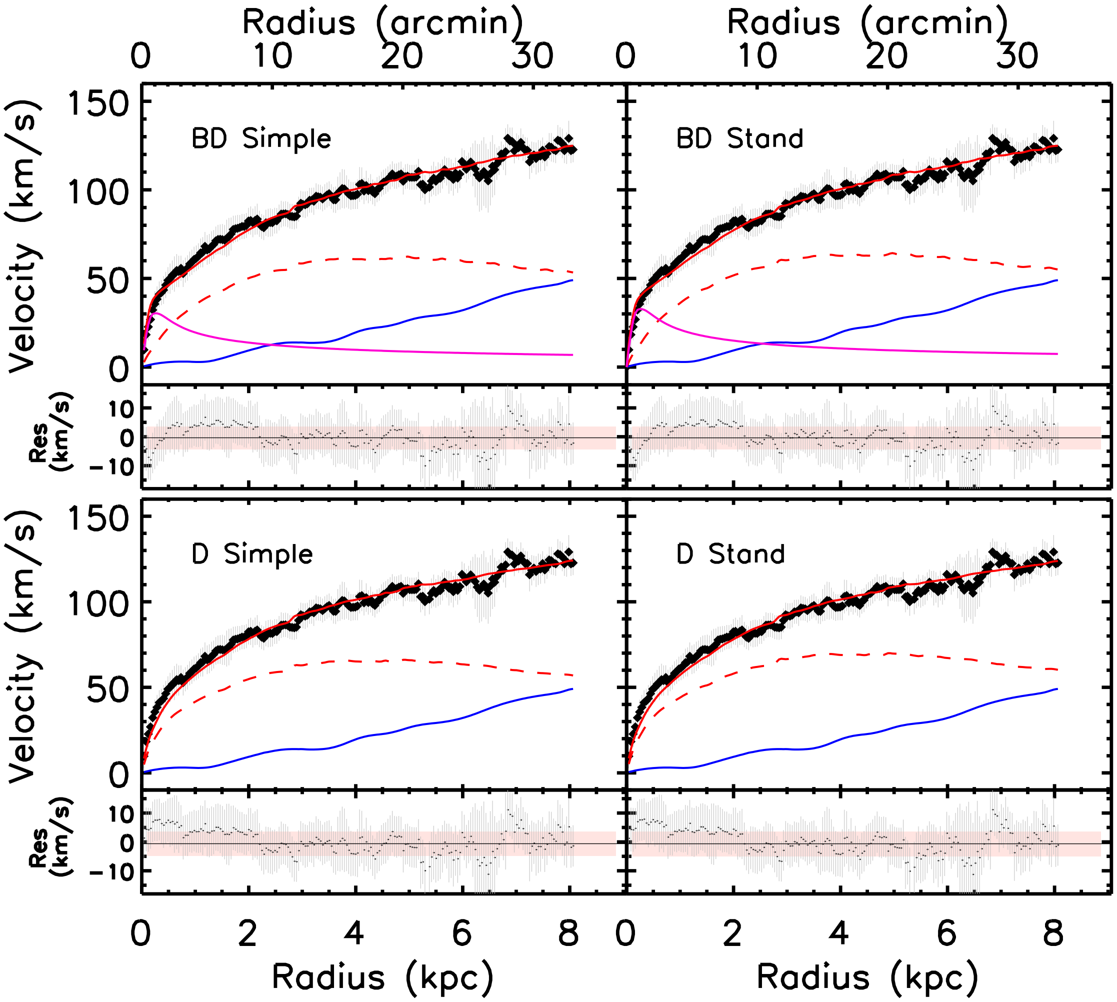

Figure 19. MOND models with the Hα RC: the models at the top are for bulge+disk and at the bottom for disk-only. The left side is for the simple interpolation and the right side for the standard interpolation. In each case, the residuals are given in the small bottom panels.

Druard, C., Braine, J., Schuster, K. F., Schneider, N., Gratier, P., Bontemps, S., Boquien, M., Combes, F., Corbelli, E., Henkel, C., Herpin, F., Kramer, C., van der Tak, F., & van der Werf, P. 2014, ArXiv e-prints

Famaey, B. & Binney, J. 2005, MNRAS, 363, 603

Famaey, B. & McGaugh, S. S. 2012, Living Reviews in Relativity, 15, 10

Fraternali, F., Oosterloo, T., Sancisi, R., & van Moorsel, G. 2001, ApJLett, 562, L47

Gentile, G., Baes, M., Famaey, B., & van Acoleyen, K. 2010, MNRAS, 406, 2493

Gratier, P., Braine, J., Rodriguez-Fernandez, N. J., Schuster, K. F., Kramer, C., Xilouris, E. M., Tabatabaei, F. S., Henkel, C., Corbelli, E., Israel, F., van der Werf, P. P., Calzetti, D., Garcia-Burillo, S., Sievers, A., Combes, F., Wiklind, T., Brouillet, N., Herpin, F., Bontemps, S., Aalto, S., Koribalski, B., van der Tak, F., Wiedner, M. C., Röllig, M., & Mookerjea, B. 2010, A&A, 522, A3

Grossi, M., Giovanardi, C., Corbelli, E., Giovanelli, R., Haynes, M. P., Martin, A. M., Saintonge, A., & Dowell, J. D. 2008, A&A, 487, 161

Hague, P. R. & Wilkinson, M. I. 2015, ApJ, 800, 15

Haynes, M. P. & Giovanelli, R. 1984, AJ, 89, 758

Hinshaw, G., Weiland, J. L., Hill, R. S., Odegard, N., Larson, D., Bennett, C. L., Dunkley, J., Gold, B., Greason, M. R., Jarosik, N., Komatsu, E., Nolta, M. R., Page, L., Spergel, D. N., Wollack, E., Halpern, M., Kogut, A., Limon, M., Meyer, S. S., Tucker, G. S., & Wright, E. L. 2009, ApJS, 180, 225

Ibata, R. A., Lewis, G. F., McConnachie, A. W., Martin, N. F., Irwin, M. J., Ferguson, A. M. N., Babul, A., Bernard, E. J., Chapman, S. C., Collins, M., Fardal, M., Mackey, A. D., Navarro, J., Peñarrubia, J., Rich, R. M., Tanvir, N., & Widrow, L. 2014, ApJ, 780, 128

Jarrett, T. H., Chester, T., Cutri, R., Schneider, S. E., & Huchra, J. P. 2003, AJ, 125, 525

Kam, S. Z., Carignan, C., Chemin, L., Amram, P., & Epinat, B. 2015, Accepted for publication in MN-

RAS(arXiv:1503.02538)

Kormendy, J. & Freeman, K. C. 2004, in IAU Symposium, Vol. 220, Dark Matter in Galaxies, ed. S. Ryder, D. Pisano, M. Walker, & K. Freeman, 377

Kothes, R., Landecker, T. L., & Gray, A. D. 2010, in Astronomical Society of the Pacific Conference Series, Vol. 438, Astronomical Society of the Pacific Conference Series, ed. R. Kothes, T. L. Landecker, & A. G. Willis, 415

Landecker, T. L., Dewdney, P. E., Burgess, T. A., Gray, A. D., Higgs, L. A., Hoffmann, A. P., Hovey, G. J., Karpa, D. R., Lacey, J. D., Prowse, N., Purton, C. R., Roger, R. S., Willis, A. G., Wyslouzil, W., Routledge, D., & Vaneldik, J. F. 2000, A&AS, 145, 509

Lockman, F. J., Free, N. L., & Shields, J. C. 2012, AJ, 144, 52

McConnachie, A. W., Ferguson, A. M. N., Irwin, M. J., Dubinski, J., Widrow, L. M., Dotter, A., Ibata, R., & Lewis, G. F. 2010, ApJ, 723, 1038

McConnachie, A. W., Irwin, M. J., Ibata, R. A., Dubinski, J., Widrow, L. M., & al. 2009, Nature, 461, 66

Milgrom, M. 1983a, ApJ, 270, 371

—. 1983b, ApJ, 270, 365

Navarro, J. F., Frenk, C. S., & White, S. D. M. 1997, ApJ, 490, 493

Navarro, J. F., Hayashi, E., Power, C., Jenkins, A. R., Frenk, C. S., White, S. D. M., Springel, V., Stadel, J., & Quinn, T. R. 2004, MNRAS, 349, 1039

Navarro, J. F., Ludlow, A., Springel, V., Wang, J., Vogelsberger, M., White, S. D. M., Jenkins, A., Frenk, C. S., & Helmi, A. 2010, MNRAS, 402, 21

Neto, A. F., Gao, L., Bett, P., Cole, S., Navarro, J. F., Frenk, C. S., White, S. D. M., Springel, V., & Jenkins, A. 2007, MNRAS, 381, 1450

Oh, S.-H., de Blok, W. J. G., Walter, F., Brinks, E., & Kennicutt, Jr., R. C. 2008, AJ, 136, 2761

Oosterloo, T., Fraternali, F., & Sancisi, R. 2007, AJ, 134, 1019

Putman, M. E., Peek, J. E. G., Muratov, A., Gnedin, O. Y., Hsu, W., Douglas, K. A., Heiles, C., Stanimirovic, S., Korpela, E. J., & Gibson, S. J. 2009, ApJ, 703, 1486

Randriamampandry, T. H. & Carignan, C. 2014, MNRAS, 439, 2132

Relaño, M., Verley, S., Pérez, I., Kramer, C., Calzetti, D., Xilouris, E. M., Boquien, M., Abreu-Vicente, J., Combes, F., Israel, F., Tabatabaei, F. S., Braine, J., Buchbender, C., González, M., Gratier, P., Lord, S., Mookerjea, B., Quintana-Lacaci, G., & van der Werf, P. 2013, A&A, 552, A140

Sanders, R. H. 1996, ApJ, 473, 117

Sanders, R. H. & McGaugh, S. S. 2002, ARA&A, 40, 263

Sanders, R. H. & Verheijen, M. A. W. 1998, ApJ, 503, 97

Tosaki, T., Kuno, N., Onodera, Rie, S. M., Sawada, T., Muraoka, K., Nakanishi, K., Komugi, S., Nakanishi, H., Kaneko, H., Hirota, A., Kohno, K., & Kawabe, R. 2011, PASJ, 63, 1171

van der Hulst, J. M., Terlouw, J. P., Begeman, K. G., Zwitser, W., & Roelfsema, P. R. 1992, in Astronomical Society of the Pacific Conference Series, Vol. 25, Astronomical Data Analysis Software and Systems I, ed. D. M. Worrall, C. Biemesderfer, & J. Barnes, 131

Warner, P. J., Wright, M. C. H., & Baldwin, J. E. 1973, MNRAS, 163, 163

Zaritsky, D., Elston, R., & Hill, J. M. 1989, AJ, 97, 97